

## **Distribution Agreement**

In presenting this dissertation as a partial fulfillment of the requirements for an advanced degree from Emory University, I hereby grant to Emory University and its agents the non-exclusive license to archive, make accessible, and display my thesis or dissertation in whole or in part in all forms of media, now or hereafter known, including display on the world wide web. I understand that I may select some access restrictions as part of the online submission of this thesis or dissertation. I retain all ownership rights to the copyright of the thesis or dissertation. I also retain the right to use in future works (such as articles or books) all or part of this thesis or dissertation.

Signature:

---

Andrew James Prussia

---

Date

Part I: Measles virus entry into cells and the inhibition of fusion and replication  
Part II: The nature of cyclostreptin's interaction with microtubules

By

Andrew James Prussia  
Doctor of Philosophy

Chemistry

---

Dennis C. Liotta, Ph.D.  
Advisor

---

James P. Snyder, Ph.D.  
Advisor

---

Stefan Lutz, Ph.D.  
Committee Member

---

David G. Lynn, Ph.D.  
Committee Member

Accepted:

---

Lisa A. Tedesco, Ph.D.  
Dean of the Graduate School

---

Date

Part I: Measles virus entry into cells and the inhibition of fusion and replication  
Part II: The nature of cyclostreptin's interaction with microtubules

By

Andrew James Prussia  
B. S., Pensacola Christian College

Advisors:  
Dennis C. Liotta, Ph.D.  
James P. Snyder, Ph.D.

An abstract of  
A dissertation submitted to the Faculty of the Graduate School of Emory University  
In partial fulfillment of the requirements for the degree of  
Doctor of Philosophy  
in Chemistry  
2009

## Abstract

### Part I: Measles virus entry into cells and the inhibition of fusion and replication

### Part II: The nature of cyclostreptin's interaction with microtubules

By Andrew James Prussia

In recent years, resurgence in measles virus infections has occurred in the developed world due to decreased vaccination coverage. To counter this virus and related viruses in the paramyxovirus family, two key functions of the viral lifecycle have been targeted: fusion of the viral and cellular membranes, mediated by viral attachment and fusion glycoproteins; and the replication of the viral genome, mediated by the viral RNA-dependent RNA polymerase complex (RdRp). Using a structural model of the measles virus fusion protein, a series of fusion inhibitors were developed, yielding a compound with 600-3000 nM activity depending on the viral strain. Viral resistance to these inhibitors was demonstrated by mutations that were located on the fusion protein but at positions distal to the predicted binding site. Through models of both the prefusion and postfusion conformations of the fusion protein, a structural proposal consistent with the experimental fusion activities was developed for both the mechanism of action and the occurrence of resistance. Use of these models also facilitated the prediction of a fusion protein containing an engineered disulfide bond that inhibits fusion by stabilization of the prefusion form, but also has restored fusion activity in reducing conditions. Additionally, a model for the interaction of the fusion and attachment proteins was proposed based on available structural information and secondary structure predictions that is fully consistent with experimental results. Finally, a quantitative structure activity relationship was developed for the newly discovered, potent inhibitors of measles virus RdRp.

Cyclostreptin is a recently discovered natural product with cytotoxic activity caused by microtubule stabilization. It is the only known microtubule-stabilizing agent (MSA) which covalently binds to tubulin, but also exhibits the fast binding kinetics seen for other MSAs. Buey et al. found that Thr220, in the type I microtubule pore, is labeled by cyclostreptin, leading the authors to propose Thr220 resides at the previously predicted low-affinity site. Using structural considerations of the microtubule pore and tubulin dimer, an alternative explanation is proposed viewing the microtubule pore as a structural entity that presents a kinetic barrier to ligand passage to the known taxane binding site.

Part I: Measles virus entry into cells and the inhibition of fusion and replication  
Part II: The nature of cyclostreptin's interaction with microtubules

By

Andrew James Prussia  
B. S., Pensacola Christian College

Advisors:  
Dennis C. Liotta, Ph.D.  
James P. Snyder, Ph.D.

A dissertation submitted to the Faculty of the Graduate School of Emory University  
In partial fulfillment of the requirements for the degree of  
Doctor of Philosophy  
in Chemistry  
2009

Acknowledgements:

*Professional*

My advisors, Drs. James Snyder and Dennis Liotta, for all their mentoring and support. You both are motivating and challenging, but at the same time personal and approachable.

Ph.D. committee members Drs. Stefan Lutz and David Lynn, for your thoughtful discussions and encouragement not just during formal meetings, but in casual settings as well.

Dr. Richard Plemper, for the incredible collaboration in virology, without which none of this project would be possible. It has been a pleasure to work with you and your lab members these past several years, including Dr. Jin Lee, Dr. Joshua Doyle, Dr. Melinda Brindley, Tanja Paal, Laura White, and Courtney St. Clair.

Drs. Aiming Sun, Weiqiang Zhan, Jaeki Min, and Maina Ndungu, for providing the other incredible collaboration which makes this project possible, namely your expertise in medicinal chemistry.

Drs. Debbie Mohler, Frank McDonald, and Justin Gallivan for teaching me so much chemistry in your classes.

All the Liotta group members, but especially:

Drs. Ana Alcaraz and Ashutosh Jogalekar. You guys have been there the entire way with me and made up so much of my graduate school experience. I will miss seeing both of you.

Those who preceded me and gave me so much mentoring, including Serdar Kurtkaya and Drs. Ami Lakdawala, Jim Nettles, Pakh Thepchatri, and Matthew Geballe

Those of you behind me in the modeling lab: Haipeng Hu, Mi-Sun Kim, Jin Liu, and Qi Shi; I've enjoyed working with all of you.

And the relative newcomer, Dr. Pieter Burger, thanks for your encouragement during the thesis writing process and the fresh perspective in the lab.

*Personal*

My lovely wife, Heather, who is the most important person in the world to me. Thank you for believing in me and being willing to be married to a graduate student all these years.

My son, Gavin, who has taught me the joy of what it is to be a father.

My next child, due October 31, 2009, who I already know will be an incredible addition to our family.

My parents Stan and Mollie Prussia, who have given me so much love and support my entire life.

My older and younger brothers, both of who are my best friends: thanks for “protecting my brain” many times as chemistry is my only marketable skill.

My chemistry professors at Pensacola Christian College, Dr. Carlos Alvarez and the late Dr. William McCoy: thanks for your examples and personal investment in me.

# Table of Contents

<b>List of Figures</b> .....	<b>xi</b>
<b>List of Tables</b> .....	<b>xiv</b>
<b>Part 1: Measles virus entry into cells and the inhibition of fusion and replication</b> .....	<b>1</b>
<b>Chapter 1: Viruses and their entry into cells</b> .....	<b>2</b>
<b>1.1 Classes of viral fusion proteins</b> .....	<b>4</b>
1.1.1 Class 1 fusion .....	4
1.1.2 Class 2 fusion .....	13
1.1.3 Class 3 Fusion.....	18
<b>1.2 Inhibition of viral fusion</b> .....	<b>21</b>
1.2.1 HIV fusion inhibition .....	22
1.2.3 Respiratory Syncytial Virus fusion inhibition .....	28
<b>1.3 The unique challenge of measles virus entry</b> .....	<b>30</b>
<b>Chapter 2: Early model of the measles virus fusion protein and the discovery of fusion inhibitors</b> .....	<b>32</b>
<b>2.1 Model based on Newcastle Disease Virus fusion protein</b> .....	<b>32</b>
<b>2.2 Discovery of fusion inhibitors of measles virus</b> .....	<b>36</b>
2.2.1 Measles virus fusion protein is confirmed as the target for OX-1 .....	38
2.2.2 Engineered mutations in MeV F induce resistance to OX-1 .....	38
2.2.3 Docking model of OX-1 to the Val94 microdomain.....	39
<b>2.3 Design of a more potent fusion inhibitor</b> .....	<b>41</b>
<b>Chapter 3: Structure-based design of fusion inhibitors</b> .....	<b>43</b>
<b>3.1 AM-4 analogs</b> .....	<b>43</b>
3.1.1 SAR for compounds with a mono-substituted acetanilide phenyl ring .....	45
3.1.2 SAR for compounds with a disubstituted acetanilide phenyl ring .....	47
3.1.3 SAR for compounds with modifications on the distal phenyl ring and the intermediate linker region .....	50
<b>3.2 Balance between the polar interactions and the desolvation penalty</b> .....	<b>52</b>
<b>3.3 AS-48 as a model fusion inhibitor</b> .....	<b>53</b>
<b>Chapter 4: Resistance to AS-48 fusion inhibition</b> .....	<b>55</b>
<b>4.1 Adaptation study of MeV to AS-48</b> .....	<b>55</b>
<b>4.2 Resistance-conferring mutations located in a model of the MeV F 6HB</b> .....	<b>58</b>
4.2.1 Homology model of the MeV F 6HB .....	58
4.2.2 Models of the MeV F 6HB with resistance-conferring mutations .....	61
<b>4.3 Destabilizing effect of the mutations</b> .....	<b>62</b>
4.3.1 Peptide inhibition with wild-type and mutated HR-B domains .....	63
4.3.2 Molecular dynamics studies of wild-type and mutated 6HB structures.....	64
4.3.3 Mutation of the HR-A residue interacting with Asn462 .....	66
4.3.4 Coimmunoprecipitation efficiency of MeV F with a Flag-tagged variant of the HR-B derived peptide.....	66
<b>4.4 Mutations affect the fusion activation of MeV F</b> .....	<b>67</b>
4.4.1 Transport competence of mutant MeV F constructs restored at 30°C.....	67
4.4.2 AS-48 stabilizes a transport-competent prefusion conformation .....	69
<b>4.5 Dual roles of the MeV F residue 462</b> .....	<b>70</b>

<b>Chapter 5: Conformational changes in MeV F during fusion.....</b>	<b>72</b>
<b>5.1 Limitations of the NDV based model of MeV F .....</b>	<b>72</b>
<b>5.2 New model of the postfusion form of MeV F.....</b>	<b>73</b>
<b>5.3 Prefusion model of MeV F .....</b>	<b>75</b>
<b>5.4 Structural features and changes in the prefusion and postfusion MeV F models ....</b>	<b>75</b>
5.4.1 Pre- and postfusion MeV F models imply large domain movements during fusion	76
5.4.2 The hydrophobic character of the HR-A and HR-B domains is consistent with the proposed model of fusion.....	80
5.4.3 The large, water-filled cavity in the prefusion protein is a metastable feature that provides MeV F with a source of potential energy.....	81
5.4.4 The Val94 microdomain is rearranged and occluded in the prefusion model	85
<b>5.5 The nature of the AS-48 binding to the Val94 microdomain.....</b>	<b>88</b>
5.5.1 Defined antisera against the Val94 microdomain .....	88
5.5.2 Conformational state of MeV F targeted by AS-48 .....	91
<b>5.6 Structural proposal for the development of AS-48 resistance .....</b>	<b>94</b>
5.6.1 MeV F residues 462 and 367 are located at the critical interface between the HR-B and DI domains in the prefusion conformation of F.....	94
5.6.2 Mutations at MeV F residues 462 and 367 disrupt the hydrophobic interactions holding the HR-B and HR-linker to the DI domain.....	95
5.6.3 Mutations at position 462 enhance fusion activity at lower temperatures ..	100
<b>5.7 Limitations of the AS-48 molecular scaffold .....</b>	<b>101</b>
<b>Chapter 6: Fusion inhibition through stabilization of prefusion MeV F.....</b>	<b>104</b>
<b>6.1 An engineered disulfide bridge in prefusion MeV F .....</b>	<b>104</b>
6.1.1 Molecular modeling of disulfide bonds in prefusion MeV F .....	104
6.1.2 Expression and fusion activity of F candidates with engineered disulfide bonds	107
6.1.3 Oligomerization of F variants with engineered disulfide bonds. ....	108
6.1.4 Reactivation of fusion activity by DTT-treatment confirms proper folding of F-Edm 452C/460C and arrest in a prefusion conformation.....	110
<b>6.2 Screening for small molecule inhibitors of prefusion MeV F .....</b>	<b>113</b>
6.2.1 Computational identification of the target site in the prefusion MeV F model	113
6.2.2 Further refinement of the prefusion MeV F structure .....	114
6.2.3 Virtual screen at the HR-B / head domain interface.....	117
6.2.4 Biological testing of the compounds selected by virtual screening .....	119
<b>Chapter 7: Functional interaction between paramyxovirus fusion and attachment proteins.....</b>	<b>122</b>
<b>7.1 Differential activation of F and H in morbilliviruses .....</b>	<b>124</b>
7.1.1 MeV H efficiently triggers CDV F-ODP but not CDV F-Lederle.....	124
7.1.2 Minimal domain required for heterotypic triggering of CDV F-ODP .....	126
7.1.3 Four point mutations disrupt productive interaction of F-ODP with MeV H127	
7.1.4 Location of the four point mutations in a structural model of CDV F .....	128
7.1.5 Changes in the strength of H and F interaction due to mutations .....	129
7.1.6 Assay reversal demonstrates the H stalk domain determines productive interaction of MeV H with CDV F-Lederle .....	130
7.1.7 A five-residue fragment in the MeV H stalk determines specificity for F-Lederle	131
7.1.8 Co-expression of F and H chimeras reveals interdependence of the identified residues in productive H-F interaction.....	132

7.1.9	Role of identified F residues in homotypic fusion .....	133
<b>7.2</b>	<b>Structural model of morbillivirus H-F interaction .....</b>	<b>135</b>
7.2.1	Structural prediction of the MeV H stalk domain .....	136
7.2.2	Structural model for the entire MeV H ectodomain .....	138
7.2.3	Hypothetical MeV H – CDV F interaction model.....	138
<b>7.3</b>	<b>Probing the spatial organization of H-F complexes.....</b>	<b>142</b>
7.3.1	Effect of engineering N-glycosylation sites into the H stalk.....	143
7.3.2	H residues 111 and 114 are determinants for F triggering .....	147
7.3.3	Only stalk elongation downstream of residues 111 and 114 is compatible with F triggering.....	150
7.3.4	Extensive stalk insertions argue against specific contacts between H and F head domains .....	154
7.3.5	Overall consistency of the H-F interaction model with experimental evidence.....	156
<b>7.4</b>	<b>H-F interaction model with tetrameric H.....</b>	<b>158</b>
7.4.1	Predicting the tetrameric MeV H structure .....	160
7.4.2	Compatibility of the MeV H tetramer model with natural glycosylation sites.....	165
7.4.3	Incorporating tetrameric MeV H in the H-F interaction model.....	166
<b>Chapter 8:</b>	<b>RNA-dependent RNA polymerase inhibitors .....</b>	<b>170</b>
<b>8.1</b>	<b>Qualitative SAR for compound 1 analogs .....</b>	<b>171</b>
<b>8.2</b>	<b>Quantitative SAR for compound 1 analogs .....</b>	<b>175</b>
<b>8.3</b>	<b>SAR conclusions for compound 1 analogs .....</b>	<b>180</b>
<b>Chapter 9:</b>	<b>Conclusions and future directions .....</b>	<b>181</b>
<b>9.1</b>	<b>MeV fusion inhibition .....</b>	<b>181</b>
<b>9.2</b>	<b>H-F interaction .....</b>	<b>182</b>
<b>9.3</b>	<b>RdRp inhibition.....</b>	<b>182</b>
<b>Part 2:</b>	<b>The nature of cyclostreptin’s interaction with microtubules.....</b>	<b>184</b>
<b>1.1</b>	<b>The binding of microtubule stabilizing agents .....</b>	<b>185</b>
<b>1.2</b>	<b>Docking of cyclostreptin to the microtubule .....</b>	<b>189</b>
1.2.1	No defined MSA binding site is present in the microtubule pore .....	189
1.2.2	CS binding most favorable at the taxane binding site .....	190
<b>1.3</b>	<b>Constrained molecular dynamics of MSAs in the microtubule pore .....</b>	<b>195</b>
1.3.1	MSA diffusion across the microtubule pore.....	195
1.3.2	Blockage of MSA diffusion by cyclostreptin .....	198
1.3.3	CS labels Thr220 due to its exposure in the microtubule pore.....	200
<b>1.4</b>	<b>Molecular dynamics simulation of the <i>apo</i>-tubulin dimer .....</b>	<b>202</b>
1.4.1	CS binding at the taxane site is blocked by the M-loop .....	202
1.4.2	Thr220 remains exposed in <i>apo</i> - and MSA-bound tubulin dimer.....	205
<b>1.5</b>	<b>Conclusions on the nature of MSA binding to microtubules.....</b>	<b>205</b>
1.5.1	Weak microtubule polymerization by CS is explained by its limited effect on the M-loop .....	205
1.5.2	CS labeling of Asn228 could occur through migration during MS.....	206
1.5.3	Two activation energies for CS binding to tubulin are unlikely .....	211
1.5.4	Implications for the design of new MSAs .....	212
<b>References</b>	<b>.....</b>	<b>213</b>

## List of Figures

### Part 1: Measles virus entry into cells and the inhibition of fusion and replication

Figure 1-1: Model of the viral fusion process	4
Figure 1-2: Schematic examples of class 1 fusion proteins	6
Figure 1-3: Structural examples of class 1 fusion proteins	11
Figure 1-4: Schematic examples of class 2 fusion proteins	14
Figure 1-5: Structural examples of class 2 fusion proteins	16
Figure 1-6: Schematic and structural examples of class 3 fusion proteins	20
Figure 1-7: Structure of the HIV fusion inhibitor enfuvirtide	24
Figure 1-8: Small molecule HIV fusion inhibitors	24
Figure 1-9: Small molecule inhibitors of influenza fusion	27
Figure 1-10: Inhibitors of RSV fusion	29
Figure 2-1: Phylogenetic tree for the paramyxovirinae subfamily of paramyxoviridae	35
Figure 2-2: Homology model for MeV F based on NDV F	35
Figure 2-3: Focused screen of compounds for antiviral activity	37
Figure 2-4: The binding model for OX-1	40
Figure 2-5: Binding model for AM-4	42
Figure 3-1: Three sectors of 2-phenylacetanilide envisioned as a scaffold of AM-4	43
Figure 3-2: Docking models for <b>3a</b> , <b>4a</b> and <b>3f</b>	46
Figure 3-3: Comparison between the docking models for AM-4, <b>7i</b> , and <b>8</b>	48
Figure 3-4: Docking models for disubstituted nitro compounds <b>11g</b> and <b>11f</b>	50
Figure 3-5: Docking model for <b>7e</b> with a <i>p</i> -OMe group on the distal phenyl group	52
Figure 3-6: Balance between polar interactions and the energy of solvation	53
Figure 4-1: Locations of spontaneous mutations conferring resistance	60
Figure 4-2: Localization of residue 462 in the MeV F core structure	62
Figure 4-3: Peptide competition assay	64

Figure 4-4: MD simulations of the mutant and wild type 6HBs	66
Figure 4-5: Temperature sensitivity of F mutants 94G 462S and 94G 462N	69
Figure 5-1: Homology models of MeV F based on different postfusion templates	74
Figure 5-2: Secondary structure diagrams of MeV F protein homology models	77
Figure 5-3: Morphing simulation from the prefusion to postfusion structures	79
Figure 5-4: Potential energy sources in fusion refolding	84
Figure 5-5: Changes in the Val94 microdomain occurring during fusion	85
Figure 5-6: Co-immunoprecipitation experiments with AS-48 and two antibodies	90
Figure 5-7: Proposed fusion pathway for MeV F	93
Figure 5-8: Position of resistance-conferring mutations at Asn462 and Ala367	97
Figure 5-9: Predicted structures for resistance-conferring mutations	99
Figure 5-10: Enhanced fusion activity of MeV F N462S and N462K variants	101
Figure 6-1: Predicted geometries of disulfide bonds in the prefusion MeV F trimer	106
Figure 6-2: F-Edm 452C/460C double mutant lacks fusion activity	108
Figure 6-3: Disruption of F-Edm 452C/460C trimers requires reducing conditions	110
Figure 6-4: Reactivation of F-Edm 452C/460C fusion activity in reducing conditions	112
Figure 6-5: Predicted small molecule binding site at the HR-B / DII interface	114
Figure 6-6: Results of the 1 ns MD simulation of the prefusion MeV F model	117
Figure 6-7: Three examples of compounds selected by virtual screening	119
Figure 7-1: CDV F-ODP but not CDV F-Lederle is triggered by MeV H	126
Figure 7-2: Identified residues in a structural model of the prefusion CDV F	129
Figure 7-3: Residues in a MeV H N-terminal domain are determinants for F	131
Figure 7-4: Residues identified in F and H act interdependently	133
Figure 7-5: Residues implicated in homotypic MeV fusion	135
Figure 7-6: Secondary structure predictions for MeV H	137
Figure 7-7: Sequence alignment of MeV H stalk to cortexillin I	138
Figure 7-8: Two possible hypotheses of H-F alignment	140

Figure 7-9: Ribbon representation of a hypothetical H-F interaction modes	144
Figure 7-10: Assessment of H variants for transport, receptor binding, and fusion	146
Figure 7-11: H stalk residues 111 and 114 are determinants for H-F interaction	149
Figure 7-12: Insertion and deletion of HR elements in the H stalk	153
Figure 7-13: Insertion of multiple heptad repeat elements	156
Figure 7-14: Predicted MeV H head domain dimer structure by RosettaDock	162
Figure 7-15: RosettaDock results for MeV H tetramer prediction	164
Figure 7-16: Compatibility of N-glycosylation sites in the MeV H tetramer model	166
Figure 7-17: Hypothetical interaction model of tetrameric H with F	168
Figure 8-1: Sectors of RdRp inhibitor compound 1 used as an SAR template	171
Figure 8-2: Variation scaffolds of piperidine analogues	174
Figure 8-3: QSAR results for RdRp inhibitors	178

## **Part 2: The nature of cyclostreptin's interaction with microtubules**

Figure 1: Structure of cyclostreptin	187
Figure 2: Shape and lipophilic character of tubulin and taxane site ligands	190
Figure 3: Results of docking cyclostreptin in the microtubule	193
Figure 4: Comparison of the lipophilic character of CS and the microtubule pore	195
Figure 5: MD trajectories of MSAs through the microtubule pore	198
Figure 6: MD trajectories of MSAs through the cyclostreptin microtubule pore	200
Figure 7: Snapshot of CS after 38 ps of MD through the microtubule pore	202
Figure 8: Displacement of M-loop and exposure of Thr220 in the free tubulin dimer	204
Figure 9: Docking pose which places CS in the taxane site near His229	208
Figure 10: Proposed mechanism of CS migration	210

## List of Tables

### Part 1: Measles virus entry into cells and the inhibition of fusion and replication

Table 3-1: Antiviral MeV IC <sub>50</sub> 's for mono-substituted acetanilides	46
Table 3-2: Antiviral MeV IC <sub>50</sub> 's for di-substituted phenol <b>7</b> series	48
Table 3-3: Antiviral MeV IC <sub>50</sub> values for disubstituted nitro and aniline series	50
Table 4-1: Identification of mutations conferring resistance	57
Table 8-1: Antiviral MeV biological activities for <b>1</b> analogues	172

## Abbreviations

Six-helix Bundle (6HB)

Three-helix Bundle (3HB)

Heptad Repeat (HR)

Fusion Protein (F)

Transmembrane Domain (TM)

Fusion Peptide (Fpep)

Measles Virus (MeV)

Newcastle Disease Virus (NDV)

Influenza Hemagglutinin (HA)

Human Parainfluenza Virus 3 (hPIV3)

Parainfluenza Virus 5 (PIV5)

Half Maximal Inhibitory Concentration ( $IC_{50}$ )

Measles Virus Edmonston Strain (MeV-Edm)

Molecular Dynamics (MD)

Dithiothreitol (DTT)

Nanosecond (ns)

Picosecond (ps)

Femtosecond (fs)

Root Mean Square Deviation of Backbone Atoms ( $RMSD_{backbone}$ )

Canine Distemper Virus (CDV)

CDV-Onderstepoort (CDV-ODP)

Paramyxovirus Hemagglutinin (H)

Paramyxovirus Hemagglutinin-Neuraminidase (HN)

Human Parainfluenza Virus 2 (HPIV2)

RNA-dependent RNA polymerase complex (RdRp)

Half Maximal Effective Concentration ( $EC_{50}$ )

Molecular Field Topology Analysis (MFTA)

Structure-Activity Relationships (SAR)

Quantitative Structure-Activity Relationships (QSAR)

Cytopathic Effect (CPE)

Selectivity Index (SI)

Cyclostreptin (CS)

Microtubule Stabilizing Agent (MSA)

Paclitaxel (PTX)

# **Part 1: Measles virus entry into cells and the inhibition of fusion and replication**

## Chapter 1: Viruses and their entry into cells

Viruses represent a unique class of organism which cannot exist without more advanced forms of life. They take advantage of the cellular machinery to accomplish a singular goal: replication. Although viruses utilize different shapes, hosts, proteins, and mechanisms in this goal, successful viruses persist only because they continue to replicate. Because of this exploitation of cells, viruses, like their namesakes in computer science, can afford to be simple, inefficient, and imprecise. They must only strike a balance between virulence and infectivity: if they kill the infected organism before spreading to other hosts, the virus's extinction will result.

For viruses enveloped in a lipid bi-layer, a key step in the viral life-cycle is the fusion of the viral and cellular membranes, allowing the viral genetic material to enter the cell and begin to utilize the cell's resources.<sup>1,2</sup> Although fusion of two membranes is thermodynamically favorable, a ~ 40-50 kcal/mol barrier must be overcome for fusion to occur.<sup>3,4</sup> Enveloped viruses overcome this barrier with the free energy released by conformational changes in their fusion proteins. These fusion proteins are membrane-bound, have large ectodomains, and fold into a metastable state. They are activated for fusion by proteolysis of either in the fusion protein itself or another viral surface protein. While their molecular architecture varies across the families of viruses, the core mechanisms for catalyzing fusion are remarkably similar. These mechanisms require lowering the transition state energies at multiple steps to enable fusion. Viral fusion proteins accomplish this by coupling the barriers between steps in membrane fusion to stabilizing conformational changes in the protein. The process does not require ATP and is irreversible.<sup>5</sup>

The existence of viral fusion proteins in metastable states would not serve the virus well if the conformational change occurred without a nearby cellular membrane to target. Viruses thus have triggering mechanisms which allow them to sense the presence of a nearby target membrane either through the low pH environment of the endosome or through cellular surface proteins.<sup>1</sup> In some viruses, the triggering mechanism is a function of the fusion protein itself; other viruses are thought to use additional viral proteins to sense target membranes and transmit that information to the fusion protein.<sup>6</sup>

The fusion process is illustrated in **Figure 1-1** for viruses which use an additional protein for the triggering mechanism. Prior to fusion, multiple spikes from fusion (yellow) and attachment (green) proteins decorate the viral envelope (bottom membrane).<sup>1</sup> Both proteins are attached to the viral envelope through helical transmembrane domains (shown as gray for the fusion protein). The fusion proteins' conformational changes are initiated in this example by a receptor on the cell surface (represented by X). Binding to this receptor by the viral attachment protein triggers the fusion proteins to begin their conformational changes. In this example, a hydrophobic fusion peptide (FP, shown as black) inserts into the target cellular membrane, in the process forming a three helix coiled coil composed of heptad repeat region HRA (shown as red cylinders). This movement is followed by the positioning of another heptad repeat region, HRB (shown as blue cylinders), which is connected to the viral membrane, into the complimentary grooves of the HRA coiled coil, and forming an extremely stable six helix bundle. Doing so forces the viral and cellular membrane in proximity, destabilizing their structure and causing membrane merger and ultimately pore formation. As indicated by the far right panel, multiple fusion proteins are required for this process; 4-6 fusion

proteins are considered necessary for each pore formation. Also shown in this figure are exogenous HRA and HRB peptides which can act as inhibitors to the fusion process by preventing the formation of the six helix bundle. Although this basic outline for the fusion process remains the same, different viruses vary this theme by incorporating fusion triggering in the fusion protein itself, using structural elements other than helices to stabilize the postfusion structure, using fusion loops instead of peptides, and varying the oligomerization state.

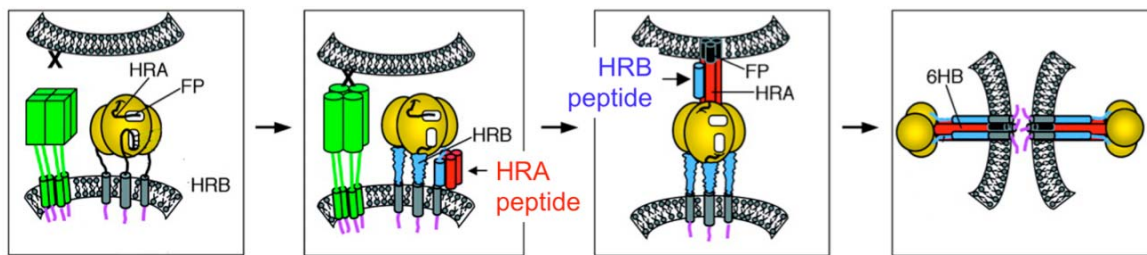


**Figure 1-1:** Model of the viral fusion process, adapted from Russel et al.<sup>7</sup>

## 1.1 Classes of viral fusion proteins

Common features seen in all viral fusion proteins are a large ectodomain, a single transmembrane domain and a cytoplasmic tail.<sup>2</sup> Viral fusion proteins have traditionally been classified as class 1, 2 and 3 according to structural criteria. Important differences within classes and similarities between classes have since emerged causing some to question its current applicability.<sup>1</sup> Nonetheless, the nomenclature is retained here due for its simplicity and pedagogic value, anticipating that the community may reassess these classes in the future.

### 1.1.1 Class 1 fusion

Class 1 fusion proteins represent the largest segment of known fusion proteins in the viral families. These proteins are synthesized as three identical polypeptide chains which assemble into trimers. (Recent reviews are available by Harrison,<sup>1</sup> Weissenhorn et

al.,<sup>8</sup> Lamb et al.,<sup>5,9</sup> Earp et al.,<sup>2</sup> and Colman et al.<sup>10</sup>) The uncleaved precursor is in an inactive form and undergoes subsequent cleavage by a host cell protease or viral protein to create the metastable form. The proteolytic step allows the protein to circumvent the problem of initially folding a protein into a conformation that is in a metastable state instead of the more stable, postfusion state: prior to cleavage, the energetic difference between these two states must be much lower, allowing folding to the prefusion state. (Initial folding and premature folding to the postfusion state are also likely, though these proteins will not assist in fusion.<sup>11,12</sup>) The resulting two subunits remain associated through only non-covalent interactions in some viruses; in other viruses the subunits are additionally linked through disulfide bonds. The cleavage occurs at a specific site on the protein, N-terminal to a hydrophobic stretch of residues referred to as the fusion peptide. It is these 20-25 residues that will insert into the target cell's membrane. Another unique structural feature of class 1 fusion is the formation of six-helix bundles (6HB) in the postfusion conformation of the protein. These 6HBs are formed from heptad repeat (HR) sequences within the fusion protein with each subunit contributing an inner helix and an outer helix. The resulting structures are characterized by their stability: they form spontaneously with expressed peptides and exhibit melting points near 100 °C.<sup>5,9</sup> In all class 1 fusion proteins, these HR regions are sequentially located near the transmembrane anchors for the viral and target membranes (**Figure 1-2**). Thus, formation of the 6HB is thought to be closely coordinated with the merger of the membranes.

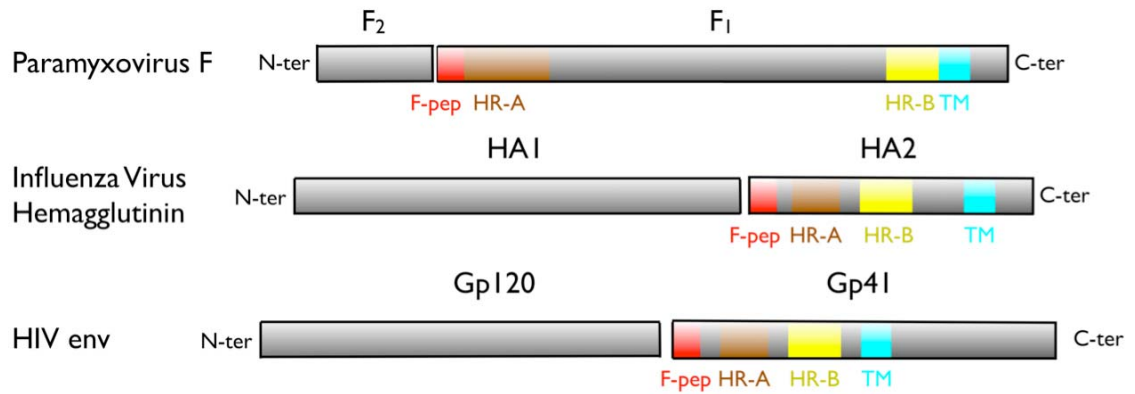


**Figure 1-2:** Schematic examples of class 1 fusion proteins. All fusion proteins in this class are synthesized as polypeptides which assemble into inactivated trimers. Activation occurs through cellular proteolysis at sites N-terminal to the hydrophobic fusion peptide (F-pep). The cleaved proteins are thus generated in a metastable state primed for fusion because the F-pep is released for possible interaction with the target membrane, although it is also possible for the uncleaved protein to spontaneously refold to a postfusion form.<sup>11</sup> Heptad repeat (HR) regions adjacent to the fusion peptides (HR-A) and transmembrane domains (HR-B) are distant from each other in the prefusion form of the proteins, but form closely associated, stable 6HBs postfusion. The formation of these 6HBs is thought to be coordinated with merger of the viral and cellular membranes.

While the basic outline of class 1 fusion proteins are similar, there is little sequence homology between virus families, and the structures of the fusion proteins vary considerably.<sup>5</sup> (**Figure 1-3**) This probably reflects the diverse stimuli needed for fusion activation in each virus family. For example, influenza hemagglutinin has the ability to detect and respond to the low pH environment of the endosome. Paramyxovirinae (excepting Human Metapneumovirus, which fuses at low pH<sup>13</sup>) can fuse at the neutral pH of extracellular space but rely on another viral surface glycoprotein to bind to cellular receptors and trigger the fusion protein (excepting Respiratory Syncytial Virus, which can fuse without the aid of its partner glycoprotein, G<sup>14</sup>). HIV also has both cellular receptor binding and fusion activity in its envelope protein, yet can fuse at neutral pH.

For class 1 fusion proteins, prefusion and postfusion structures are known for only two families of viruses, orthomyxoviridae and paramyxoviridae (**Figure 1-3**). The well-known orthomyxovirus, influenza, was the first to have structures determined. In a landmark study published in 1981, John Skehel and Don Wiley revealed the structure of the prefusion form of the hemagglutinin protein (HA).<sup>15</sup> The postfusion form was finally determined in 1994<sup>16</sup> and the uncleaved precursor in 1998.<sup>17</sup> These structures revealed the large conformational changes occurring during fusion. Prior to fusion, the HA1 fragment resides at the top of the protein and surrounds the HA2 fragment. At this point, the fusion peptides are safely packed between helices of the HA2 subunits. HA1 surrounds HA2 and contains the sialic acid-binding domain, allowing the virus to attach itself on cellular glycoproteins or glycolipids with this sugar exposed until endocytosis occurs. Within the low pH environment of the endosome, HA is activated for fusion. The specific residues involved in this activation are unclear; mutagenesis shows that there is a

level of redundancy to this pH-regulated process as loss of one residue site may not change the protein's fitness or pH dependence. Once activation occurs, HA1 separates from HA2 and remains connected only through a disulfide bond located near the viral membrane. This separation releases the fusion peptides and allows them to target the cellular membrane. Nearby the fusion peptide, the HR-A residues sequentially unravel from their previous secondary structure and move to the top of the protein, greatly extending HA2's central three-helix bundle. This three-helix bundle forms the grooves with which the HR-B residues will closely associate. HR-B, which is sequentially close to the transmembrane domain, also unravels from its previous secondary structure and zips up the inner three-helix bundle with outer helices and an extended coil. This zipping up of the structure forces the membranes into proximity and to ultimately merge. While it appears in **Figure 1-3** that the postfusion protein has been moved up, this is because the bottom of the central three-helix bundle is unraveled and moved to form the outer helix. Residues 76-105, making up the center of the three-helix bundle, change very little from prefusion to postfusion structure.

Both prefusion and postfusion structures for paramyxoviruses were determined recently. The first atomic level structure was solved in 2003 by manipulating the Newcastle Disease Virus (NDV).<sup>18</sup> At the time it was not clear whether the NDV fusion protein (NDV F) was crystallized in its prefusion or postfusion state, although some evidence pointed toward the post fusion form. Although the protein had been purified as an uncleaved precursor, proteolysis had occurred and large portions of the protein were not resolved, particularly the fusion peptide and HR-B regions. The NDV F structure was later revealed as postfusion by comparison to the X-ray structure for the uncleaved

ectodomain of human parainfluenza virus 3 fusion protein (hPIV3 F), which had crystallized with a 6HB.<sup>11</sup> The same collaboration which determined the hPIV3 F structure, Theodore Jardetzky and Robert Lamb, later determined the uncleaved prefusion structure of parainfluenza virus 5 fusion protein (PIV5 F).<sup>19</sup> Through comparison of hPIV3 F and PIV5 F, even larger conformational changes than influenza's HA are revealed. Prior to fusion, the HR-B domain forms a three-helix bundle with itself and is attached to the viral membrane through the sequentially nearby TM domain. The fusion peptide resides in the globular head, at the interface between the DI and DII domains maintained in both structures and the DIII domain which undergoes substantial changes. The protein is activated for fusion through the assistance of another viral surface glycoprotein which binds to cellular receptors (named hemagglutinin (H), hemagglutinin-neuraminidase (HN), or simply glycoprotein (G), depending on the viral genus) and starts the conformational changes in the fusion protein through a mechanism which is still unclear. What is more clear are the conformational changes that must occur in the fusion cascade: the fusion peptide and adjacent HR-A domain unravel from their positions on the globular head and move upward, inserting the fusion peptide into the target membrane. In doing so, the HR-A domains form the central three-helix bundle (3HB) of the post-fusion structure. Concurrently, the 3HB formed by the HR-B domains in the prefusion structure dissociates and disconnects from the globular head, also moving the top of the protein and ultimately forming a 6HB with the HR-A domains. While moving to the top of the protein, the HR-B domains remain connected to the viral membrane through adjacent TM domains, thus forcing the cellular membrane attached by the fusion

peptides to the HR-A domain into proximity of the viral envelope and finally causing merger of the membranes.

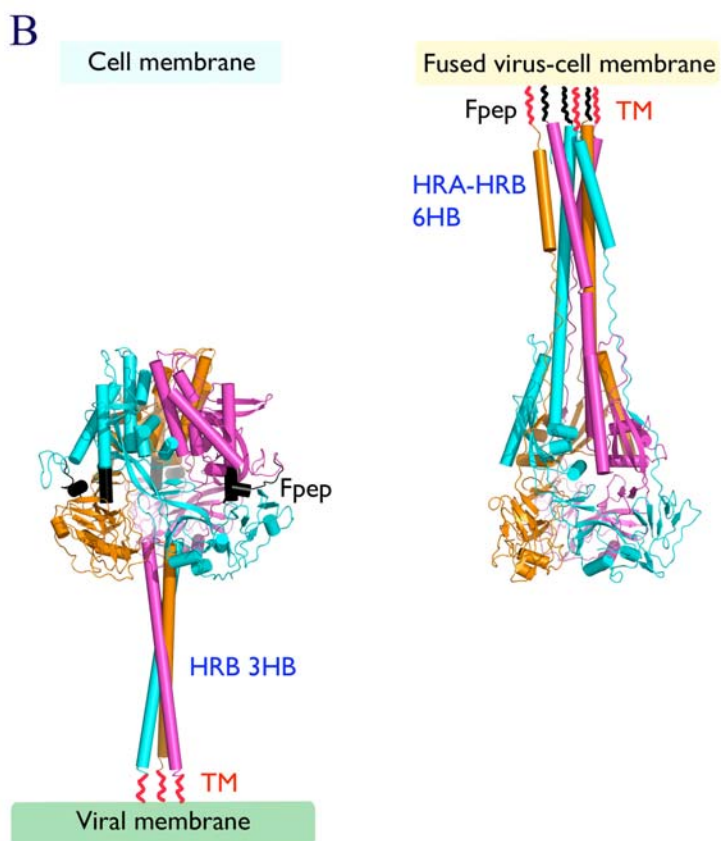
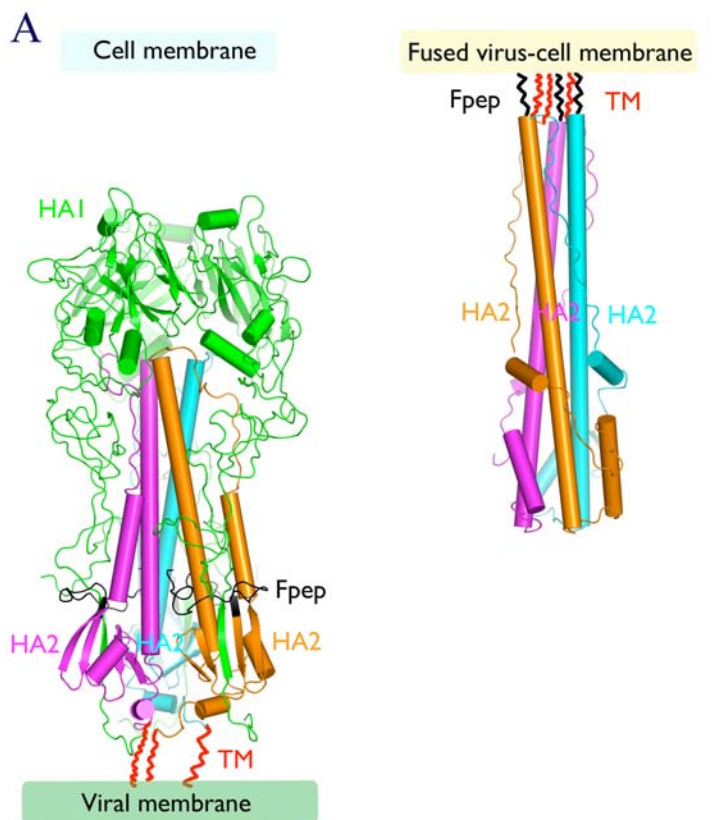


**Figure 1-3** (previous page): Structural examples of class 1 fusion proteins. The prefusion forms are shown on the left and the postfusion forms on the right. (A) Influenza hemagglutinin (PDB codes 1HGE<sup>20</sup> and 1QUI<sup>21</sup> for prefusion and postfusion structures, respectively), shown with HA1 colored green and HA2 colored magenta, cyan, and orange by subunit. The fusion peptide (Fpep) is colored black. The transmembrane (TM) domain is not resolved in the structure but its position is shown with red lines. The structures are aligned by HA2 residues 76-105, which form part of the central three-helix bundle which is retained in both conformations. During fusion, HA1 separates from HA2 and the HA2 subunit rearranges to form a six-helix bundle and coiled-coil interaction. Although not shown in the structure, HA1 remains attached to the HA2 through a disulfide bonds (not shown) between residues 134 and 14 on HA1 and HA2, respectively. (B) Paramyxovirus fusion protein (PDB codes 2B9B<sup>19</sup> and 1ZTM<sup>11</sup> for prefusion and postfusion structures, respectively), colored by subunit. The Fpep and TM domain are also colored black and red, respectively. Portions of the protein that are unresolved are drawn as black and red lines. The structures are aligned by the DI and DII domains (~154 residues), which are structurally conserved in both structures. During fusion, the fusion peptide and adjacent HR-A domains move upward, forming a long, central three-helix bundle (3HB) into which the HR-B helices will insert. PyMol version 0.98<sup>22</sup> was used to prepare this figure.

### 1.1.2 Class 2 fusion

Class 2 viral fusion proteins, as seen in members of the flavivirus and alphavirus families, use a much different strategy for penetrating cellular membranes.<sup>1, 2, 6, 8</sup> These viruses have two envelope proteins, referred to as prM and E for flaviviruses and pE2 and E1 for alphaviruses (**Figure 1-4**). The E/E1 protein contains the fusion activities; the prM/pE2 protein functions as a chaperone in the folding of E/E1, preventing misfolding to the post-fusion conformation. After these proteins are assembled together in the endoplasmic reticulum, furin cleaves off a portion of the ectodomain of the prM/pE2 protein, priming the E/E1 protein for low pH-induced fusion. This is in contrast to class 1 fusion proteins, which are activated for fusion by cleavage on the fusion protein directly. After this cleavage, the PE2 protein remains associated to E1 in alphaviruses as a heterodimer and is now named E2. The E2/E1 heterodimer is transported to the plasma membrane for subsequent viral budding where E2 provides receptor binding activity and E1 the fusion activity. Flaviviruses, on the other hand, bud in the endoplasmic reticulum as immature virions with 60 trimers of prM/E. At this stage, the prM protein covers the E protein much like the E2 does E1 in alphaviruses. As the immature virion is transported in the exocytic pathway, cleavage of the prM protein removes most of its ectodomain, leaving only 40 residues. The loss of inter-protein contacts causes the E protein to reorganize as 90 E-E homodimers on the flavivirus surface. Mature flaviviruses thus have smooth, spikeless surfaces, with their E-E homodimers providing both receptor binding and fusion activities, lying parallel to the membrane in a manner reminiscent of a bear trap. Mature alphaviruses, by contrast, have spikes on their viral surfaces from the E2 portion of the heterodimer that provide the receptor binding activity.

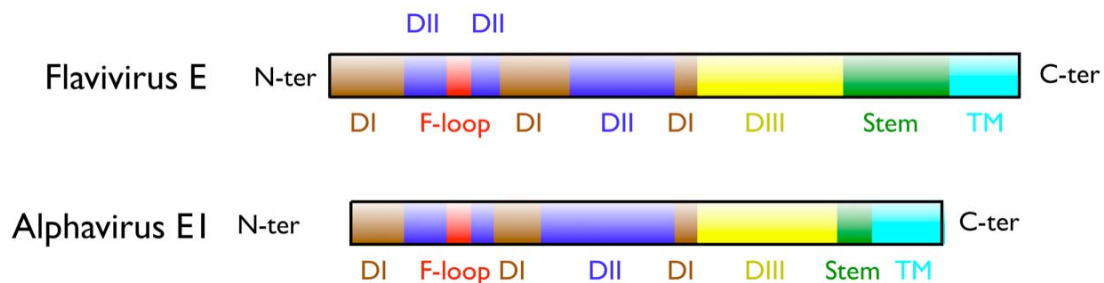


**Figure 1-4:** Schematic examples of class 2 fusion proteins. Fusion proteins in this class are synthesized with another viral envelope protein which functions as a chaperone, enabling folding to the prefusion, metastable state. The DI and DIII domains are beta-barrel motifs which form stable 6-domain bundles reminiscent of the 6HB of class 1 fusion proteins. Like HR-A and HR-B, these DI and DIII domains are loosely associated with each other prefusion, but form tight interactions postfusion. Prior to fusion, the proteins are arranged in dimers on the viral surface, but after activation through the low pH of the endosome, the proteins assemble into trimers, formed by intersubunit interactions of the DII domains.

The prefusion and postfusion X-ray crystal structures for both virus families reveal that class 2 fusion proteins use similar concepts in fusion, but completely different structural elements (**Figure 1-5**).<sup>23-26</sup> Instead of a fusion peptide, both E and E1 proteins contain a hydrophobic fusion loop of ~17 residues which buries into the target cellular membrane. Prior to fusion, the fusion loop is concealed at the interface of the E-E homodimers in flaviviruses and the E2/E1 interface in alphaviruses. The fusion loop is in the DII domain of the protein, which consists of a long, extended beta-sheet. The DII domain is connected to two tight beta-barrel domains named DI and DIII. The stem domain connects the DI domain to the transmembrane domain. In a manner reminiscent of HR-A and HR-B, these DI and DIII domains are loosely associated with each other prefusion, but form tight interactions postfusion. In another key divergence from class 1 fusion, class 2 proteins utilize a change in oligomeric state when activated for fusion. In response to the acidic environment of the endosome, the fusion proteins go from E-E homodimers and E2/E1 heterodimers to E and E1 trimers formed by interactions of the DII domains. In doing so, the fusion loops are exposed and bury themselves into the target membrane. At this point, the viral and cellular membranes are tied together, but not yet fused. Fusion is accomplished by moving the DI domain in a position in which it stably interacts with the DIII domain, carrying with it the stem and transmembrane domain. The stem then forms stable interactions with the DII domain and forces the viral membranes in proximity and ultimately promotes fusion.

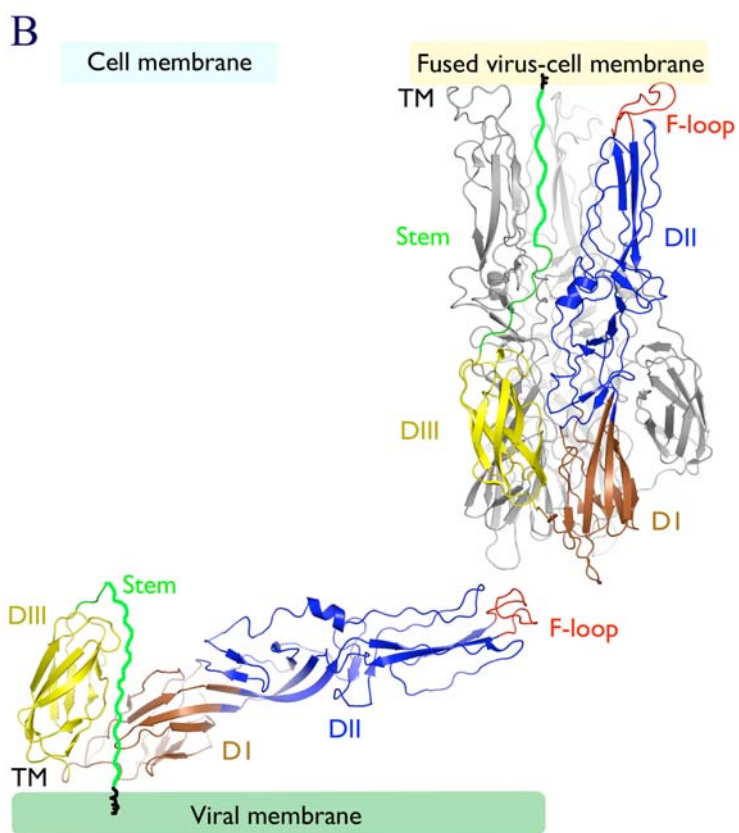
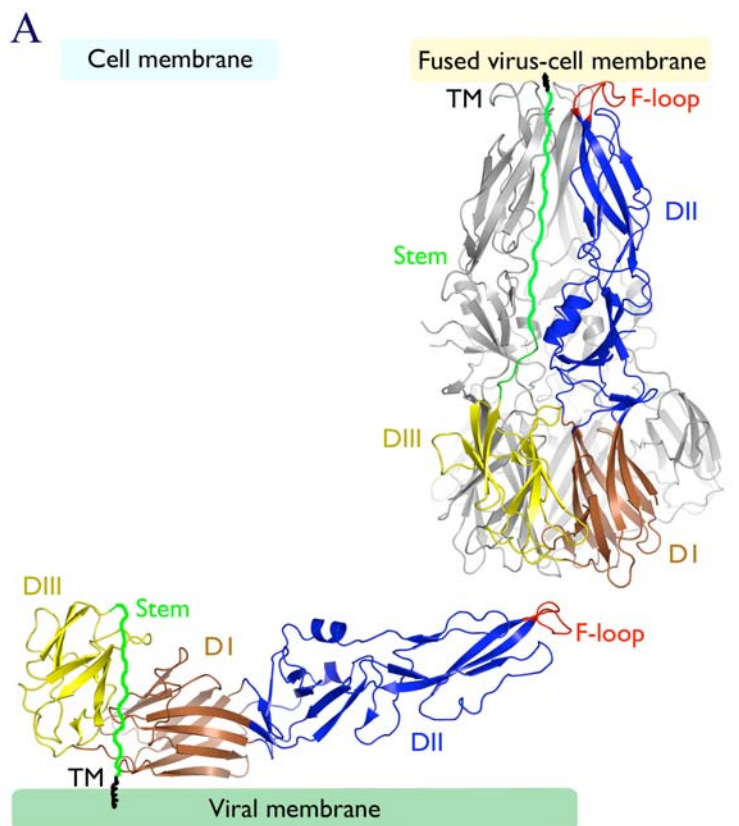


**Figure 1-5** (previous page): Structural examples of class 2 fusion proteins: flavivirus E protein (A, PDB codes 1URZ<sup>26</sup> and 1SVB<sup>25</sup> for prefusion and postfusion structures, respectively), and alphavirus E1 protein (B, PDB codes 1RER<sup>23</sup> and 2ALA<sup>27</sup> for prefusion and postfusion structures, respectively). A single monomer of the prefusion dimer is shown on the left. The post fusion trimer is shown on the right with one monomer colored and the others gray. Their domains are colored as in **Figure 1-4**. The transmembrane (TM) and stem domains are mostly unresolved in the structures and are drawn as black and green lines, respectively. During fusion, the prefusion dimer separates and assembles into trimers that point the fusion loops outward. The fusion loops bury into the membrane, connecting both the viral and target membranes. The DIII domains then move into grooves formed by the DI domains in the trimer. In the process, they carry the stem and transmembrane domains and force the viral and target membranes in proximity. The stem domain then zips up the DII domain forming stable interactions and causing membrane merger. Structurally, flavivirus and alphavirus fusion proteins are much more alike than influenza and paramyxovirus fusion proteins, although they differ in the prefusion state by receptor binding activities and by utilizing different partners in forming the dimer. Flavivirus E protein (A) forms homo-dimers and retains both receptor and fusion activities, while the alphavirus E1 protein forms a heterodimer with its folding partner, E2, which provides for receptor binding. PyMol version 0.98<sup>22</sup> was used to prepare this figure.

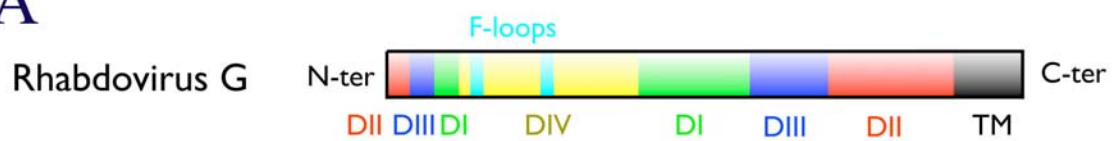
### 1.1.3 Class 3 Fusion

Class 3 viral fusion proteins represent the most recently discovered mechanism of viral fusion, observed in rhabdoviruses such as vesicular stomatitis virus and the more familiar rabies virus.<sup>28</sup> Class 3 fusion is a dichotomy in many ways from other types of viral fusion: the fusion protein, referred to as G, exhibits reversibility between its neutral pH prefusion form and its low pH postfusion form. Instead of a single highly hydrophobic fusion peptide or loop, the fusion protein uses two amphipathic loops which do not associate with membranes as tightly as Class 1 or 2 fusion peptides or loops. Consistent with the pH reversibility, the G protein does not undergo a cleavage step to become a metastable prefusion form. In fact, this pH dependent equilibrium between different states is a necessary consequence because the G protein is transported through the acidic compartments of the *trans*-Golgi apparatus, yet it can recover its prefusion state at the viral surface. Even with these differences, the protein still functions as a homo-trimer with an ectodomain of ~500 residues for each subunit. It also undergoes large conformational changes reminiscent of paramyxovirus fusion.

Prefusion<sup>29</sup> and postfusion<sup>30</sup> forms have been determined for the vesicular stomatitis virus, revealing these large conformational changes. The protein contains four domains: a beta-sheet rich lateral domain (domain I), a central trimerization domain (domain II), a pleckstrin homology domain (domain III, a phosphatidylinositol lipid binding domain), and the fusion domain (domain IV) (**Figure 1-6**). The fusion loops form part of domain IV, while the transmembrane domain is connected to the C-terminal end of domain III. Prior to fusion, the protein takes the shape of a tripod. Its fusion loops are exposed, but pointing toward the viral membrane. After the G protein binds to a

cellular receptor and the virus is endocytosed by the cell, the low pH environment of the endosome triggers the conformational changes. The specific cellular receptor is still unknown, but is thought to be phosphatidylserine for vesicular stomatitis virus. For rabies virus, several receptors have been proposed such as gangliosides and the nicotinic acetylcholine receptor. The conformational changes occurring during fusion do not change the tertiary structure of domains I, II and IV, but rather rearrange their relative orientations because of changes in the hinge regions between domain IV and domain III. The central trimerization domain (domain II) on the other hand does experience a major refolding from an extension of a helix by four turns. During fusion, domain IV swings to the top of the protein, forming contacts with the other DIV domains in the trimer and pointing the fusion loops into the target membrane. In the process, domain IV forms closer interactions with domain I and the central helix of domain III is extended. The conformational changes are complete when domain II, connected to the transmembrane domain, moves to form a six-helix bundle with the central helix of domain III. Doing so brings the transmembrane domain, inserted into the viral envelope, and the fusion loops, connected to the target membrane, into proximity and causes subsequent membrane merger.

A



B

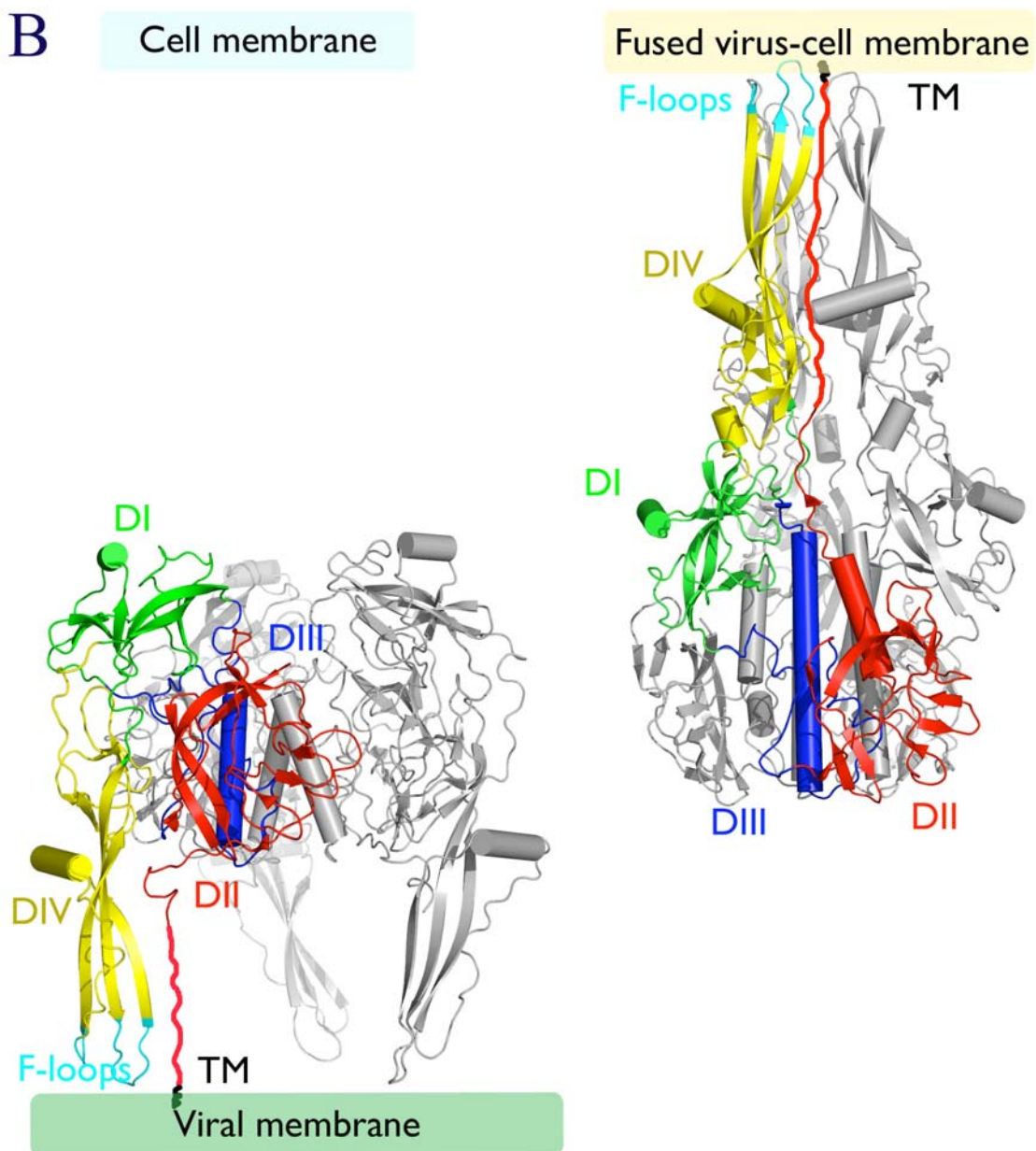


**Figure 1-6** (previous page): Schematic (A) and structural (B) examples of class 3 fusion proteins. The protein is colored by domains in (A) and by the same color scheme in (B) except the other two monomers of the trimer are gray. In (B), the prefusion form (PDB code 2J6J<sup>29</sup>) is shown on the left; the postfusion form (PDB code 2CMZ<sup>30</sup>) is shown on the right. Unlike Classes 1 and 2, fusion proteins in this class do not require a cleavage step in the fusion protein itself or partnering viral glycoproteins. Also uniquely, their conformational changes are reversible and they use two fusion loops that are part of the long beta-sheet DIV domain to enable fusion competence. DIII contains a central helix which forms a six-helix bundle in the postfusion form with a portion of DII. The major hinge joint is located between DI and DIV, enabling the protein to swing the fusion loops to the target membrane during fusion. Once the DIV domain is swung up, the DII domain can then move into position, carrying with it the transmembrane domain and forming a six-helix bundle with the central helix. PyMol version 0.98<sup>22</sup> was used to prepare this figure.

## 1.2 Inhibition of viral fusion

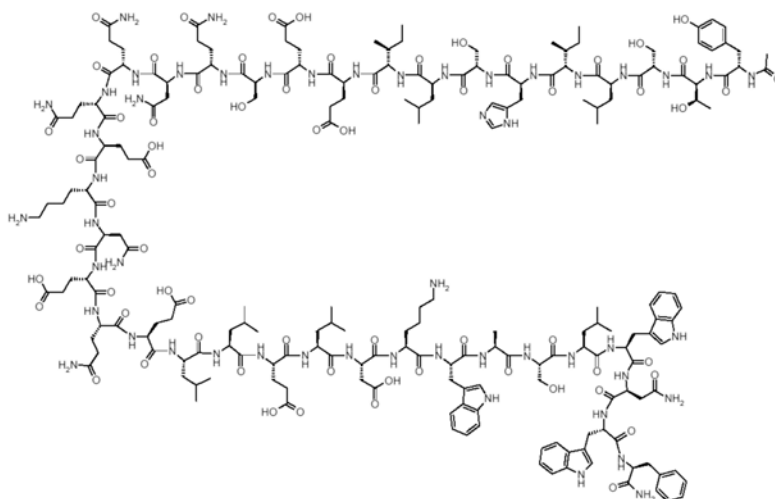
As a key step in the viral lifecycle, fusion has been a desired target of inhibition. An appropriate inhibitor needs to selectively bind a fusion protein at some step in the fusion pathway and prevent the merger of the two membranes by blocking the conformational changes necessary for fusion. Some neutralizing antibodies use this method to block viral infection.<sup>1</sup> Conceptually, this could occur in two ways: stabilization of the prefusion form of the protein, preventing the fusion conformational changes from ever beginning, or secondly, blocking a conformational step in the middle of the fusion by stabilizing some intermediate structure. In practice, most fusion inhibitors function by the second mechanism and are biologics such as peptides, but recent efforts have also been made to discover small molecules that can block fusion with varying degrees of success.

### 1.2.1 HIV fusion inhibition

Even at a time when little structural information was known for class 1 fusion viruses, researchers discovered the anti-fusion activity of HR-A- and HR-B derived peptides from the HIV fusion protein (**Figure 1-7**).<sup>10, 31, 32</sup> These peptides were synthesized in part because of their highly helical predicted secondary structure in HIV gp41 and the assumption that they may play a role in stabilizing the postfusion form of the protein. Fortuitously, these peptides are potent inhibitors of HIV fusion, the HR-B based peptide being more potent than the HR-A-based peptide. The HR-A-based peptide was also observed to form coiled-coils in solution, while the HR-B based peptide was largely unstructured in solution. These findings were corroborated when the postfusion X-ray crystal structure of gp41 was determined,<sup>33</sup> showing that HR-A and HR-B domains formed a tightly interacting six-helix bundle. The HR-A domains form the inner three helices; the HR-B domains form the outer three helices; thus explaining the secondary structure of the independent peptides in solution and mechanism of inhibition. The peptides compete with the protein's own heptad repeat domains during the conformational changes in fusion: the HR-B based peptide targets the inner three-helix bundle formed by HR-A, while the HR-A-based peptide forms bundles in solution that bind the protein's HR-B domains. The activity of the HR-B derived peptide was exploited by researchers at Trimeris and Roche to develop a new drug for HIV infection, enfuvirtide (known as T20 or by its trade name Fuzeon). Enfuvirtide is a linear 36 amino acid peptide based on the HR-B domain of gp41 (**Figure 1-7**). The drug won accelerated FDA approval in 2003 and normal approval in 2004. While effective in combination with other HIV drugs, enfuvirtide suffers from the administration and production problems

associated with a large peptide. Due to its lack of shelf stability, the drug must be reconstituted by the patient with sterile water and then injected subcutaneously. Almost all patients develop local injection site reactions in response to the drug.<sup>34</sup> Because the drug is synthesized through a time consuming, multi-step solid and solution phase peptide synthesis, production cost is high, resulting in treatment cost per patient of ~ US \$20,000 a year.<sup>35</sup> For these reasons, enfuvirtide is mainly used as a salvage treatment in patients who have developed multi-drug resistance to other HIV inhibitors.<sup>36</sup>

There has been some progress in finding small molecules that function as fusion inhibitors of HIV. By high throughput screening of compounds that compete with the outer HR-B peptide in the six-helix bundle of gp41, Harrison and colleagues discovered four inhibitors, the best of which inhibits HIV with a half maximal inhibitory concentration (IC<sub>50</sub>) of 5  $\mu$ M (**Figure 1-8**).<sup>37</sup> Thus, these small molecules are able to block the formation of a protein-protein interface which previously required a larger peptide. Small molecules have also been discovered that can bind gp120 in its pre-fusion conformation, stabilizing that conformation and raising the barrier to the initial steps of fusion (**Figure 1-8**).<sup>38</sup> The site for these molecules is probably a pocket in gp120 that closes up when gp120 binds the CD4 receptor, given the change in gp120 structure before and after binding to CD4.<sup>39</sup> The best molecule in this class is quite potent with a median IC<sub>50</sub> of 12 nM against a panel of 11 HIV strains. These results seem to illustrate that it is easier to achieve high potency with a molecule that targets the pre-fusion form of the protein rather than a molecule that targets a short-lived intermediate in the fusion cascade.



CH<sub>3</sub>CO-Tyr-Thr-Ser-Leu-Ile-His-Ser-Leu-Ile-Glu-Glu-Ser-Gln-Asn-Gln-Gln-Glu-Lys-Asn-Glu-Gln-Glu-Leu-Leu-Glu-Leu-Asp-Lys-Trp-Ala-Ser-Leu-Trp-Asn-Trp-Phe-NH<sub>2</sub>

**Figure 1-7:** Structure of the HIV fusion inhibitor enfuvirtide. The first viral fusion inhibitor, enfuvirtide demonstrated the effectiveness of using an HR-B derived peptide to block formation of the six-helix bundle during the conformational changes occurring in the fusion cascade.

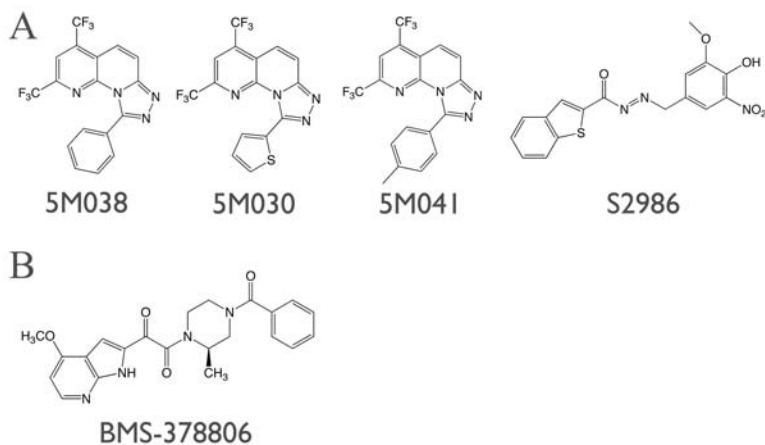


**Figure 1-8:** Small molecule HIV fusion inhibitors. (A) Molecules which block formation of the six-helix bundle of gp41, preventing fusion using a similar mechanism as enfuvirtide. (B) A molecule which binds to the prefusion form of gp120, preventing receptor binding induced conformational changes.

### 1.2.2 Influenza fusion inhibition

As in HIV inhibition, HR-B derived peptides for hemagglutinin function as fusion inhibitors, but are less effective than enfuvirtide in HIV.<sup>40</sup> This probably reflects the shorter six-helix bundle seen in the post-fusion HA (**Figure 1-3**). The post-fusion form of the protein is likely stabilized by longer, more diffuse interaction between the helices of the six-helix bundle and the interactions of the extended loop with the inner three-helix bundle.

Small molecules have also been discovered which function as fusion inhibitors of influenza HA. In an early example of structure-based design, researchers at UCSF computationally predicted binding sites on HA which would prevent exposure of the fusion peptide and then computationally screened a compound library at the most promising binding site.<sup>41</sup> The best 48 molecules were experimentally tested, yielding several leads with  $IC_{50}$ 's of 1 to 20  $\mu$ M, the most promising of which was *tert*-butyl hydroquinone (**Figure 1-9**). By preventing exposure of the fusion peptide, these molecules were proposed to function by increasing the stability of the prefusion state, raising the energy barrier to fusion. Later, the group followed this study with further docking at sites in influenza HA and discovered a compound, diiodofluorescein, that acts as an inducer rather than an inhibitor of the fusion conformational changes.<sup>42</sup> Diiodofluorescein caused irreversible inhibition of infectivity without covalent binding because once the protein has undergone the irreversible conformational changes, it can no longer assist membrane merger. Structural information on the nature of *tert*-butyl hydroquinone binding was realized in 2008 by X-ray crystallography, showing that *tert*-butyl hydroquinone binds HA in a slightly different position than predicted by

modeling.<sup>43, 44</sup> The compound is not located adjacent to the fusion peptide, but rather in-between two helices that form the extended HR-A helix in the postfusion structure (**Figure 1-9**). To form this extended helix, the outer helix in the prefusion form must disengage from the inner helix. The rather simple hydrophobic *tert*-butyl hydroquinone stabilizes these interactions enough to function as a low micromolar inhibitor. Interestingly, the binding site for *tert*-butyl hydroquinone is blocked in strains of the virus which contain Group 1 HAs. These viruses are not inhibited by the compound. The lack of binding site in these viruses results in resistance to the compound.<sup>44</sup>

Another panel of fusion inhibitors against influenza HA was discovered by researchers at Bristol-Myers-Squibb. The lead compound, BMY-27709 (**Figure 1-9**), was initially discovered through screening against influenza in a multicycle growth assay and had an IC<sub>50</sub> of 3-8 μM against H1 and H2 subtypes of influenza.<sup>45</sup> These subtypes encompass both Group 1 and Group 2 influenza HAs, so it is unlikely that these compounds target the same binding site as *tert*-butyl hydroquinone. Indeed, a photoaffinity labeling study identified cross-linking residues near the location of the fusion peptides.<sup>46</sup> Sequence analyses of drug-resistant viruses also mapped amino acid changes responsible for resistance to this site.<sup>47</sup> Subsequent structure-activity studies of the BMY-27709 yielded compounds with sub-micromolar activity in cell protection assays, but the compounds were not active against the H3 subtype of influenza.<sup>48</sup>

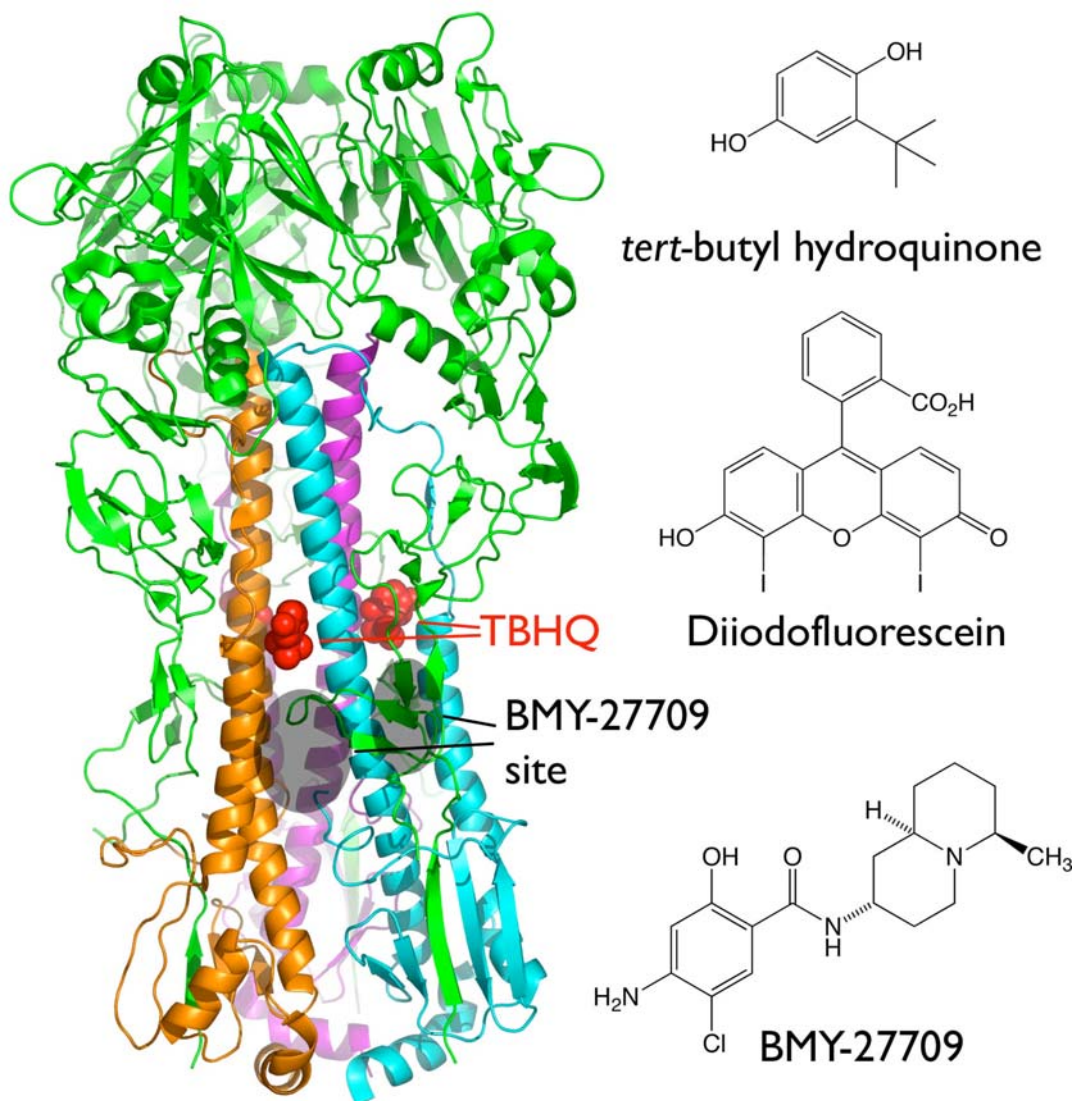


**Figure 1-9:** Small molecule inhibitors of influenza fusion. On the left, the X-ray crystal structure of *tert*-butyl hydroquinone (TBHQ) complexed with the prefusion form of hemagglutinin. TBHQ (shown as red spheres) stabilizes the prefusion conformation through hydrophobic interactions between the inner and outer helices of HR-A. The predicted BMY-27709 binding site based on resistance-conferring mutations and photoaffinity labeling is shown as a black oval. On the right, the structures of influenza inhibitors are shown. Diiodofluorescein inhibits the virus by acting as an inducer of premature fusion conformational changes instead of stabilizing the prefusion form.

### 1.2.3 Respiratory Syncytial Virus fusion inhibition

Respiratory Syncytial Virus (RSV), in the pneumovirinae subfamily of paramyxoviruses, has also been targeted by fusion inhibitors. As in other class 1 fusion viruses, HR-B based peptides function as inhibitors, competing the fusion protein's own HR-B domain in the formation of the six-helix bundle. Extensive research has also been performed in the pursuit of small molecule inhibitors of fusion by groups at Bristol-Myers-Squibb,<sup>49-56</sup> Johnson & Johnson,<sup>57-59</sup> and ViroPharma.<sup>60-62</sup> (**Figure 1-10**) The mechanism of action of all these panels of compounds have been determined as fusion inhibition acting on the fusion protein and not cellular or viral receptors. Photoaffinity labeling studies with an analog of the BMS compound resulted in labeling of residues in the HR-A domain.<sup>63</sup> Thus, the compound was perceived to act as an inhibitor of six-helix bundle formation. The J&J compound showed a resistance profile similar to the BMS compound, namely, mutations in the HR-B domain that interact with the HR-A site, and therefore assumed to be binding at the same site. The ViroPharma compound is also assumed to be binding at the same site based on competition assays with the J&J compound and a tritiated analog of the VP compound. These compounds are all nanomolar inhibitors of RSV, a surprising feat if the compounds indeed block protein-protein interactions in a transient intermediate structure. An alternative explanation to the assumed mode of action might be that the compound acts on the prefusion form of the RSV fusion protein.

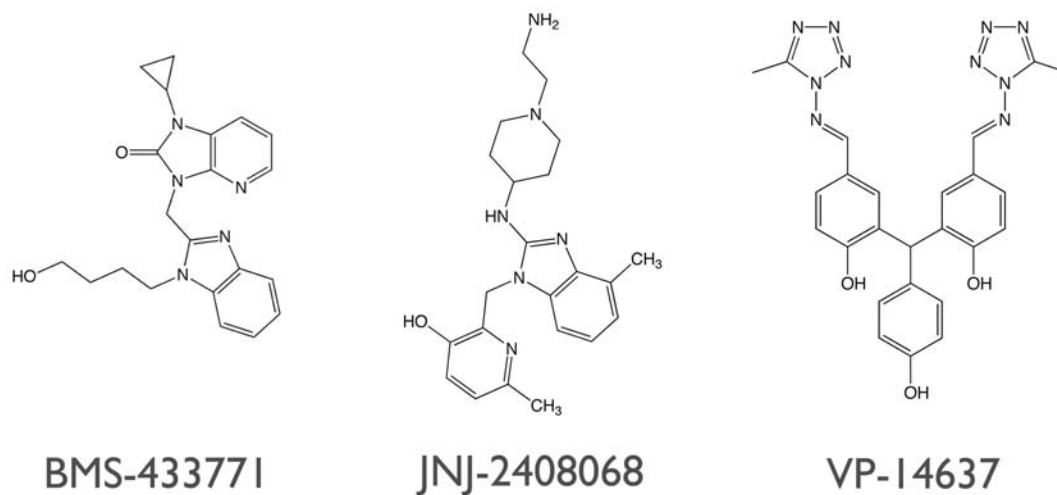


**Figure 1-10:** Inhibitors of RSV fusion. All three compounds have been shown to target the fusion protein and encounter similar resistance profiles. A photoaffinity analog of BMS-433771 was shown to bind the HR-A domain. The tritiated version of VP-14637 has been shown to compete with JNJ-2408068.

### 1.3 The unique challenge of measles virus entry

The measles virus, a member of the paramyxovirus family, remains among the most lethal human pathogens and accounts for approximately 200,000 deaths annually despite the existence of an effective vaccine.<sup>64</sup> Many of these deaths are due to low vaccination rates in the developing world, but there have been increased incidents of outbreaks in the developed world because of decreased vaccination compliance.<sup>65</sup> Parental concern with the vaccine's safety, though widely regarded as unfounded, has led to immunity levels dropping below the ~ 95% level required to prevent local outbreaks<sup>66</sup> and has resulted in the highest case numbers in over a decade in several European countries in 2008.<sup>67-69</sup> The high level of immunity is required because measles virus is one of the most infectious viruses identified, with reproductive number,  $R_0$ , of 12-18.<sup>66</sup> Thus, in a population with no immunity, an average of 12-18 secondary cases will result from a typical single infection. For comparison, the reproductive numbers for the smallpox virus and the SARS coronavirus are only 5-7 and 2-3, respectively.<sup>66</sup>

An important contributor to the virulence of measles virus is its effective machinery for cellular entry at neutral pH. Like other paramyxovirinae, measles accomplishes fusion by the cooperative action of two transmembrane envelope glycoproteins, the hemagglutinin and fusion proteins.<sup>5, 6, 8-10, 19, 70-73</sup> Hemagglutinin recognizes the cell surface receptor, CD46 or SLAM/CD150W, depending on virus strain,<sup>71-73</sup> and triggers the fusion protein in its metastable, prefusion state to undergo large-scale conformational changes, ultimately concluding in a stable postfusion conformation and membrane merger. The virus's effectiveness at fusion is exemplified by the cell to cell fusion that occurs both *in vitro* and *in vivo*, resulting in the cytopathic

hallmark of multinucleated giant cells.<sup>74</sup> Cell to cell fusion is thought to allow the virus an alternative strategy for virus propagation as opposed to budding new virions, possibly minimizing exposing to the immune system's neutralizing antibodies.

Measles virus is thus an attractive model system for study, not only to gain mechanistic insight into viral entry, but also to discover inhibitors of entry which could yield drugs reducing worldwide human morbidity and mortality. Combining current prophylactic (vaccination) with new therapeutic (antivirals) approaches could allow better management of currently encountered measles virus outbreaks. Conceivable areas of immediate use include improved case management of acute and persistent disease, rapid control of local outbreaks before vaccines and trained personnel are available or in cases of declined vaccination, and protection of the immunocompromised and infants prior to vaccination. The past several years have seen a rapid evolution in the general understanding of viral entry and its inhibition. Research described in this thesis also evolved with and contributed to this understanding. While pioneering work on influenza and HIV provided a groundwork to understanding the process of fusion and inhibition in paramyxoviruses, important distinctions were found in paramyxoviruses in general and measles virus in particular.

## Chapter 2: Early model of the measles virus fusion protein and the discovery of fusion inhibitors

*Portions of this chapter are based on “Structural features of paramyxovirus F protein required for fusion initiation,” published in the journal Biochemistry in 2003<sup>75</sup> and “A target site for template-based design of measles virus entry inhibitors,” published in the Proceedings of the National Academy of Sciences of the USA in 2004.<sup>76</sup>*

Interest in modeling the structure of the measles virus fusion protein (MeV F) was realized by the discovery that fusion proteins from the Edmonston and wild-type strains confer distinct cytopathic effects and strengths of interaction with its hemagglutinin protein through a single residue difference at position 94.<sup>77</sup> Through sequence comparison with the known structure of Newcastle Disease Virus fusion protein (NDV F), it was predicted that this residue resides on a heptad repeat domain distinct from HR-A and HR-B, the HR-C domain.

### 2.1 Model based on Newcastle Disease Virus fusion protein

To gain insight into the structural importance of the residue at position 94, a homology model was developed for MeV F using the X-ray crystallography structure for NDV F by Drs. Ami Lakdawala and Kim Gernert.<sup>75</sup> At that time, the only available structures for paramyxovirus fusion proteins were the NDV F structure<sup>18</sup> and protein fragments for RSV<sup>78</sup> and SV5<sup>79</sup> consisting of the stable 6HB. NDV is a member of a separate genus of paramyxovirinae from MeV, the avulaviruses (**Figure 2-1**). Because NDV is not closely related to MeV, the fusion proteins share only 27% amino acid identity and 48% similarity. However, all the cysteine residues within the fusion protein

ectodomain are conserved, suggesting the same framework of intramolecular disulfide bridges and an overall similar protein fold.

Using the NDV F based homology model of MeV F, the residue at position 94 (amino acid valine for the Edmonston strain, which was used to build the model) was localized to the helical HR-C domain of F<sub>2</sub> (**Figure 2-2**). The residue was predicted to be facing toward the center of the F trimer. With a Connolly surface applied to the model, Val94 was predicted to form the bottom of a hydrophobic pocket composed of hydrophobic residues Pro224, Ile225, Leu256, Leu257, and Ile269 with hydrophilic residues Arg268 and Thr270 forming the upper rim of one side of the cavity. To ascertain if the MeV F model predicted this microdomain correctly, the corresponding microdomain of NDV F was exchanged in an MeV F chimera containing amino acids 86-100 of NDV F<sub>2</sub> instead of the normal MeV F<sub>2</sub> amino acids. When coexpressed in cells with MeV hemagglutinin (MeV H), the MeV F chimera was highly fusogenic. The construct demonstrated fusion activity at least as efficient as that of unchanged Edmonston when incorporated into the MeV genome, suggesting that these HR-C regions are functionally interchangeable between NDV F and MeV F and lending credence to the accuracy of the model.

Mutational analysis of the microdomain through single, double, and multiple mutations showed that the microdomain can accommodate variations, but the general nature of the pocket needs to be preserved to maintain fusion activity. For example, small amino acid substitutions on one side of the microdomain can be compensated for by larger residues on the opposite side. This effect is seen with the Leu256Ala, Leu257Ala double mutant, which reduces the fusion capacity by 50%. However fusion activity can

be restored by replacement of Val94 by the larger methionine. This result was corroborated by molecular dynamics simulations of the mutated proteins, where the Leu256Ala and Leu257Ala double mutant is predicted to expose the base of the cavity, but replacement of Val94 by Met94 is predicted to shield the base of the cavity.



**Figure 2-1:** Phylogenetic tree for the paramyxovirinae subfamily of paramyxoviridae. The other subfamily (not shown) is pneumovirinae, containing Respiratory Syncytial Virus and Metapneumovirus.

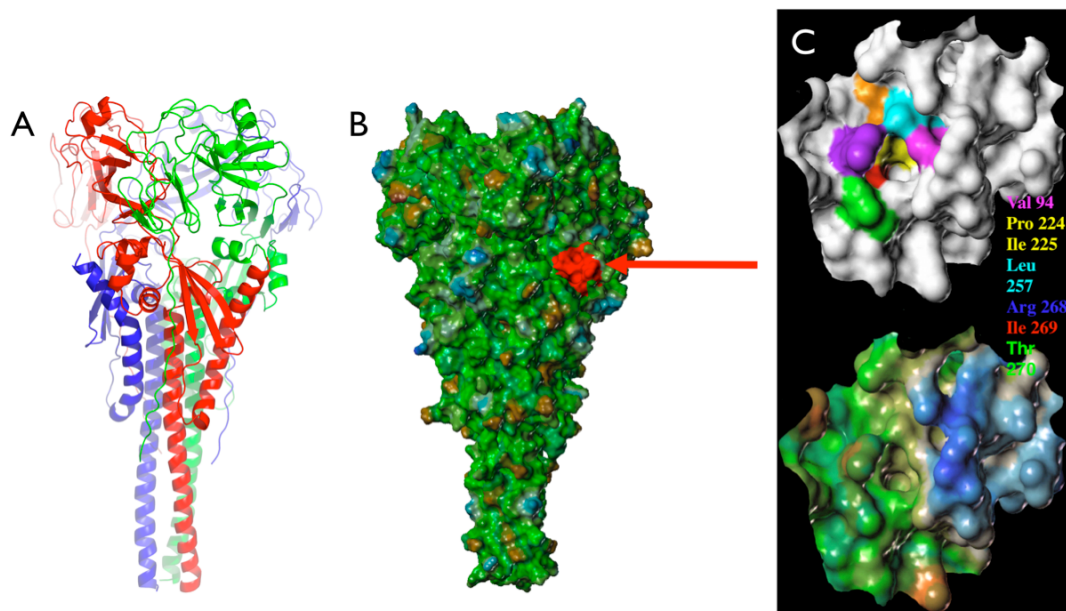


**Figure 2-2:** Homology model for MeV F based on NDV F (PDB code 1G5G<sup>18</sup>). (A) The secondary structure of the MeV F model, shown as cartoon and colored by subunit. (B) The Connolly surface of the MeV F model, colored by lipophilic character (blue = hydrophilic, green = neutral, brown = lipophilic), with the Val94 microdomain highlighted red. (C) Close view of the Val94 microdomain, shown as a Connolly surface and colored by residue (top frame) and lipophilic character (bottom frame).

## 2.2 Discovery of fusion inhibitors of measles virus

The above experiments demonstrated the importance of the Val94 microdomain to the fusion activity of the measles virus. The shape and lipophilic character of the microdomain suggested that this site could potentially bind small molecules capable of inhibiting fusion.<sup>76</sup> Inhibitors were predicted to have molecular geometries of 7-12 Å in two orthogonal directions, with a hydrophobic portion to interact with the base of the cavity and polar functionality to interact with the hydrophilic rim. The Plemper group performed a small screen with a panel of compounds, containing 32 ligands of six classes (**Figure 2-3**). The activity of these compounds was assessed in a newly developed screen based on a recombinant MeV strain carrying GFP as an additional transcription unit, allowing determination of inhibition through monitoring the absence of fluorescent infectious centers and multinucleated syncytia. The screen identified two compounds of different classes which suppressed viral activity, OX-1 and AM-2, (**Figure 2-3**) while all the other compounds lacked viral activity or were clearly cytotoxic. In a cell proliferation assay, AM-2 revealed a 50% cytotoxic concentration ( $CC_{50}$ ) less than 50  $\mu\text{M}$ , suggesting its antiviral effect might be attributed to cytotoxicity. OX-1, however, had  $CC_{50}$  greater than 600  $\mu\text{M}$ . OX-1 was also shown specifically inhibit the MeV (Edmonston strain) with an  $IC_{50}$  of 55  $\mu\text{M}$  with no effect on a related paramyxovirus, human parainfluenza 2.

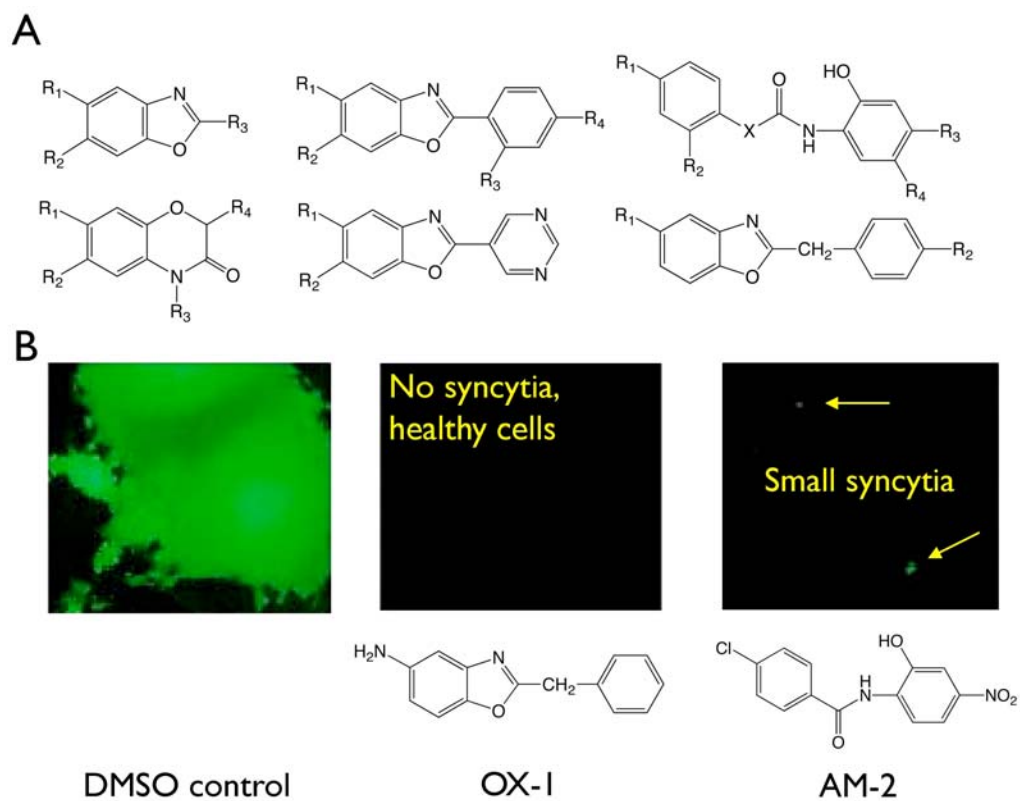


**Figure 2-3:** Focused screen of compounds for antiviral activity. (A) 32 compounds of the six classes shown were assayed at 600  $\mu\text{M}$  against a MeV strain modified to express GFP. (B) Resulting leads from the assay. OX-1 and AM-2 prevented infectious centers and syncytia, but AM-2 was shown to have a  $\text{CC}_{50}$  of less than 50  $\mu\text{M}$ . OX-1, however, was not cytotoxic.

### 2.2.1 Measles virus fusion protein is confirmed as the target for OX-1

Cells transiently transfected with expression plasmids encoding MeV F and H undergo cell to cell fusion that can be quantified by use of a reporter-based quantitative fusion assay. OX-1 was shown to inhibit activity in these engineered cells with an  $IC_{50}$  of 100  $\mu$ M, suggesting the compound directly affects the entry process. Protein biosynthesis and transport was ruled out as a mechanism of action for OX-1 because *in vitro* evaluation of MeV F protein surface steady-state levels demonstrated biochemically that MeV F protein biosynthesis and intracellular transport are unaffected by OX-1 concentrations up to four times the  $IC_{50}$ . Though cellular entry was confirmed as OX-1's method of inhibition, the molecule could be interfering with the MeV hemagglutinin's attachment to target cells. However, time of addition studies showed that inhibition is reversible and that receptor binding is not affected. Pretreating target cells or viruses with OX-1 or removing OX-1 sixty minutes after infection did not reduce viral yield. Only allowing OX-1 to be incubated with viral particles and cells reduced the viral titer. Applying a low-pH treatment which normally inactivates the virus only works sixty minutes after infection if used with OX-1. This suggests that OX-1 keeps the virus exposed in the extracellular space. Additionally, OX-1 was found to strongly suppress the lipid mixing that results from the merging of the outer layers of donor and target membranes in the fusion process.

### 2.2.2 Engineered mutations in MeV F induce resistance to OX-1

OX-1 was assayed against previously described MeV recombinants that were developed to evaluate the nature of the Val94 microdomain, including constructs with Val94Ala, Val94Gly, and Val94Met. In these assays, increased or complete resistance to

inhibition was observed for the Val94Ala ( $IC_{50} = 124 \mu\text{M}$ ) and Val94Gly recombinants ( $IC_{50} = 600 \mu\text{M}$ ). In contrast, the Val94Met recombinant was more susceptible to OX-1 inhibition ( $IC_{50} = 20 \mu\text{M}$ ).

### 2.2.3 Docking model of OX-1 to the Val94 microdomain

*In silico* docking of OX-1 into the Val94 microdomain was performed by manual docking and by application of the automated docking algorithm DOCK. The resulting complexes were refined with SYBYL 6.9 by low temperature molecular dynamics (MD) (20 K, TVN ensemble; 5 ps). A three-point interaction model proved consistent with both the predicted size of the cavity and the distribution of polar and nonpolar centers (**Figure 2-4**). According to this model, the amino group of OX-1 engages in a hydrogen bond with Glu339 at the top of the microdomain, the oxygen of the oxazole ring is anchored by Arg268, and the phenyl ring is buried in the hydrophobic base of the cavity. When the Val94Ala and Val94Gly point mutations discussed above are incorporated into the model and refined by MD, the cavity is predicted to contract and fill the volume previously occupied by the valine side chains, forcing the ligand out of the cavity, consistent with the resistance observed by these mutation. The Val94Met point mutation, on the other hand, is predicted to expand the target area for OX-1, allowing favorable docking and corroborating the increased inhibition by OX-1 (**Figure 2-4**).

The activity of OX-1 analogs in the screening assay were consistent with the three-point interactional model (**Figure 2-4**). For example, the analog lacking the  $\text{CH}_2$  unit between the two aromatic rings is inactive, as this flat compound cannot achieve interaction with both the hydrophobic base of the pocket and the polar interactions. An analog of OX-1 that lacks the amino group delivers a third of the activity of OX-1 ( $IC_{50} =$

150  $\mu\text{M}$ ), presumably due to loss of interaction with Glu339.

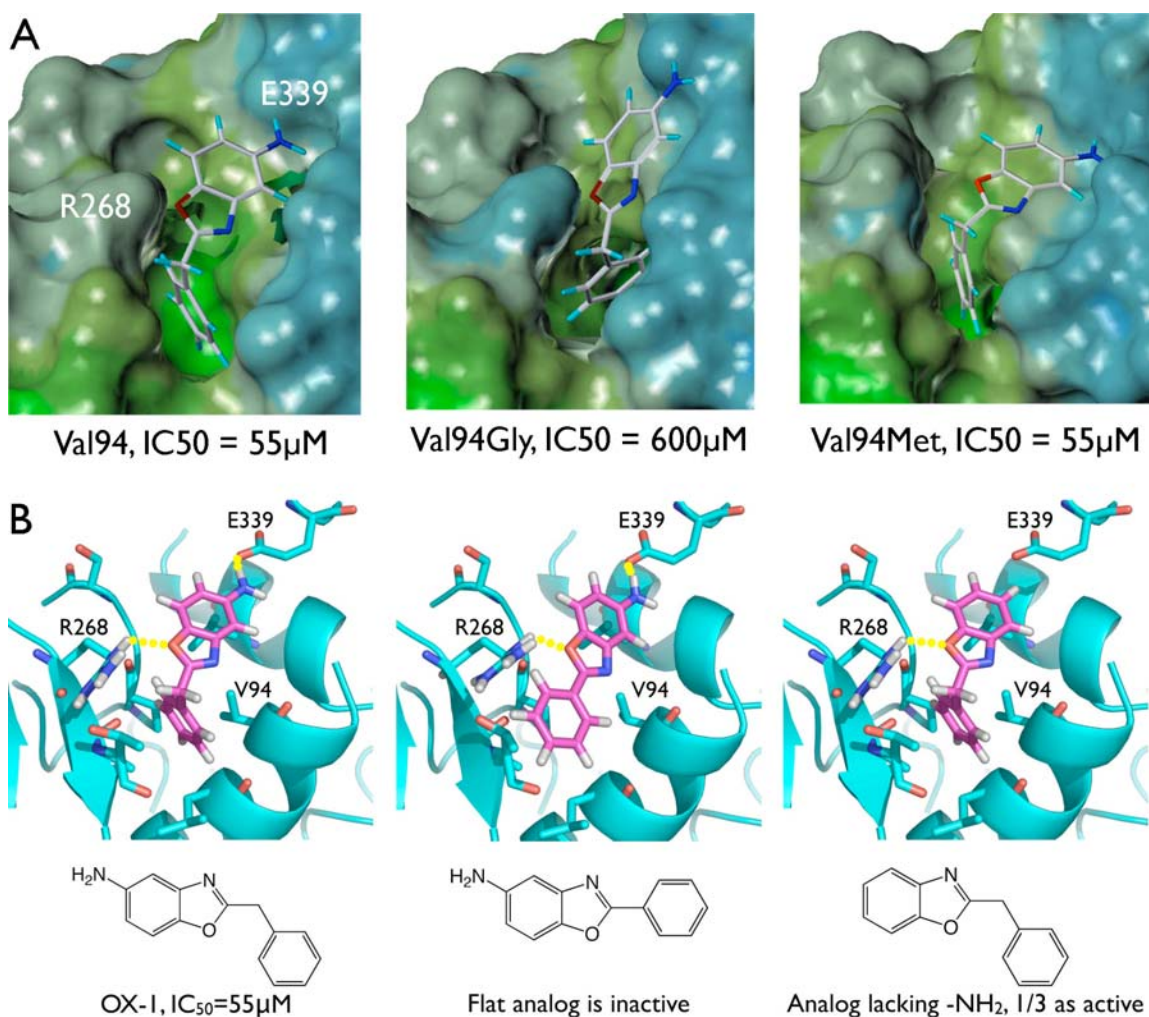


**Figure 2-4:** The binding model for OX-1 is supported by mutations in the Val94 microdomain and structure activity relationships of OX-1 analogs. (A) Docking results for OX-1 to unchanged MeV F (left panel), MeV F harboring a Val94Gly mutation (middle panel), and MeV F harboring a Val94Met mutation (right panel). The Val94Gly mutation gives resistance to OX-1 inhibition by shrinking the hydrophobic pocket needed for binding. The Val94Met mutation shows an increase in OX-1 inhibition because the molecule can effectively bind in the expanded hydrophobic pocket. (B) Analogs of OX-1 are inactive if they lack hydrophobic interaction (middle panel) and show a decrease in activity if they lack a polar interaction (right panel).

### 2.3 Design of a more potent fusion inhibitor

To increase the antiviral activity of OX-1, a variety of candidate structures were synthesized and assessed for antiviral activity. An acyclic variant of OX-1, AM-4, incorporating an amide and an *ortho*-hydroxy group, appeared favorable based on its ability to form multiple hydrogen bonds with Arg268 and its increase in flexibility (**Figure 2-5**). When tested against MeV, AM-4 had an IC<sub>50</sub> of 0.26 μM, a 200-fold increase in activity over OX-1. As with OX-1, AM-4 had no activity against hPIV2, and it showed a similar resistance profile to MeV with mutations of Val94Gly and Val94Ala. Although its CC<sub>50</sub> was 17 μM, the increase in activity results in a high therapeutic index ratio of 65.

Unfortunately, it was later determined that AM-4 has a half-life of less than 16 hours under physiological conditions, most likely because of facile oxidation in air.<sup>80</sup> Although the transformation was not demonstrated, the *para* orientation of the OH and NH<sub>2</sub> groups on the heterosubstituted aromatic ring suggests the molecule may readily oxidize to a quinone analog. The compound lost partial activity after 30 minutes and complete activity after 16 hours of pre-incubation under physiological conditions. In NMR monitoring experiments in CDCl<sub>3</sub> solvent and under atmospheric oxygen, AM-4 slowly darkened with some precipitation and the spectrum gradually showed the presence of impurities. To solve this stability problem, efforts were then made to use the scaffold of AM-4 to achieve stable, but still highly potent analogs.

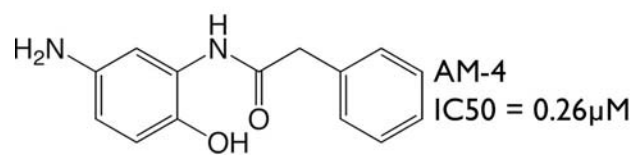
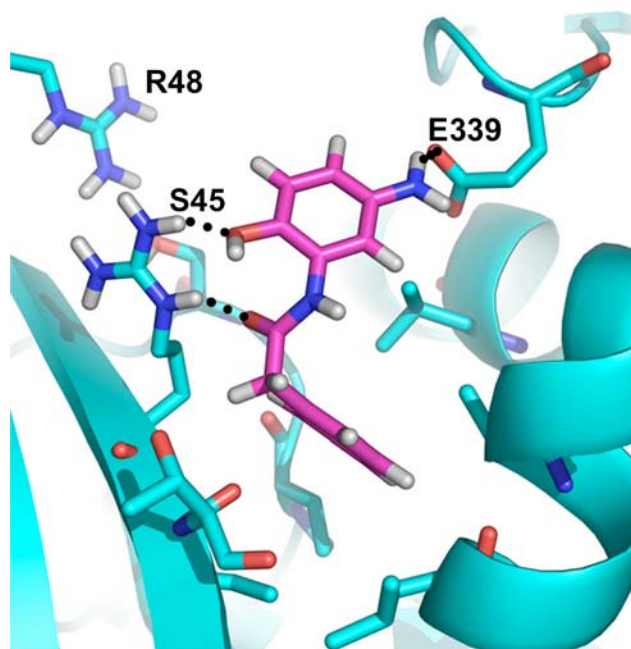


**Figure 2-5:** Binding model for AM-4 exhibits an ideal docking mode to the Val94 microdomain, but degrades rapidly under physiological conditions.

## Chapter 3: Structure-based design of fusion inhibitors

*Portions of this chapter are based on “Nonpeptide inhibitors of measles virus entry,” published in the Journal of Medicinal Chemistry in 2006.<sup>81</sup>*

With a structural model of a fusion protein microdomain important to MeV entry, evidence that small molecules designed for this microdomain were binding at the site, and a compound with nanomolar inhibition, yet stability problems, this project seemed ideal for a structure-based lead optimization strategy. To accomplish this aim, efforts were made to pursue design, synthesis, and biological testing of a number of AM-4 analogs.<sup>81</sup>

### 3.1 AM-4 analogs

The high level of activity of AM-4 was intriguing, suggesting that it might be possible to design an ideal inhibitor that matched the activity of AM-4, but one stable in storage as well as physiological conditions. AM-4 analogues were envisioned by modification of the AM-4 scaffold in three sectors: the acetanilide phenyl ring, the distal phenyl ring, and the intermediate linker region (**Figure 3-1**).

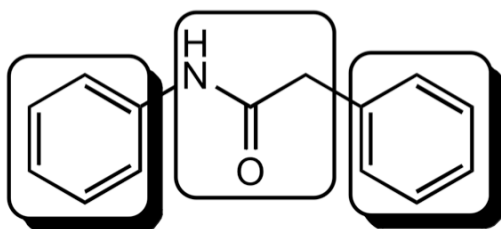


**Figure 3-1:** Three sectors of 2-phenylacetanilide envisioned as a scaffold of AM-4 and subjected to synthetic modification.

The structure activity relationships (SAR) were developed by docking the compounds into the cylindrical Val94 microdomain of the previously developed MeV F homology model. First, low energy conformations of the ligands were derived by Monte

Carlo conformational searching using the MMFF force field<sup>82-84</sup> in Macromodel v6.5 (Schrödinger, Inc., New York, NY) and a 7 kcal/mol energy cutoff window. Then the ligand conformations were manually docked into the cylindrical MeV fusion protein pocket occupied by Val94 using the assistance of Sybyl's DOCK, a manual docking algorithm, and visualization of the protein as its Connolly surface (Sybyl7.0, Tripos Discovery Software, St. Louis).<sup>85, 86</sup> All complexes were relieved of short steric contacts with low temperature molecular dynamics (20K, TVN ensemble; 3-5 ps, Tripos force field) followed by active site minimization (Powell gradient,<sup>87</sup> convergence threshold of 0.05 kcal/(mol\*Å), Tripos force field). Regions of the protein greater than 12 Å away from the ligand were held fixed to prevent unfolding of the protein in the absence of explicit solvation.

The synthesis of the compounds was performed by current and former members of the Liotta research group: Drs Aiming Sun, Weiqiang Zhan, and Mr. Ernest Murray. The biological activity of the compounds was determined by members of the Plemper research group: Drs. Joshua Doyle, Li-Ting Cheng, and Jeong-Joong Yoon. Inhibitory activity of the compounds was determined through two different assays. In the first of the two assays, compound activity was quantified on the basis of a suppression of viral induced cytopathicity. Selected compounds were then further evaluated in a more involved cell-based viral replication assay to determine effective concentrations based on reduction of viral yields. The cytopathicity assay was also used with selected compounds with a MeV variant harboring resistance to the optimized inhibitor AS-48 due to a mutation at position 462 in the F protein. (See Section 3.3 and Chapter 4) Cytotoxicity of the compounds was determined using a cellular proliferation assay.

### 3.1.1 SAR for compounds with a mono-substituted acetanilide phenyl ring

The binding model of OX-1 (**Figure 2-4**) depicts the aniline NH<sub>2</sub> as a rather strong hydrogen bond donor to Glu339 and the oxazole oxygen as a weak H-bond acceptor from Arg268. As a consequence we anticipated that the monosubstituted anilines (**Table 3-1**) combined with the amide carbonyl would improve activity. This hypothesis proved correct for *m*-NH<sub>2</sub> substitution (**4a**), but not *p*-NH<sub>2</sub> substitution (**4b**). The binding model for these molecules shows that while the *m*-NH<sub>2</sub> group of **4a** is positioned to interact with Glu339, the *p*-NH<sub>2</sub> group of **4b** is not positioned for effective interaction (**Figure 3-2**).

Fortunately, an intermediate in the synthesis of **4a** showed the potential for additional interaction with residues Ser45 and Arg48. This *m*-NO<sub>2</sub> compound (**3a**) exhibits an approximate 2-fold improvement in IC<sub>50</sub> in the anti-MeV assay by comparison with the *m*-NH<sub>2</sub> analog **4a**. Simplistically, it would appear that the anilino phenyl ring adopts conformations that maximize the binding the case of **3a** and **4a**. Thus, the *m*-NH<sub>2</sub> in **4a** is directed at Glu339 as in OX-1, while the *m*-NO<sub>2</sub> in **3a** interacts with Arg48 and Ser45. The *m*-CN substituted compound (**3g**) shows similar inhibition to **3a**, while the *p*-NO<sub>2</sub> places the nitro group in a less favorable subsite and has 10-fold less activity than the *m*-NO<sub>2</sub> compound. The *o*-NO<sub>2</sub> completely loses activity because no low-energy conformations can sustain these interactions. The smaller hydroxyl group in the *m*-OH substituted compound (**3e**) falls between the H-donating arginines and serine, achieving only weak inhibition. However, the *m*-OH is able to recover 4-fold, drawing interactions from Arg268, but not surpassing the activity of the *m*-NH<sub>2</sub> analog **4a** (**Figure 3-2**).

**Table 3-1:** Antiviral MeV IC<sub>50</sub>'s for mono-substituted acetanilides OX-1, **3** series, and **4** series.

entry	compound	Y, R <sub>2</sub> <sup>a</sup>	IC <sub>50</sub> (μM) <sup>b</sup>	IC <sub>50-res</sub> <sup>c</sup>	CC <sub>50</sub>	SI <sup>e</sup>
1	<b>OX-1</b>		55	>150	>600	>10
2	<b>3a</b>	C, <i>m</i> -NO <sub>2</sub>	8.5	ND	>600	>71
3	<b>3b</b>	C, <i>p</i> -NO <sub>2</sub>	16	ND	550	34
4	<b>3c</b>	C, <i>o</i> -NO <sub>2</sub>	>100	ND	>600	ND
5	<b>3d</b>	C, <i>o</i> -COOH	60	ND	>600	>10
6	<b>3e</b>	C, <i>m</i> -OH	25	ND	>600	>24
7	<b>3f</b>	C, <i>o</i> -OH	13	>150	525	40
8	<b>3g</b>	C, <i>m</i> -CN	6.5	>150	>600	>92
9	<b>3h</b>	N, 5-F	109	ND	>600	>6
10	<b>4a</b>	C, <i>m</i> -NH <sub>2</sub>	19	>150	>600	>32
11	<b>4b</b>	C, <i>p</i> -NH <sub>2</sub>	135	ND	>600	>4

<sup>a</sup>The *o*-, *m*- and *p*- designations refer to substitution relative to NHCO. <sup>b</sup>IC<sub>50</sub> concentrations were calculated based on the suppression of virus-induced cytopathicity. <sup>c</sup>IC<sub>50</sub> concentrations of selected compounds against a MeV variant resistant to inhibition by AS-48 due to a point mutation at position 462 in the F protein. ND: not determined. <sup>d</sup>CC<sub>50</sub>: cytotoxicity concentration at 50% maximal dose. <sup>e</sup>Selectivity index (CC<sub>50</sub>/IC<sub>50</sub>).

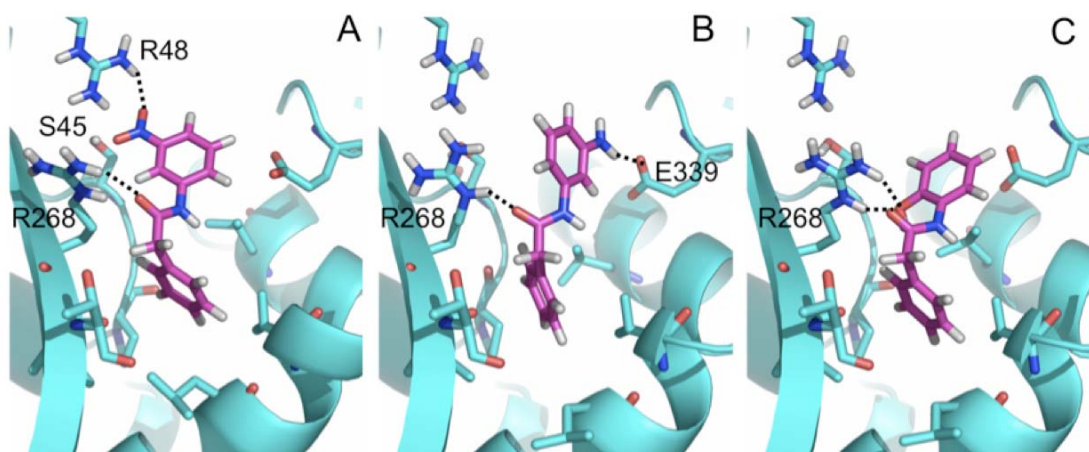


**Figure 3-2:** Docking models for **3a**, **4a** and **3f**. (A) The amide C=O and *m*-NO<sub>2</sub> of **3a** accept an H-bond from Ser45, while *m*-NO<sub>2</sub> is likewise H-bonded to Arg48. (B) The *m*-NH<sub>2</sub> of **4a** acts as proton donor to Glu339. (C) The amide C=O and *o*-OH of **3f** accept H-bonds from Arg268.

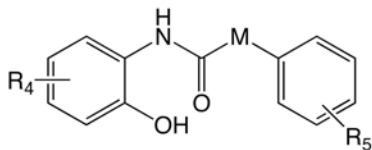
### 3.1.2 SAR for compounds with a disubstituted acetanilide phenyl ring

Because of the activity of AM-4, a series of disubstituted benzamides bearing an *o*-OH group was investigated, this time avoiding *para*-substituted electron donating groups that might be amiable to oxidation. Simple substitution of the *o*-OH with fluorine resulted in complete loss of activity, so a series of compounds with NH<sub>2</sub>, NO<sub>2</sub>, CONH<sub>2</sub>, COOMe, and CF<sub>3</sub> substitution were investigated (**Table 3-2**). Unfortunately, no stable analogs bearing an *o*-OH group matched the level of activity observed for AM-4 (**7b**, **7d**, **7i**, **7j**, or **7k**), with the most active having an IC<sub>50</sub> of 47 μM. Modeling suggests that these disubstituted analogs cannot accommodate both moieties simultaneously as exemplified by **7i** (**Figure 3-3**).

One way to avoid the stability issues with AM-4 is to replace the *o*-OH with *o*-CH<sub>2</sub>OH to give compound **8**, thereby eliminating the hydroquinone moiety in the anilide ring. The *m*-CH<sub>2</sub>OH analog was also investigated. Although both compounds proved to be shelf-stable, neither had antiviral activity at concentrations up to 100 μM. Docking of **8** in the F-protein pocket suggests that the origin of inactivity is a ligand conformation that prevents the CH<sub>2</sub>OH and the C=O groups from simultaneously interacting with Arg268, while shifting the structure somewhat out of the pocket. As a result, Arg48 and Ser45 are too distant to interact with the CH<sub>2</sub>OH group. The activity of **8** also suffers from a high internal strain energy (8.6 kcal/mol relative to the global minimum), a value rather high in comparison to the quantity for **7a** (1.7 kcal/mol relative to the global minimum).

**Table 3-2:** Antiviral MeV IC<sub>50</sub>'s for disubstituted phenol **7** series.

entry	compound	R <sub>4</sub> , <sup>a</sup> M, R <sub>5</sub>	IC <sub>50</sub> (μM) <sup>b</sup>	CC <sub>50</sub> <sup>c</sup>	SI <sup>d</sup>
1	<b>AM-4</b>	<i>m</i> -NH <sub>2</sub> , CH <sub>2</sub> , H	0.26	17	65
2	<b>7b</b>	<i>p</i> -NH <sub>2</sub> , CH <sub>2</sub> , H	75	>600	>8
3	<b>7c</b>	<i>p</i> -NH <sub>2</sub> , CH <sub>2</sub> O, H	- <sup>e</sup>	ND	ND
4	<b>7d</b>	<i>m</i> -NO <sub>2</sub> , CH <sub>2</sub> , H	47	450	10
5	<b>7e</b>	<i>m</i> -NO <sub>2</sub> , CH <sub>2</sub> , <i>m</i> -OME	>100	>600	ND
6	<b>7f</b>	<i>m</i> -NO <sub>2</sub> , CH <sub>2</sub> , <i>p</i> -OMe	>100	600	<6
7	<b>7g</b>	<i>m</i> -NO <sub>2</sub> , CH <sub>2</sub> O, H	>100	600	<6
8	<b>7h</b>	<i>p</i> -NO <sub>2</sub> , CH <sub>2</sub> O, H	>100	>600	ND
9	<b>7i</b>	<i>m</i> -CONH <sub>2</sub> , CH <sub>2</sub> , H	127	>600	>5
10	<b>7j</b>	<i>m</i> -COOMe, CH <sub>2</sub> , H	66	>600	>9
11	<b>7k</b>	<i>m</i> -CF <sub>3</sub> , CH <sub>2</sub> , H	>100	>600	ND



<sup>a</sup>The *m*- and *p*- designations refer to substitution relative to NHCO. <sup>b</sup>IC<sub>50</sub> concentrations were calculated based on the suppression of virus-induced cytopathicity. <sup>c</sup>CC<sub>50</sub>: cytotoxicity concentration at 50% maximal dose. <sup>d</sup>Selectivity index (CC<sub>50</sub>/IC<sub>50</sub>) <sup>e</sup>Not active below the cytotoxic dose.

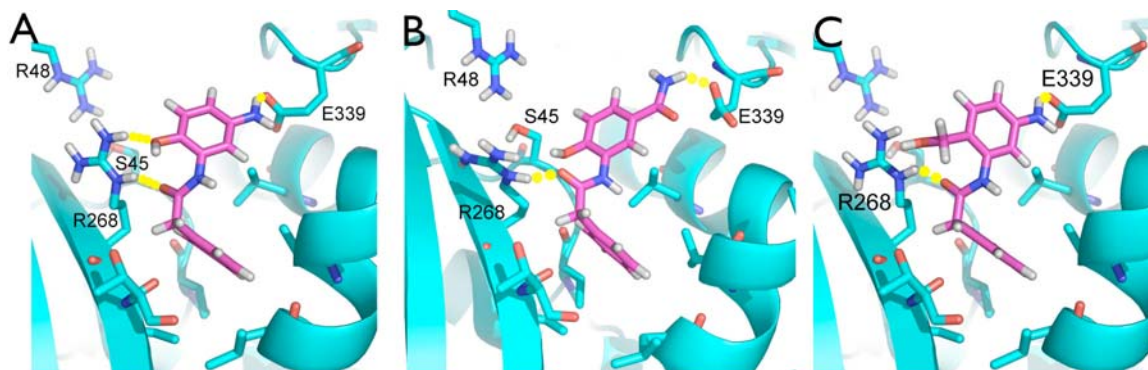
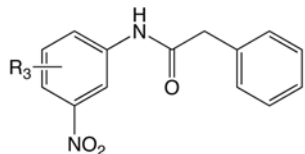


**Figure 3-3:** Comparison between the docking models for AM-4, **7i**, and **8**. (A) Both polar moieties of AM4's acetanilide phenyl can interact with protein simultaneously. (B) The protein cannot accommodate both moieties of **7i** simultaneously. This compound has an IC<sub>50</sub> of only 127μM. (C) Replacement the AM-4's *o*-OH with *o*-CH<sub>2</sub>OH to yield **8**. The protein also cannot accommodate both moieties in this molecule and is inactive at concentrations up to 100μM.

The activity of the monosubstituted compounds bearing nitro and amino groups suggested that activity could be improved with the right disubstituted compound bearing one of these groups and additional functionality. The motivation stemmed from the observation that the *m*-NO<sub>2</sub> analogue **3a** exhibits what appears to be productive hydrogen bonding with Arg48 and Ser45, while the *m*-NH<sub>2</sub> analogue **4a** shows hydrogen bonding with Glu339. The nitro series **11** and aniline series **14** proved to be only moderately fertile, though it did lead to analogues in the low micromolar range (**Table 3-3**). The issue again appears to be the difficulty in both polar moieties interacting with the protein in a way that fully compensates for their interaction with solvent, as seen in the example of **11g**, with a *m*-CONH<sub>2</sub> group and IC<sub>50</sub> of 3.7 μM, though this compound is an improvement over the activity of **3a** (**Figure 3-4**). The most active member, **11f** (also known as AS-48), with an *o*-CONH<sub>2</sub> group, emerged from this study as the most potent disubstituted compound. It appears to be the best example of a disubstituted compound gaining interaction with the protein by utilizing all of its polar groups (**Figure 3-4**).

**Table 3-3:** Antiviral MeV IC<sub>50</sub> values for disubstituted nitro series **11** and aniline series **14**.

entry	compound	R <sub>3</sub>	IC <sub>50</sub> (μM) <sup>a</sup>	IC <sub>50</sub> -res <sup>b</sup>	CC <sub>50</sub> <sup>c</sup>	SI <sup>d</sup>
1	<b>11a</b>	<i>p</i> -OH	63	ND	>600	>10
2	<b>11b</b>	<i>p</i> -F	>100	ND	450	<5
3	<b>11c</b>	<i>m</i> -NO <sub>2</sub>	30	>150	>600	>20
4	<b>11d</b>	<i>o</i> -benzyl ester	68	75	75	1
5	<b>11e</b>	<i>m</i> -NH <sub>2</sub>	11	>150	>600	>55
6	<b>11f<sup>e</sup></b>	<i>o</i> -CONH <sub>2</sub>	3	>150	325	108
7	<b>11g</b>	<i>m</i> -CONH <sub>2</sub>	3.7	>75 <sup>f</sup>	170	46
8	<b>11h</b>	<i>m</i> -NHOH	6	>75 <sup>f</sup>	325	54
9	<b>11i</b>	<i>m</i> -COOMe	4	>150	440	110
10	<b>11j</b>	<i>m</i> -COOH	5	>150	>600	>100
11	<b>11k</b>	<i>m</i> -CH <sub>2</sub> OH	6	>150	>600	>100
12	<b>14a</b>	<i>m</i> -CONH <sub>2</sub>	18	ND	>600	>33
13	<b>14b</b>	<i>m</i> -COOH	55	ND	>600	>11
14	<b>15c</b>	<i>m</i> -NH <sub>2</sub>	>100	ND	ND	ND



<sup>a</sup>IC<sub>50</sub> concentrations were calculated based on the suppression of virus-induced cytopathicity.

<sup>b</sup>IC<sub>50</sub> concentrations of selected compounds against an MeV variant resistant to inhibition by AS-48 due to a point mutation at position 462 in the F protein. ND: not determined. <sup>c</sup>CC<sub>50</sub>: cytotoxicity concentration at 50% maximal dose. <sup>d</sup>Selectivity index (CC<sub>50</sub>/IC<sub>50</sub>). <sup>e</sup>Also known as AS-48.

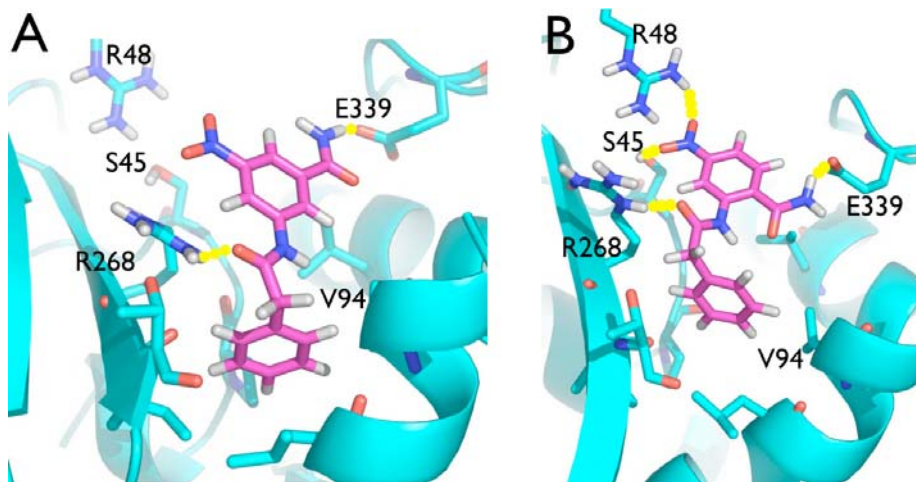


**Figure 3-4:** Docking models for disubstituted nitro compounds **11g** (A) and **11f** (B). **11f** places its polar functionality in a slightly more optimal position and achieves greater activity than **11g**.

### 3.1.3 SAR for compounds with modifications on the distal phenyl ring and the intermediate linker region

Modification of the phenyl group proved deleterious in every case. Several benzyl group modifications within the active *o*-NO<sub>2</sub> series were explored. Methoxy substitutions on the benzyl group in the *p*- or *m*-positions completely lost activity (**7e** and **7f**,

respectively, **Table 3-2**). When these compounds are docked in the structural model, the methoxy groups cause the molecule to be pushed up out of the pocket (**Figure 3-5**). *M*-fluoro and *p*-fluoro analogues had  $IC_{50}$ 's of 47 and 9  $\mu$ M, respectively, while the *o*-fluoro and *o,o'*-difluoro derivatives are inactive at  $>75$   $\mu$ M. *O*-iodo, *m*-iodo, and *p*-iodo substitutions all lead to compounds with drastic loss of activity. An attempt to introduce polarity into the distal phenyl without adding steric bulk by substituting the phenyl ring with pyridine analogs with nitrogens at all three possible positions also led to compounds with drastic loss of activity. Perhaps this result is not surprising since the ring nitrogens increase the desolvation penalty by 3.9-4.4 kcal/mol, without engaging in a productive polar interaction. (See Section 3.2) Thus, it appears that to achieve activity, the molecule must place a moiety in this sector no larger or more polar than a phenyl group.

Modifications to the intermediate linker region also damaged activity in every case examined. Extending the linker between the amide and phenyl from  $CH_2$  to  $CH_2O$  and beyond hurt activity, as illustrated by **7c**, **7g**, and **7h** (**Table 3-2**). Replacement of the anilide amide of **7d** with  $NH-SO_2$  resulted in complete loss of activity, as did other analogous sulfonamides. The reverse amide of **11e** ( $IC_{50} = 11$   $\mu$ M) showed a 2-fold loss of activity ( $IC_{50} = 23$   $\mu$ M). These observations suggest that the acetanilide amide has the best geometry to position the molecule's functionality into the Val94 microdomain.

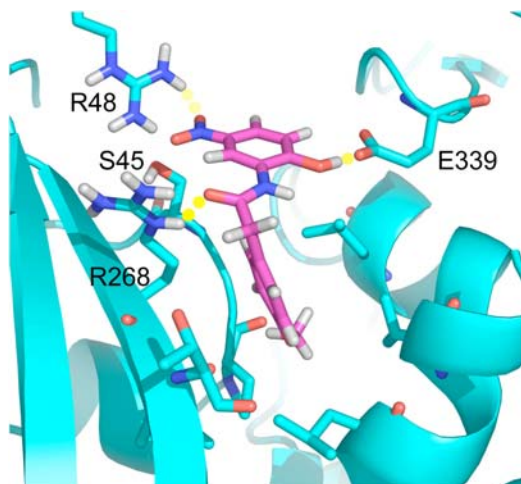


**Figure 3-5:** Docking model for **7e** with a *p*-OMe group on the distal phenyl group ( $IC_{50} > 100 \mu M$ ). Groups such as this which extend the phenyl group or the intermediate linker region cause the molecule to be pushed up out of the pocket, resulting in inactivity.

### 3.2 Balance between the polar interactions and the desolvation penalty

A problem faced when adding polar groups to the scaffold is a higher desolvation penalty. In order to achieve binding and subsequent activity, all the polar groups' interaction with water must be compensated by interaction with the protein. To investigate the relationship of the solvation energy and activity, all the compounds assayed had their energies of solvation calculated as a single point calculation on the ligands' global minima by AMSOL<sup>88</sup> with the PM3 Hamiltonian<sup>89</sup> and the SM5.4.PDP solvent model.<sup>88</sup> This method has proved to be highly accurate, with mean unsigned errors for the energies of solvation of 0.5 kcal/mol for 215 neutral solutes and 4.3 kcal/mol for 34 charged solutes.<sup>88</sup> For these compounds, the results show that active compounds generally fall in a window with energies of solvation from about -20 to -10 kcal/mol (**Figure 3-6**). A compound with an energy of solvation in this range is not

necessarily active however, unless its polar functionality can interact with the protein, as evidenced by the inactive compounds forming the top line in the graph of **Figure 3-6**.

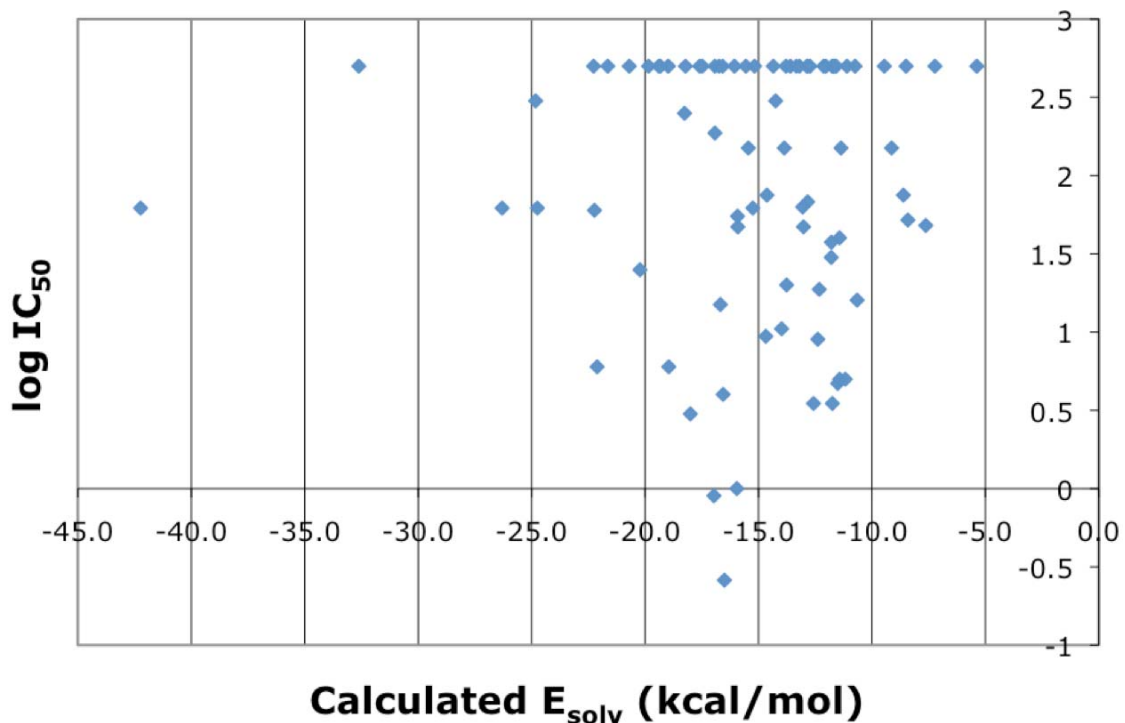


**Figure 3-6:** Balance between polar interactions and the energy of solvation and its effect on activity. The most active compounds have an energy of solvation between -20 to -10 kcal/mol. (Inactive compounds were set to an activity of 500 $\mu$ M to place them on the graph.)

### 3.3 AS-48 as a model fusion inhibitor

AS-48 (**11f** in **Table 3-3**) emerged from this study as not only the most active compound, with an IC<sub>50</sub> of 0.6–3.0  $\mu$ M, depending on MeV strain, but also showed stability under physiological conditions and low cytotoxicity.<sup>80</sup> It was verified as a fusion inhibitor using methods similar to those employed for OX-1 (Section 2.2.1). Namely, the compound inhibited cell-to-cell fusion activity induced by plasmid-encoded MeV H and F glycoproteins. It also caused the virus' infectivity to be abolished by brief pH 3.0 shock even after incubation, suggesting that AS-48 keeps the virus extracellular and exposed.

AS-48 was also evaluated against a range of eight MeV strains currently circulating worldwide; it was effective for all these strains with  $IC_{50}$ 's ranging from 0.6 to 3.0  $\mu$ M. Additionally, AS-48 showed no activity against entry of the related paramyxovirus hPIV-2 or the lentivirus HIV-1, demonstrating the target specificity of this compound for MeV. As with OX-1 and AM-4, engineered mutations at position 94 that block this microdomain in MeV F conferred resistance to AS-48, while the Val94Met mutation that opened the microdomain caused increased sensitivity to AS-48. It is noteworthy that all known wild-type strains carry a methionine at position 94.

However, even with these desirable properties, the level of activity of AS-48 was still too low to be considered as a drug, and lack of further optimization of this scaffold was somewhat discouraging. At the time, the reason for this activity limit was unclear, but later revealed to be the result of targeting a transient intermediate of MeV F in the fusion cascade (Chapter 5). Though limited as a potential drug, AS-48 did serve well both as a proof of principle for paramyxovirinae fusion inhibition by small molecule compounds, and also a probe with which to investigate the conformational changes occurring during fusion (Chapter 4).

## Chapter 4: Resistance to AS-48 fusion inhibition

*Portions of this chapter are based on “Two domains that control prefusion stability and transport competence of the measles virus fusion protein,” published in the Journal of Virology in 2006.<sup>81</sup>*

While point mutations in the Val94 microdomain had been shown to affect the activity of OX-1, AM-4, AS-48, and related compounds, it was not known where spontaneous mutations resulting from inhibitor pressure might occur that would confer resistance. One might expect these mutations to appear in the Val94 microdomain as primary resistance mutants, but it is also possible for resistance to be modulated by domain changes distant from the postulated binding site, as has been demonstrated for the HIV entry inhibitor enfuvirtide (**Figure 1-6**).<sup>90,91</sup> Conceivably, secondary-site resistance mutants like these could control the fusion protein activation or the stability of intermediates in the fusion cascade.

### 4.1 Adaptation study of MeV to AS-48

To determine how MeV would spontaneously gain resistance to AS-48, an adaptation study was performed by Joshua Doyle in the Plemper research group.<sup>92</sup> Five escape mutants that induced extensive syncytium formation in the presence of compound were isolated and the F-encoding genes were analyzed by reverse transcription-PCR, followed by DNA sequencing and transfer into expression vectors. The biological activity of these expression constructs was verified by monitoring their ability to induce cell-to-cell fusion upon cotransfection of MeV H and F expression plasmids in the presence and absence of compound. For the five escape mutants analyzed, resistance to inhibition was achieved by changes in the F protein. Additionally, a more complete study of 25 primary

MeV strains analyzed for resistance identified a single sub-Saharan strain of genotype B3-2 that was resistant. To assess the contribution of individual mutations to the resistant phenotype, all the changes were rebuilt individually in the Edmonston strain MeV fusion protein (F-Edm), except for the case of the B3-2 strain, which was rebuilt in the B1 strain MeV fusion protein (F-B1). In five out of the six resistant strains, resistance was mediated by mutation of F residue N462, whereas mutant III gained resistance by a change at position 367 (**Table 4-1**). In mutant V, an accompanying Met94Val exchange in the Val94 microdomain was found, which had previously been shown to decrease sensitivity to inhibition as a point mutation. These mutations were also engineered into recombinant virions and shown to have >25-fold resistance to inhibition for position 462 mutations and ~15-fold resistance to the Ala367Thr mutation, confirming the results of the plasmid-based fusion assay.

**Table 4-1:** Identification of mutations conferring resistance to compound-mediated inhibition.

Identifier	Strain <sup>a</sup>	Compound <sup>b</sup>	Passage <sup>c</sup>	Resistance <sup>d</sup>	Molecular basis <sup>e</sup>
I	MeV-Edm	OX-1	4	>25	F-Asn462Ser
II	MeV-KS	AS-48	6	>25	F-Asn462Asp
III	MeV-KS	AS-48	6	15	F-Ala367Thr
IV	MeV-KS	AS-48	7	>25	F-Asn462Asp
V	MeV-KS	AS-48	7	>25	F-Met94Val F-Asn462Asp
VI <sup>f</sup>	MeV-B3-2			>25	F-462Lys

<sup>a</sup>Input strain used for each independent adaptation procedure. MeV-KS is a strain originated from Kansas. <sup>b</sup>Compound used for adaptation (OX-1, 60  $\mu$ M; AS-48, 15 $\mu$ M [final concentration]).

<sup>c</sup>Passage number at which extensive cytopathic effect was observed in the presence of compound. <sup>d</sup>Resistance (*n*-fold) to AS-48 of recombinant virions harboring the identified point mutation compared to that of the input strain or a recombinant MeV-Edm F-B3-2 (462Asn) variant. <sup>f</sup>Naturally resistant wild-type isolate, assessed for compounds OX-1 and AS-48.

## 4.2 Resistance-conferring mutations located in a model of the MeV F 6HB

Structurally, the location of these mutations was puzzling. With the exception of mutant V presenting both Met94Val and Asn462Asp mutations, all the mutations in the mutants were located distal to the Val94 microdomain. The mutation in mutant III, Ala367Thr, was located in the DI domain of the NDV-based homology model of MeV F, approximately 40Å away from Val94. The 462 mutations were located on the HR-B domain of the protein and not resolved in the NDV F structure; thus, they were not included in the homology model for MeV F (**Figure 4-1**).

### 4.2.1 Homology model of the MeV F 6HB

Fortunately, structural information was available for two paramyxovirus 6HBs,<sup>79</sup> enabling development of a 6HB model structure of MeV F and evaluation of the mutations' effects at position 462 (**Figure 4-1**). The homology model was built on the basis of the coordinates reported for SV5 F because this virus exhibits the most sequence identity with MeV in its fusion protein. Sequence alignment was performed with ClustalW,<sup>94</sup> using a gap open penalty of 10.0, a gap extension penalty of 0.1, and the Gonnet matrix. When the MeV fusion protein sequence was aligned with the sequence of the SV5 fusion protein, 35% sequence identity, 22% strongly similar, and 13% weakly similar results were found for the portion of the protein to be modeled. Homology modeling was accomplished with PRIME software (Schrödinger),<sup>95</sup> using the SV5 fusion protein fragment structure<sup>79</sup> as a template (PDB code 1sv5). This fragment (residues 132 to 195 and 450 to 487 by MeV numbering) encompasses the 6HB (both the HR-A and HR-B domains). The MeV F sequence was modeled onto this structure, and the other two

subunits of the trimer were generated by transposing the structure to the symmetrical positions of the other subunits. Sections absent in the crystal structure were not modeled. The resulting structure was refined using PRIME's structure refinement module. The lowest energy rotamers for all nonconserved side chains were predicted and incorporated into the model. The final structure (**Figure 4-1**) was evaluated using the WHAT IF Ramachandran-based  $z$  score and the WHAT IF  $z$  score for the local amino acid environments.<sup>96</sup> The Ramachandran  $z$  score was 4.73, similar to the  $z$  score for the crystal structure (4.64). The  $z$  score for the local amino acid environments was slightly better for the model (2.22) than for the crystal structure (2.66).

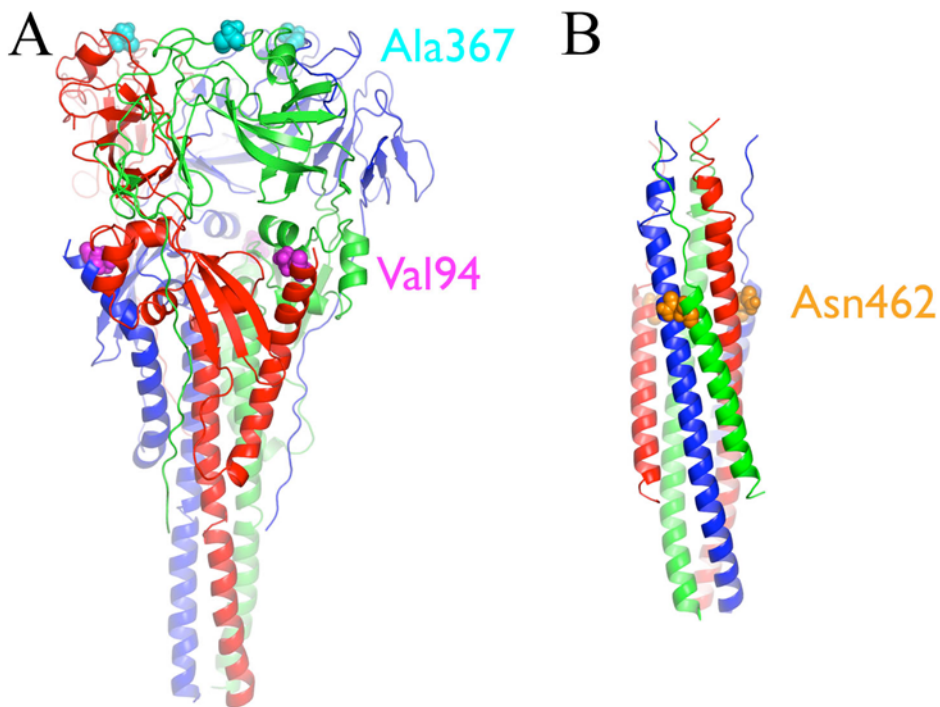


**Figure 4-1:** Locations of spontaneous mutations conferring resistance to fusion inhibitors. (A) In the NDV-based homology model (PDB code 1G5G<sup>18</sup>) of MeV F (shown as ribbons, colored by subunit) the Ala367Thr mutation (cyan spheres) occurs on the DI domain and distant to the Val94 microdomain (Val94 displayed as magenta spheres). (B) In the SV5-based homology model (PDB code 1SVF<sup>79</sup>) of the MeV F 6HB (shown as ribbons, colored by subunit), the Asn462 mutations occur on the HR-B domain, which form the outer helices of the 6HB.

With the new MeV F six-helix bundle model, the mutations at Asn462 were located within the outer helices (HR-B domains) of the 6HB. Because of its high frequency of mutation, analysis efforts were concentrated on residue 462. This residue is localized in the vicinity of the contacting hydrophobic faces of HR-B and the HR-A trimer and is postulated to engage in an electrostatic interaction with Glu170 in the HR-A domain (**Figure 4-2**). The mutations at residue 367 were later examined in light of the prefusion model of MeV F, but this structure was not yet available. Thus, it was difficult to envision what role an Ala36Thr mutation would play in a domain (DI) that did not

appear to be important for fusion. In contrast, the Asn462 mutations were located in a domain (HR-B) already recognized for its role in the stabilization of the postfusion structure. Our interest in this residue was also piqued because researchers at Bristol-Myers-Squibb had recently found that a potent fusion inhibitor for RSV bound to a nearby equivalent residue on the HR-A domain.<sup>63</sup> It was unknown if AS-48 was acting at two sites: one in the Val94 microdomain and one in the 6HB, or if AS-48 was acting solely at the 6HB and the previous mutagenesis data had been misinterpreted. A third hypothesis, that the mutations increased fusion activation in a way that was not yet structurally evident, was also considered.

#### 4.2.2 Models of the MeV F 6HB with resistance-conferring mutations

To investigate how the mutations may perturb the structure, models of the 6HB mutants were developed. If AS-48 directly interferes with interaction of the HR-B domain with the HR-A core trimer, then mutations of residue 462 that confer resistance are anticipated to increase the affinity of HR-B for HR-A. These mutants (Asn462Ser, Asn462Asp, and Asn462Lys) were generated by mutating the residue within the model and using PRIME's side chain prediction feature to determine the lowest-energy rotamers for the mutant residue. The Lovell rotamer library, derived from Protein Data Bank side chain populations, was used to select the lowest-energy rotamer. The resulting structures all predicted disruption of the hydrogen bonding and hence decreased rather than increased 6HB stability due to lack of contact with Glu170 (Asn462Ser), charge incompatibility (Asn462Asp), or steric constraints (Asn462Lys) (**Figure 4-2**).

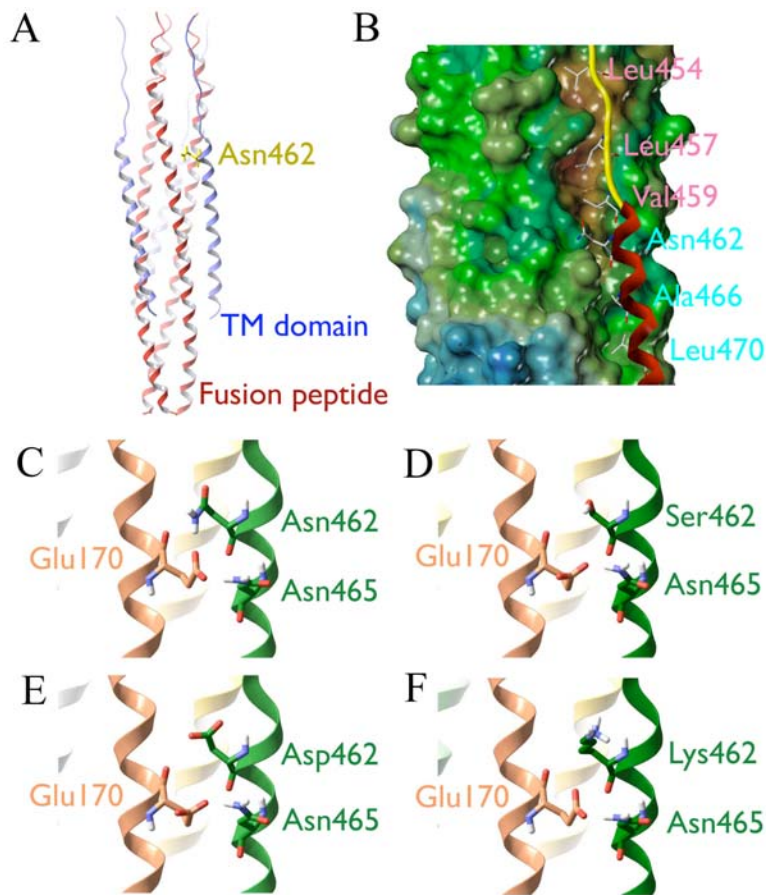


**Figure 4-2:** Localization of residue 462 in the MeV F core homology model. (A) Ribbon model of the MeV 6HB; N termini of HR-B domains are facing up. For clarity, residue 462 is highlighted in only one of the three HR-B domains. (B) Surface model of the MeV 6HB, shown with only one HR-B ribbon for clarity. Residues Val459, Leu457, and Leu454 are predicted to interact with a hydrophobic groove in the HR-A trimer. HR-A residue Glu170 is predicted to engage in hydrogen bonding with residues Asn462 and Asn465. (C to F) Enlarged ribbon models of HR-A and HR-B highlighting the interaction described above (C).

### 4.3 Destabilizing effect of the mutations

While the static models of the MeV F 6HB structures predicted destabilization of the interactions between HR-A and HR-B, the complex interactions of polar groups among each other and with water may give a different result in a dynamic system.

### 4.3.1 Peptide inhibition with wild-type and mutated HR-B domains

Synthetic HR-B derived peptides have been shown to inhibit membrane fusion and hence viral entry for many viruses, including MeV, most likely by competing with endogenous HR-B for binding to HR-A, analogous to the predicted mode of action of enfuvirtide (Section 1.2.1). A correlation between inhibitor potency and the stability of the corresponding helix bundle complexes has been demonstrated for peptidic, helix-derived inhibitors of HIV membrane fusion.<sup>97</sup> Thus, a peptide competition assay was deployed to assess the molecular modeling results predicting destabilization of the 6HB by the spontaneously emerging mutations. In this assay, performed by Joshua Doyle in the Plemper group, His-tagged variants of MeV HR-B derived peptides harboring either wild-type asparagine (N) or mutant serine (S) at the equivalent of position 462 were expressed, purified, and tested for the ability to inhibit viral entry and hence compete with endogenous HR-B for docking to HR-A.

The peptide containing the Asn462Ser exchange was unable to inhibit MeV-Edm even at very high concentrations of 600 µg/mL. A recombinant MeV-Edm with an F Asn462Ser mutation was generated that, although more sensitive than the parent virus, likewise showed only partial inhibition by this peptide (**Figure 4-4**). In contrast, the unmodified peptide (462N) reduced viral loads of MeV-Edm by >99% at 300 µg/mL, while recombinant virions containing point mutations at F residue 462 conferring resistance to the compounds revealed even greater sensitivity to this peptide (**Figure 4-4**). These findings indicate a reduced affinity of all mutant HR-B variants for the HR-A

trimer.

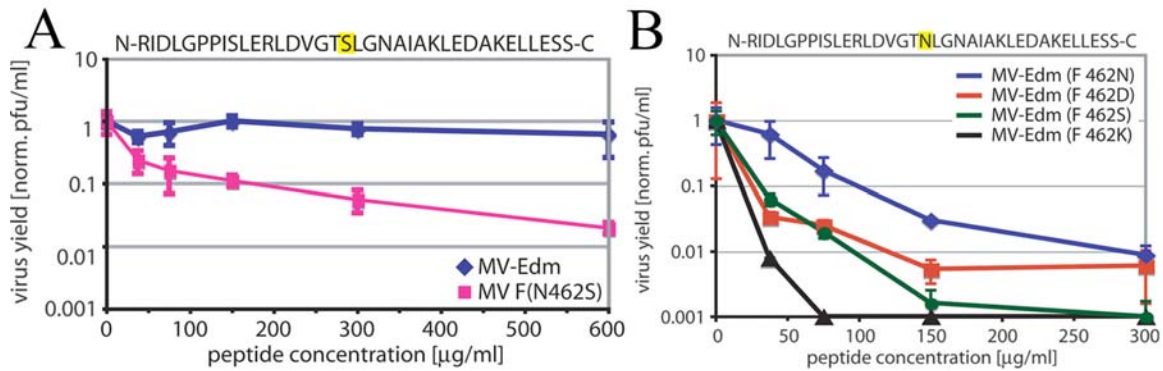


**Figure 4-3:** Peptide competition assay determining the efficiencies of virus inhibition by synthetic HR-B derived peptides.<sup>92</sup> (A) Cells infected with unmodified recombinant MeV-Edm F or mutant MeV F (N462S) in the presence of increasing concentrations of a modified peptide containing one of the spontaneously produced mutations (462S, shown in yellow; sequence shown above the graph). (B) Peptide competition assay of all the recombinant MeV F variants generated, using an unmodified synthetic peptide (462N shown in yellow; sequence shown above the graph).

### 4.3.2 Molecular dynamics studies of wild-type and mutated 6HB structures

To structurally investigate how the mutations may disrupt the stability of the 6HB, molecular dynamics (MD) simulations were performed of the wild-type and the three mutated structures using the GROMACS package.<sup>98, 99</sup> The structures were simulated using the OPLS-AA force field<sup>100</sup> and solvated with the TIP4P water model.<sup>101</sup> A hydrated rectangular box (5 by 5 by 12 nm; volume, ~327 nm<sup>3</sup>) containing ~9,300 water molecules was built around each structure. Sodium cations were randomly placed throughout the water pool to bring the total charge in each system to zero. Each hydrated complex was energy minimized to remove any high-energy contacts and subjected to 50 ps of position-restrained MD at 300K to allow water to soak into the structure. Each system was then subjected to 50ps of MD at 300K, followed by 50 ps of simulated annealing MD with temperature increases of 5 K/ps (300 to 550K). Time steps of 0.002

ps were used in all simulations. HR-A was constrained using position restraints of 1,000  $\text{kJ}\cdot\text{mol}^{-1}\cdot\text{nm}^{-2}$  on the backbone atoms in the simulations to account for the absence of the remainder of the fusion protein in this model. Solvent-accessible surface areas over the last 50 ps were calculated using the `g_sas` function within the GROMACS package.

In the resulting simulations, the wild-type structure maintains the interactions seen in the static structure, whereas the mutants generally have more interaction with solvent. Because the interactions between HR-A and HR-B are dominated by hydrophobic interactions, one measure of the stability of the 6HB is the amount of solvent-exposed hydrophobic surface area. When the latter were calculated over the last 50 ps of the simulations, they show that the mutants lose hydrophobic interaction between HR-A and HR-B because more hydrophobic surface is exposed to solvent (**Figure 4-3**). Over the last 10 ps of simulation, wild-type HR-B exhibits an average hydrophobic solvent-accessible area of  $78.6 \text{ nm}^2$ , compared to  $80.2 \text{ nm}^2$ ,  $81.9 \text{ nm}^2$ , and  $83.6 \text{ nm}^2$  for 462Ser, 462Asp, and 462Lys structures, respectively. In contrast, the hydrophilic surface area is similar, indicating that the amount of polar interaction with solvent does not differ for the four structures.

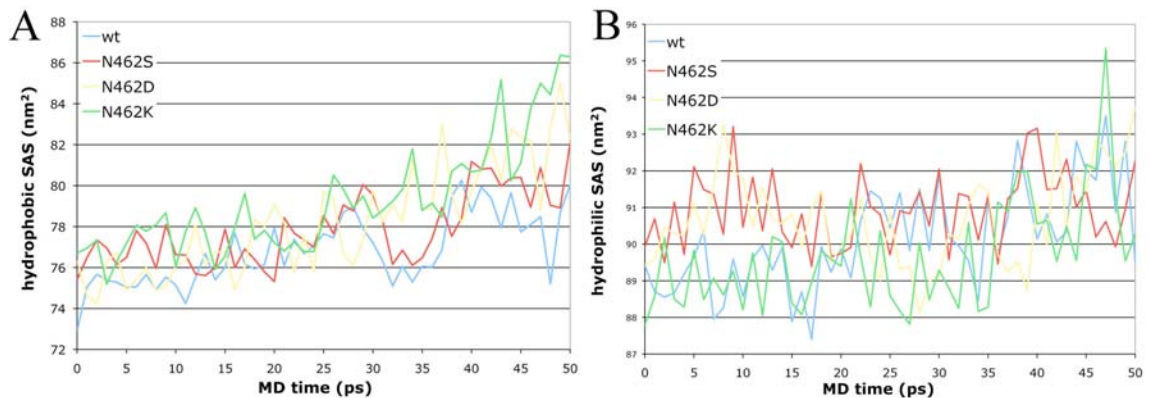


**Figure 4-4:** MD simulations predict greater destabilization of the mutant 6HBs compared to the wild type. The mutants increase the peptides' hydrophobic exposure to water through the course of the simulation, indicating greater dissociation. (A) Hydrophobic solvent-accessible surface (SAS) areas are shown for 50 ps of MD simulation. (B) Hydrophilic exposures to water were similar for the four structures, with average hydrophilic SAS areas over the last 10 picoseconds of simulation between 91.1 nm<sup>2</sup> and 92.0 nm<sup>2</sup>.

#### 4.3.3 Mutation of the HR-A residue interacting with Asn462

To further address whether AS-48 interferes with the interaction of HR-B to the HR-A helices, the residue Asn462 is predicted to interact with on the HR-A domain, Glu170, was mutated to alanine in a recombinant virion. This drastic change should result in increased resistance of these recombinants to compound-mediated inhibition if AS-48 physically engages this microdomain in HR-A. However, the Glu170Ala point mutations elicited no change in sensitivity to inhibition compared to unmodified MeV F.

#### 4.3.4 Coimmunoprecipitation efficiency of MeV F with a Flag-tagged variant of the HR-B derived peptide

The final experiment by the Plemper group to test the absence of AS-48 binding interfering with formation of the MeV F 6HB evaluated the coimmunoprecipitation efficiency of MeV F with a HR-B derived peptide bearing a Flag tag for antibody binding. If AS48 does bind in the HR-A domain, the coprecipitation efficiency should

decrease when AS-48 is added under assay conditions. The results show, however, that AS-48 actually increased coprecipitation efficiency, indicating the arrest of the F trimer in a conformation that facilitates docking of the peptide. (See Section 5.5)

#### **4.4 Mutations affect the fusion activation of MeV F**

Further experiments by the Plemper group investigated the interplay between mutations at position 94 and 462 and their effect on surface expression and fusion activity. A series of F variants harboring mutations in both domains were generated, coexpressed with MeV H, and their ability to induce syncytium assessed. Several variants demonstrated interdependent effects on fusion activity: the 94V 462K and 94G 462S combinations resulted in an approximate 90% loss of activity, while the 94G 462K construct failed to induce any syncytium formation. Activity loss in these F variants mostly coincided with a reduction in their intracellular transport competence as measured by surface biotinylation.<sup>92</sup> Some constructs were transport-competent, however, as in the case of the 94M 462K and 94V 462S variants which reached 65% and 100% of the fusion activity of F-Edm, respectively. Interestingly, introduction of either 94M or 462K alone in F-Edm reduces activity while the combination of 94M and 462K restores fusion activity.

##### **4.4.1 Transport competence of mutant MeV F constructs restored at 30°C**

Lack of transport competence could be based on misfolding or decreased conformational stability of the mutant F trimers, potentially resulting in exposure of hydrophobic domains such as the fusion peptide or internal domains. Either would explain the reduction in surface expression of the F variants. However, if the reduced surface expression is the result of decreased conformational stability, incubation at

reduced temperature should restore both transport competence and fusion activity since it reduces the likelihood of intracellular F prematurely folding to the postfusion form.

When the transport competence was assessed by the Plemper group upon incubation at 30°C or 37°C, fully restored surface expression was observed for several mutants at the lower temperature (**Figure 4-5**). These mutants were also able to induce syncytium formation upon coexpression of MeV H at 30°C, showing that they still have fusion activity, albeit only at the lower temperature. Such a result is consistent with the mutations decreasing the conformational stability of the prefusion F trimer if premature refolding results in blockage of intracellular transport.

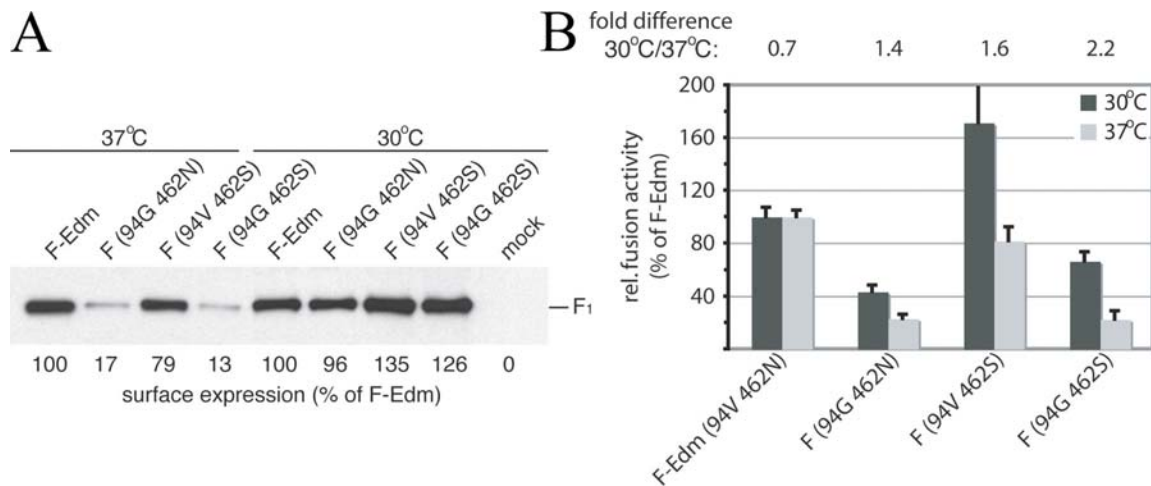


**Figure 4-5:** F mutants 94G 462S and 94G 462N are temperature sensitive. (A) Surface expression of cells expressing F variants after incubation at 37°C and 30°C. Transport to the surface is restored at the lower temperature. (B) Fusion activity of cells expressing MeV H and the F variants, incubated at 30°C and 37°C. Fusion activity is increased at 30°C for all the F mutants, whereas the fusion activity of F-Edm remains unchanged at the lower temperature.

#### 4.4.2 AS-48 stabilizes a transport-competent prefusion conformation

It was reasoned that if AS-48 stabilizes an intermediate form of MeV F in the fusion cascade, it might be possible for the compound to restore surface expression of the mutant F trimers if reduced conformational stability was indeed the cause for intracellular retention of these constructs. Based on permeability predictions of AS-48 using the QikProp package,<sup>102</sup> we expect the compounds to be membrane permeable and thus capable of docking to the F protein inside the host cell. Indeed, addition of AS-48 restored transport competence of the temperature-sensitive F variants at 37°C in a dose-dependent fashion. Not only was transport competence restored, but when several double mutants were cotransfected with MeV H in the presence of AS-48, a dose-dependent increase in fusion activity was also observed. These findings suggest that AS-48 stabilizes the mutant F constructs, allowing them to reach the surface in a form that is still

capable of inducing membrane fusion. And while AS-48 can stabilize the F structure enough to reach the surface, it does not interact tightly enough with the mutated F proteins to prevent membrane fusion when triggered by H. However, based on this data, the possibility that compound-facilitated F folding and fusion inhibition are mechanistically distinct events cannot be completely excluded.

#### 4.5 Dual roles of the MeV F residue 462

The preceding experiments indicate that residue 462 in MeV F not only influences the stability of the 6HB in the postfusion form, but also the stability of the prefusion form and therefore its susceptibility to activation. The destabilization effect in the 6HB did not indicate the source of resistance: MeV F does not gain resistance simply by increasing the stability of its 6HB and thus, its postfusion form. Perhaps this is unsurprising, as the 6HB is known to be an extremely stable structure. Subtly changing polar interactions between HR-A and HR-B may indeed affect a measurable response in its stability, but the change in stability does not affect the fusion activity of the protein. What appears to matter is the balance between stability and ease of activation of the prefusion form. While viral pathogenesis is the result of much more than the fusion protein, it is interesting to note that all currently circulating viral strains appear to have been selected for stability at the expense of ease of activation (Asn at position 462), except for the one variant of the Sub-Saharan B3-2 strain (Lys at position 462). These viral strains are susceptible to inhibition by AS-48 (excepting the B3-2 strain), but under inhibitor pressure, will develop spontaneous mutations at position 462, the same position at which one variant of B3-2 strain also harbors a different residue. These mutations come at price, however: the increased possibility the protein may prematurely refold before being expressed on the

surface. This is consistent with the result that all the 462 mutants tested gain surface expression and fusion activity at 30°C relative to MV-Edm F. Such a role for residue 462 is not without precedent. A similar conclusion was drawn for SV5 F residues 447 and 449, both of which are also on the HR-B domain.<sup>7</sup> Unfortunately, no structural interpretation for this effect for either SV5 or MeV was possible at the time because of the lack of a prefusion X-ray crystal structure, preventing the development of these structural models.

## Chapter 5: Conformational changes in MeV F during fusion

*Portions of this chapter are based on “Measles virus entry inhibitors: a structural proposal for mechanism of action and the development of resistance,” published in the journal Biochemistry in 2008.<sup>103</sup>*

Although the community was aware that major conformational changes occurred in paramyxovirinae fusion proteins through probing by biochemical means<sup>104</sup> and electron microscopy,<sup>105</sup> the full extent of the conformational changes was not anticipated. Thus, when the prefusion structure of PIV5 F was determined in 2006 through joint efforts of the Jardetzky and Lamb research groups,<sup>19</sup> efforts were made to understand the previous experimental and modeling data surrounding MeV fusion inhibition in light of the additional structural information.

### 5.1 Limitations of the NDV based model of MeV F

The Newcastle Disease Virus (NDV) F protein was the first atomic level structure of a paramyxovirus fusion protein and served as the template for the MeV F homology model used for both detailing the structure of the Val94 microdomain and the structure-based design of fusion inhibitors targeting this site. The protein used for the analysis contained a mixture of precursor F<sub>0</sub> and proteolytically cleaved F. It also lacked structural information for the fusion peptide, HR-A, and HR-B domains, leading to confusion in the literature of whether this structure was closer to the prefusion or postfusion forms of the protein.<sup>2, 10</sup> The NDV F structure was later revealed as post-fusion by comparison to the X-ray crystal structure for the uncleaved ectodomain of human parainfluenza virus 3 fusion protein (hPIV3 F), which had crystallized with a six-helix bundle.<sup>11</sup> Because a

homology model in the best case can only incorporate the structural information of its template structure, the MeV F structure also had these limitations.

## 5.2 New model of the postfusion form of MeV F

The X-ray crystal structure of the hPIV3 F protein (Brookhaven Protein Data Bank access code 1ZTM) allowed the development of a more complete MeV F structural model, this time known to be in the postfusion form.<sup>11</sup> This postfusion model was generated by performing sequence alignment of MeV F (Edmonston strain) to hPIV3 (strain 47885) by the ClustalW algorithm,<sup>94</sup> using a gap open penalty of 10.0, a gap extension penalty of 0.1, and the Gonnet matrix. The alignment between the sequences resulted in 26% identity and 51% similarity with all cysteines conserved. Sections of MeV F corresponding to missing segments of the crystal structure were not modeled. These included the amino- and carboxy-termini (residues 1-26 and 488-550) and a section from residues 100-144 corresponding to the fusion peptide and a portion of the HR-A domain. The homology model was then constructed with the PRIME software package (Schrödinger).<sup>95</sup> PRIME does not allow subunits to be built simultaneously, so each subunit was assembled and then merged into a complete trimer. The models were refined using PRIME's side chain prediction protocol on all residues to generate the lowest energy rotamer for each sidechain. The quality of the structure was evaluated by means of WHAT IF structure validation checks.<sup>96</sup> These checks showed that the postfusion model had Ramachandran and local amino acid environment z-scores of -4.5 and -1.1 respectively. This compares with -4.6 and -1.0 for the X-ray crystal structure of hPIV3 F, indicating the structural quality of the model structure is comparable to the experimental structure.

The resulting postfusion model of MeV F is very similar to the NDV-based model, with a root mean square deviation in backbone atom positions ( $\text{RMSD}_{\text{backbone}}$ ) of 3.0Å. It is also similar to the 6HB MeV F model based on the SV5 fusion protein fragment structure<sup>79</sup>, with an  $\text{RMSD}_{\text{backbone}}$  of 2.8Å (**Figure 5-1**). These results again confirm that the NDV-based model shows the protein in the postfusion form. Further modeling work utilized the hPIV3-based model as the more complete postfusion model.

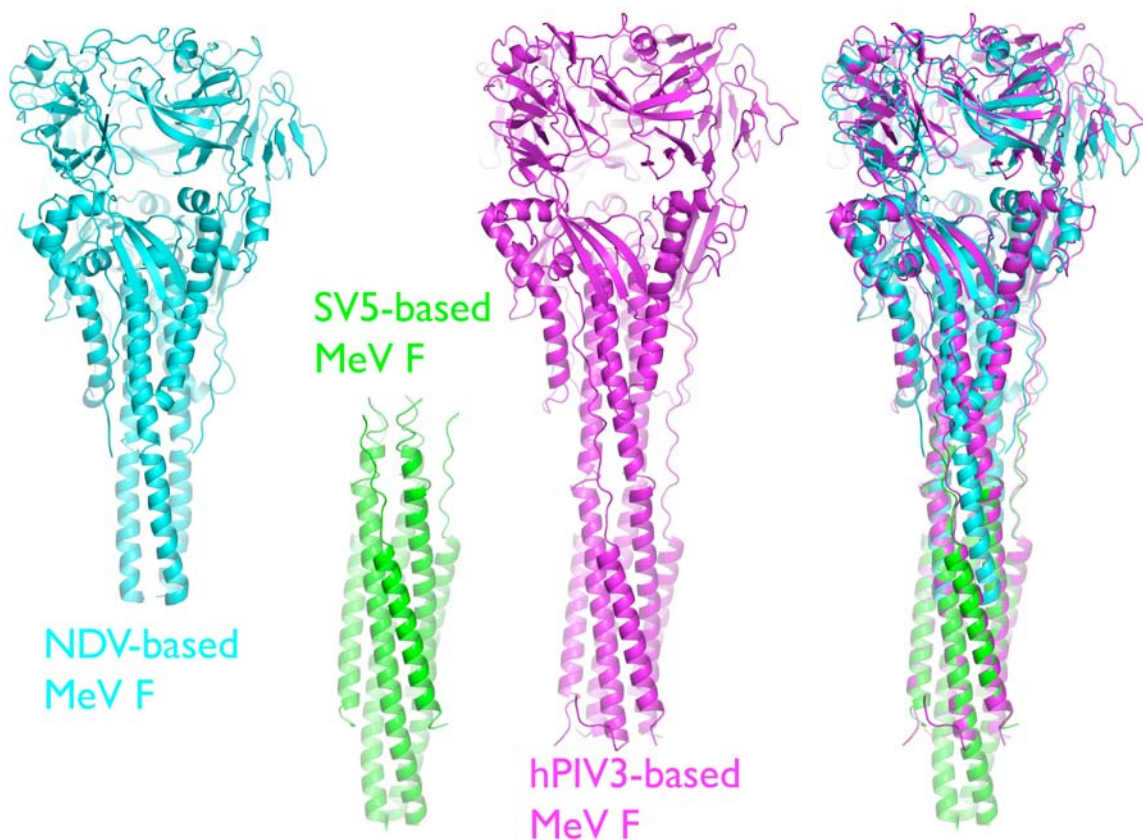


**Figure 5-1:** Homology models of MeV F based on different postfusion template structures. The proteins are shown as cartoons. The far right panel shows the structural alignment between the three models.

### 5.3 Prefusion model of MeV F

The prefusion model of MeV F was built on the basis of the coordinates reported for the prefusion PIV5 F structure<sup>19</sup> (Brookhaven Protein Data Bank access code 2B9B) using the same methods as the hPIV3-based model. Namely, sequence alignment of MV F (Edmonston strain) to PIV5 F (W3A strain) was accomplished with the ClustalW algorithm<sup>94</sup>, using a gap open penalty of 10.0, a gap extension penalty of 0.1, and the Gonnet matrix. A minor adjustment in the HR-C domain was performed to prevent a gap in the helix. The proteins share 29% identity and 48% similarity, with all of the cysteine residues conserved. Sections of MV F corresponding to missing segments of the crystal structure, the amino- and carboxy-termini (residues 1-26 and 515 -550) were not modeled. This homology model was also constructed with the PRIME software package (Schrödinger),<sup>95</sup> building each subunit individually and then merging to form the complete trimer, followed by refinement using PRIME's side chain prediction protocol on all residues. WHAT IF checks were again used to evaluate the quality of this structure resulting in a Ramachandran z-score of -4.4 and local amino acid environment z-score of -1.0, while the X-ray crystal structure of PIV5 F scores -4.0 and -0.5, respectively.

### 5.4 Structural features and changes in the prefusion and postfusion MeV F models

With models of both prefusion and postfusion MeV F, investigation was made into the structural features and changes that occur during fusion.

### 5.4.1 Pre- and postfusion MeV F models imply large domain movements during fusion

As seen by comparison of the template structures of Yin et al.<sup>19</sup>, the pre- and postfusion models are trimeric structures in which most of the residues have moved large distances in the transition between the two conformations (**Figure 5-2**). The most highly conserved regions in the pre- and postfusion models are the DI and DII domains (residues 27-46, 289-378; and 385-431, respectively). When DI and DII of the pre- and postfusion structures are superimposed, the resulting  $\text{RMSD}_{\text{backbone}}$  for these regions is 6.2 Å (**Figure 5-2C**), similar to the measurement by Yin et al.<sup>19</sup> comparing the DI and DII domains of PIV5 F and hPIV3 F. The  $\text{RMSD}_{\text{backbone}}$  for the entire structure (common residues 27-99 and 145-487), however, is 50 Å. The greatest movement occurs in the HR-A, HR-B, and HR-B linker domains (common residues 145-214 and 432-487) with a combined  $\text{RMSD}_{\text{backbone}}$  of 91 Å (**Figure 5-2, D and E**). Moderate movements in the DIII domain with an  $\text{RMSD}_{\text{backbone}}$  of 13 Å are also evident even without including HR-A (common residues 47-99 and 215-288). These large residue displacements underscore that paramyxovirus fusion involves extraordinarily large and deep-seated rearrangements of protein structure.<sup>5, 9, 19</sup>

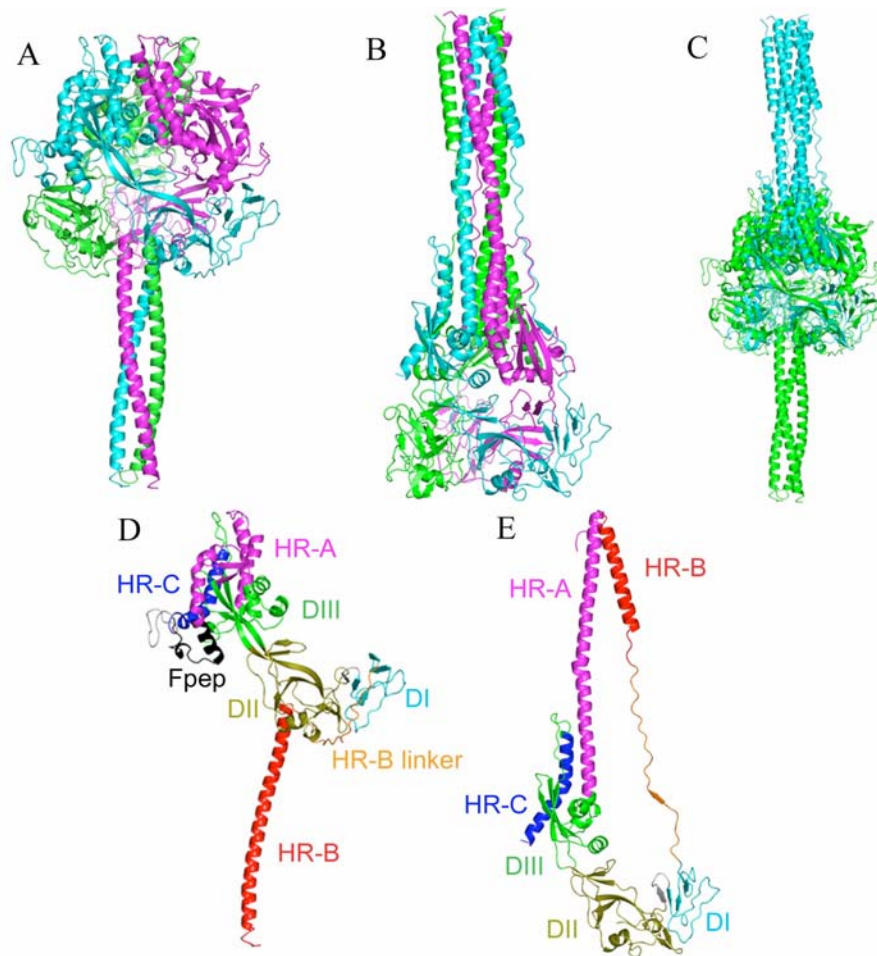


**Figure 5-2** (previous page): Secondary structure diagrams of MeV F protein homology models highlight the domain movements occurring during fusion. Prefusion (A, based on PIV5 F [PDB code 2B9B<sup>19</sup>]) and postfusion (B, based on hPIV3 F [PDB code 1ZTM<sup>11</sup>]) conformations are colored by subunit. Note the 3-helical bundle on the left and the 6HB on the right. (C) Prefusion (green) and postfusion (cyan) models superimposed by DI and DII domains. Overall backbone RMSD is 50Å. (D) Single subunit of prefusion model colored by domains. (E) Postfusion model of the same subunit as (D), colored by domains, and similarly oriented by DI and DII domains.

To illustrate the refolding pathway from prefusion to postfusion structures, a morphing simulation accomplished by applying the multi-chain mode of the Yale Morph Server (<http://molmovdb.org/morph>). The morph was performed in 30 steps using CNS adiabatic mapping.<sup>106</sup> Limited minimization is done for each step. The starting and

ending structures were aligned by superimposing the backbone atoms of the DI and DII domains. To account for experimental evidence which suggest the HR-B 3HB melts prior to the formation of the HR-A 3HB,<sup>9</sup> the morph was broken into three sections, DIII+HR-A, HR-B, and DI+DII, which were then assembled back into the full structure. The final morph thus shows HR-B and DI+DII moving in 5 steps, followed by 30 steps of DIII+HR-A, followed by 25 steps of the HR-B and DI-DII (**Figure 5-3**). This figure does not represent a suggested refolding pathway for the fusion protein, but serves to illustrate the conformational steps in a way that is consistent with current experimental data.

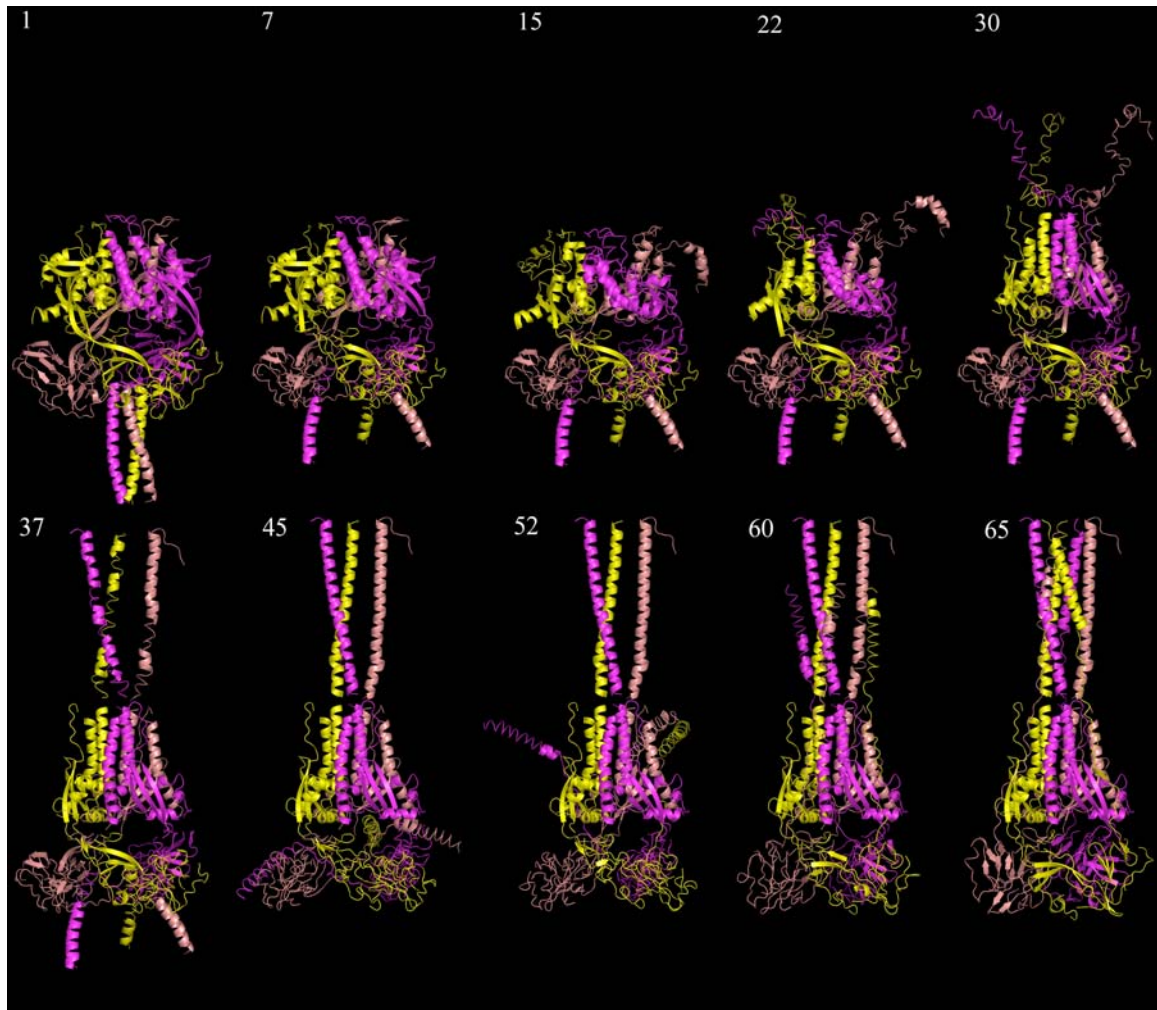


**Figure 5-3:** A solely illustrative morphing simulation from the prefusion to postfusion structures of MeV F. Ten frames are shown of the total 65 steps in this morph. In this illustration, the 3HB of the HR-B domain first dissociates, followed by the release and insertion of the fusion peptides into the target membrane (not shown). When the fusion peptides move together, the HR-A domains are brought into proximity and form a 3HB. This is followed by the HR-B domains swinging around the protein and inserting into the hydrophobic grooves of the HR-A 3HB, resulting in the formation of the 6HB.

#### 5.4.2 The hydrophobic character of the HR-A and HR-B domains is consistent with the proposed model of fusion

In the prefusion structure, HR-B is predicted to form a 3-helical bundle by self-association instead of serving as the outer coil of the 6HB as in the postfusion structure (**Figure 5-2**). Other class 1 viral fusion proteins such as HIV's gp41 and influenza's hemagglutinin also form 6HB structures postfusion through a similar mechanism, but only in paramyxoviruses are the HR-B domains considered to form self-associated, extracellular 3HBs.<sup>1, 5</sup> (Depending on the pathogen under investigation, the N-terminal heptad repeat is referred to as HR-A, HR-N, or HR-1. The C-terminal heptad repeat is referred to as HR-B, HR-C, or HR-2.)

To investigate the hydrophobic character of the HR-A and HR-B domains in the pre- and postfusion models, lipophilicity-mapped Connolly surfaces were generated using Sybyl's MOLCAD module. The area of hydrophobic surfaces was calculated using only the portion of the surface that showed hydrophobic properties. For these structures, a lower bound of -0.04715 for the lipophilic property (as suggested in the Tripos Bookshelf<sup>107</sup>) was used to exclude surface with more hydrophilic character, leaving surface contributions from only the hydrophobic atoms.

The HR-B 3-helical bundle in the prefusion model places the hydrophobic residues inward for inter-subunit contacts, while the hydrophilic residues face outward to solvent. However, in the postfusion model, the hydrophobic residues of HR-B face a hydrophobic groove formed by two subunits of HR-A (**Figure 5-4, A-D**). HR-B loses a turn in its helix in the transition from prefusion to postfusion and is less hydrophobic overall than HR-A. HR-B (residues 456-487) possesses 534 Å<sup>2</sup> and 477 Å<sup>2</sup> of

hydrophobic surface area in the pre- and postfusion conformations respectively, while HR-A (residues 146-183) is measured at 1174 and 1271 Å<sup>2</sup> of hydrophobic surface, respectively (**Figure 5-4, A-D**). HR-A presents roughly twice the hydrophobic surface per residue than HR-B, and, in fact, increases its hydrophobic surface upon fusion to obtain favorable hydrophobic contacts with HR-B. HR-B's lesser hydrophobic surface area relative to HR-A is advantageous for the fusion protein because the HR-B 3-helix bundle is considered to dissociate in order for the protein to achieve the postfusion conformation.

### 5.4.3 The large, water-filled cavity in the prefusion protein is a metastable feature that provides MeV F with a source of potential energy

In the prefusion form, the MV F homology model incorporates a feature similar to that present in the X-ray structure of PIV5 F, namely a 35 Å diameter spherical cavity in the head of the protein. To investigate how solvent water molecules would interact with this cavity in the pre- and postfusion forms, solvated structures were generated using molecular dynamics (MD) with the GROMACS package<sup>98,99</sup> and simulated using the OPLS-AA force field<sup>100</sup> and the TIP4P water model.<sup>101</sup> Hydrated rectangular boxes with periodic boundaries were built around the two models with dimensions of 105 nm by 105 nm by 170 nm and 90 nm by 90 nm by 180 nm for the prefusion and postfusion structures, respectively. A total of 63,000 and 49,000 explicit water molecules were simulated for the pre- and postfusion structures, respectively. Chloride anions were randomly placed throughout the water to bring the total charge in each system to zero. Both hydrated complexes were subjected to 500 steps of steepest descent minimization using the above parameters to remove any high energy contacts between water and

protein, and then simulated for 50 picoseconds of position restrained MD at 300K and 1.0 atm of pressure to allow the waters to soak into the structure. The resulting structures were manually analyzed to determine the number of waters in the cavities and channels.

The resulting solvated structure of the prefusion model resulted in approximately 550 water molecules in the cavity (**Figure 5-4E**). In the postfusion form, the latter is replaced by a quartet of channels (one axial channel, three radial channels), but only 400 water molecules are accommodated by them when solvated in silico (**Figure 5-4F**). The entropic cost of transferring a water molecule from liquid to a protein has been estimated to be between 0 and 7 cal mol<sup>-1</sup> K<sup>-1</sup>, corresponding to a free energy cost between 0 and 2 kcal/mol at 300K.<sup>108</sup> Most of the water molecules in the prefusion solvent pool are loosely associated with the protein. It can be expected that individual water molecules will not contribute entropy penalties near the upper bound of 2 kcal/mol, but a sizeable entropic penalty can be associated with the total water pool. On the other hand, water molecules in an open channel (**Figure 5-4F**) are expected to experience a reduced entropic penalty relative to water sealed in a cavity. Another useful measure for describing this effect is the additional buried hydrophobic surface area between the prefusion and postfusion forms. Because different fragments of the protein are missing in the two models, a direct comparison cannot be made. However, if the solvent accessible surface area between the common fragments (residues 27-99 and 144-487) are calculated, the postfusion form buries 4850 Å<sup>2</sup> of surface area that was exposed to solvent either in the cavity or on the exterior of the prefusion form of the protein. It is generally thought that buried surface area provides 25 cal mol<sup>-1</sup> per Å<sup>2</sup> of hydrophobic free energy gain at 300 K.<sup>109-111</sup> This yields a rough estimate of 121,000 cal/mol or 121 kcal/mol of

hydrophobic free energy gain from prefusion to postfusion conformations. Non-hydrophobic energy changes are not addressed here; but the contribution of buried surface area to the relative stability of the postfusion conformation does serve to illustrate the considerable potential energy stored in the prefusion conformation, particularly in the large cavity in the head of the trimer.

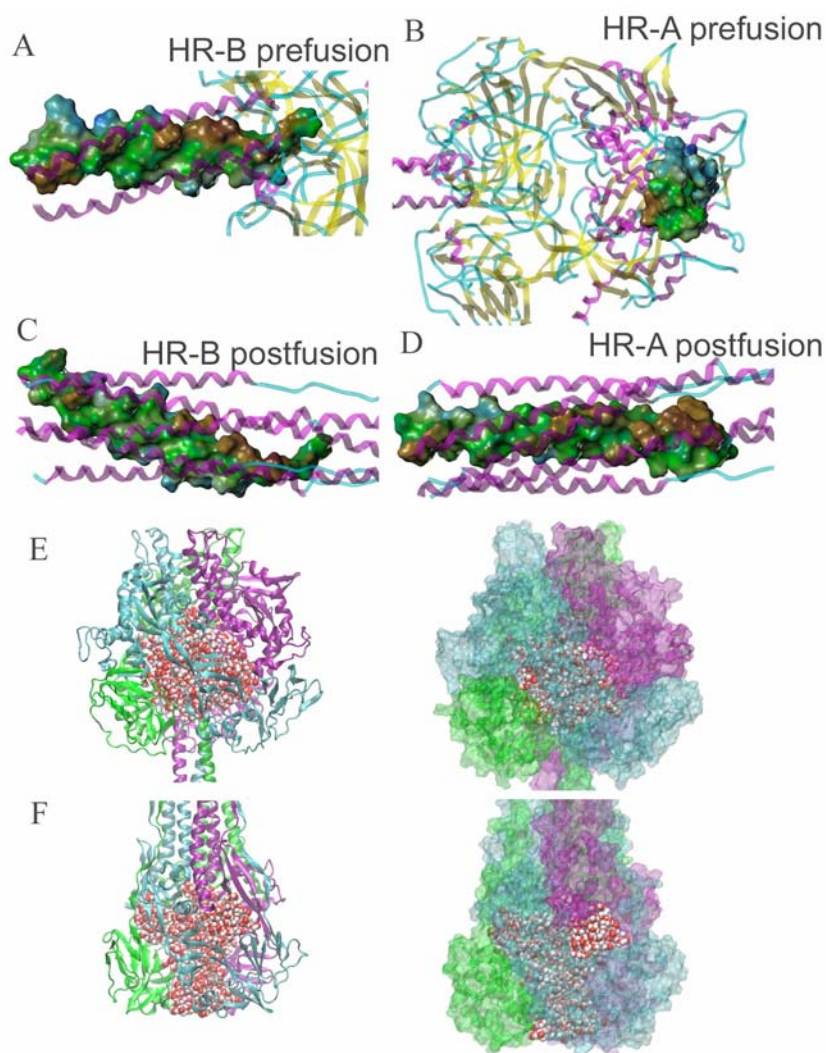


**Figure 5-4:** Potential energy sources in fusion refolding. (A-D) Hydrophobic surfaces of one HR-A and HR-B subunit in prefusion and postfusion models (brown = hydrophobic, green = neutral, blue = hydrophilic). (E-F) Water-filled cavity and channels in prefusion and postfusion models. Protein is shown as cartoon or surface, colored by subunit; water is shown as vdW spheres. (E) Prefusion model sustains a cavity with 550 water molecules held inside. Surface representation on the right shows that the cavity is almost completely sealed. (F) Postfusion model has an axial channel and three radial channels filled with 400 water molecules. Surface representation shows the openings of the channels at the top and the sides.

#### 5.4.4 The Val94 microdomain is rearranged and occluded in the prefusion model

The microdomain around Val94 has been shown to be important for fusion activity (See Chapter 2, references 71 and 72). It is formed by contacts between the DIII and HR-C domains from one subunit and the DIII domain of a neighboring subunit. Experiments have deduced that mutations disturbing the hydrophobic base and a hydrophilic residue at the rim of the microdomain ablate fusion activity, but mutations to smaller residues in the base (Leu256Ala and Leu257Ala) can be compensated by the mutation to a larger residue at the opposite side of the base (Val94Met) (See Section 2.1). The resulting triple mutant maintains all the fusion activity of wild-type MeV F. These structural observations are based on the homology model of NDV F. By contrast, this microdomain in the prefusion form of MeV F adopts an alternative spatial arrangement (**Figure 5-5, A-B**). Thus, the C $\alpha$  atoms of leucines 256 and 257 are separated from Val94 by 23 and 25 Å, respectively, while in the new postfusion model, they are separated by only 7 and 10 Å, respectively. Accordingly, the prefusion model does not immediately suggest a structural explanation for how the Val94Met mutation compensates for the other mutations, restores proper folding into a transport-competent conformation, and maintains fusion activity. We cannot rule out the possibility that the model fails to place these residues qualitatively correctly or that long-range effects may play a role.

Another possibility is propelled by an independent line of experiments, which show that AS-48 and OX-1 rescue intracellular transport competence and fusion activity in a dose dependent fashion from a Val94Gly/Asn462Ser double mutant that is normally not surface-expressed (See Section 4.4.2, reference 88). The Asn462Ser mutation gives

resistance to AS-48, but in combination with Val94Gly, surface expression is eliminated in the absence of compound. Taking into account that AS-48 recognizes and stabilizes a fusion-intermediate conformation of F, this finding suggests that F Val94Gly/Asn462Ser spontaneously assumes an intermediate conformation with a well-formed AS-48 docking site. The latter, if stabilized by AS-48 from premature 6HB formation, is still remarkably transport competent. Applied to the F 94M/256A/257A situation, by analogy this triple-mutant F variant may spontaneously assume an intermediate conformation that brings residues 94 and 256/257 in close proximity as proposed in our previous studies,<sup>92</sup> is still transport-competent and, once matured and surface expressed, mediates fusion in combination with MV H protein. While our experimental data support the latter hypothesis, a definite conclusion is beyond the scope of static models and cannot be reached with the experimental tools currently available.

For mutations that maintain surface expression but lack fusion activity, our models do provide a structural basis. Such is the case for the Thr270Ala mutation, which has 100% surface expression compared to wild-type, but only 55% fusion activity.<sup>75</sup> In the prefusion model, Thr270 of the DIII domain hydrogen bonds Ser144 of the HR-A domain directly adjacent to the fusion peptide, providing an important point of contact that anchors the fusion peptide to the head of the protein prior to fusion activation (**Figure 5-5C**). Mutating Thr270 to Ala removes this interaction and may cause the fusion peptide to dissociate from its interface with the DIII domain without proper activation. Such an event is expected to compel MeV F to embark on the conformational pathway to a post-fusion structure without a cellular membrane to target. Non-productive, irreversible conformational changes like this would reduce the ability of the virus to enter

cells since more of its fusion proteins are wasted in “misfires.” Mutation of Thr270 to Ser elicits no change in hydrogen bonding causing fusion activity to be maintained at 93%.<sup>75</sup>

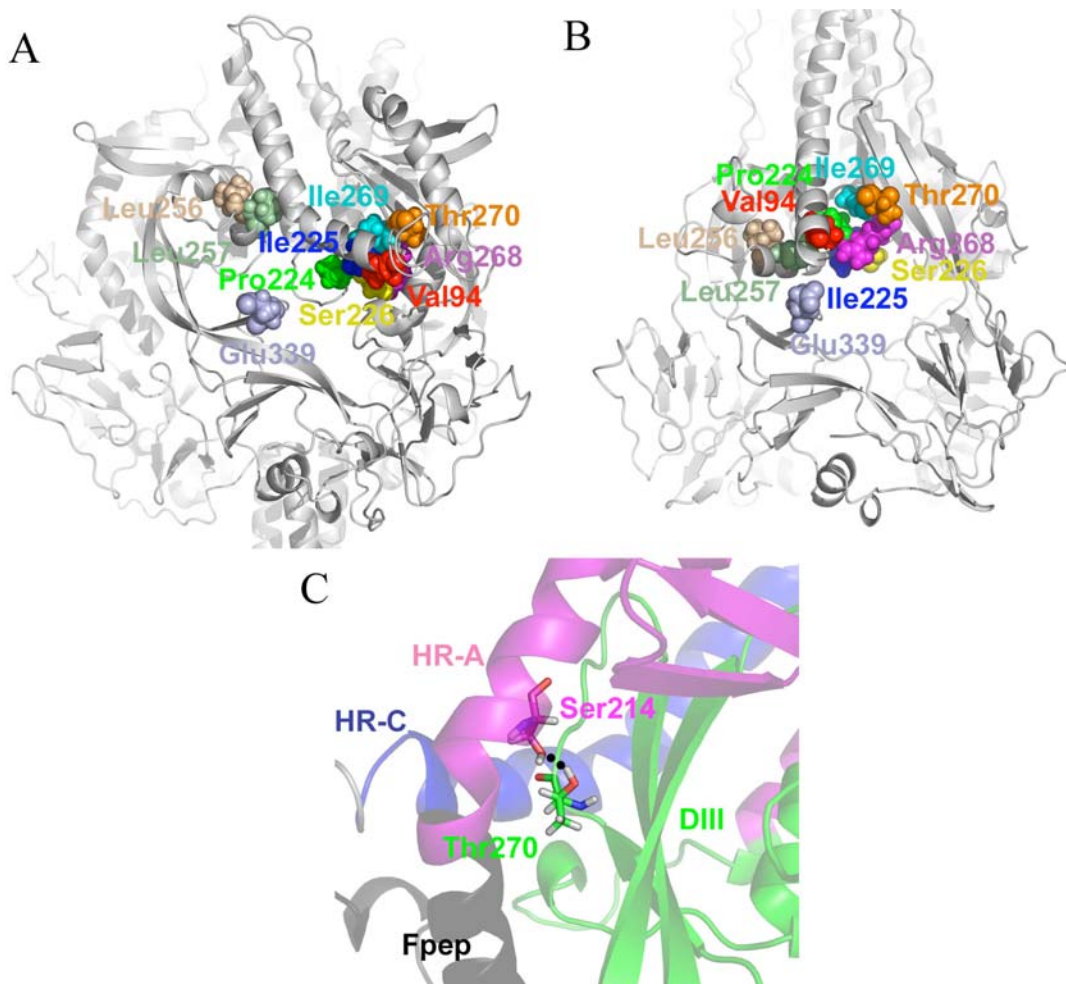


**Figure 5-5:** Changes in the Val94 microdomain occurring during fusion. Prefusion (A) and postfusion (B) models are displayed with Val94 microdomain residues as vdW spheres with the protein shown as secondary structure. In the prefusion model the microdomain is covered by the fusion peptide and HR-A; structural rearrangements occur in the DIII and HR-C domains to bring the microdomain together. (C) Interaction between Thr270 and Ser144 (shown as sticks) in the pre-fusion model. This interaction appears to anchor HR-A and Fpep to the protein head prior to fusion.

## 5.5 The nature of the AS-48 binding to the Val94 microdomain

The structural rearrangements and occlusion of the Val94 microdomain in the prefusion form make it clear that AS-48 and related entry inhibitors could not prevent fusion by binding to the prefusion structure. To further test whether AS-48 is binding at the Val94 site and investigate which conformational form of MeV F that AS-48 is targeting, a series of bench and molecular modeling experiments were devised or reinterpreted in light of the prefusion model.

### 5.5.1 Defined antisera against the Val94 microdomain

To further test whether AS-48 is binding at the Val94 site, the Plemper group developed two polyclonal antibodies against synthetic peptides including HR-C residues 88-103 and DIII residues 240-259, respectively (**Figure 5-6**). Both peptides encompass residues that are near the Val94 microdomain (**Figure 5-6, B-C**), but only the former peptide covers this residue. Both peptide domains are more exposed and closer to each other in postfusion than prefusion (337 and 79 Å<sup>2</sup> increased surface areas for residues 88-104 and 240-259, respectively). In immunoprecipitation experiments with AS-48 performed by the Plemper group, the order of addition greatly influences the amount of precipitated protein/antibody complex. Adding AS-48 before the antibody directed against the epitope for 88-103 essentially eliminates subsequent antibody binding. Adding the antiserum before AS-48 does not change the efficiency of precipitation. The antiserum directed against the 240-259 residues confirmed the specificity of these findings: adding AS-48 prior to this antiserum even increases the amount of precipitate, suggesting enhanced accessibility of the epitope. Adding antiserum before AS-48 again does not change the amount of precipitate. These results suggest that AS-48 blocks

interaction of the 88-103 antibody to the Val94 microdomain; while with the 240-259 antibody, AS-48 prolongs exposure of this epitope along the fusion conformational pathway. Both results strongly suggest that AS-48 is indeed binding at this location, albeit to an undefined conformational state of the protein.

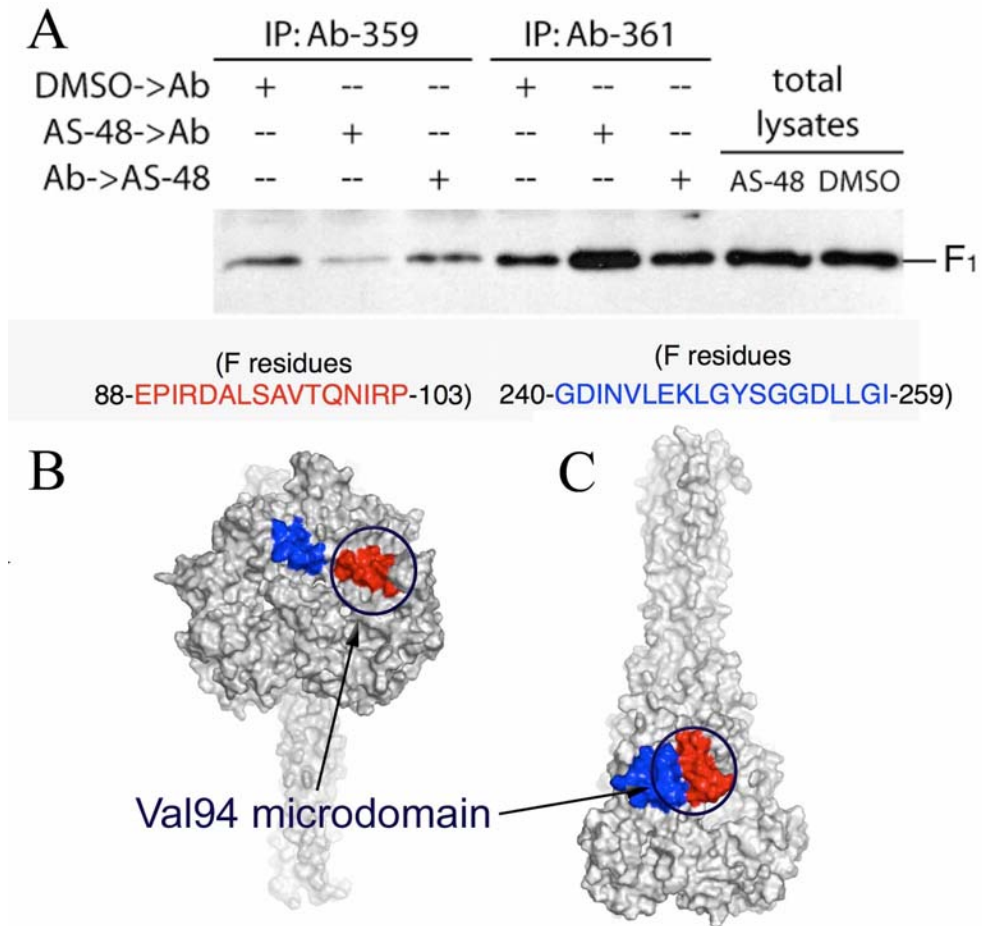


**Figure 5-6:** Co-immunoprecipitation experiments with AS-48 and two antibodies directed at epitopes in the Val94 microdomain. (A) Ab-359, directed against residues 88-104, and Ab-361, directed against residues 240-259 have opposing effects on the amount of complex precipitated when added prior to AS-48. When introduced after AS-48 addition, both antibodies precipitated amounts of complex similar to antibody-only conditions. Prefusion (B) and postfusion (C) models are shown as surfaces with residues 88-104 and 240-259 colored red and blue, respectively. The location of the Val94 microdomain in both models is highlighted by circles. The epitopes are closer and considerably more exposed post-fusion (337 Å<sup>2</sup> and 79 Å<sup>2</sup> increased surface area for residues 88-104 and 240-259, respectively).

### 5.5.2 Conformational state of MeV F targeted by AS-48

Previously, we deployed an epitope-tagged peptide from the HR-B domain of MeV F to explore the conformational status of MeV F in the presence of AS-48 (See section 4.3.4 and reference 88). The compound did not prevent the HR-B peptide from binding to the HR-A coiled-coil, which would be expected if AS-48 acts through physical docking to HR-A. Rather, it increased the co-precipitation efficiency of the epitope-tagged HR-B peptide compared to solvent-only treated controls. These results infer that AS-48 arrests MV F in a conformational intermediate that has formed an extended HR-A 3HB, but has not yet formed the 6HB or completed the subsequent refolding process (**Figure 5-7, A-C**).

To visualize the formation of the Val94 microdomain, a morphing simulation of the DIII domain from the prefusion to the postfusion structure was accomplished by applying the multi-chain mode of the Yale Morph Server (<http://molmovdb.org/morph>). The morph was performed in 30 steps using CNS adiabatic mapping.<sup>106</sup> The starting and ending structures were aligned by superimposing the backbone atoms of the DI and DII domains, then truncated to residues 47-99 and 194-288 of the DIII domain. Fusion peptide and HR-A residues encompassing residues 113-193 move dramatically from prefusion to postfusion structure, and thus were not included to simplify analysis of the conformational changes in the Val94 microdomain. Using MAESTRO (Schrödinger),<sup>112</sup> AS-48 was manually docked into the Val94 microdomain at each of the 30 timesteps to estimate the point of fusion blockade; namely at which step the pocket opens up sufficiently to permit the ligand to bind without steric congestion.

Based on the morphing simulation of the DIII domain in combination with manual docking of AS-48 to the intermediates from the morph, the binding pocket does not form until late in the simulation. We propose that AS-48 binds an intermediate resembling frame 25 (**Figure 5-7D**), and thus prevents fusion by interfering with the final conformational rearrangements necessary to bring the HR-B domains in proximity to the HR-A 3HB. HR-B linker residues 434-441 form beta sheet-like contacts with the defined DIII beta sheet containing residues 48-57. Conceivably, AS-48 could prevent the beta sheet from moving into its final position by disrupting interactions with the HR-B linker and interfering with the placement of HR-B in the 6HB. The 240-259 peptide antibody target exposes 1044 Å<sup>2</sup> surface area to solvent in the intermediate predicted to bind AS-48 (**Figure 5-7D**, frame 25), as compared with its surface in the post-fusion model (943 Å<sup>2</sup>). If AS-48 inhibits this intermediate, a prolonged interaction of this epitope with its antibody could occur, resulting in additional protein-antibody precipitated complex. This is exactly the result of the aforementioned immunoprecipitation experiment when AS-48 is added before the antiserum directed against 240-259 epitope. The Val94 microdomain is expected to be almost fully formed in the intermediate structure, providing the binding site that matches the structure-activity relationships derived for analogs of the compound (See Chapter 3, reference 77) and the experimental results obtained from F mutants exposed to AS-48.

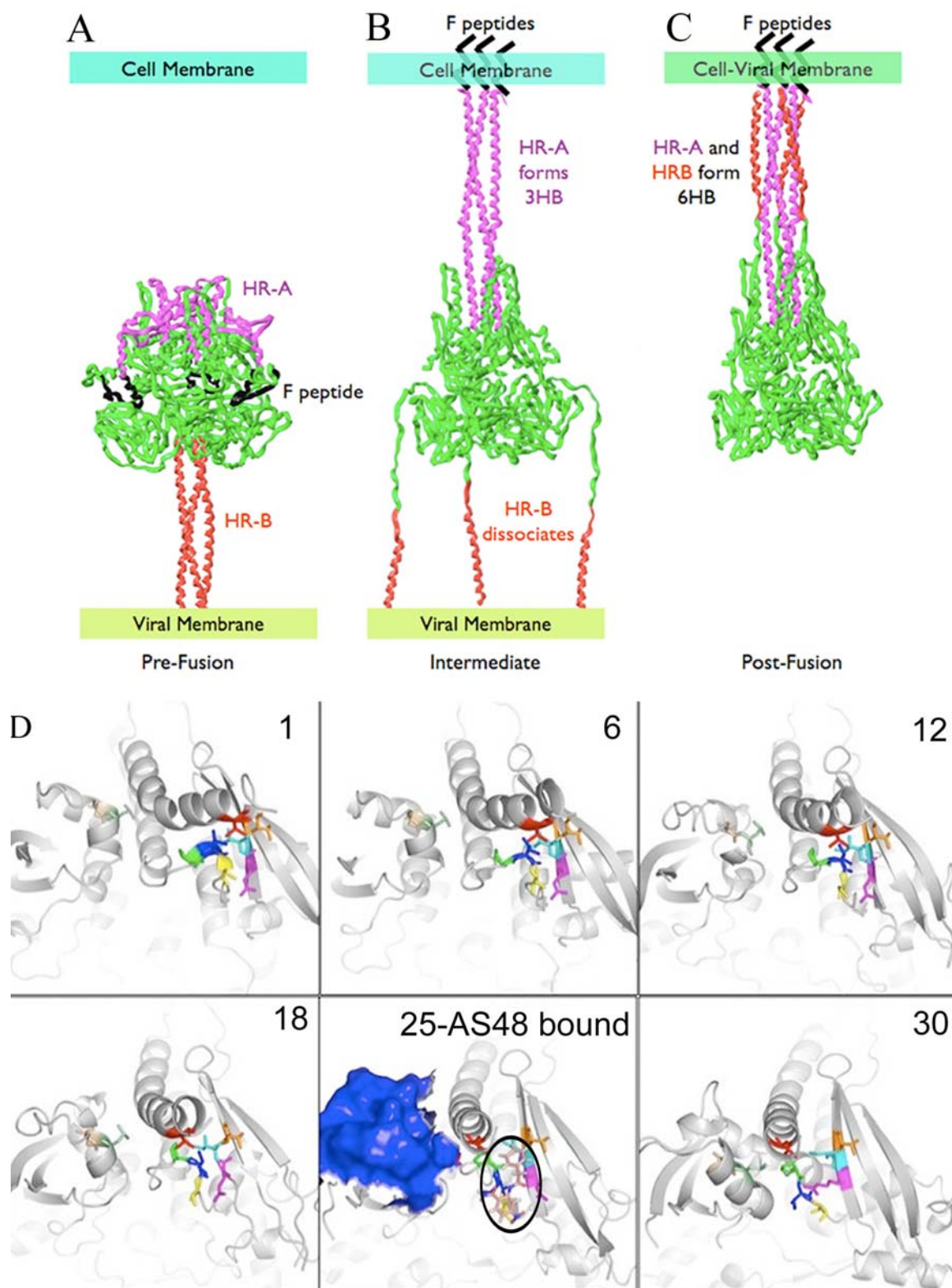


**Figure 5-7**, previous page: Proposed fusion pathways for the entire MeV F (A-C, similar to pathway by Yin et al.<sup>19</sup>) and the DIII domains (D). (A) Prior to fusion, MeV F exists in a metastable state with water-filled cavity, HR-B in a 3HB, and the fusion peptide and HR-A wrapped around the head of the protein. (B) Activation causes fusion peptides to bury within the cell membrane, formation of the HR-A 3HB, and dissociation of HR-B. (C) Final post-fusion structure with completely collapsed water-filled cavity and fully formed HR-A and HR-B 6HB. (D) Results of morphing simulation of the DIII domain, shown in 6 of the 30 frames. Residue coloring is the same as Figure 3A-B. AS-48 (shown as sticks, colored with pink carbons and outlined in black) is docked into frame 25 and is proposed to inhibit fusion by disrupting interactions between DIII and the HR-B linker. In this frame, the 240-259 epitope (shown as blue surface) is fully exposed for interaction with the Ab-361 antibody.

## 5.6 Structural proposal for the development of AS-48 resistance

To better understand the role of residues 462 and 367 in conferring resistance, the status of these residues was examined in the prefusion and postfusion models and interpreted in light of the experimental fusion activities of MeV F 462 variants at 37 and 30°C

### 5.6.1 MeV F residues 462 and 367 are located at the critical interface between the HR-B and DI domains in the prefusion conformation of F

In prefusion MV F, Asn462 is found near the beginning of HR-B at the intersection of HR-A and DI domains (**Figure 5-8A**). However, in postfusion MeV F, Asn462 is located on HR-B on the outer coil of the six-helix bundle formed by HR-A and HR-B (**Figure 5-8C**). In both structures, Asn462 is facing  $\sim 90^\circ$  away from the center of the helical bundle, but in the postfusion form, it is predicted to hydrogen bond with Glu170 of HR-A found in another subunit. In the pre-fusion form, it hydrogen bonds to an adjacent residue (Gly460) on the same subunit. The second mutation, Ala367, is part

of the DI domain and is near Asn462 in the prefusion form ( $C_{\alpha}$  to  $C_{\alpha}$  distance of 12 Å), but very distant in the postfusion form ( $C_{\alpha}$  to  $C_{\alpha}$  distance of 114 Å). Ala367 goes from a nonpolar environment in the prefusion form to a relatively solvated form in the postfusion structure. The Asn462 and Ala367 positions in the pre-fusion conformation suggest that mutations here may be conferring resistance by destabilizing a network of non-covalent interactions between the top of the HR-B domains and the base of the prefusion F head that must be disengaged for HR-B 3HB to dissociate (vide infra) and form the intermediate structure (**Figure 5-8B**). Further experiments described below suggest that destabilization of these interactions could accelerate the fusion kinetics, overcoming the inhibitory effect of AS-48.

### 5.6.2 Mutations at MeV F residues 462 and 367 disrupt the hydrophobic interactions holding the HR-B and HR-linker to the DI domain

The models suggest that HR-B and the HR-B linkers are only loosely bound to the DI domain in the head of prefusion MeV F. Most of the interaction between the HR-B/HR-B linker domains and the rest of the protein occurs at the base of the head where HR-B meets the DI domain. The mutations that confer resistance to AS-48 are located in this critical region (**Figure 5-8D**). (Ala367 makes up part of the hydrophobic network that holds these three domains (HR-B, HR-B linker, and DI) together. This residue, along with Thr314, Leu354, and Leu355 are part of the DI domain residues in this network. HR-B's portion of the network is formed by Leu457 and Thr461, while Leu454 and Ile452 form the HR-B linker's portion of the network. Of the eight hydrophobic residues of HR-B and the HR-B linker forming contacts with the head of the protein, five of these residues (Leu457, Leu454, Ile452, Pro451, and Pro450) are from this network. The

remaining three hydrophobic residues (Leu448, Ile446, and Val432; not shown) are dispersed along the length of the HR-B linker. These observations suggest that this concentrated hydrophobic region is critical for holding the HR-B/HR-B linker domains in the pre-fusion conformation. Mutations to more polar or smaller residues in this region will disrupt the hydrophobic network and most likely decrease the barrier for dissociation of HR-B/HR-B linker domains from the head of the fusion protein. Such mutations are seen in AS-48 resistant mutants: Ser, Asp, or Lys replace Asn at position 462, and Thr replaces Ala at position 367, implying that the virus overcomes inhibition by AS-48 through conversion of F to a less stable, constitutively more active variant.

To investigate the effect of these changes, the corresponding residues in the prefusion model were mutated and their lowest energy rotamer using PRIME's side-chain prediction protocol was found (**Figure 5-9**).<sup>95</sup> In the resulting structures, Asp and Lys mutations at position 462 introduce a charged species into this hydrophobic network (**Figure 5-9, B and C**), increasing the attraction for water molecules which can break up these interactions. Ser is not more polar than Asn462 (**Figure 5-9A**), but when mutated in the prefusion model, the smaller residue increases the exposure to solvent (**Figure 5-9D**). The Thr mutation at position 367 introduces a polar hydroxyl group into this deeply hydrophobic area (**Figure 5-9, E and F**), likely inducing the same kind of effect as the Asn462 mutations.

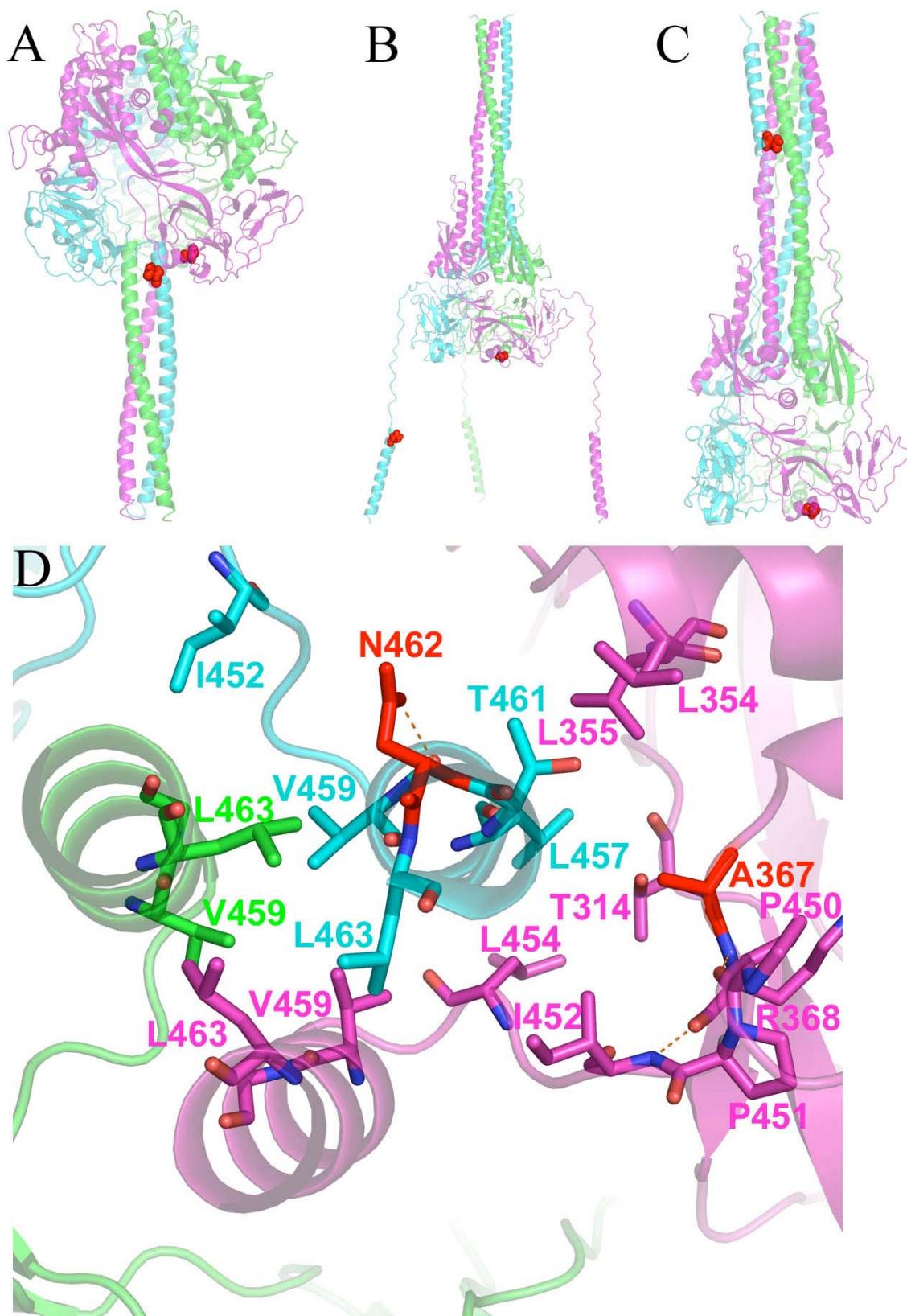


**Figure 5-8** (previous page): Position of resistance-conferring mutations at Asn462 and Ala367. (A) Prefusion model shows that these residues are proximal and part of the key interactions holding HR-B to the head of the protein prior to fusion. (B) Proposed intermediate structure revealing that Asn462 and Ala367 must separate to achieve the conformational intermediate. (C) Postfusion model showing that Asn462 ends up in the 6HB while Ala367 remains in the DI domain of the MV F head. (D) View of the HR-B/HR-B linker interface with the head of MV F in the prefusion model. Residues providing key hydrophobic interactions are shown as sticks. Eight hydrophobic residues provide interaction of the HR-B/HR-B linker to the head. Five of the residues (Leu457, Leu 454, Ile452, Pro451 and Pro450) are from this network. The other three hydrophobic residues (Leu448, Ile446, and Val432, not shown) are located upstream on the HR-B linker.

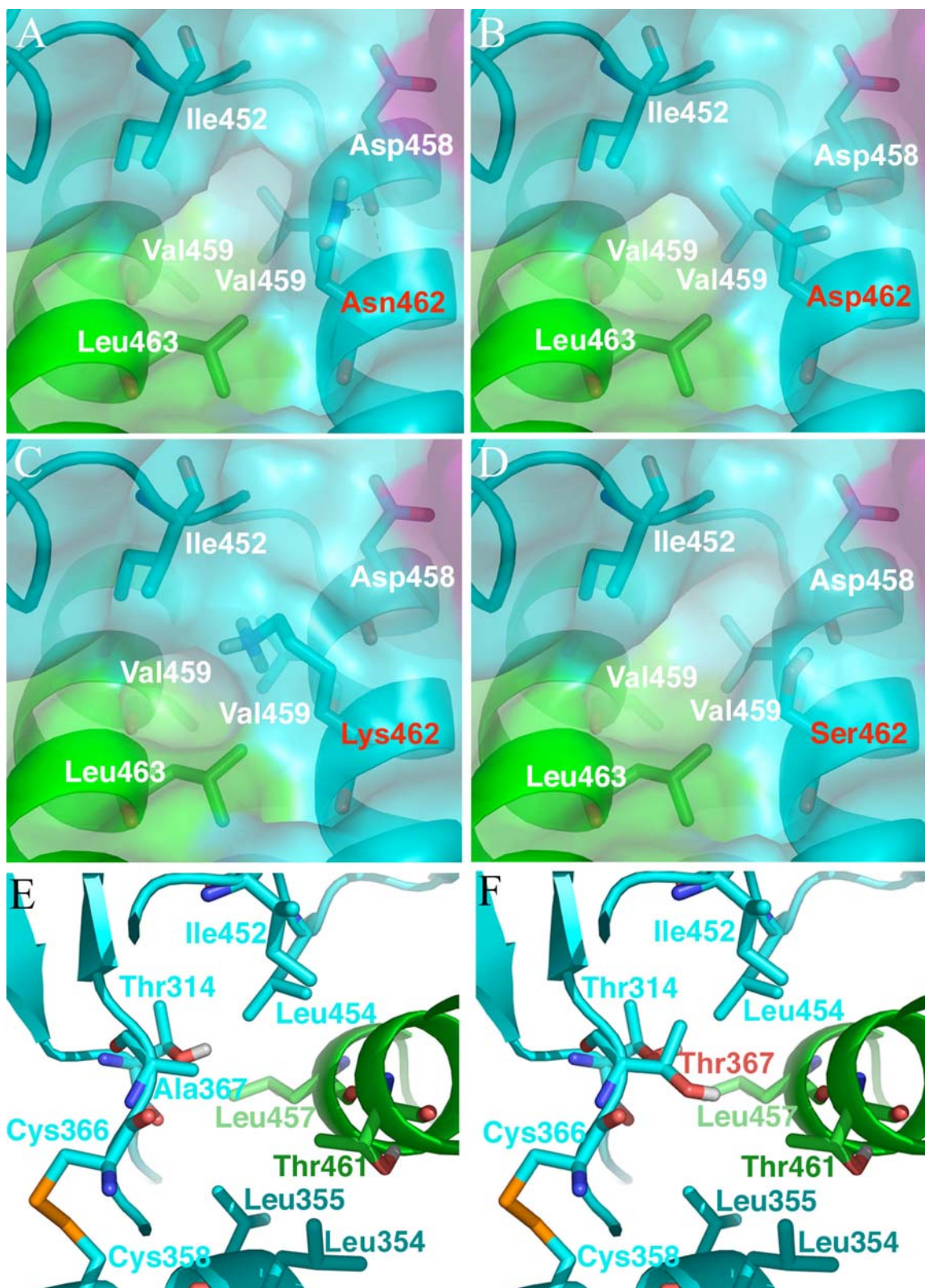


**Figure 5-9**, previous page: Predicted structures for resistance-conferring mutations. **(A-D)** Asn462 mutations at the interface of HR-B and DI domains in the pre-fusion model. The protein is shown as secondary structure with its Connolly surface. Selected residues are shown as sticks. In wild-type **(A)**, Asn462 hydrogen bonds the backbone oxygen of Asp458. The Asn462 → Asp mutant **(B)** introduces a negative charge into this critical hydrophobic environment. The Asn462 → Lys mutant **(C)** introduces a positive charge. The Asn462 → Ser mutant **(D)** does not introduce a charge, but as a smaller residue, it increases the solvent exposure of the hydrophobic interactions compared to wild-type. **(E-F)** Ala367 mutations at the interface of HR-B and DI domains in the pre-fusion model. The protein is shown as secondary structure. Selected residues are shown as sticks. In wild-type **(E)**, Ala367 is part of the network of hydrophobic interactions. The Ala367 → Thr mutant **(F)** introduces a polar hydroxyl directly into the hydrophobic network.

### 5.6.3 Mutations at position 462 enhance fusion activity at lower temperatures

Fusion activities of the MeV F mutants N462S and N462K upon co-expression with MeV H were tested at both 30 and 37°C (**Figure 5-10A**). In both mutant constructs, the fusogenicity is markedly increased at 30°C. Even at 37°C, the N462K variant experiences more fusion activity than unmodified MeV F at the same temperature. Consistent with this, lateral spread of a recombinant MeV harboring F N462K is increased through the cell monolayer (**Figure 5-10B**). The N462K variant is increased within the cell monolayer. Such results are consistent with a decrease in the dissociation barrier between the HR-B/HR-B linker domains and the head of the fusion protein, assuming this barrier plays a deciding role in fusion activation. For PIV5 F, Russell et al.<sup>7</sup> have suggested this region acts as a “conformational switch” based on mutations of PIV5 F residues L447 and I449 (MeV F equivalent residues L457 and V459, **Figure 5-8D**). Thus, aliphatic mutations attenuated fusion activity, but aromatic residues promoted

hyperactive fusion.<sup>7</sup> A similar effect is implicated in some HIV-1 resistance mechanisms in response to enfuvirtide.<sup>113</sup> Accordingly, it appears that mutations promoting hyperactive fusion accelerate fusion kinetics, narrowing the time window for productive AS-48 docking and leading to resistance in MeV F.

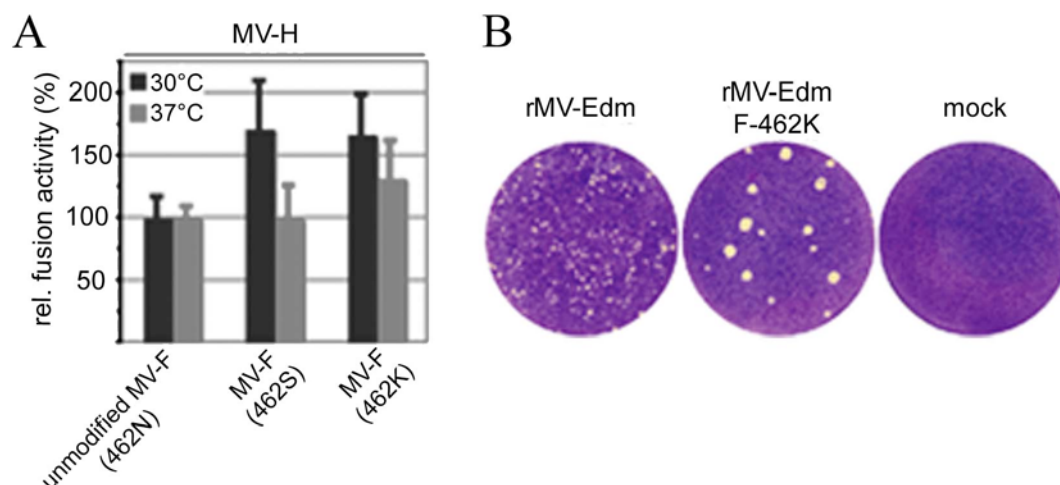


**Figure 5-10:** (A) MeV F variants N462S and N462K show enhanced fusion activity at 30°C indicating reduced conformational stability. The 462K variant shows increased fusogenicity also at physiological temperature. Quantification of fusion activity of F variants after co-transfection of Vero cells with equal amounts of plasmid DNA encoding MeV H and F, and incubation at 30°C or 37°C as indicated. The values represent means of four experiments and are expressed as the percentage of fusion activity observed for unmodified MeV F after incubation at 30°C or 37°C, respectively. (B) In the context of infection with recombinant MeV, the F-462K variant confers increased lateral spread through the target cell monolayer. Infected cells were subjected to crystal violet-staining 30 hours post-infection to visualize virus-induced syncytia.

## 5.7 Limitations of the AS-48 molecular scaffold

Despite extensive structural modification applied to the AS-48 molecular scaffold, the analogous compounds were never able to break the  $\sim 1 \mu\text{M}$  inhibition barrier. Prior to the development of the pre-fusion model, it was difficult to justify the lack of increased activity for all of the analogs produced. In light of the pre-fusion structure, it is now

possible to understand that the specific conformation of MeV F that AS-48 and its related inhibitors is able to target (**Figures 5-7D** and **3-4B**) is only a brief intermediate within the conformational cascade of the protein. Binding to the post-fusion structure would be non-inhibitory, as the protein has already brought the viral and cell membranes together. AS-48 increases the binding of an HR-B based peptide (see Section 4.3.4 and reference 88). This result suggests that the intermediate protein conformation that AS-48 targets is a late stage intermediate in which the HR-A 3HB has formed and the postulated Val94 binding site has been exposed in contrast to being shielded by the HR-A residues (**Figure 5-5**). Based on the morphing simulation of the DIII domain, we suspect that AS-48 disrupts interactions of the HR-B linker necessary to position HR-B near HR-A, interrupting the formation of the 6HB; that is, not by inducing a conformational change in the protein, but by increasing the energy barrier from an intermediate structure to the post-fusion structure. Targeting an intermediate viral protein structure has been successful in some cases, for example the peptide HIV entry inhibitor enfuvirtide,<sup>114</sup> which achieves an EC<sub>50</sub> in the low nanomolar range, but at the expense of a 36-residue peptide which requires subcutaneous injection. Enfuvirtide also benefits from the relatively long lifetime (several minutes) of the HIV-1 gp41 extended intermediate.<sup>115</sup> Other fusion protein intermediates may only exist for a few seconds.<sup>1</sup> For structure-based ligand design, lack of detailed structural information for the intermediate poses a significant challenge.

AM4 has shown the greatest degree of inhibition of all entry inhibitors related to AS-48, but is unstable at physiological conditions as this compound is essentially a masked quinone which degrades upon facile air oxidation to uncharacterized products.<sup>80</sup> Its high level of inhibition can likely be ascribed to the reactivity of its resulting quinone

as a Michael acceptor in the binding site, perhaps subject to nucleophilic attack by the hydroxyl of Ser45 (**Figure 3-3A**), although no attempt was made to determine the labeled residue. Cysteine labeling seems unlikely as all extracellular cysteines are predicted to form disulfide bonds. However, with reactivity comes instability. AM-4 loses all inhibitory activity in 16 hours, corresponding to the loss of NMR spectrum integrity and precipitation in deuterated chloroform.<sup>80</sup> Although irreversible binding by AM-4 may result in increased inhibition, such covalent interaction with proteins are undesirable for a compound projected as a possible drug candidate, even if the compound were shelf stable.

## Chapter 6: Fusion inhibition through stabilization of prefusion MeV F

*Portions of this chapter are based on “Reversible inhibition of the fusion activity of measles virus F protein by an engineered intersubunit disulfide bridge,” published in the Journal of Virology in 2007.<sup>116</sup>*

In search of a new candidate target site for antivirals in prefusion F, it was hypothesized that fusion may be blocked by stabilizing interactions in the prefusion F head or between the head and stalk of different subunits. To obtain proof of concept of fusion arrest, disulfide bridges engineered to covalently link these microdomains were examined.<sup>116</sup> Afterwards, an attempt was made to identify a small molecule that mimics this action using a virtual screen against this site.

### 6.1 An engineered disulfide bridge in prefusion MeV F

Since the acquired mutations at positions 462 and 367, located in the interface of the HR-B and head domains, appear to promote hyperactive fusion by destabilizing the prefusion conformation, it was hypothesized that an engineered disulfide bond stabilizing this region may have the opposite effect: elimination of fusion activity. In such a construct, however, the fusion activity could possibly be restored by reduction of these disulfide bonds.

#### 6.1.1 Molecular modeling of disulfide bonds in prefusion MeV F

The prefusion model of MeV F was analyzed *in silico* using Sybyl<sup>117</sup> (Tripos) and the Lovell rotamer library<sup>118</sup> to identify residues in the targeted domains with the potential to form disulfide bonds when mutated pairwise to cysteine, without necessitating large-scale domain movements. An intersubunit disulfide bond between

residues 452 and 460 (Ile452 and Gly460 in unmodified MeV F), postulated to link the base of the head to the prefusion stalk, and an intersubunit bond between residues 307 and 448 (Gly307 and Leu448 in unmodified MeV F), postulated to link adjacent loops in the head domain, appeared promising based on their side-chain geometries. All these residues are highly conserved among F proteins derived from different MeV genotypes and other members of the morbillivirus genus (canine distemper virus [strains examined, Onderstepoort and Lederle]) and rinderpest virus (strains examined, RBOK and Kabete O). Both centers were treated to mutation, bond formation and refinement by short 20K molecular dynamics (MD) runs (using Macromodel v9.5<sup>119</sup> [Schrödinger, Inc.]) and subsequent force field minimization using OPLS2005<sup>100, 120, 121</sup> and GB/SA solvation,<sup>122</sup> resulting in reasonable disulfide geometries for both disulfide pairs (**Figure 6-1**). The S-S bonds between residues 452/460 and 307/448 display  $\chi_3$  angles of -103.1 and 90.8°, respectively. While both angles are close to the disulfide ideal, the 307/448 bond perturbs the original structure slightly more than does the 450/462 bond. The root mean square deviations (RMSD) between the protein backbone atoms within an 8 Å sphere around the disulfide bonds are 0.73 Å and 1.43 Å, respectively. Thus, formation of a disulfide bond between residues 452 and 460 was predicted to be a slightly more effective modification.

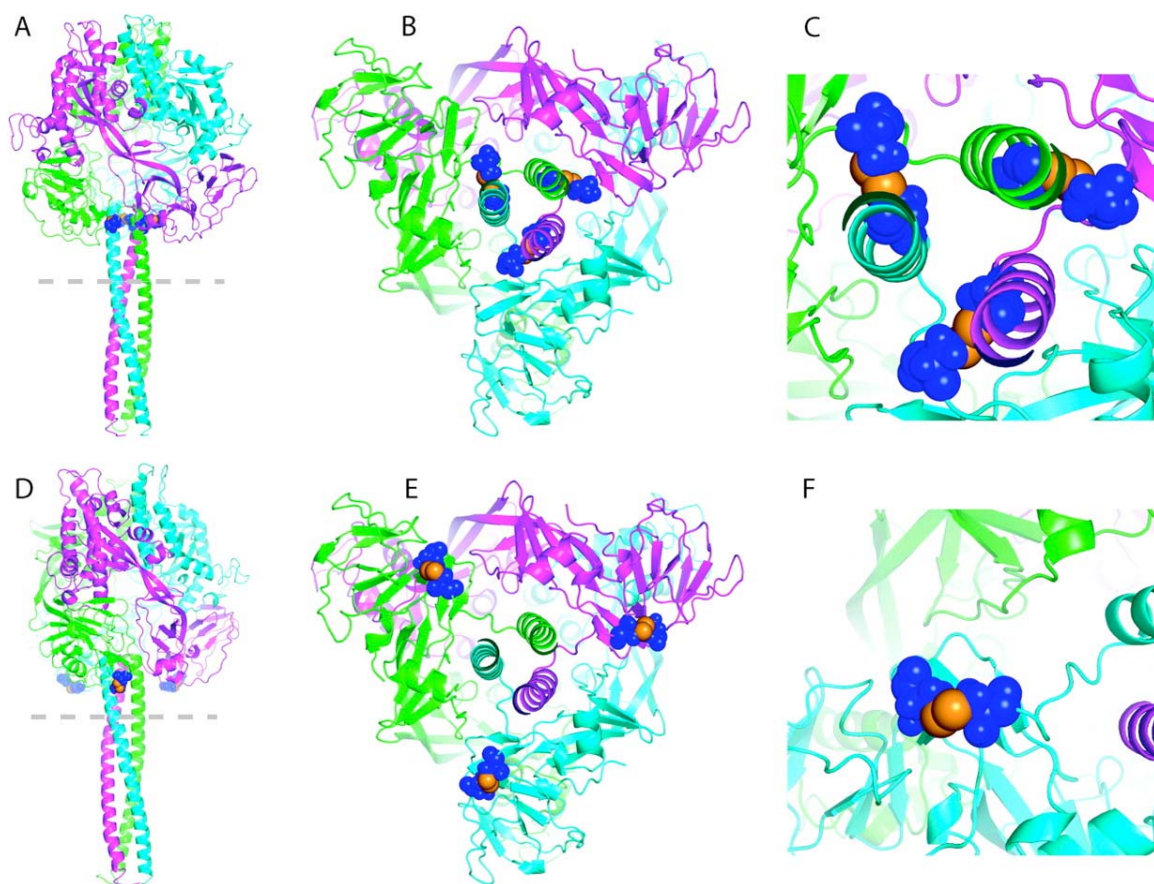


**Figure 6-1:** Predicted geometries of disulfide bonds introduced into the prefusion MeV F trimer homology model. (A, B, and C) A disulfide bond between residues 452 and 460 is predicted to establish an intersubunit link between the top of the HR-B prefusion stalk and the base of the globular head domain. Side view of the trimer (A), view from the dotted line in panel A up the HR-B stalk (B), and close-up view of the intersection of stalk and head domain (C). Cysteine side chains of engineered bonds are highlighted in blue, individual sulfur atoms are shown in orange. (D, E, and F) A disulfide bond between residues 307 and 448 is predicted to link two loops in the base of the prefusion head domain of the same monomer. Individual views and coloring of engineered bonds as described for panels A through C.

### 6.1.2 Expression and fusion activity of F candidates with engineered disulfide bonds

The Plemper groups realized these pairwise changes to cysteines in expression plasmids carrying the F gene of the MeV-Edmonston (MeV-Edm) vaccine strain. After co-transfecting with cells, the resulting F-Edm 452C/460C variant showed efficient proteolytic maturation of the F<sub>0</sub> precursor, similar to unmodified F-Edm (**Figure 6-2A**). In contrast, no maturation could be detected for the F-Edm 307C/448C construct, suggesting misfolding and likely intracellular retention. This was confirmed when plasma membrane steady-state levels of the different constructs were assessed by surface biotinylation. The F-Edm 452C/460C mutant largely maintained intracellular transport competence, showing a surface steady-state level of approximately 70% of unmodified F-Edm, whereas F-Edm 307C/448C was virtually undetectable at the cell surface (**Figure 6-2B**). To assess fusion activity of the mutant variants, a quantitative cell-to-cell fusion assay was employed by the Plemper group. Importantly, both mutant F variants failed to induce cell-to-cell fusion (**Figure 6-2C**). Microscopic examination of the extent of syncytium formation confirmed this observation (**Figure 6-4**). While this was expected in the case of F-Edm 307C/448C considering its lack of transport competence, absence of fusion activity of proteolytically cleaved and surface expressed F-Edm 452C/460C provides the first evidence for successful intersubunit disulfide bond formation.

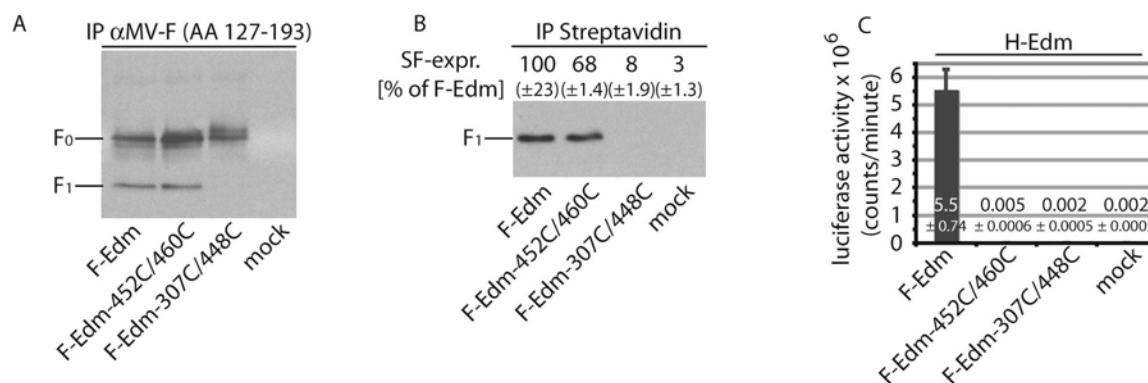


**Figure 6-2:** An F-Edm 452C/460C double mutant is proteolytically activated and intracellular transport-competent, but lacks fusion activity. (A) Immunoprecipitation (IP) of F-Edm, F-Edm 452C/460C and F-Edm 307C/448C from cleared Vero cell lysates obtained 36 hours post-transfection. An antiserum directed against residues 127-193 in the F HR-A domain was employed. Precipitated material was subsequently subjected to immunostaining using antibodies directed against the cytosolic F tail. Both the F<sub>0</sub> precursor and the proteolytically matured F<sub>1</sub> fraction of F-Edm and F-Edm 452C/460C are present, while for F-Edm 307C/448C only the uncleaved F<sub>0</sub> precursor is visible. (B) Only the F-Edm 452C/460C mutant but not F-Edm 307C/448C is expressed at the cell surface, based on surface biotinylation to assess plasma membrane steady-state levels of MeV F. (C) Quantitative cell-to-cell fusion assays reveal that both F-Edm variants lack fusion activity.

### 6.1.3 Oligomerization of F variants with engineered disulfide bonds.

To test the oligomerization status of F-Edm 452C/460C displayed at the cell surface, surface immunoprecipitation was carried out by the Plemper group using an antiserum directed against the F-Edm HR-A domain. Following immunoprecipitation, samples were separated by gel electrophoresis under reducing and non-reducing conditions, and F antigenic material detected on immunoblots using an F tail-specific antiserum. Under reducing conditions, the majority of the F-Edm and the F-Edm 452C/460C antigenic material migrated at a molecular weight corresponding to the

proteolytically cleaved F<sub>1</sub> form (**Figure 6-3**, left panel), confirming the initial observations. When the same samples were examined under non-reducing conditions, the majority of the F-Edm 452C/460C material migrated at a molecular weight corresponding to an F trimer and only small amounts of dimeric and monomeric material could be detected (**Figure 6-3**, right panel). This was in contrast to non-covalently linked F-Edm trimers, which under these conditions completely disintegrated and migrated exclusively as F monomers.

Stability of F-Edm 452C/460C oligomers was further assessed by the Plemper group using sucrose gradient centrifugation. SDS-treatment had virtually no effect on the distribution of the F-Edm 452C/460C antigenic material in the gradient. This was in contrast to parental F-Edm, the majority of which shifted to fractions of lower density upon disruption of non-covalent protein-protein interactions through SDS. Independent of SDS-treatment, approximately equal amounts of lower and higher molecular weight F-Edm 452C/460C material were detected in total cell lysates. This likely reflects a slight delay in intracellular homo-oligomerization and is consistent with the reduction of F-Edm 452C/460C surface expression observed in our initial experiments. Taken together, these results indicate that covalent, intersubunit bonds are present in the majority of surface expressed F-Edm 452C/460C material.

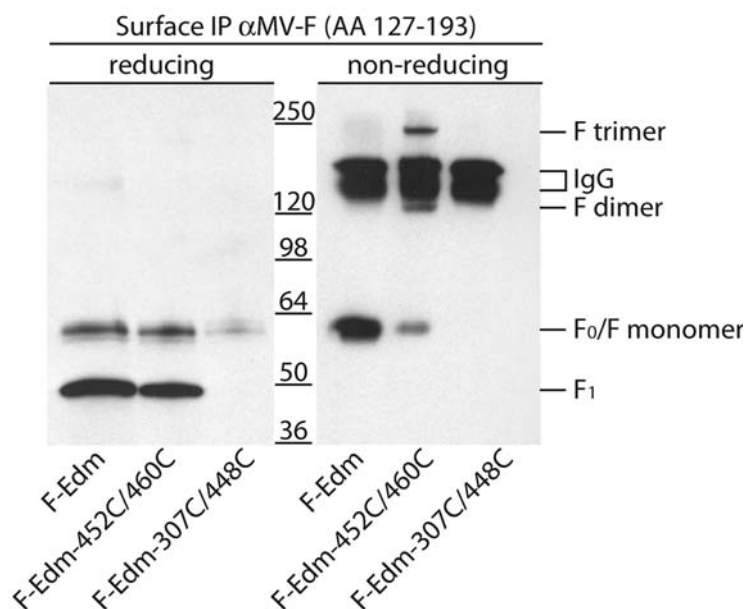


**Figure 6-3:** Disruption of F-Edm 452C/460C trimers requires reducing conditions, indicating presence of intersubunit disulfide bonds. Surface immunoprecipitation (IP) of F-Edm, F-Edm 452C/460C and F-Edm 307C/448C using the antiserum directed against the HR-A domain, followed by gel electrophoresis under reducing and non-reducing conditions and immunodetection with F-tail specific antibodies. Under non-reducing conditions, the majority of the F-Edm 452C/460C antigenic material migrates as trimer, while parental F-Edm migrates exclusively as monomer. Reduction of disulfide bonds through DTT-treatment (reducing) results in migration of the majority of F-Edm and F-Edm 452C/460C antigenic material as F<sub>1</sub> monomers.

#### 6.1.4 Reactivation of fusion activity by DTT-treatment confirms proper folding of F-Edm 452C/460C and arrest in a prefusion conformation

To test whether partial reduction of disulfide bonds results in reactivation of F-Edm 452C/460C fusion activity, the Plemper group co-expressed this mutant and H-Edm in cells treated with different concentrations of dithiothreitol (DTT), followed by acetylation of free thiol-groups with 1 mM iodacetamide<sup>123</sup> and assessment of fusion

activity. Microscopic analysis revealed the highest degree of reactivation of F-Edm 452C/460C fusion activity upon treatment with 25 mM DTT (**Figure 6-4A**, data not shown for other DTT concentrations). Following treatment, multinucleated cells (syncytia) indicating cell-to-cell fusion formed, while no syncytia formation took place in control samples not treated with DTT. Furthermore, parallel assessment of cells co-expressing H-Edm and F-Edm revealed that treatment of unmodified F-Edm with DTT somewhat reduces fusion activity (**Figure 6-4A**), presumably through reduction of natural intrasubunit disulfide bonds present in the F ectodomain.

Fusion activity of untreated and DTT-treated samples was quantified using a luciferase-reporter cell-to-cell fusion assay. DTT-treated cells expressing H-Edm/F-Edm 452C/460C showed fusion at 20% that of untreated cells expressing H-Edm/F-Edm (**figure 6-4B**). In contrast, treatment reduced fusion activity of H-Edm/F-Edm-expressing cells to 60% of untreated controls. This equals to an approximately 4-fold increase in fusion activity for F-Edm 452C/460C-expressing cells upon DTT-treatment compared to a 1.6-fold reduction upon treatment in the case of F-Edm. These findings strongly support proper overall folding of F-452C/460C trimers and indicate reversible covalent fixation of the trimer in a prefusion conformation.

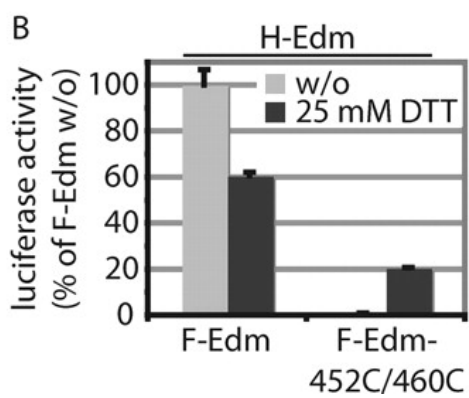
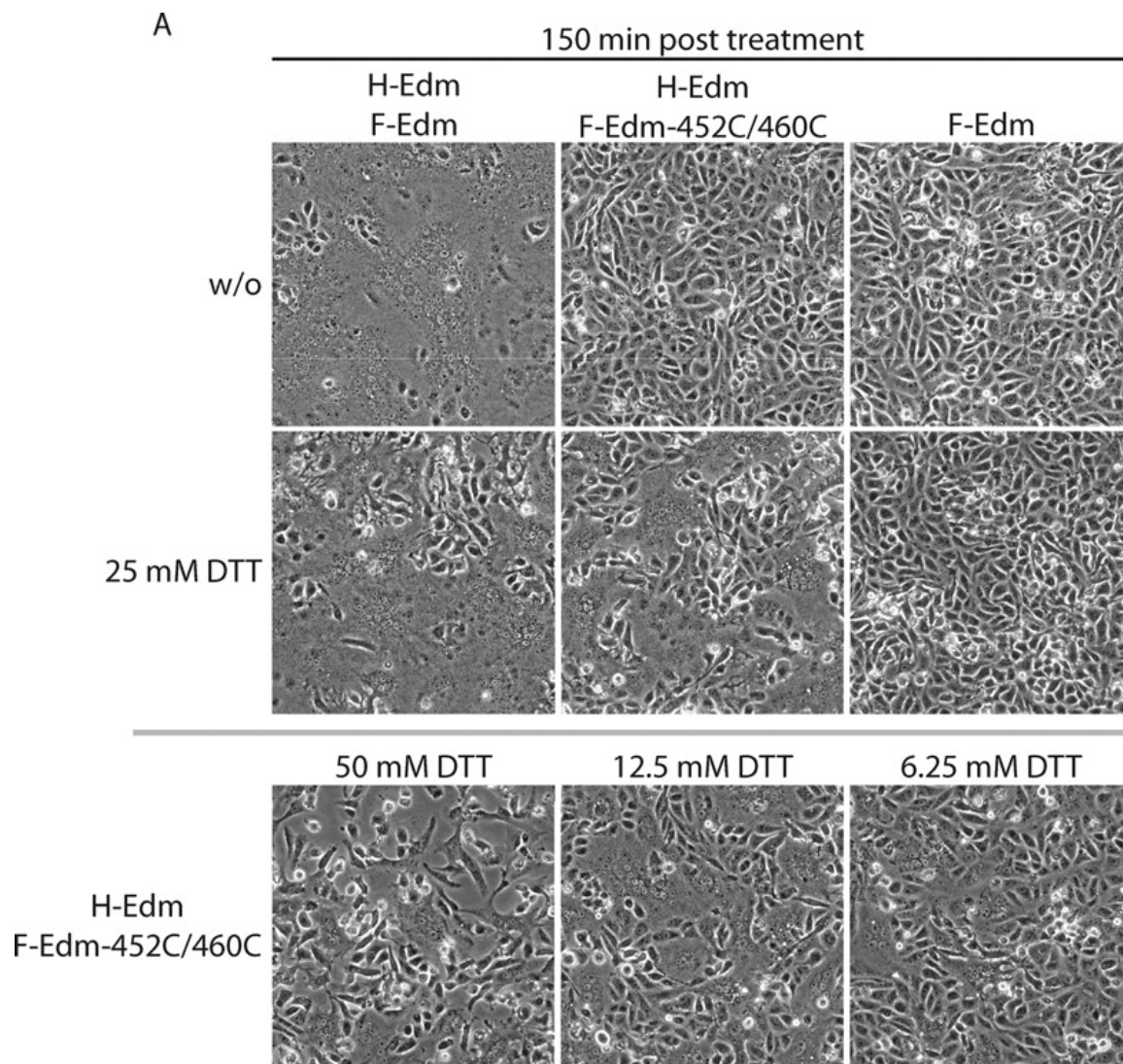


**Figure 6-4** (previous page): DTT-treatment of cells co-expressing H-Edm and F-Edm 452C/460C results in reactivation of F-Edm 452C/460C fusion activity. (A) Microphotographs of Vero cells co-transfected with plasmid DNA encoding H-Edm or F-Edm, H-Edm or F-Edm 452C/460C, or transfected with H-Edm encoding plasmids alone. Thirty hours post-transfection, cells were treated with DTT or left untreated (w/o), followed by an iodacetamide wash to acetylate free thiol groups and microscopic assessment of fusion activity 150 minute posttreatment. F-Edm 452C/460C expressing cells formed syncytia after treatment but not in the absence of DTT. (B) Quantification of fusion activity of cells transfected as in (A) using the luciferase reporter assay. While DTT-treatment reduces fusion activity of F-Edm by approximately 40% as compared to untreated (w/o) H-Edm/F-Edm expressing cells, it restores activity of F-Edm 452C/460C to levels corresponding to 20% of untreated F-Edm. No fusion activity was detected in untreated cells expressing H-Edm and F-Edm 452C/460C.

## 6.2 Screening for small molecule inhibitors of prefusion MeV F

Since an engineered intersubunit disulfide bond successfully demonstrated that fusion could be inhibited by stabilization of the prefusion form of MeV F, efforts were made to identify a small molecule that could also target this site and stabilize the prefusion conformation.

### 6.2.1 Computational identification of the target site in the prefusion MeV F model

While the interface of the HR-B and head domains was the known site of the acquired mutations at positions 462 and 367, as well as a successfully engineered disulfide bond, it was not known if this site could potentially bind a small molecule. To investigate this, a SiteMap<sup>124</sup> (Schrödinger) evaluation was performed on the entire prefusion MeV F model. SiteMap functions by a generating a grid to locate contiguous points that lie in exterior, concave regions of the receptor that have hydrophobic and

hydrophilic properties similar to the dataset of 157 tight-binding ( $<1\mu\text{M}$ ) ligand-receptor complexes. When applied to the prefusion model, the HR-B and head domain interface was indicated as the third most favored binding site in the structure (with a SiteScore of 0.99, compared to the 157 complexes which result in an average SiteScore of 1), the first site being located in the transmembrane domain and the second in the hollow interior sphere of the MeV head domain (**Figure 6-5**). These results indicated that this site could potentially bind a small molecule.

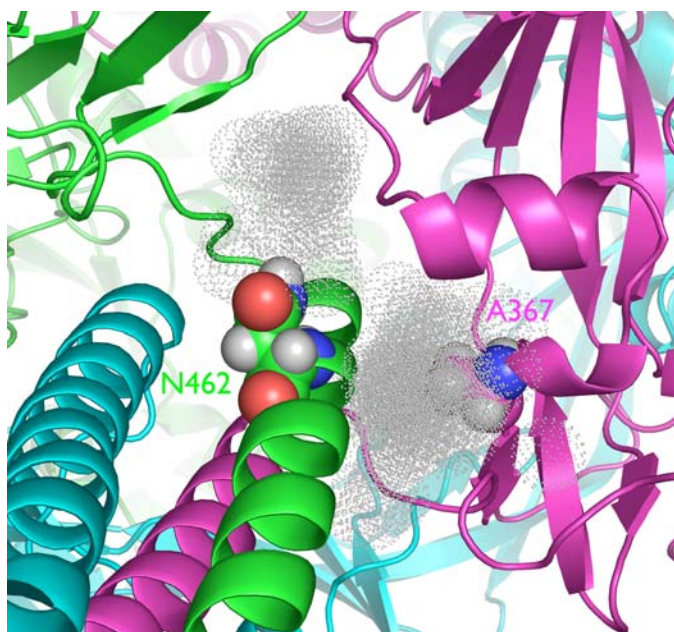


**Figure 6-5:** Predicted small molecule binding site at the interface of the HR-B domains and the DII domains of the MeV F head. The SiteMap grid points for this site are shown as gray dots, protein as ribbons colored by subunit, and Asn462 and Ala367 as spheres.

### 6.2.2 Further refinement of the prefusion MeV F structure

When the homology model of prefusion MeV F was developed, PRIME's side chain prediction protocol was implemented to determine the most energetically favored rotamer of all the side chains. This method does not affect the backbone torsional angles, however, which remain similar to that of the template structure. For most regions of the

structure, this is a sufficient approximation for the model structure. However, near this predicted small molecule binding site on the HR-B linker, two sequentially adjacent prolines (Pro450 and Pro451) were in an unfavorable geometry (**Figure 6-6**). To refine these residues as well as the rest of the protein, a molecular dynamics (MD) simulation in explicit water was performed for one nanosecond on the MeV F prefusion model. The MD simulation was performed using the GROMACS package.<sup>98, 99</sup> The structures were simulated using the OPLS-AA force field<sup>100</sup> and solvated with the TIP4P water model.<sup>101</sup> Using the solvated prefusion structure (Section 5.4.2) a 6 ps simulation was performed at 20K to remove any gross steric clashes from the structures. The simulation was then restarted and the temperature increased to 300K over 200 ps. The simulation was then continued at 300K for 1 ns. Simulations from 20 to 100K were performed with NVT conditions (constant number of particles, volume, and temperature) while subsequent simulations (from 100 to 300K and the following 1 ns simulation at 300K) were performed with NPT conditions (constant number of particles, pressure, and temperature). The 6 ps simulation at 20K used a time step of 1 fs; all other simulations used a 2 fs time step. All simulations used the Berendsen thermostat<sup>125</sup> and particle mesh Ewald electrostatics treatment<sup>126</sup> with a cutoff of 9Å. The resulting structure after 1 ns of simulation was minimized using PRIME<sup>95</sup> (Schrödinger).

The prefusion MeV F structure was stable in the 1 ns MD simulation, ending with an  $\text{RMSD}_{\text{backbone}}$  of  $\sim 2.0\text{\AA}$  for the head domain when compared to the original structure (**Figure 6-6**). Because the HR-B 3HB is not anchored in a transmembrane domain, the bottom of this structure experiences some distortion over the course of the simulation. If the entire protein is included in the RMSD calculation, the  $\text{RMSD}_{\text{backbone}}$  is increased to

2.5Å because of this distortion. These results suggest that the prefusion model is near energy minima that may closely approximate the actual metastable state. During the course of the simulation, the problematic proline residues 450 and 451 flipped their orientation into a much more favorable geometry (**Figure 6-6**).

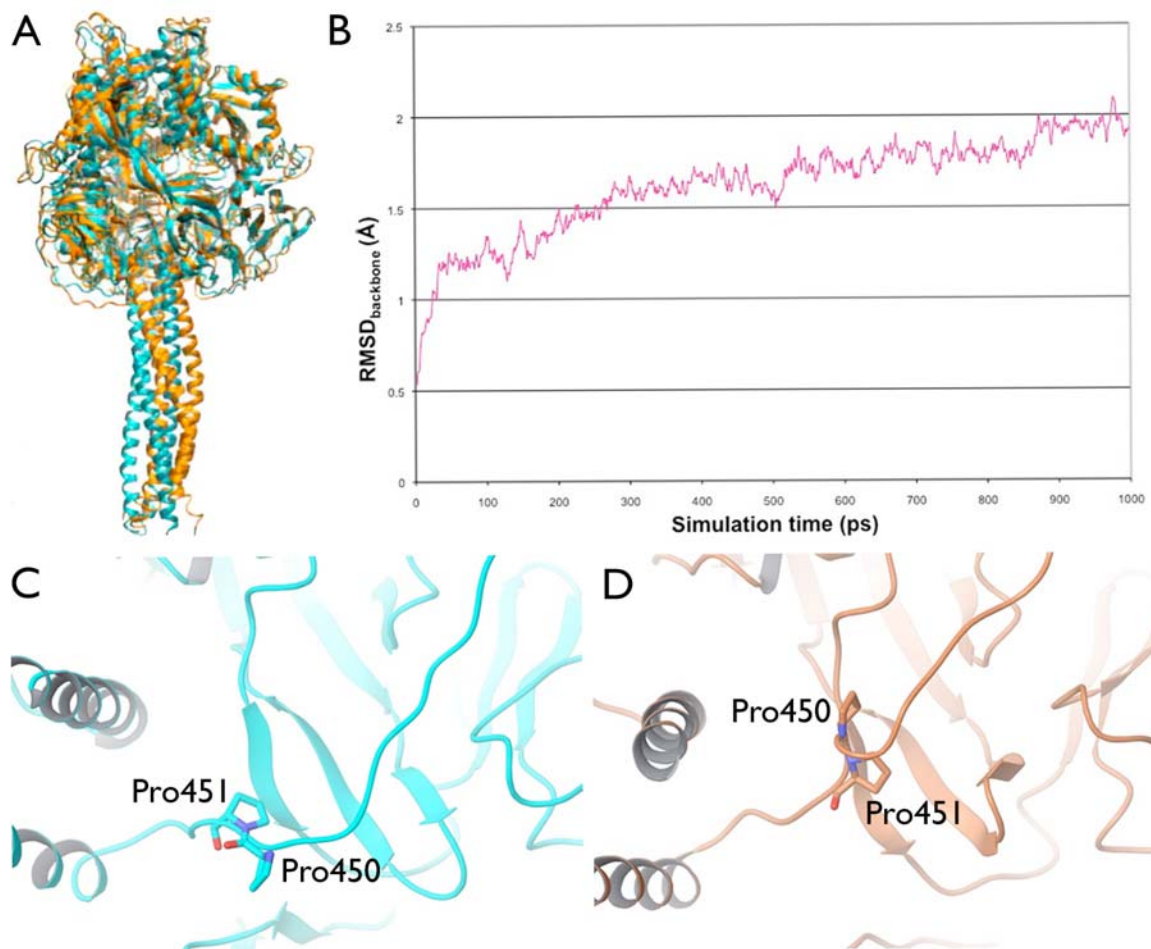


**Figure 6-6:** Results of the 1 ns MD simulation of the prefusion MeV F model. (A) Structural alignment of the original (cyan) and MD-structure (orange) shows that the majority of the protein is stable in the simulation. (B) The  $\text{RMSD}_{\text{backbone}}$  calculated over the course of the simulation for the residues of the head domain allows a metric of this stability. After initial movements early in the simulation, the structure plateaus into a stable conformation. (C) Unlikely conformation of the proline residues 450 and 451 on the prefusion MeV model before MD. (D) Stable conformation of these residues after the MD simulation followed by minimization.

### 6.2.3 Virtual screen at the HR-B / head domain interface

The ~ 60,000 compound Maybridge Screening Set<sup>127</sup> as included in the Catalyst DB software (Accelrys) was used in the virtual screen. These ligands were prepared for docking using LigPrep<sup>128</sup> (Schrödinger), which ionized the structures for a target pH

range of  $7.0 \pm 1.5$ . The Virtual Screen Workflow<sup>129</sup> (Schrödinger) was utilized to perform the screen. This workflow consists of three docking stages. The first stage performs the efficient, but relatively inaccurate High Throughput Virtual Screening (HTVS) docking. The ligands that are retained are then passed to the next stage, which performs Standard Precision (SP) docking; the survivors of this stage are passed on to the third stage, which performs Extra Precision (XP) docking. In this virtual screen the top-scoring 10% in each stage were retained for each subsequent step, resulting in ~ 600 ligands after the XP docking step. The binding energy of each of these poses was predicted using the MM-GBSA method,<sup>130</sup> allowing for 12Å of receptor flexibility in the minimization of the complex. The 200 poses with the most favorable binding energies were visually evaluated, eliminating poses with solvent-exposed hydrophobic regions, polar regions buried in hydrophobic areas, and strained ligand conformations such as *cis*-esters. After this visual inspection 117 poses appeared reasonable. To reduce the number of similar compounds needing to be assayed, the Tanimoto similarity coefficient<sup>131</sup> was calculated between all the compounds using Instant JChem<sup>132</sup> (ChemAxon); sets of compounds with > 0.7 Tanimoto similarity were reduced to the single ligand which had the best predicted binding energy, leaving 103 compounds. Three of these compounds, in their predicted docking pose with MeV F, are shown in **Figure 6-7**.

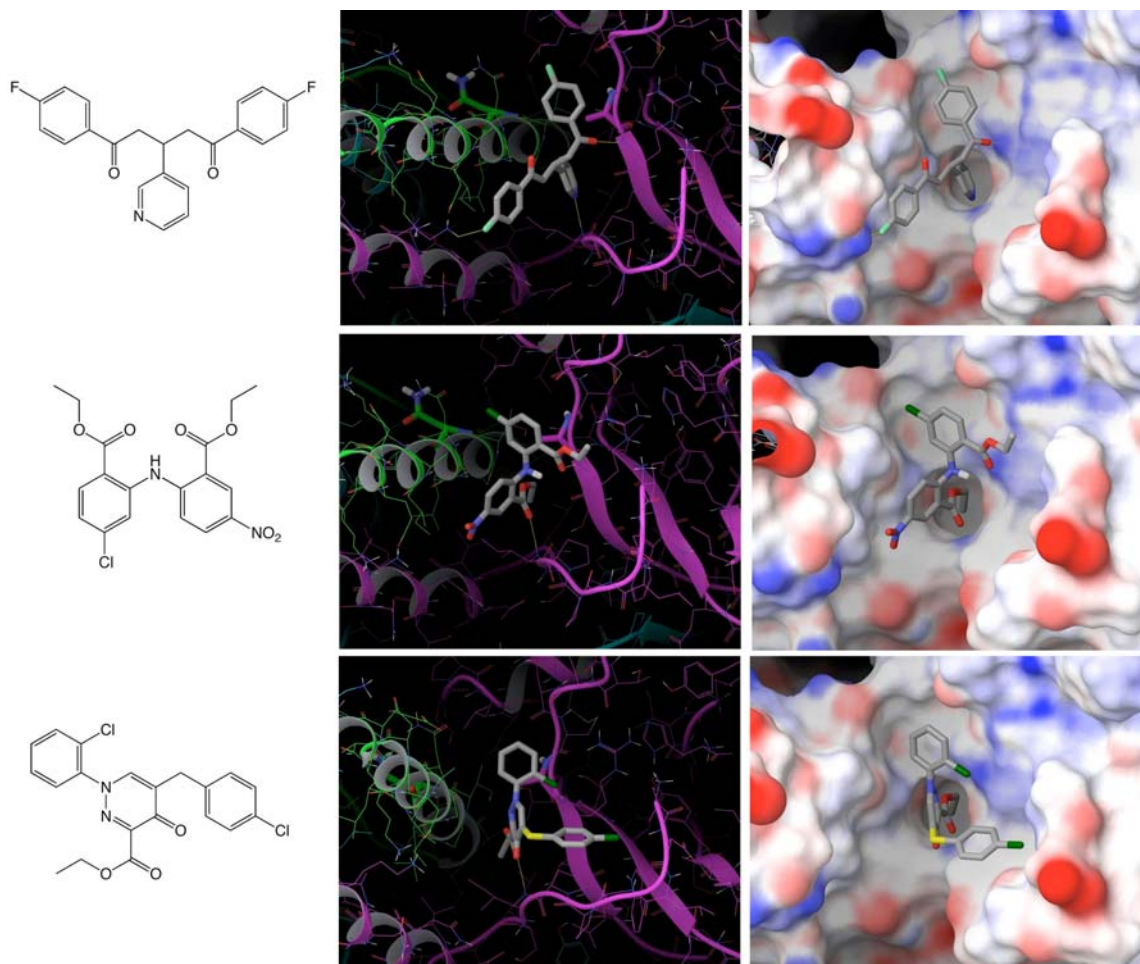


**Figure 6-7:** Three examples of compounds selected by virtual screening as potential binders to the interface of the HR-B and DII domains. The left panel shows the structures of the ligands. The middle panel shows the predicted pose of the ligand in the receptor with the ligand shown as grey sticks and the protein as ribbon colored by subunit with its sidechain as lines. The right panel shows the ligand pose with the receptor's Connolly surface colored by electrostatic potential (red = negative, blue = positive, white = neutral).

#### 6.2.4 Biological testing of the compounds selected by virtual screening

The inhibitory activity of the candidate compounds was assessed by suppression of viral cytopathic effect. In this assay cells are infected with MeV in the presence of compound in two-fold dilutions with starting concentrations of 75  $\mu\text{M}$  (concentration range examined 0.3  $\mu\text{M}$  to 75  $\mu\text{M}$ ). At 96 hours after infection, virus-induced cytopathic

effect was quantified through the staining of cells with crystal violet, which allows determination of the extent of syncytia and cell death. Unfortunately, none of the candidate compounds inhibited viral activity in this assay.

The failure of this screening to identify potential inhibitors could be the result of at least 3 different factors: a) The target binding site may not be correctly represented in the refined prefusion homology model. Although it did allow the successful design of an engineered disulfide bond, it may not be accurate enough to evaluate small molecules binding in this site. b) The compounds were incorrectly ranked by the docking and MM-GBSA procedure. Even in virtual screening scenarios where a high-resolution structure and a dataset of known actives are available, a non-trivial percentage of the ranked compounds must be tested to identify the first active compound.<sup>133</sup> Docking programs such as Glide typically do perform much better than a random selection of compounds. However, in this virtual screen it not known what percentage of the dataset is active; therefore, the minimum number of compounds that must be tested to identify an active is uncertain, though it is likely greater than 103. It is also possible the Maybridge screening database simply contains only a few active compounds, making them statistically very difficult to identify. c) Binding at the interface of the HR-B and DII domains does not stabilize the prefusion form enough to inhibit fusion. The stabilization provided by covalently linked subunits is much greater than that possible in small molecule binding. It is also possible that the HR-B domains may be in a state of dynamic equilibrium between a 3HB and an unstructured conformation such as seen in the first two frames of **Figure 5-3**. The engineered disulfide bonds could eliminate this equilibrium through their covalent

bonds but small molecule compounds would have to stabilize the 3HB state enough to cause the equilibrium to favor this state.

## Chapter 7: Functional interaction between paramyxovirus fusion and attachment proteins

*Portions of this chapter are based on “Functional interaction between paramyxovirus fusion and attachment proteins,” published in the Journal of Biological Chemistry in 2008.*<sup>134</sup>

While the previous chapters have focused on the fusion protein of MeV, membrane fusion does not occur for members of paramyxovirinae without the attachment glycoprotein (H, HN or G depending on the genus),<sup>1, 5, 6, 9, 19, 70, 127</sup> (Respiratory Syncytial Virus is the exception: it can fuse without the aid of its G protein.<sup>14</sup>) The attachment protein mediates receptor binding and is thought to trigger conformational rearrangements in the metastable F protein, which ultimately results in membrane fusion. However, the nature of this interaction between fusion and attachment proteins is unclear. Partial structures of the ectodomain of attachment proteins have been solved for multiple paramyxovirinae including MeV,<sup>135-138</sup> and reveal a globular head domain with the typical six-blade propeller fold of sialidase structures. Hemagglutinin-neuraminidase (HN) attachment proteins are indeed found on paramyxoviruses that enter cells through binding to sialic acid.<sup>74</sup> However, viruses of the genera henipavirus<sup>139-141</sup> and morbillivirus (which includes MeV, see **Figure 2-1**) recognize protein receptors, such as CD46 and/or SLAM/CD150w for MeV.<sup>71, 73, 142-144</sup> MeV H was crystallized as a homodimers,<sup>135, 137</sup> although other paramyxovirinae attachment proteins have been crystallized as both homodimers and homotetramers (formed by a dimer of dimers).<sup>136, 138</sup> No structural information for the attachment protein’s stalk region, which is thought to

connect the globular head domain to the viral membrane, is revealed in any of the X-ray crystal structures.

Multiple studies have demonstrated that specific interactions between compatible paramyxovirinae F and attachment proteins are imperative for the formation of functional fusion complexes.<sup>134, 145-150</sup> However, the molecular nature of these interactions and the spatial organization of functional glycoprotein hetero-oligomers have remained largely unknown. For paramyxovirus HN proteins, several studies have shown that the structurally undetermined stalk region determines specificity for different F proteins, suggesting that F-interacting residues may reside in this region.<sup>151-153</sup> 148 149 150 The applicability of this finding to morbillivirus H was unknown, however, and little information was available for the specific residues in the H stalk that mediate this interaction. Even less information was available for the nature of F microdomains that mediate interaction with attachment proteins. Multiple domains have been suggested to mediate specificity of HPIV2 F for its HN,<sup>154, 155</sup> but further studies using N-glycan shielding<sup>148</sup> and structural information<sup>19, 138</sup> argued against these proposed direct contacts. Electron microscopy of viral particles showed glycoprotein spikes of apparently equal length, leading many to suggest that the head<sup>156</sup> domains of both F and attachment proteins should be laterally aligned.<sup>74</sup> However, these images do not possess the resolution to differentiate between H and F based spikes or to distinguish between laterally aligned head domains and densely packaged H and F head domains of different heights above the viral envelope.

Starting with the observation that MeV H is able to engage in productive heterotypic interaction with F proteins derived from some but not all isolates of closely

related Canine Distemper Virus (CDV) (**Figure 2-1**), efforts were made by the Plemper group to determine the molecular basis for this differential activation, and thus, residues involved in functional interaction between H and F. In parallel with these efforts, a model of H and F interaction was generated to provide a structural basis for these findings.<sup>156</sup> Further experiments utilized structural predictions based on the model to verify and further refine the hypothetical interaction.<sup>157</sup>

## 7.1 Differential activation of F and H in morbilliviruses

The Plemper group discovered an interesting inconsistency in the nature of CDV F and MeV F activation by MeV H in the literature. For these closely related viruses, combinations of MeV and CDV-derived F and H proteins were one of the few cases where heterotypic complexes could be functional.<sup>156, 158, 159</sup> However, another study reported that MeV cannot functionally replace CDV H in triggering CDV F.<sup>160</sup> This could imply that F proteins derived from some CDV strains or MeV strains might be able to productively interact with heterotypic H, whereas those from other strains may not. Because of the high similarity between these proteins, identification of the individual residues responsible for this specificity was possible.

### 7.1.1 MeV H efficiently triggers CDV F-ODP but not CDV F-Lederle

When Vero cells expressing dogSLAM (thus expressing a receptor permissive for both CDV and MV-Edm H binding) were co-transfected with plasmids for CDV F and MeV H of several different strains by the Plemper group, efficient cell to cell fusion resulted for all homotypic constructs, but only some heterotypic constructs. A strong strain preference was found in the productive interaction of CDV F with MeV H, with CDV F-Onderstepoort (CDV F-ODP) being triggered efficiently by MeV H, whereas no

fusion occurred upon co-transfection of cells with CDV F-Lederle and MeV H (**Figure 7-1**). A quantitative cell to cell fusion assay confirmed these microscopic observations. To test whether CDV F-Lederle is still capable of physically interacting with MeV H, the Plemper group used a co-immunoprecipitation assay. Both F-ODP and F-Lederle were found to form hetero-oligomers with MeV H, however, co-precipitation efficiency of F-ODP with MeV H was substantially higher than that of F-Lederle. This result indicates there are different degrees of heterotypic interaction and support the hypothesis that productive heterotypic interaction of CDV F with MeV H depends on the strain background of the CDV F examined.

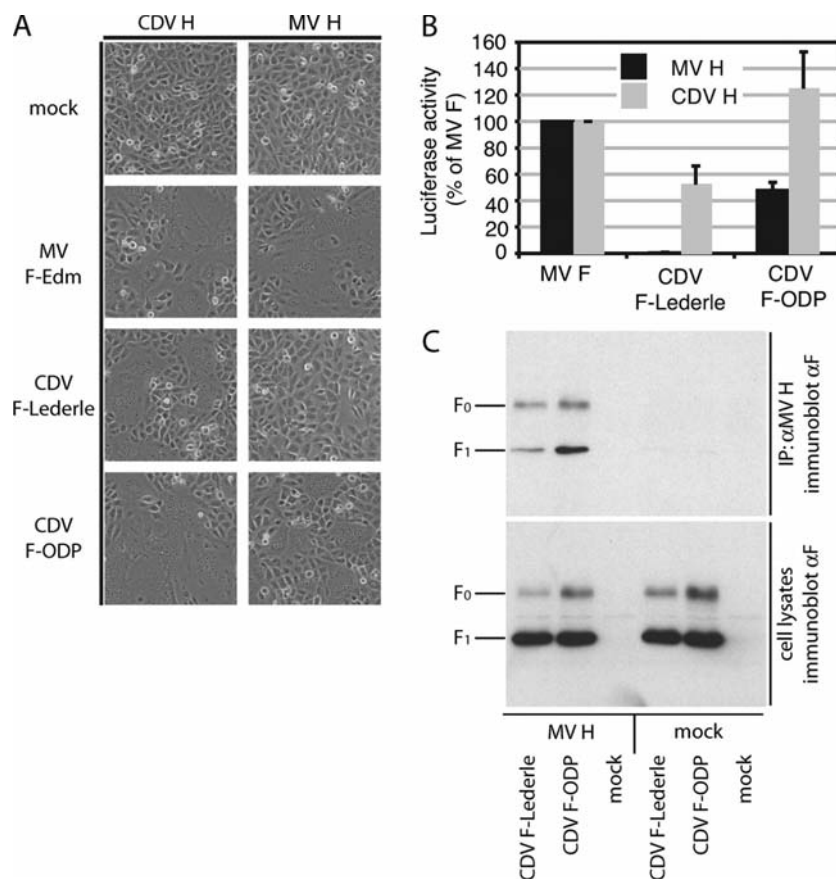


**Figure 7-1:** CDV F-ODP but not CDV F-Lederle is triggered by MeV H. (MeV is abbreviated MV in this figure.) (A) Micrographs of Vero-dogSLAM cells co-transfected with plasmid DNA encoding MeV or CDV glycoproteins as specified. (B) Quantification of cell to cell fusion activity expressed as the percentages of activity measured for MeV F and the respective H. (C) CDV F variants show different strengths of interaction with MeV H. Co-immunoprecipitation of CDV F-ODP and Lederle with MeV H. The lysates of co-transfected cells were subjected to immunoprecipitation using specific antibodies directed against an epitope in the MeV H ectodomain. Co-precipitated F (upper panel) was detected in comparison with F present in lysates prior to precipitation (lower panel) by immunoblotting using a specific antiserum directed against an epitope in the cytosolic tail of CDV F.

### 7.1.2 Minimal domain required for heterotypic triggering of CDV F-ODP

Because F-Lederle and F-ODP share > 95% protein identity, it is likely that chimeras derived from both proteins are fusion-competent, in contrast to heterotypic

chimeras combining F proteins from different paramyxoviruses. To test the prediction that there are specific regions in CDV F that effect the differential triggering, the Plemper group generated a series of reciprocal chimeras using suitable restriction sites that are conserved in both CDV F genes. When the fusion activity of these constructs was determined, productive interaction of F-ODP with MeV H was traced to an N-terminal region of F. To further narrow the domain responsible for differential triggering, engineered restriction sites were used, revealing a fragment spanning the C-terminal 73 amino acids of the F<sub>2</sub> subunit (encompassing the fusion peptide and the HR-A domains) as responsible for differential triggering. If a Lederle version of this fragment is introduced into F-ODP, the ability to form functional fusion complexes with MeV H is lost, but interaction with CDV H is fully maintained. Further shortening of this segment reduced the degree of differential triggering. Specific changes in this 191 amino acid domain between both CDV F variants are thus responsible for productive heterotypic triggering of F-ODP.

### **7.1.3 Four point mutations disrupt productive interaction of F-ODP with MeV H**

There are six residues that differ between F-Lederle and -ODP in the 191 amino acid domain. Directed mutagenesis by the Plemper group of an arginine to lysine at position 317 was found to substantially reduce triggering by MeV H when changed in the F-ODP background. Combining Lys317 with changes at three of the five remaining positions (residues 164, 219, or 233) further reduced heterotypic triggering, whereas the other two residues (159 and 178) did not. The greatest effect, closely resembling the

fusion activity observed for the 191 amino acid chimera, was observed when the residues 164, 219, 233, and 317 were changed in conjunction.

#### 7.1.4 Location of the four point mutations in a structural model of CDV F

To locate these residues in the three-dimension context of the prefusion F trimer, a structural model of CDV F on the basis of coordinates reported for the prefusion F of PIV5 was generated (Protein Data Bank code 2B9B).<sup>19</sup> Primary sequence comparison using ClustalW revealed 26% identity and 59% similarity between CDV F and PIV5 F (the CDV F precursor sequence (residues 1-135) was excised). The homology between these sequences is similar to that observed between hPIV3 F and Newcastle disease virus F.<sup>161</sup> X-ray crystal structures for both of the latter in the post-fusion state show very similar three-dimensional folds, despite a slight rotation in the interface of the HR-A coiled-coil and the DI-DII domains.<sup>11</sup> It was thus expected that faithful models of prefusion F could be achieved based on similar homologies. The CDV F model was constructed using PRIME<sup>130</sup> (Schrödinger). Each subunit was individually built and then combined into a trimer, which was further refined by using the PRIME side chain prediction model on all residues. In the resulting prefusion model of CDV F, the side chains of residues 164, 219, and 233 are each predicted to be surface-exposed, whereas residue 317 is buried in the prefusion trimer (**Figure 7-2**).

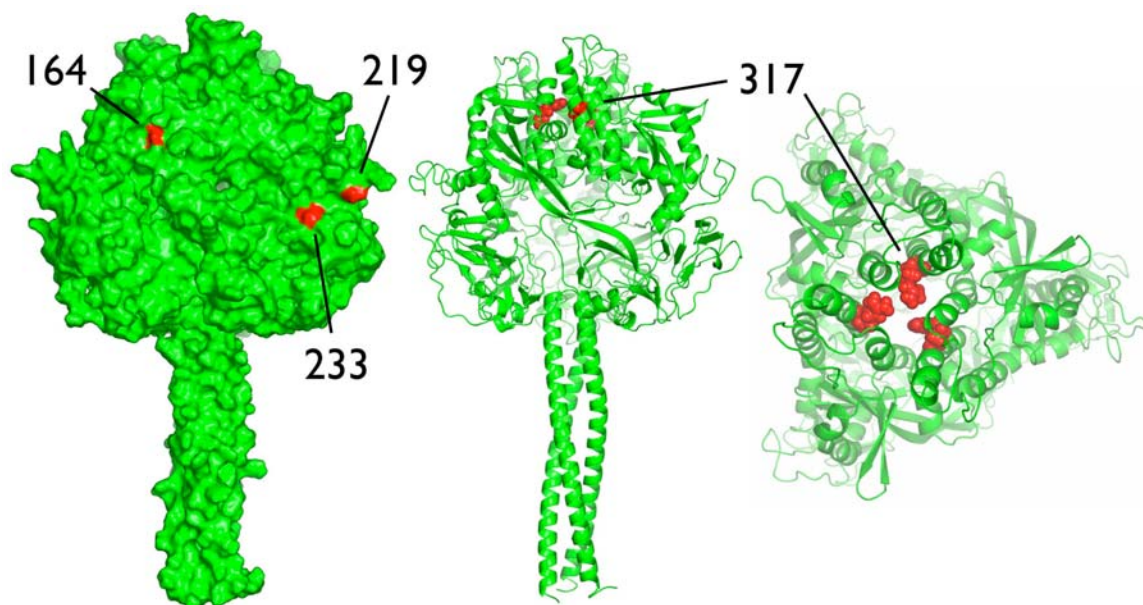


**Figure 7-2:** Visualization of the identified residues in a structural model of the prefusion CDV F-ODP trimer. In the left panel, all four residues (164, 219, 233, and 317) are highlighted in red. Residues 164, 219, and 233 are predicted to be surface-exposed; residue 317 is predicted to be buried in the trimer (visible only in the ribbons models; center panel, side view; right panel, top view).

### 7.1.5 Changes in the strength of H and F interaction due to mutations

To assess the contribution of different mutations to the strength of H-F interaction, the Plempner group performed co-precipitation of the individual F-ODP variants with MeV H. Co-precipitation efficiency of mature, fusion competent F variants was somewhat reduced as compared with unmodified F-ODP, indicating a lowered strength of physical interaction. However, no linear trend emerged between one and four point mutation constructs, suggesting that changes in physical and functional interaction of these ODP mutants with MeV H are not directly proportional. These findings do indicate that four discrete point mutations modulate the physical interaction of F-ODP and MeV H and govern the ability of both proteins to form functional fusion complexes.

### 7.1.6 Assay reversal demonstrates the H stalk domain determines productive interaction of MeV H with CDV F-Lederle

The Plemper group then performed a reversal of the previous chimera assay to identify residues on morbillivirus H that are responsible for differential triggering of the CDV F-Lederle and –ODP. MeV H is covalently linked into dimers by tandem intersubunit disulfide bonds that engage cysteines at positions 139 and 154.<sup>149</sup> These cysteines are conserved in CDV H, leading to the hypothesis that a fragment comprising the cytosolic tail, transmembrane anchor, and stalk domain up to the first disulfide bond may be transferable between CDV and MeV H as a modular unit without losing functionality. To test this hypothesis and assess whether CDV F-specificity of MeV H is associated with this N-terminal fragment or downstream domains, the Plemper group generated a MeV H mutant in which the N-terminal 139 residue fragment is derived from CDV H. Quantification of cell to cell fusion activity and microscopic assessment upon co-expression of this H construct with MeV F or CDV F-Lederle demonstrated that the construct is equally capable of efficiently triggering either F (**Figure 7-3**). These findings indicate that residues located in the MeV H ectodomain downstream of the N-terminal stalk region are not involved in differential F triggering, consistent with previous studies that had only implicated stalk domains of the HN proteins of related paramyxoviruses in mediating F specificity.<sup>148, 151-153, 162, 163</sup> 163

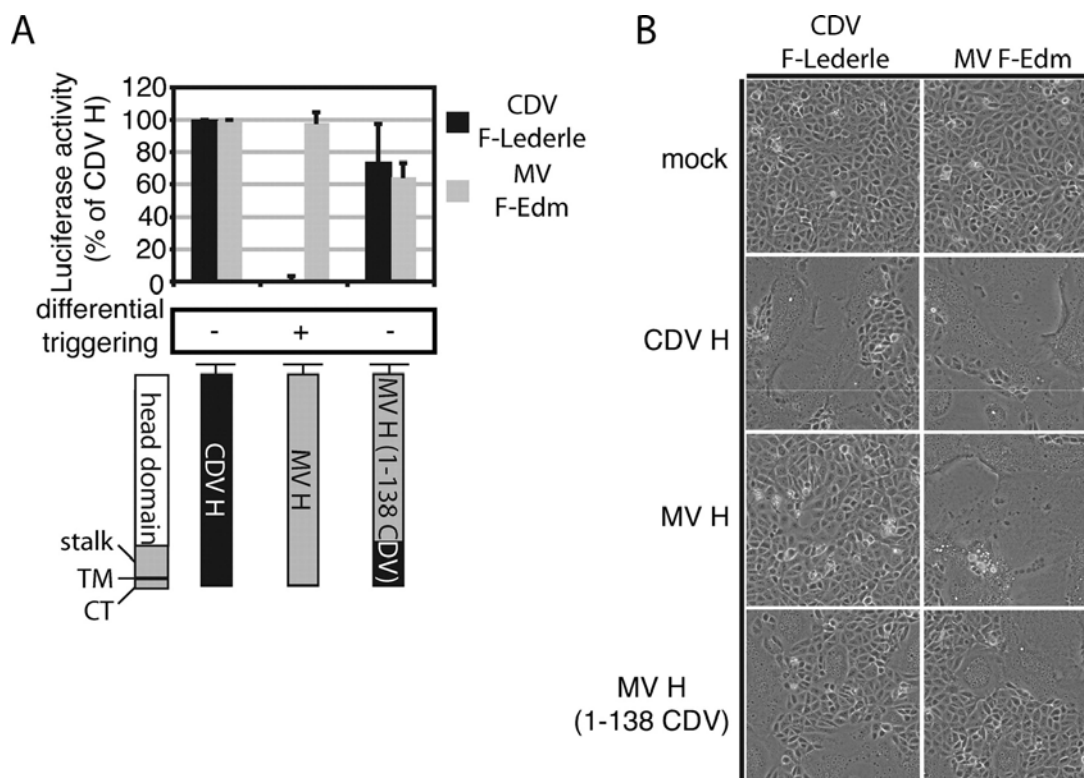


**Figure 7-3:** Residues in a MeV H N-terminal domain are determinants for F specificity (MeV is abbreviated MV in this figure). (A) Quantification of fusion activity upon activation of CDV F-Lederle or MeV F with CDV H, MeV H, or an MeV/CDV H chimera specified in the schematic below the graph. The values are expressed as a percentage of activity observed for either CDV F-Lederle or MeV F co-expressed with CDV H. (B) Microphotographs of Vero-dogSLAM cells co-transfected with the constructs outlined in (A).

### 7.1.7 A five-residue fragment in the MeV H stalk determines specificity for F-Lederle

To test whether individual residues in MeV H can be identified that contribute to F-Lederle activation, a conserved region downstream of residue 90 was chosen as a base to systematically narrow the 139 amino acid fragment. Through recombination PCR, two additional MeV H chimeras were generated by the Plemper group that harbor either CDV residues 1-90 (cytosolic tail, transmembrane domain, and N-terminal residues of the stalk domain) or 98-138 (C-terminal residues of the stalk domain up to the first disulfide

bridge). Assessment of homotypic and heterotypic F triggering revealed that only the 98-138 construct was capable of productively interacting with F-Lederle. Further differentiation of this 41-residue fragment through recombination PCR backed up by directed mutagenesis highlighted a linear five-residue fragment (residues 110-114) to be accountable for the degree of F-Lederle activation in the 98-138 construct. Although this chimera, MeV H (110-114CDV), activates F-Lederle only 40% as efficiently as the MeV H (1-138CDV) chimera, no other linear domain in the 138-residue stretch was found to contribute to F-Lederle specificity when assessed individually. Further shortening of the 110-114 fragment reduced fusion activity upon co-expression with F-Lederle. All but one of the H chimeras were capable of triggering homotypic MeV F (fusion activity upon co-expression with MeV F > 50% of standard MeV H), suggesting that other functions such as surface expression and receptor binding are largely intact. These data demonstrate that residues in the extracellular H stalk domain determine whether a functional interaction can be established between MeV H and CDV F-Lederle.

#### 7.1.8 Co-expression of F and H chimeras reveals interdependence of the identified residues in productive H-F interaction

To assess whether the residues individually identified in F and H act interdependently and thus determine reciprocal specificity, the Plemper group co-expressed the strictly CDV H-dependent F-ODP (164-, 219-, 233-, and 317-Lederle) variant with different MeV H chimeras capable of triggering F-Lederle and examined fusion activities (**Figure 7-4**). The presence of the N-terminal 138-amino acid domain of CDV H fully restored the ability of MeV H to productively interact with the F-OPD (164-, 219-, 233-, and 317-Lederle) variant, and co-expression with MeV H (110-114CDV)

resulted in some fusion activity, albeit to a lesser degree than observed with MeV H (1-138CDV). These data confirm that productive interaction is restored when mutations of residues 164, 219, 233, and 317 in F-ODP are combined with changing the 110-114 stretch in MeV H. These residues thus act interdependently in determining reciprocal glycoprotein specificity.

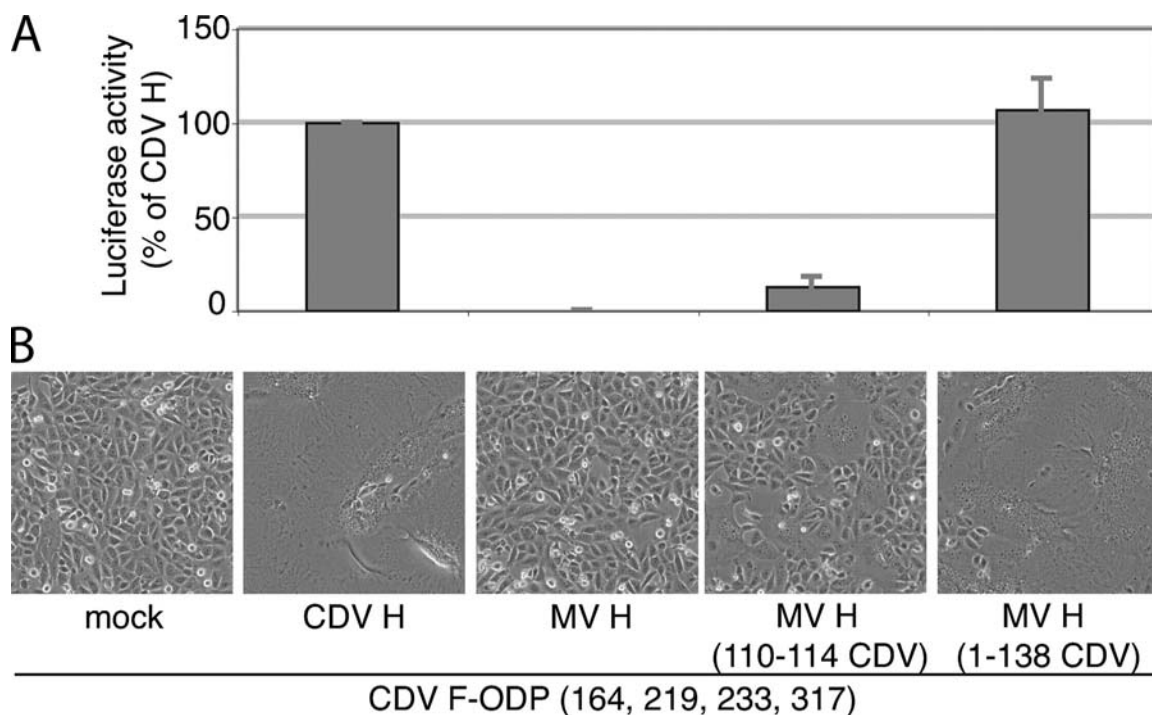


**Figure 7-4:** Residues identified in F and H act interdependently. Quantitative (A) and qualitative (B) assessment of fusion activity of cells co-transfected with CDV F-ODP (164-, 219-, 233-, and 317-Lederle) variant and CDV H, MeV H, or chimeras derived thereof (as specified). The quantification results are expressed as percentages of activity observed for cells co-expressing CDV F-ODP (164-, 219-, 233-, and 317-Lederle) and homotypic CDV H.

### 7.1.9 Role of identified F residues in homotypic fusion

To assess the importance of F residues 164, 219, 233, and 317 for the formation of productive fusion complexes under homotypic conditions, the Plemper group mutated the homologous residues (positions 52, 107, 121, and 205) individually in the MeV F

background. Changes at either position 52 or 107 had virtually no effect on F fusion activities or surface expression. In contrast, a conservative alanine to leucine change at MeV F position 121 resulted in nearly complete intracellular retention of the mutant protein. Despite this block in intracellular transport, cell to cell fusion was 21% of unmodified MeV F, indicating that the very small fraction of surface-expressed material is sufficient to mediate detectable activity. The opposite phenotype was observed when alanine 121 was changed to lysine. Intracellular transport was similar to unmodified F, indicating proper folding and proteolytic maturation. Upon co-expression with MeV H, however, no fusion activity could be detected. For MeV F residue 205, a conservative change of the lysine to histidine or glutamine reduced fusion activity by 19% and 79%, respectively. A more drastic change at this position (K205A) fully eliminated fusion activity.

In contrast to MeV F residue 205, the structural model of MeV F predicts residue 121 exposed at the surface of the prefusion trimer. (**Figure 7-5**) To test whether mutation of this residue to lysine physically affects homotypic interaction, co-immunoprecipitation with MeV H was employed by the Plemper group. The F-A121K variant returned an approximate 81% reduction in co-precipitation efficiency with MeV H as compared with unmodified F, highlighting this residue as a determinant for physical H-F interaction.

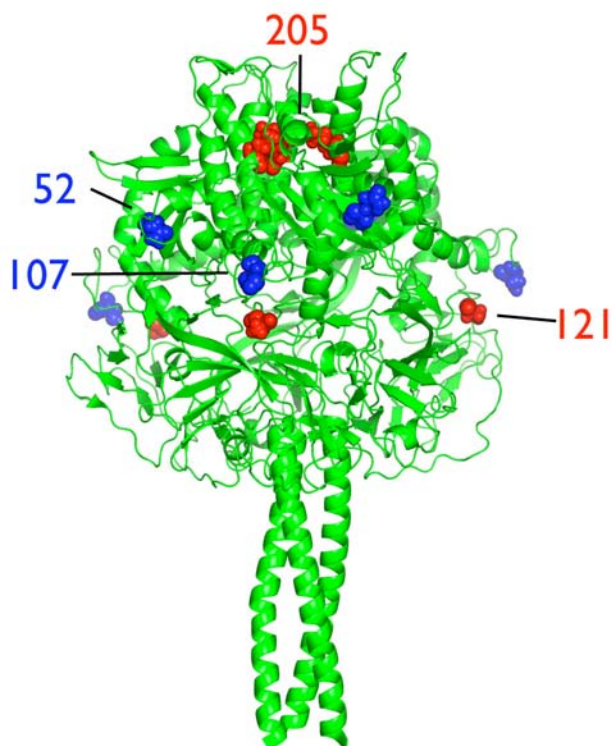


**Figure 7-5:** Residues implicated in homotypic MeV fusion. Structure shown is the prefusion homology model based on PIV5 F (PDB code 2B9B<sup>19</sup>). Positions 52 and 107 (blue spheres) have virtually no effect on homotypic MeV F fusion activities or surface expression, suggesting their functional importance is restricted to heterotypic H-F complexes. However residues 121 and 205 (red spheres) were important contributors to F triggering.

These results demonstrate that of the four candidate residues identified in the heterotypic assay, MeV residues 121 and 205 are determinants for strength of homotypic MeV H-F interaction (residue 121) and the extent of fusion activity (residues 121 and 205).

## 7.2 Structural model of morbillivirus H-F interaction

To place the residues implicated in functional H-F interaction in the context of the available structural information, a structural model was built for MeV H in addition to the prefusion CDV F model. With X-ray crystal structures available for the MeV H head

domain (residues 154-607),<sup>135, 137</sup> the critical structural information missing for this protein is the stalk domain (residues 58-153). Although the oligomeric state of native MeV H has not formally been determined and may well resemble a tetramer<sup>164</sup> in accordance with other paramyxovirus attachment proteins,<sup>136, 138, 165, 166</sup> homodimers were modeled for this initial model. Section 7.4 will explore the possible structure of MeV H tetramers.

### 7.2.1 Structural prediction of the MeV H stalk domain

To determine if any homologous structures to the MeV H stalk domain were available, a BLAST search of the non-redundant Protein Data Bank database was performed using PRIME<sup>130</sup> (Schrödinger). Unfortunately, only small stretches of residues had any meaningful alignment with protein structures in the database. With no available information on the nature of the structure, efforts were turned to sequence-based prediction of the MeV H stalk. Transmembrane domain prediction applied to the MeV H sequence strongly indicated a TM domain in MeV F spanning residues 38-57.<sup>167</sup> Thus, a structural model for residues 58-153 was desired. Additionally, it was known that disulfide bonds exist for cysteine residues 139, in addition to the disulfide bond between cysteines residues 154, which is the first N-terminal residue resolved in the X-ray crystal structure. Secondary structure predictions by SSpro<sup>168</sup> and PSIPRED<sup>169</sup> suggested a helical nature of the MeV H stalk, particularly residues 58-122, of which 81% were predicted helical by SSpro (**Figure 7-6**). For comparison, SSpro predictions for known helical structures, such as the HR-A domain of paramyxovirus F and the helical domains or cortexillin are 86% and 89%, respectively. Also evident in the MeV H sequence are clear heptad repeat regions starting at Leu60 and ending at Asp128. Other viral

glycoproteins, such as prefusion PIV5 F,<sup>19</sup> have globular head domains connected to the viral membrane by long, coiled-coil stalk domains. Circular dichroism analysis of the PIV5 H stalk domain also supports a helical coiled-coil configuration of the stalk.<sup>170</sup> Thus, to obtain a hypothetical model of the entire ectodomain, the MeV H stalk was modeled as a coiled coil based on the helical cortexillin I structure (Protein Data Bank code 1D7M).<sup>171</sup>

```

                58                                     114
                a d a d a d a d a d a d a d a d a d
MeV H  IRLHRAAIYTAIEIHKSLSTNLDVTNSIEHQVKDVLTPLFKIIGDEVGLRTP QRFTDL
SSpro  HHHHHHHHCHHHHHHHCHCCHHHHHHHHHHHHHHHHHHHHHHHHHHHHHHHHHHHHH
PSIpred CEEEEEEEEHECCCCCCCCCHHHHHHHHHHHHHHHHHHHHHHHHHHHHHHHHHHHHH
                115                                     152
                a d a d
MeV H  VKFISDKIKFLNPDREYDFRDLTWCINPPERIKLDYD
SSpro  HHHHHHHHCCCCCCCCCHHCCEEEECCEEEECCH
PSIpred HHHHHHHHCCCCCCCCCCCCCEEECCCHHHEEECHHH

```

**Figure 7-6:** Secondary structure predictions (H, E, and C for helical, beta-sheet, and loop residues, respectively) for MeV H. Only the residues in the stalk domain are shown, though the calculation was performed on the entire sequence. In the SSpro calculation, 81% of residues 58-122 are predicted to be helical. Heptad repeat residues (a and d) are shown above the sequence. The residue numbers are shown at the top left and right of each line.

To build this coiled coil structure for the MeV H stalk, residues 58-154 were threaded in the cortexillin structure using PRIME<sup>130</sup> (Schrödinger) with the alignment shown in **Figure 7-7**. A heptad repeat stutter at I99 and L105 is incorporated by introducing a single residue gap in the alignment after P108. Proline residues 94 and 127 are also expected to introduce kinks in the helix structure, but have been modeled as helical prolines. Prior to building the model, this alignment was determined to place cysteine residues 139 facing each other in the resulting coiled coil in geometry favorable



residues 219 and 233 predicted to be positioned at approximately the same level above the viral envelope as the 110-114 microdomain in the helical H stalk (**Figure 7-8**).

Although these residues could contribute to H-F specificity through long range effects, this observation alternatively makes direct contacts structurally conceivable. The latter would likewise proved a straightforward explanation for the results of previous studies showing a specific role of the paramyxovirus HN protein stalk in function and physical interaction with F.<sup>148, 151-153, 163</sup> 173

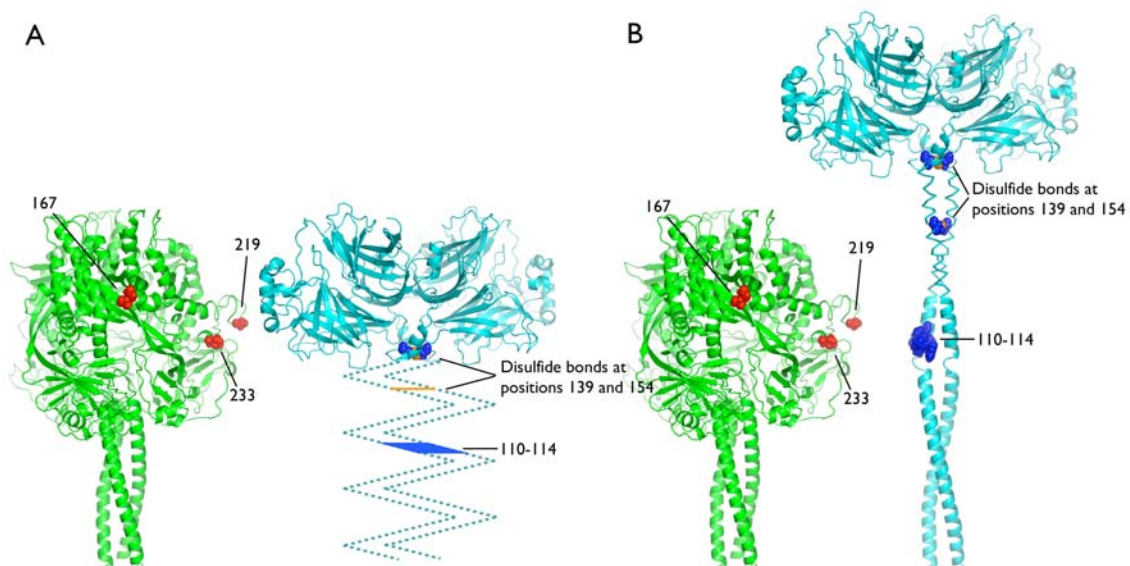


**Figure 7-8:** Two possible hypotheses of H-F alignment. H stalk domains are represented in unknown (A) or helical (residues 58-122) (B) conformation. The helical H stalk places H residues 110-114 and F residues 233 and 219 at the lateral face of the prefusion CDV F trimer at an equal distance above the viral envelope, making short range interaction structurally conceivable (B). The ribbon models of the H and F oligomers are aligned at their transmembrane domains. Helical modeling of H stalk residues 58-122 is based on the predictions of SSpro.<sup>168</sup> Cysteines 139 and 154 engaging in intersubunit disulfide bonds are shown.

Direct contact of the H stalk with the prefusion F head would mandate positioning of the globular H head domain above the F trimer to avoid steric interference and thus require an extended H stalk as suggested in **Figure 7-8B**. Interestingly, an early electron microscopy study suggests prominent spikes on the measles virus surface to correspond to the attachment protein, whereas the fusion function was considered to reside closer to the virus membrane.<sup>173</sup> Consistent with this suggestion, a recent electron cryomicroscopy analysis of hPIV5 particles concludes that defined glycoprotein spikes, previously observed in electron microscopy studies of paramyxovirus particles<sup>74</sup> correspond in the case of F to the post-fusion conformation and thus represent a product of premature F

refolding.<sup>12</sup> Defined spikes corresponding to prefusion F were not detected in this cryo-electron microscopy study, but a dense corona-like surface layer was found, compatible with a tight packaging of the glycoprotein complexes and overshadowing of the F trimers by H as implied by the hypothetical model shown in **Figure 7-8B**.

The experiments by the Plemper group demonstrated that mutation of the MeV F residue 121 (the homologue of CDV F residue 233) causes a substantial reduction in physical interaction of matured F with homotypic MeV H. Residue 121 is part of the fusion peptide, which is propelled toward the target membrane during F refolding.<sup>5,9</sup> Its predicted position on a lateral corner of the prefusion trimer renders it accessible for MeV H. Increasing hydrophilicity of the fusion peptide could interfere with its association with target membranes, blocking fusion, if refolding of the F-A121K variant can be triggered. However, co-precipitation experiments performed by the Plemper group assessed the physical interaction of proteolytically matured F with H in the absence of fusion. In contrast to matured F, the F-A121K mutation had very little effect on the intracellular interaction of immature F<sub>0</sub> with H. This likely reflects that paramyxovirus F reportedly is subject to some conformational change upon cleavage,<sup>174</sup> which may affect the interaction with the attachment protein. Only matured F is fusion-competent, however, and thus able to form functional fusion complexes with H. Importantly, the physical homotypic interaction of these matured F proteins with H prior to fusion is impaired by the A121K mutation.

Although the positioning of CDV F residue 317 (MeV F 205) in the model precludes direct contact with H, residues at these positions are important contributors to F triggering in the homotypic setting of MeV H and F complexes. This residue lies at the

interface of HR-A domains which must be pulled out of the MeV F head during fusion (**Figure 5-2**). Thus, residues at this position in the top of the F head appear ideally located to influence the initiation of F conformational rearrangements through long range effects.

In contrast to MeV F residues 121 and 205, mutating residues 52 and 107 (corresponding to CDV F residues 164 and 219) has only marginal effects on fusion activity under homotypic conditions. The functional importance of these residues is thus restricted to heterotypic glycoprotein complexes, arguing against engagement in short range interactions in homotypic complexes. In particular for F residue 52, the predicted positioning is fully consistent with this view (**Figure 7-8B**).

Additional microdomains may contribute to mediating glycoprotein specificity but may be conserved across the MeV and CDV proteins examined and thus not be detected by the assay. Further experiments guided by the model of H-F interaction based on the current data are necessary to elucidating the nature of these domains and with the ultimate goal of leading to an interaction model with residue level accuracy.

### 7.3 Probing the spatial organization of H-F complexes

To further elucidate the organization of functional paramyxovirinae fusion complexes, the central predictions of the proposed H-F interaction models were subjected to experimental analysis. By employing carbohydrate shielding, directed mutagenesis, and variation of the lengths of the H stalk domain, the proximity of different regions of the H stalk to F was examined, the role of individual residues in the H stalk 110-114 microdomain clarified, and the interaction between H and F head domains explored.

These experimental data are interpreted in the light of the hypothetical H-F interaction model.

### 7.3.1 Effect of engineering N-glycosylation sites into the H stalk

The juxtaposition of H and F in the interaction model (**Figure 7-8**) suggests that membrane proximal regions of the H stalk are not in direct contact with the F trimer. Membrane distal regions, however, could mediate a short-range interaction with the F head. Carbohydrate shielding through insertion of additional N-glycosylation sites is reportedly capable of examining the contribution of protein domains to activity,<sup>175, 176</sup> and has been used in a study to test candidate contact zones between NDV HN and F.<sup>148</sup> The Plemper group used this strategy to probe the proximity of F from the H stalk domain at a membrane proximal and membrane distal position. Since the exact rotational orientation of the H stalk is unknown, N-glycosylation sites were introduced by the Plemper group at three consecutive residues: residues 70-72 were chosen as target sites for membrane proximal N-glycans guided by molecular modeling, which suggested a large glycan structure could be accommodated at this position (**Figure 7-9**). Residues 110-112 were chosen as candidates for membrane distal N-glycans because these residues were implicated in functional H-F complexes and molecular modeling predicted that there could be short-range interactions between these residues and the F head. Thus, incorporating a glycan at this position was predicted to disrupt H-F interaction.

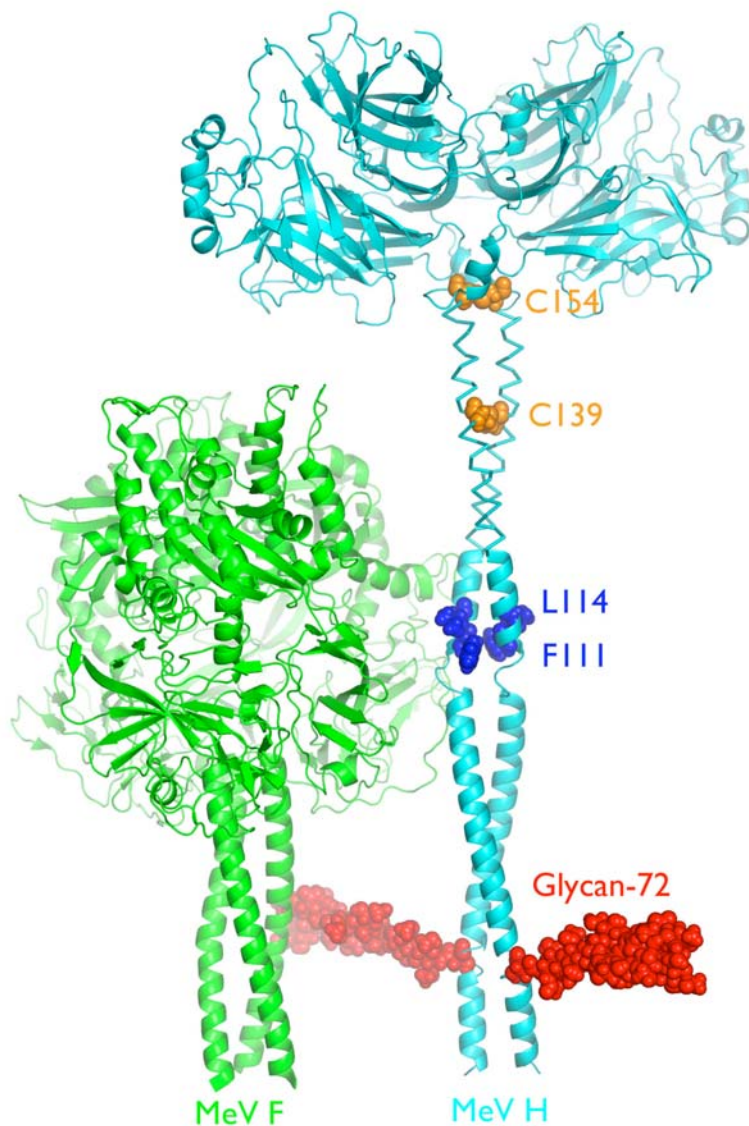
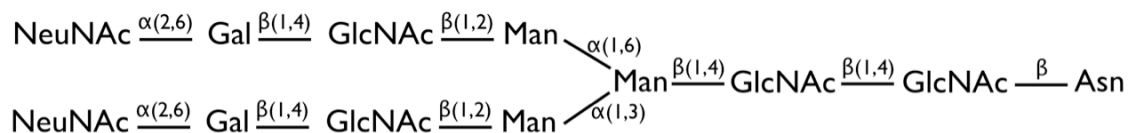


**Figure 7-9:** Ribbon representation of a hypothetical envelope glycoprotein interaction modes. H and F are colored cyan and green, respectively; with H stalk disulfides, F111/L114, and N-glycans shown as orange, blue, and red spheres, respectively. In this staggered alignment, N-glycans only added at a membrane proximal (residue 72) but not distal position (residue 111) are compatible with the formation of functional fusion complexes. A lateral alignment (**Figure 7-8A**) suggests both N-glycan positions should be accommodated.

To generate structural models of N-glycans attached to the MeV H stalk, a carbohydrate with the following structure was built using MAESTRO<sup>112</sup> (Schrödinger):



To find a reasonable, low-energy conformation of the carbohydrate attached to an asparagine amino acid, a Monte Carlo conformational search of 1,000 steps was performed with MACROMODEL<sup>119</sup> (Schrödinger) using OPLS2005<sup>100, 120, 121</sup> and GB/SA solvation.<sup>122</sup> A low energy conformation was attached to the proteins by superimposing the backbone atoms of Asn to the target glycosylation position on the MeV H stalk.

For the membrane proximal N-glycans, only the engineered site at position 72 was recognized efficiently without effecting intracellular transport competence. Such a result is consistent with the MeV H stalk model which directs this residue away from the interface of the helices, whereas positions 70 and 71 are predicted to face each other in the coiled coil. All three engineered glycosylation sites at the membrane distal positions, 110, 111, and 112 were fully surface-expressed and efficiently glycosylated, despite the fact that residues 111 and 112 are predicted to partially face the interior of the coiled coil. This may imply that interaction of the helices is modeled incorrectly for this portion of the stalk, or perhaps there is more flexibility in the helix at this position distal to both the viral envelope and the Cys139 disulfide bond.

Quantification of plasma membrane steady-state levels and SLAM binding by the Plemper group revealed intracellular transport competence and ability to interact with soluble SLAM cellular receptor for all four H variants with engineered N-glycans. Quantification of cell to cell fusion demonstrated that fusion activity and hence F triggering was only minimally affected by the addition of an N-glycan at H stalk position

72 (the membrane proximal site). In striking contrast, N-glycans at all three membrane distal sites, 110, 111, and 112, caused a complete block of F triggering (**Figure 7-10**).

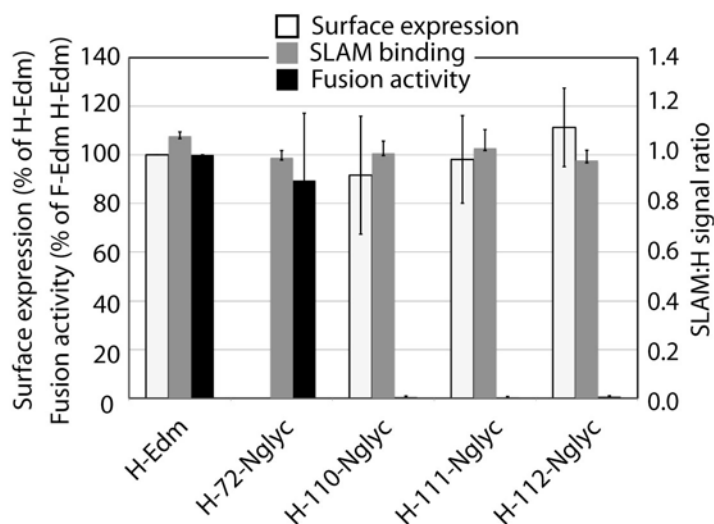


**Figure 7-10:** Assessment of surface expression, SLAM-binding capacity and cell-to-cell fusion activity of H variants. Additional N-glycans at H stalk position 72 but not 110, 111, or 112, allow the formation of functional H-F fusion complexes.

To assess if this lack of functionality is due to an altered physical interaction of the H and F proteins, a co-immunoprecipitation assay was employed by the Plemper group. Because removal of the stabilizing lipid bilayer may trigger refolding of metastable prefusion F, potentially distorting results, the chemical cross-linker DTSSP was applied prior to membrane extraction, immunoprecipitation of H, and detection of co-precipitated F. This assay revealed that N-glycans at stalk position 111 essentially block the formation of functional fusion complexes, while carbohydrates at position 72 still allow 54% of the interaction compared to standard complexes.

These data demonstrate that insertion of N-glycans at a membrane proximal or distal position of the H stalk does not result in loss of receptor binding capacity or gross protein misfolding and intracellular retention. Interference of N-glycans at the membrane

distal position with F triggering and H-F hetero-oligomerization indicates close proximity of this stalk section to F.

### 7.3.2 H residues 111 and 114 are determinants for F triggering

To assess whether a subset of residues in the previously identified 110-114 H stalk domain determine effective F triggering, the Plemper group subjected this domain to alanine-scanning mutagenesis, mutating all five residues, the first three, or the last two residues. These H variants had unchanged surface expression and SLAM-binding ability, but none were capable of triggering F in cell to cell fusion assays. Subsequent single-residue mutagenesis revealed a complete loss of F triggering by H-F111A and a significant reduction by H-L114A, while changes at each of the other three positions (110, 112, or 113) did not affect fusion activity. H-F111A and L114A showed unaltered surface expression and SLAM binding.

Such a three-residue distance between individual positions determining F triggering supports the predicted helical character of the paramyxovirinae attachment protein stalk domains,<sup>148, 170</sup> since a helical configuration posits residues 111 and 114 in immediate proximity on consecutive turns of the helix (**Figure 7-11**). To explore whether neighboring residues on preceding or subsequent turns likewise engage in F triggering, the Plemper group extended the alanine mutagenesis to stalk positions 108, and 117 and 118, respectively, which are predicted to be located at the same face of the helix as residues 111 and 114. None of these changes resulted in a significant reduction of F triggering or SLAM binding, although the P108A mutation cause an approximately 50% reduction in surface expression. In addition to impairing F triggering, mutation of residue 114 or 111 to alanine resulted in > 75% reduction in H-F physical interaction at the

plasma membrane as measured by the co-immunoprecipitation assay. Taken together, these data identify H stalk positions 111 and 114 but not residues 112 and 113 as determinants for the formation of functional fusion complexes between MeV H and F. This is consistent with a helical configuration of the stalk domains *in situ*, supporting the secondary structure predictions and *in vitro* analysis of soluble attachment protein fragments.<sup>148, 170</sup>

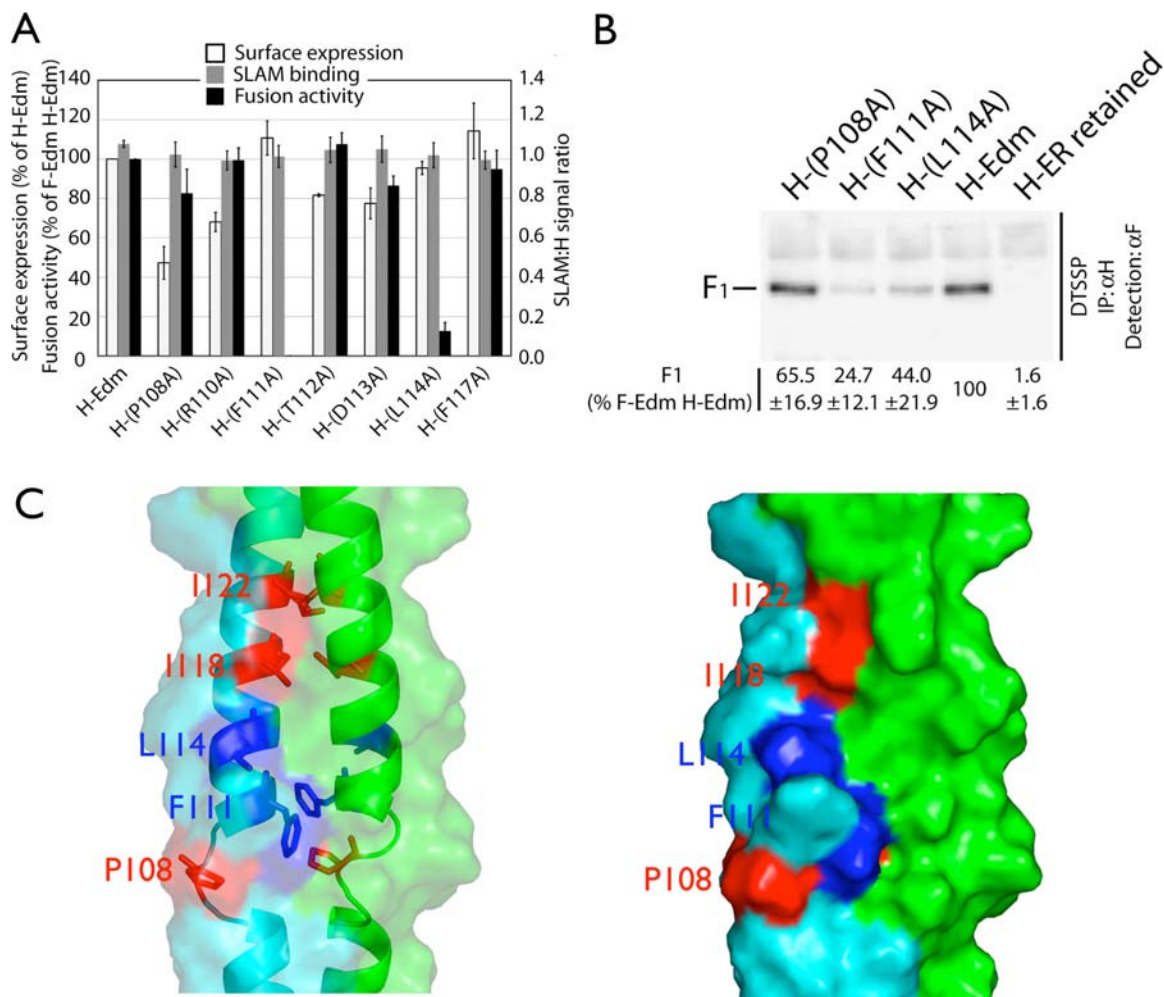


**Figure 7-11:** H stalk residues 111 and 114 are determinants for physical and functional interaction of MeV H and F. (A) Characterization of H variants harboring individual alanine point mutations. Only mutation of residues 111 or 114 substantially reduces F triggering activity. (B) Co-immunoprecipitation of surface-exposed MeV F with MeV H after DTSSP cross-linking. (C) Surface model of the H stalk domain from position 103 to 125 is shown as transparent (left panel) and opaque (right panel) solvent accessible surfaces with residues displayed at tubes. In  $\alpha$ -helical configuration an of the H stalk, residues 108, 111, 114 and 117/118 are predicted to be located adjacent to each other on consecutive turns of the helix.

### 7.3.3 Only stalk elongation downstream of residues 111 and 114 is compatible with F triggering

The proposed H-F interaction model (**Figure 7-8**) implies that shortening the stalk domain will likely disturb hetero-oligomerization to due sterical interference of a lowered H head with F, while elongation of the stalk membrane distal, but not proximal, of residues 111 and 114 may be tolerated. Deleting or inserting complete heptad repeat (HR) domains are not anticipated to compromise the predicted overall helical conformation of the stalk, but should alter its length by approximately 11Å. To test these predictions, two HRs in the H stalk (residues 84-90 or 118-124, respectively) that flank the 111/114 section and are distinct of H residues 91 to 105 were identified. Mutation of residues 91 to 105 reportedly results in reduced or abolished F triggering but increased H and F co-precipitation efficiency, (16) suggesting that this section of the stalk likely contributes to proper H-F interaction through long-range effects and should thus remain unaltered.

Four constructs were generated by the Plemper group: deletion of HR 84-90 (H- $\Delta$ (84-90)) or 118-124 (H- $\Delta$ (118-124)), or insertion of an additional copy of HR 118-124 before residue 84 (H-84 $\nabla$ 7x) or HR 84-90 before residue 118 (H-118 $\nabla$ 7x), respectively. All H variants reached the surface, although plasma membrane steady levels of H-118 $\nabla$ 7x and H- $\Delta$ (84-90) were reduced by approximately 30-50%. Also, all four constructs were fully capable of SLAM binding. However, microscopic analysis and quantitative fusion assays revealed that both HR deletions and the membrane proximal insertions (H-84 $\nabla$ 7x) completely eliminated F triggering. In contrast, stalk elongation membrane distal of the 111/114 section still allowed the formation of functional fusion

complexes, since co-expression of H-118V7x with F resulted in approximately 50% of the fusion activity of standard H and F (**Figure 7-12**).

Structural models of these MeV H stalk deletions were generated by removing HR regions from the H stalk model, save for one flanking residue on either side of the deletion (residues 85-89 for heptad repeat 84-90 and residues 119-123 for heptad repeat 118-124). The flanking residues were then used to superimpose the backbone atoms of the downstream structure to the upstream structure, generating one construct (H- $\Delta$ (84-90)) with residues 58-83 attached to 91-607 and another construct (H- $\Delta$ (118-124)) with residues 58-117 attached to 125-607. MeV H stalk insertions were modeled by duplicating the desired section of the stalk plus one flanking residue on either side for superimposing (residues 83-91, 117-125, and 83-118). These duplicate sections were inserted into the downstream structure and aligned by superimposing the backbone atoms of the overlapping residues. The upstream structure was then superimposed in the same manner to the C-terminal end of the newly extended stalk, generating the following constructs: H-84V7x, residues 58-83 + 118-124 + 84-607; and H-118V7x, residues 58-117 + 84-90 + 118-607.

In these new H-F interaction models, only the stalk elongation downstream of 111/114 (H-118V7x) is compatible with H-F interaction, positing a slight increase in the height of the H head over F (**Figure 7-12**). Both HR deletions, however, are predicted to lower the H head in relation to F, causing steric interference consistent with their lack of fusion activity. The membrane proximal HR insertion construct (H-84V7x) is predicted to increase the height of the H head over F the same distance as the membrane distal insertion construct (H-118V7x), but lacks fusion activity. This result is consistent with its

predicted disruption of the interaction of H stalk residues 111 and 114 with the F protein head. These results demonstrate that the overall stalk lengths can be increased, but the distance between the transmembrane domain and stalk section 91-117 must be preserved for effective H-F interaction and F triggering.

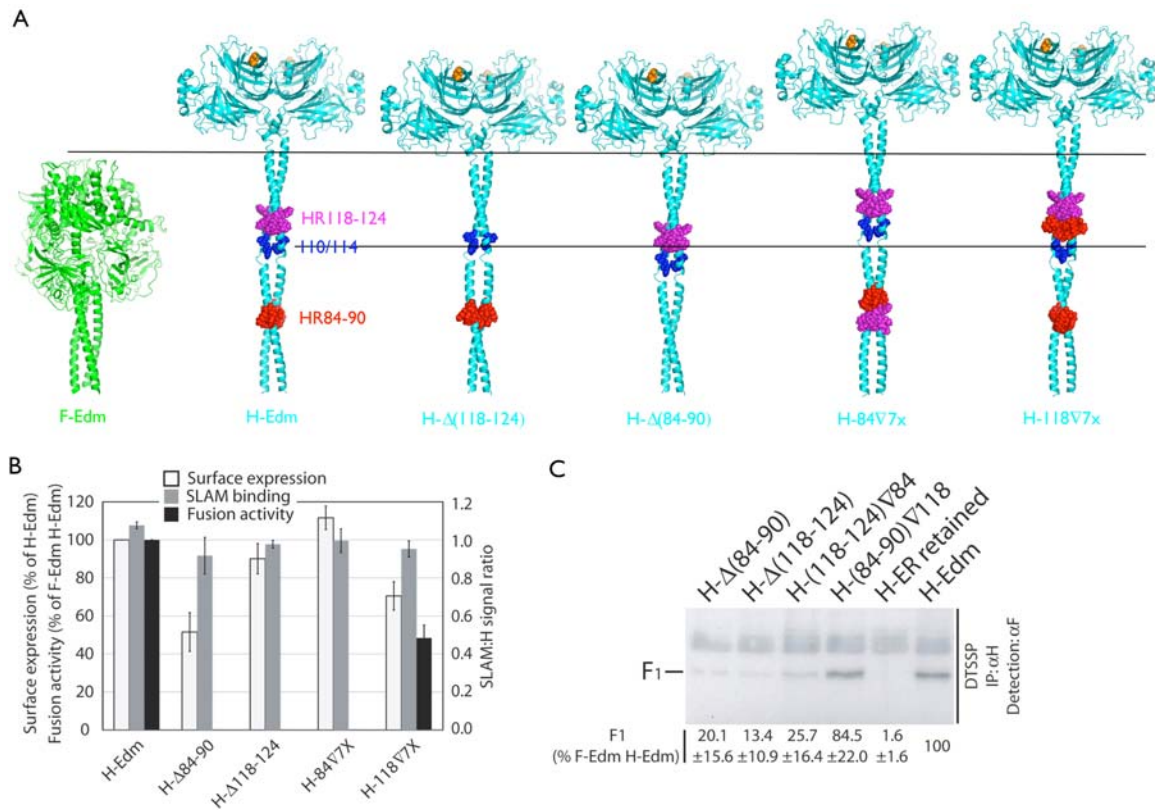


**Figure 7-12:** Insertion of a heptad repeat element into the H stalk downstream of position 117 still allows functional glycoprotein interaction. (A) Graphic representation of predicted consequences of H stalk deletions or insertions in a hypothetical H-F interaction that involves short-range contacts between the prefusion F head and the H stalk. Ribbon models of prefusion MeV F and H were aligned at the transmembrane domains as previously described. Heptad repeat elements 118-124 (magenta), and 84-90 (red) are either individually deleted (H-Δ(118-124) or H-Δ(84-90)) or inserted as additional copy before residue 84 ((H-84V7x) or 118 (H-118V7x)). The position of residues 110 and 114 (blue, black alignment bars) and alignment guides (horizontal lines) are shown. (B) Characterization of the stalk deletion and insertion variants for surface expression, SLAM binding, and fusion activity. (C) Co-immunoprecipitation of surface-exposed MeV F with MeV H after DTSSP cross-linking.

### 7.3.4 Extensive stalk insertions argue against specific contacts between H and F head domains

F triggering by H-118V7x makes it conceivable that H domains downstream of residue 117 may not engage in direct protein-protein contacts in prefusion hetero-oligomers. Alternatively, structural flexibility of the carboxy-terminal third of the stalk (residues 118-154) could compensate for a single HR insertion. To explore these hypotheses, the Plemper group further extended the stalk domain membrane distal of position 117. Insertion of a second HR domain generated variant H-118V14x with a predicted additional length of 22 Å. Compared to H-118V7x, the second additional HR domain returned very similar surface expression, was fully capable of SLAM binding, and improved F triggering to approximately 80% of standard H in cell to cell fusion assays. Further extension of the stalk domain was implemented by the Plemper group through staggered-priming mutagenesis, yielding two additional H variants, that harbor a 41-residue (H-118V41x) or 55-residue (H-118V55x) stalk elongation, respectively. Both constructs were fully capable of SLAM binding and showed plasma membrane steady-state levels of approximately 65% and 45% of standard H, respectively. Remarkable, co-expression of F with H-118V41x, featuring a stalk extension of nearly 50%, returned approximately 50% fusion activity of standard H. A drastic reduction in F triggering was found for H-118V55x, with residual activity equivalent to approximately 10% of standard H. As suggested by these fusion activities, all three H variants are capable of physically engaging F in co-immunoprecipitation assays. Hetero-oligomers of F and H-118V7x or H-118V55x were closer to standard H, while a weaker interaction was found between F and H-118V55x.

In aggregate, these findings demonstrate that inserting a supposedly rigid, heptad repeat-rich domain of 41 amino acids, which is equivalent to a pitch of approximately 75 Å in a helical conformation, is largely compatible with the formation of functional fusion complexes. A structural model for the H-118V41x construct was also generated, using the same procedure as in section 7.3.3. In the context of the H-F interaction model, the head of the H-118V41x structure is predicted to tower over the F head, precluding any possible interaction between these two domains (**Figure 7-13**).

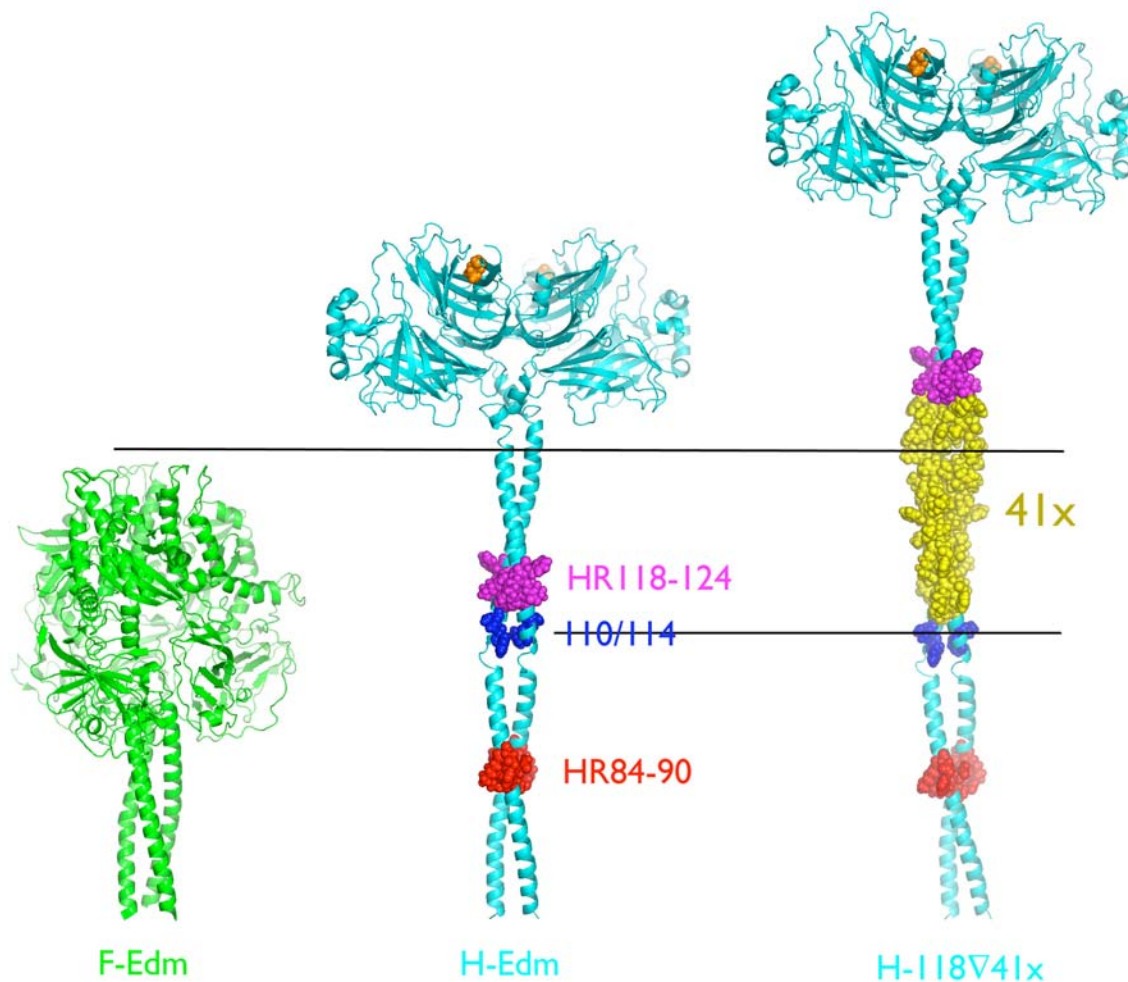


**Figure 7-13:** Membrane distal insertion of multiple heptad repeat elements is compatible with F triggering. Graphic representation of the predicted consequences of H stalk insertion H-84V41x, shown in the same configuration as **Figure 7-12**. In this structure the H head is predicted to tower over the F head. The fusion activity and physical H-F interaction of this construct suggests that direct H-head to F-head contacts are not required to trigger fusion.

### 7.3.5 Overall consistency of the H-F interaction model with experimental evidence

The H-F interaction model presented here, while not conclusively proven with a high-resolution structure, is strikingly consistent with experimental modifications designed to test its applicability. The main limitation of the model, the assumed coiled

coil structure of the H stalk, and by extension, the positioning of the H head over F, has been explored through multiple means. Firstly, N-glycan shielding at H stalk position 111 blocks both functional and physical glycoprotein interactions, suggesting a close proximity of F to this section of the stalk. While this could alternatively derive from a long-range, indirect effect of the added glycans, efficient H-111-N-glycan surface expression, unchanged receptor binding capacity, and a rigid helical configuration of the stalk supported by secondary structure predictions and circular dichroism analysis of the related PIV5 HN stalk<sup>170</sup> render this unlikely. Nearly undisturbed physical interaction and F triggering capacity of H-72-N-glycan underscore this conclusion. It is noteworthy that additional N-glycosylation sites are efficiently recognized at three consecutive positions starting with residue 100, but only at position 72 of the more membrane proximal 70-72 sites. This may imply that interaction of the helices is modeled incorrectly for this portion of the stalk. Alternatively, perhaps there is more flexibility in the helix at this position distal to both the viral envelope and the Cys139 disulfide bond.

The second piece of experimental evidence for the H-F model is that mutagenesis of individual residues 110-114 highlighted two residues (111 and 114) as determinants of both F triggering and H-F interaction. These two residues are predicted to be located on consecutive turns of the MeV H stalk helix. Although other protein structures are possible that would face these two residues the same direction, this result is entirely consistent with a coiled coil for this portion of the H stalk. A previous study has demonstrated that mutation of MeV H stalk residues 84, 92, 98, or 99 blocks F triggering but increases H-F interaction by 1.4-fold or greater. (16) It is possible these and the 111/114 changes introduced into the MeV H stalk residues impair F triggering through long-range effects,

but the direct correlation between glycoprotein association and fusion activity observed for residues 111 and 114 makes it conceivable that these two residues engage in short-range interactions, while the other residues affect fusion through a repositioning of interacting microdomains that increases the physical interaction of H to F, but perturbs its fusion triggering ability.

The final piece of experimental evidence for the H-F interaction model is the effect that shortening or lengthening the H stalk has on H-F physical interaction and fusion triggering. Shortening the H stalk either before or after residues 84-117 blocks both hetero-oligomerization and triggering. This is compatible with both a lateral and a staggered alignment of the H and F head domains. However, increasing the length of the H stalk before residue 84 by 11 Å disrupts H-F physical interaction and F triggering, while increasing the length after 117 the same amount still allows the formation of functional fusion complexes. This demonstrates that the position of section 84-117 relative to F is critical for productive hetero-oligomerization. While the H-F interaction model does suggest that the membrane-facing side of the H head may be proximal to the top of F, stalk elongation after residue 117 argues against precise protein-protein contacts between these two portions of the proteins, in particular when considering that an insertion of 41 HR residues is compatible with the formation of functional fusion complexes. Extension is not completely unlimited, of course, as the insertion of a 55 HR residues causes a drop in both F triggering and H-F physical interaction.

#### **7.4 H-F interaction model with tetrameric H**

The presented model of H and F interaction, although consistent with the experimental testing, does not immediately suggest a structural mechanism for triggering

F. Additionally, while it does posit the H head towers over F, it does not suggest a particular arrangement of the H head in relation to F. Interestingly, no major conformational changes were observed between X-ray crystal structures of monomeric PIV5 HN, hPIV3 HN, and henipavirus G solved alone or in complex with their receptor.<sup>153, 177, 178</sup> Since the dimer-of-dimer interface of PIV5 HN is substantially smaller than the dimer interaction, a possible mechanism for F triggering has been suggested to be that receptor binding effects the intersubunit interface, resulting in a partial disassembly of the tetrameric head of the HN attachment protein, changing its the interaction with F and inducing triggering. By analogy, a change in the intersubunit interface a MeV H homo-tetramer upon receptor binding would not require complex signaling through the stalk domain and thus be consistent with the maintained functionality of the H-118V41x variant. To date, MeV H head domain fragments have only been crystallized as monomers<sup>135</sup> and homo-dimers.<sup>137</sup> It is not known, however, whether crystals of soluble head domains accurately reflect the oligomeric state of native, membrane-embedded MeV H. Reorganization of a hypothetical dimer of dimers would provide a straight-forward explanation of how engagement of distinct binding site in the H head domain by CD46 and SLAM results in effective F triggering.<sup>172, 179</sup>

To structurally investigate the oligomeric state of MeV H, a tetrameric model was generated through computational protein-protein docking. The predicted tetrameric model is consistent with the tetrameric structures of known paramyxovirus attachment proteins and its own glycosylation sites. When positioned in relation to MeV F, a reasonable interaction model is generated and provides a basis for experimental verification.

### 7.4.1 Predicting the tetrameric MeV H structure

To test the ability of computation protein-protein docking algorithms to predict accurate oligomeric MeV structures, these programs were evaluated in the test case of dimeric MeV H head domains. MeV H head fragments have been crystallized as a dimer and in functional MeV H are linked by two disulfide bonds, one between Cys139 residues, and another between Cys154 residues.<sup>149</sup> The X-ray crystal structure of MeV H (Protein Data Bank code 2ZB5),<sup>137</sup> contains coordinates for residues 154-607. Structural information is missing for some intervening portions, including residues 169-186, 239-247, and 502-504. The protein-protein docking programs were evaluated by moving one subunit out of position in the dimer, submitting the structure for prediction, and the measuring the root mean square deviation in the positions of the backbone atoms ( $\text{RMSD}_{\text{backbone}}$ ) of the predicted structures with the experimental X-ray crystal structure. Three protein-protein docking servers were tested, SymmDock,<sup>180</sup> PatchDock,<sup>180</sup> and RosettaDock.<sup>181</sup> Of these three, only RosettaDock predicted the dimer structure within  $10\text{\AA}$   $\text{RMSD}_{\text{backbone}}$  of the experimental structure in the top-scoring pose (**Figure 7-14**). None of the other programs even predicted a pose with  $< 10\text{\AA}$   $\text{RMSD}_{\text{backbone}}$  in the top 10 scoring poses. The RosettaDock pose, with an  $\text{RMSD}_{\text{backbone}}$  of  $9.7\text{\AA}$ , was deemed a satisfactory level of performance for this difficult test case which only has  $710\text{\AA}^2$  of buried surface area between the dimers. The performance of RosettaDock is likely attributed to its flexible docking approach, combined with accurate scoring.<sup>182-184</sup> The procedure first removes the side-chains, simulating the proteins as coarse-grain models. This is followed by a variable number of Monte Carlo steps displacing the protein from

its starting position, replacement of the sidechains with rotamer searching, and finally, minimization and scoring.

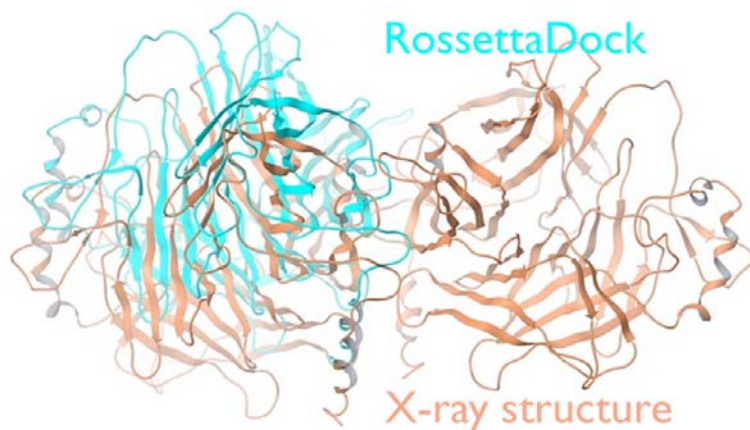


**Figure 7-14:** Predicted MeV H head domain dimer structure by RossettaDock versus the experimental X-ray crystal structure. This was the top-scoring result and had an  $\text{RMSD}_{\text{backbone}}$  of  $9.7\text{\AA}$  compared with the experimental structure.

RossettaDock was then applied to prediction of the MeV H tetramer, docking a duplicate of the dimer to the experimental dimer structure. The duplicate dimer was initially positioned  $\sim 10\text{\AA}$  away from the experimental dimer. RossettaDock was directed to perform 5,000 Monte Carlo steps, generate starting positions by translating the duplicate dimer by Gaussian random distances and angles of  $5\text{-}10\text{\AA}$  and  $10^\circ$ , respectively; creating a diffuse cloud that covers a large interaction area between the dimers (**Figure 7-15A**). Subsequently, RossettaDock replaced the sidechains, minimized, and scored the structures (**Figure 7-15B**). Each point in **Figure 7-15B** represents a pose refined and scored by RossettaDock. Poses scoring better than  $-1426$  were visually evaluated for  $C_2$  symmetry. Within these high-scoring poses only two poses with  $C_2$  symmetry were found, each the reflection the other (**Figure 7-15C**).

This pose posits an interesting arrangement of the dimers, with protrusions that fit into complementary pockets on both sides of the interface (**Figure 7-15C**). The N-terminal helices of both dimers are correctly predicted to face the viral envelope. Interestingly, this pose also exhibits the propeller-like interface between dimers seen in

the PIV5 H tetramer. This initial pose from RosettaDock lacks structural information for residues 169-186, 239-247, and 502-504: these portions of the protein were modeled as loops using PRIME's<sup>130</sup> loop refinement module (Schrödinger). These loops were not included in protein-protein docking because they were unresolved in the X-ray crystal structure and could bias the results with the particular conformation of the loops used in the docking. By adding the loops after protein-protein docking, only the resolved portions of the protein influence the result.

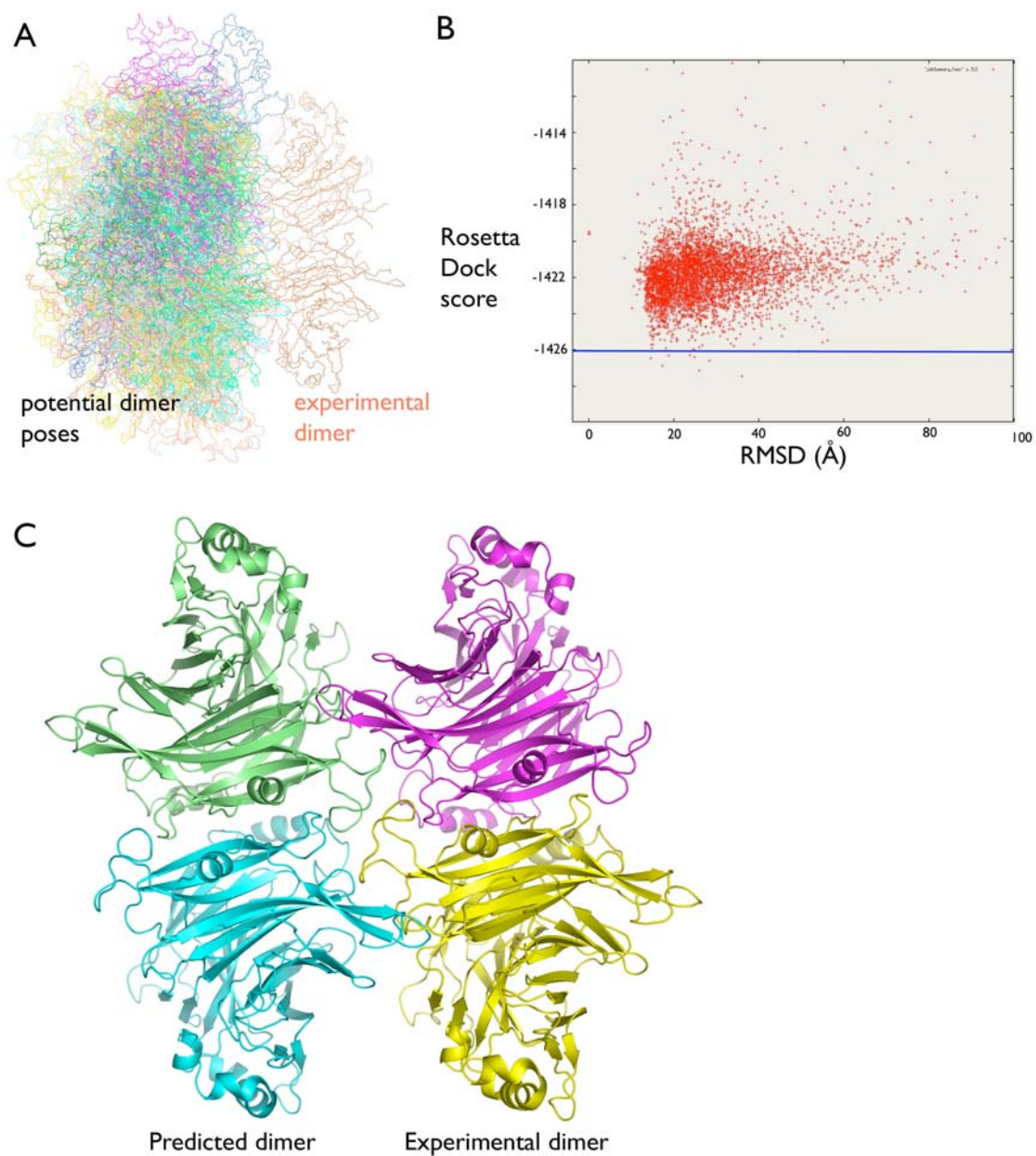


**Figure 7-15:** RosettaDock results for MeV H tetramer prediction. (A) Pose positions for 50 of the 5,000 Monte Carlo steps, shown on the left; experimental dimer shown on the right. Protein is shown as backbone lines, colored by pose. (B) Plot of each of the 5,000 pose's deviation from the starting structure in backbone RMSD versus the Rosetta docking score for that pose. Poses below the blue line were visually evaluated. (C) Highest scoring pose with  $C_2$  symmetry, shown as ribbons colored by subunit.

#### 7.4.2 Compatibility of the MeV H tetramer model with natural glycosylation sites

The MeV H tetramer was predicted based on the structure of the MeV H dimer without carbohydrates attached to the natural N-glycosylation sites. Because these carbohydrates are unresolved in the experimental structure, including them in protein-protein docking would bias the results the same way the unresolved loops would. It is possible, however, that the large carbohydrate structures would sterically prevent tetramer formation. To test this possibility, N-glycans were attached to the MeV H tetramer model at 16 N-glycosylation sites (4 per subunit, positions 168, 187, 200, and 215) and minimized by MACROMODEL<sup>119</sup> (Schrödinger) using OPLS2005<sup>100, 120, 121</sup> and GB/SA solvation.<sup>122</sup> The resulting glycosylated structures fit tightly with the carbohydrates (**Figure 7-16A**) but are no more congested than the carbohydrates attached to the N-glycosylation sites of tetrameric PIV5 HN (**Figure 7-16B**).

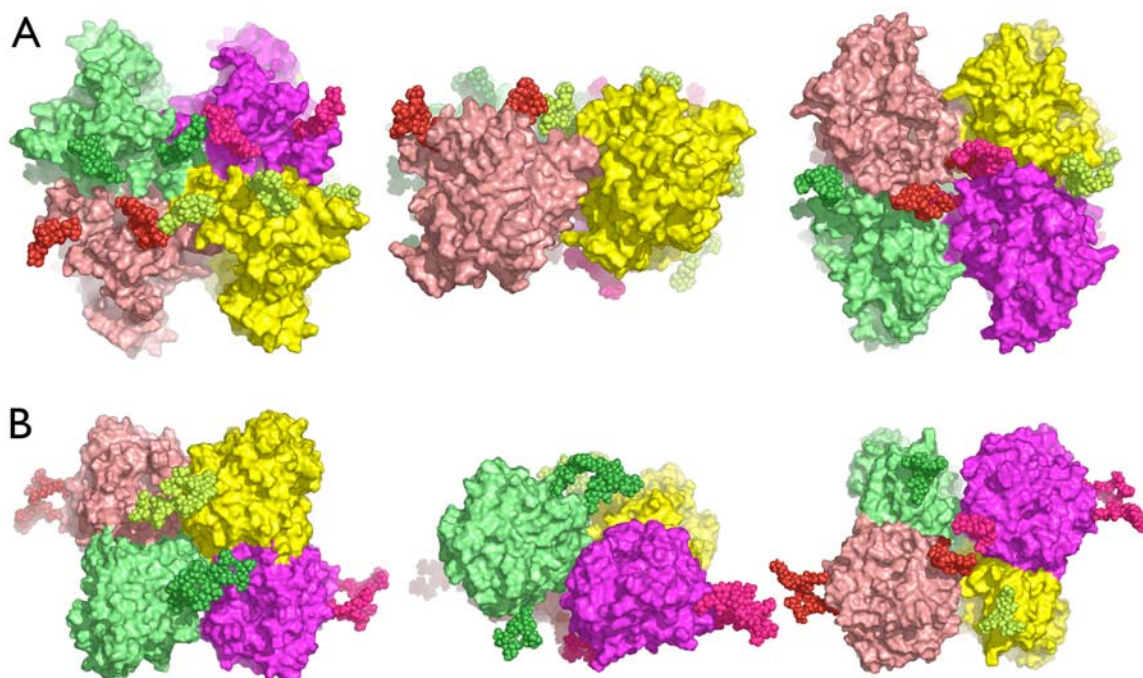


**Figure 7-16:** Compatibility of N-glycosylation sites in the MeV H tetramer model (A) and X-ray crystal structure for tetrameric PIV5 HN (B). The proteins are shown in their solvent accessible surfaces, colored by subunit. N-glycans are shown as spheres. Membrane distal face, side view, and membrane proximal face are shown in the left, center, and right panels, respectively.

#### 7.4.3 Incorporating tetrameric MeV H in the H-F interaction model

To apply the tetrameric MeV H structure to the H-F interaction model, two H stalk domains were attached to the MeV H head domains using the same procedure as in section 7.2.2. Because the propeller-like interface between the H dimers in the tetramer, a slight kink in the attachment of the stalks to the head domains is necessary to maintain a perpendicular positioning of the stalks and the plane of the head domains in relation to the viral membrane.

The resulting model of the complete MeV H ectodomain was manually positioned relative to prefusion MeV F structure and aligned by their transmembrane domains, envisioning an x-y plane at the viral membranes surface. Because both these proteins are

embedded in the viral membrane, the “z” translational degree of freedom is removed. Both proteins were modeled perpendicular to the viral membrane, eliminating the “x” and “y” rotational degrees of freedom. This procedure leaves only translation in the x-y plane and rotation in the z-axis as variables in the positioning of MeV H. With these restrictions, MeV H was oriented such that the best possible interaction with CDV F could occur, namely minimum steric contacts but maximum van der Waals and electrostatic interactions.

In the resulting model of F and tetrameric H (**Figure 7-17**), the section of the F head domain housing the key residue 121 fits naturally into the cleft formed by the pair of coiled coils in the association of H dimer of dimers. Strikingly, the two key H residues, 111 and 114, are predicted to directly face F residue 121 in nearby proximity. Though the MeV H structure is built on two critical assumptions, a coiled coil stalk and tetrameric oligomeric state, this is not a contrived result, but follows from a straightforward juxtaposition of the two structures. It also fully consistent with engineered N-glycans and H stalk extension and deletions studies.

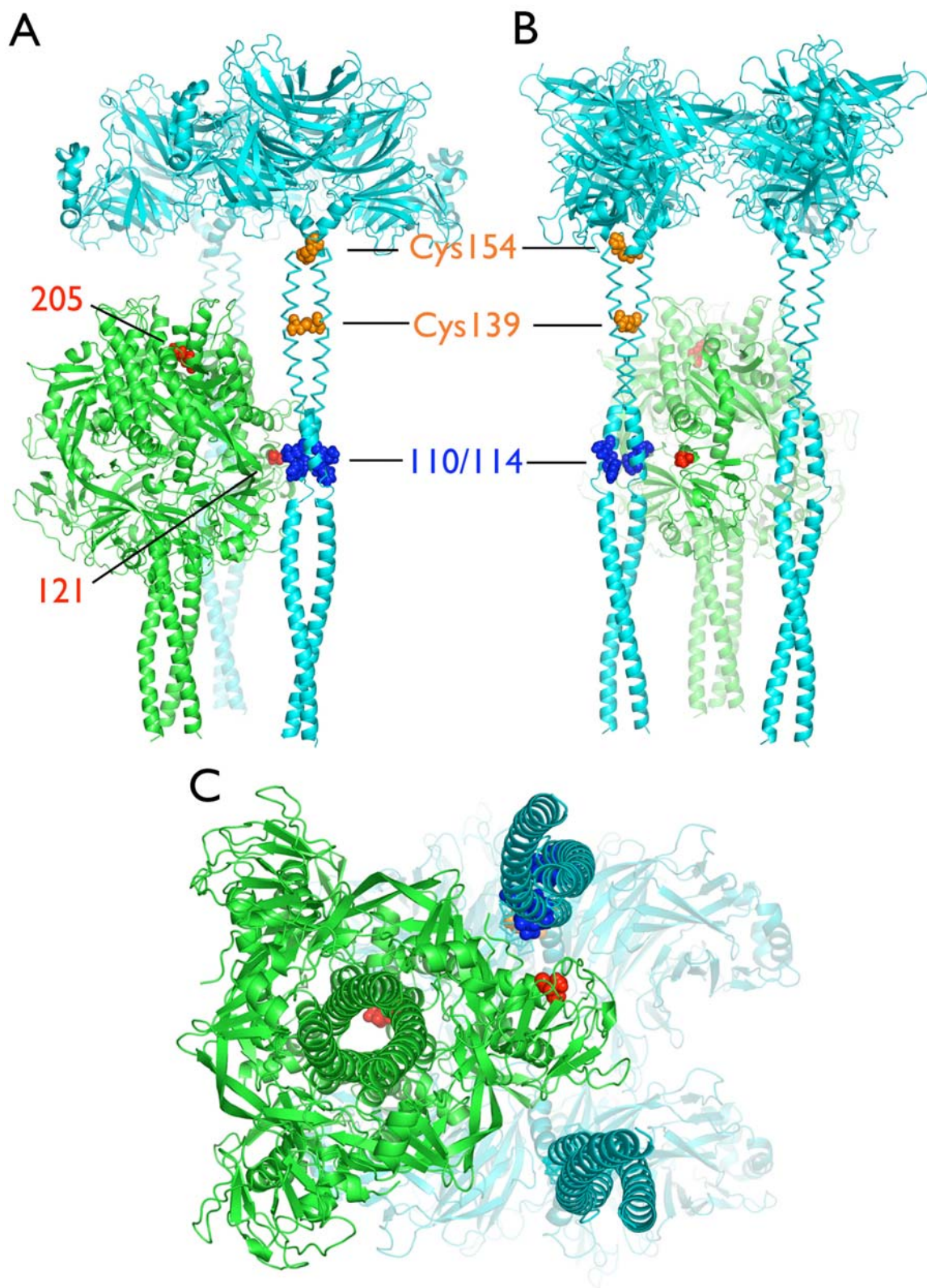


**Figure 7-17** (previous page): Hypothetical interaction model of tetrameric MeV H and trimeric F. H and F are colored cyan and green, respectively; with H stalk disulfides, F111/L114, and F121/205 shown as orange, blue, and red spheres, respectively. (A) Side view. (B) Rotated side view. (C) View from viral envelope.

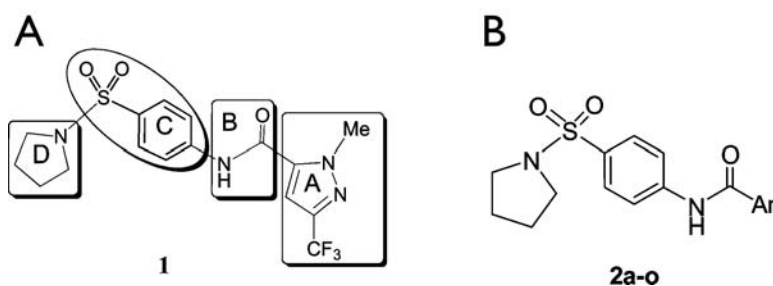
If this model is close to the actual structure of the H-F hetero-oligomers, there are important implications for fusion function. Prior to F triggering, the fusion peptide (containing F residue 121) could be contained by interactions with H stalk residues 111 and 114. Receptor binding by the H head would perturb these interactions by disrupting the interface of the tetramer, causing the H stalks to move relative to each other and F. With the fusion peptide no longer restricted by the H stalk, it is free to move toward the target membrane, beginning the fusion conformational cascade.

In the absence of a high-resolution structure of a functional H and F complex, further experimental evidence is needed to verify this hypothetical interaction model. Proof that functional H acts as a tetramer with a structure as proposed is required. Also, residues postulated to interact between H and F but not identified in the chimera assays should be assessed for their significance in fusion activity and physical H-F interaction. Cryo-electron microscopy studies currently underway may further reveal the nature of the H and F head arrangements, allowing an evaluation of the rough distances between H and F heads individually, as well as between each other. These will be interpreted to determine if the H-F interaction model is consistent.

## Chapter 8: RNA-dependent RNA polymerase inhibitors

*Portions of this chapter are based on “Potent non-nucleoside inhibitors of the measles virus NRA-dependent RNA polymerase complex,” published in the Journal of Medicinal Chemistry in 2008.*<sup>185</sup>

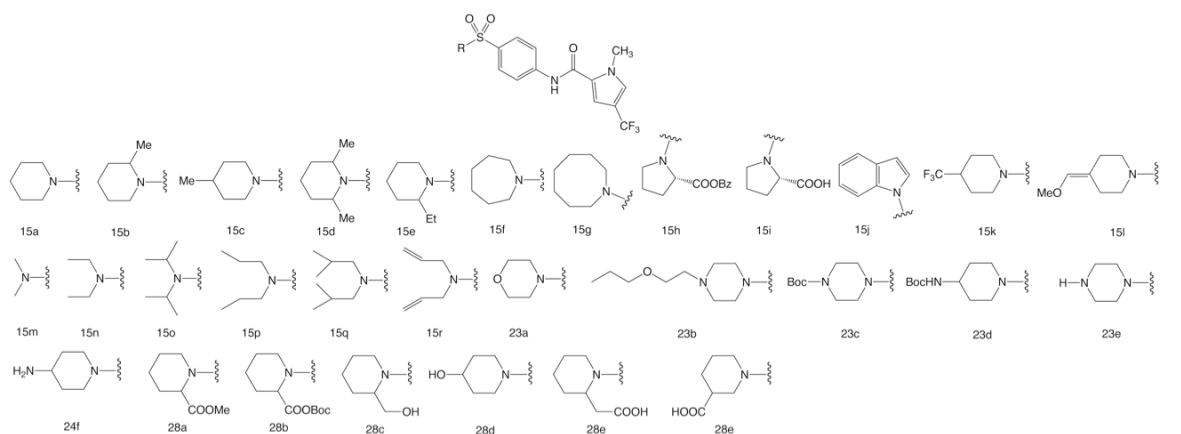
The search for MeV inhibitors was broadened by turning to cell-based high throughput screening (HTS) to capture small molecules capable of entry inhibition as well as compounds operating against other proteins critical for viral infection and reproduction. The exercise identified compound **16677** ( $EC_{50} = 250$  nM) as a well-behaved, target-specific inhibitor of MV replication (**Figure 8-1**).<sup>186</sup> Bypassing the fusion protein, **16677** (heretofore referred as **1**) was demonstrated by the Plemper group as the first-in-class non-nucleoside inhibitor of the MeV RNA-dependent RNA polymerase (RdRp) complex. Following re-synthesis of the hit compound **1** by Drs. Aiming Sun and Maina Ndungu, preliminary structural modifications focused on the right side of the molecule as depicted in **Figure 8-1B**.<sup>187</sup> Further optimization of antiviral activity for the **1** scaffold was desired and achieved by manipulation of the pyrazole (A) and pyrrolidine (D) rings by Drs. Aiming Sun and Jaeki Min.<sup>185</sup> Biological evaluation of these compounds was performed by members of the Plemper group. In the absence of any structural information RdRp complex for any paramyxoviruses, a ligand-based quantitative structure activity relationship (SAR) was developed for the analogs of **1** and used to understand the antiviral activity of these compounds.<sup>185</sup>



**Figure 8-1:** (A) Sectors of compound **1** utilized as an SAR template. (B) Aromatic ring analogues of the compound **1** pyrazole ring, **2a-o**.

### 8.1 Qualitative SAR for compound 1 analogs

Disappointedly, all attempts by the synthesis team to replace the pyrazole ring with five- or six-membered aromatic rings<sup>187</sup> or to alter substituents on the pyrazole ring (e.g., **4**, **13**, and **14**) led either to a decrease or to a complete loss of activity. A striking example is the inactivity of the series of *N*-alkyl analogues of **1** ( $EC_{50}$  30–150 nM<sup>187</sup>). Replacement of the *N*-methyl with *N*-isopropyl or *N*-benzyl (**9b** and **c**, respectively) leads to disappearance of potency in the virus titer reduction assay. While the *N*-ethyl pyrazole **9a** demonstrates good activity in ( $EC_{50}$  = 55 nM), the compound is highly toxic. In a previous limited exploration of the SAR of **1**, the synthesis team learned that installing a piperidine ring instead of the pyrrolidine ring on the left side of the molecule (**Figure 8-1A**, D ring) provided a 100-fold boost in activity while simultaneously delivering very low toxicity.<sup>187</sup> To exploit this potency advantage, a variety of alicyclic heterocyclic rings (**15a-l**) or dialkyl amines (**15m-r**) were employed as pyrrolidine replacements while retaining the remainder of compound **1** structure (**Table 8-1**).

**Table 8-1:** Antiviral MeV EC<sub>50</sub>'s, Cytotoxicities, and Selectivity Indices for **1** analogues

entry ID no.	EC <sub>50</sub> (μM) (MV-Alaska)		CC <sub>50</sub> (μM) Vero cells		SI (CC <sub>50</sub> /EC <sub>50</sub> )	
	CPE inhibition <sup>a</sup>	Virus titer reduction <sup>c</sup>	MTT cytotoxicity <sup>d</sup>	Trypan blue exclusion assay <sup>e</sup>	CPE + MMT	Titer + trypan
<b>4</b>	>75	ND	95±20	ND	<1.3	ND
<b>9a</b>	<2.3	0.055±0.013	30±2.4	ND	ND	ND
<b>9b</b>	>75	ND	>300	ND	ND	ND
<b>9c</b>	>19 <sup>c</sup>	>19 <sup>b</sup>	ND	19±1	ND	ND
<b>13</b>	>75	>75	ND	>300	ND	ND
<b>14</b>	>75	>75	ND	>300	ND	ND
<b>15a</b>	<2.3	0.014±0.02	>300	199±27	>130	14214
<b>15b</b>	<2.3	0.029±0.031	>300	54±3	>130	1862
<b>15c</b>	<2.3	0.035±0.035	>300	53±4	>130	1514
<b>15d</b>	<2.3	0.014±0.013	>300	328±28	>130	23429
<b>15e</b>	<2.3	0.087±0.116	>300	14±2	>130	160.9
<b>15f</b>	<2.3	0.005±0.0003	>300	425±65	>130	85000
<b>15g</b>	<2.3	0.045±0.034	16±0.8	ND	>7	ND
<b>15h</b>	14±2	ND	100	ND	7.1	ND
<b>15i</b>	23±10	ND	>300	ND	>13	ND
<b>15j</b>	>13 <sup>b</sup>	ND	13±0.7	ND	ND	ND
<b>15k</b>	2.3±0.7	0.02±0.02	159±12	ND	69.1	ND
<b>15l</b>	>75	ND	92±9.3	ND	<1.2	ND
<b>15m</b>	6.3±0.6	ND	>300	ND	>47.6	ND
<b>15n</b>	<2.3	0.019±0.019	>300	280±90	>130	14737
<b>15o</b>	3.5±0.4	0.53±0.02	>300	ND	>85.7	ND
<b>15p</b>	<2.3	0.19±0.32	>300	ND	>130	ND
<b>15q</b>	>13.8 <sup>b</sup>	ND	13.8±0.7	ND	ND	ND
<b>15r</b>	3.3±1.4	ND	34±0.9	ND	10.3	ND
<b>16</b>	>15 <sup>b</sup>	ND	15±0.6	ND	ND	ND
<b>17</b>	>75	ND	>300	ND	ND	ND
<b>18</b>	>75	ND	286±17	ND	<3.8	ND
<b>19</b>	>75	ND	84±23	ND	<1.1	ND
<b>20</b>	>75	ND	>300	ND	ND	ND
<b>23a</b>	43±24	ND	>300	ND	>7	ND
<b>23b</b>	>75	ND	>300	ND	ND	ND
<b>23c</b>	>75	ND	>300	ND	ND	ND
<b>23d</b>	14.1±6.6	ND	>300	ND	>21.3	ND
<b>24e</b>	28±9	ND	126±7	ND	4.5	ND
<b>24f</b>	>75	ND	>300	ND	ND	ND
<b>28a</b>	10±5.6	ND	136±3	ND	13.6	ND
<b>28b</b>	>38 <sup>b</sup>	ND	38±1	ND	ND	ND
<b>28c</b>	<2.3	0.85±0.05	159±40	ND	>69	ND
<b>28d</b>	6.8±0.9	0.57±0.04	274±19	ND	40.2	ND
<b>29e</b>	>75	ND	>300	ND	ND	ND
<b>29f</b>	>75	ND	>300	ND	ND	ND

**Table 8-1** (previous page) footnotes: <sup>a</sup>EC<sub>50</sub> not determined (ND) when CC<sub>50</sub> ≤ 15 μM. Values represent averages of four experiments ± SD; highest concentration assessed 75 μM, lowest concentration assessed 2.3 μM. <sup>b</sup>No virus inhibition detected at CC<sub>50</sub> concentration. <sup>c</sup>Determined only when CPE inhibition-based EC<sub>50</sub> concentration <2.3 μM. Values represent averages of two to four experiments ± SEM; highest concentration assessed 1 μM. (ND: not determined) <sup>d</sup>Values represent averages of at least three experiments ± SD; highest concentration assessed 300 μM. <sup>e</sup>Determined only when virus titer reduction was assessed and MTT-assay based cytotoxicity >300 μM. (ND: not determined)

Piperidine analogues **15a–e** and **15k** exhibit significant potency improvements by comparison with the original hit. All yield EC<sub>50</sub>'s in the low nM range. The 2-ethyl substitution on the piperidine ring in **15e** elicits 2–6-fold less activity than methyl substitution (**15b–15d**). The seven-membered ring variant **15f** is 10-fold more potent than the azacyclooctane analogue **15g** and about 3-fold more active than the piperidine **15a**. However, C2-substitution of the pyrrolidine ring with either an ester or a carboxylic acid (**15h** and **15i**, respectively) greatly decreases activity by about 100-fold as does introduction of an indole ring (**15j**). Interestingly, while the open-chain diethyl amine compound **15n** is highly active, the alkyl-enhanced di-isopropyl, dipropyl, and diallyl variants **15o**, **15p**, and **15r** lose 10–20 fold potency by comparison. Similarly, **15m** and **15q**, the dimethyl and di-isobutyl analogues, respectively, exhibit drops in activity.

Additional structural modifications of compound **1** by the synthesis team included synthesis of **16–20**, compounds that examine structural environments around a six-membered ring (**Figure 8-2**). Analogue **16** moves the nitrogen out of the piperidine ring of **15a** and introduces a secondary amine as an H-bond donor, while **17** incorporates a sulfonate moiety instead of a sulfonamide group. Compound **18** incorporates a methyl

group on the amide and eliminates possible hydrogen bonding of NH with a nearby amino acid residue. All three compounds **16**, **17**, and **18** occasion a complete loss of activity. Compounds **19** and **20** switch the sulfonamide *para*-amide linker in sector C to the *meta*- and *ortho*-positions, respectively. Both compounds **19** and **20** similarly show no detectable activity below 75  $\mu$ M (**Table 8-1**).

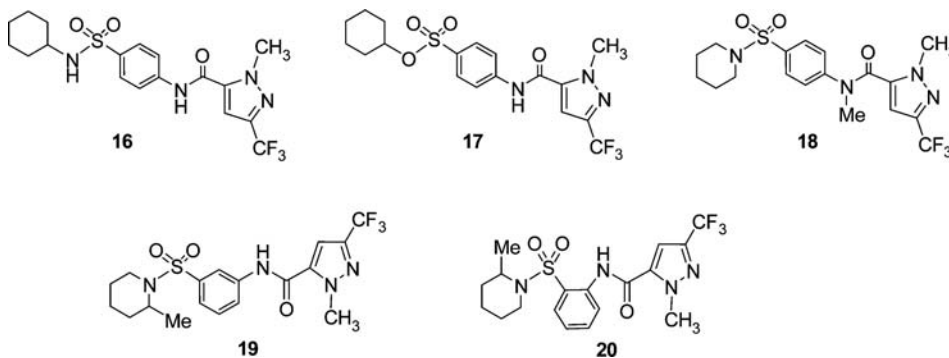


**Figure 8-2:** Variation scaffolds of piperidine analogues

Discovery of four highly active piperidine analogues in the D-sector of **1** (**15a–d**, see **Table 8-1** for biological data) encouraged the synthesis team to further examine this center in an effort to retain nM potency while improving solubility within the series. Thus, morpholine derivative **23a**, piperazines **23b–d**, **24e**, and piperidine rings decorated with hydrophilic groups **24f**, **28a–d**, and **29e–f** were prepared by the synthesis team. Unfortunately, with the exception of **28c** bearing a CH<sub>2</sub>OH group alpha to nitrogen (EC<sub>50</sub> 850 nM), none of the compounds are significantly active. Clearly, the incorporation of a hydrophilic group in this sector is detrimental to MV blockade (**Table 8-1**). This may reflect impaired passive diffusion through the plasma membrane because inhibitors of the RdRp complex activity need access to the cytosol of the infected cells.

## 8.2 Quantitative SAR for compound 1 analogs

The SAR discussion in the previous section is based on qualitative observations. In an effort to put this on a more quantitative footing, the Molecular Field Topology Analysis (MFTA) method developed by Palyulin et al.<sup>188, 189</sup> was applied to the MeV RdRp complex inhibitor series to generate a quantitative structure-activity relationship (QSAR). MFTA performs a topological analysis for a compound series, generates a molecular supergraph with descriptor values for each compound mapped at each atom vertex, and finishes with PLS-based correlation statistics to generate predictive QSAR models.

MFTAWin software (version 3.0 beta17) was applied by first performing a topological alignment of the training set structures (compounds **1**, **2j**, **2o**, **9a**, **13**, **14**, **15a**, **15c–15i**, **15k**, **15m**, **15o**, **15p**, **15r**, **23a**, **23d**, **28c**, and **28d**, plus **3s**, **5**, **7**, and **8** from reference 192) to construct a molecular supergraph, providing a common reference framework for the chosen descriptor set. Then MFTA's PLS (partial least-squares) regression function was used to build statistical models, the predictivity of which was assessed by the leave-25%-out cross-validation procedure. A variety of descriptor sets were examined; the best results (high  $R$  and  $Q^2$  values, low PLS factor count, small errors) were obtained with descriptors for Gasteiger–Marsili atomic charge ( $Q$ ), the effective environment van der Waal radius ( $R_e$ ), and group lipophilicity based on the sum of the Ghose–Crippen atomic contributions for an atom and attached hydrogens ( $L_g$ ). The veracity of this model was checked by means of an explicit test set (compounds **2n**, **2k**, **15b**, **15n**, **24e**, and **28a**, plus **6** from reference 192). These compounds were selected based on their range of activities and diversity of structures. MFTA was used to map the

test set to the previously generated molecular supergraph and to calculate their descriptor values. Then these values were applied to the previously generated QSAR equation and the test set activities predicted. The validity of the correlation was further checked by randomizing the data and structures. MFTA was also used to generate color-coded molecular supergraphs, reflecting the quantitative effect on activity of each descriptor in each position.

For these analogues of compound **1**, the  $\log(1/EC_{50})$  values for CPE inhibition without standard deviations were used as the numerical biological end points. To incorporate the virus titer data into the correlation, the titer values of compounds with CPE inhibitory activities less than 2.3  $\mu\text{M}$  were scaled to an equivalent CPE  $EC_{50}$  by a conversion factor of 10  $\mu\text{M}$   $EC_{50}$  per 1  $\mu\text{M}$  virus titer. The latter was based on the  $EC_{50}$ 's and virus titers for **15o** and **28d**. Where compounds exhibit activities greater than 75  $\mu\text{M}$ , a value of 150  $\mu\text{M}$  was assigned. Compounds with a cytotoxicity greater than 300  $\mu\text{M}$  or a therapeutic index greater than 4 were selected for MFTA. To simplify the analysis within a congeneric series, only compounds with a scaffold similar to the pyrazole ring A, amide linker B, and sulfonamide linker C were included. Thus, the training set consisted of 26 compounds. Five compounds, **9b**, **23c**, **24f**, **29e**, and **29f** were inactive and consistent outliers. Thus, these compounds were excluded from the training set. For the test set, seven compounds were used.

A variety of single local descriptors and sets of local descriptors were applied to the training set, generating a series of different models with varying predictive  $Q^2$  values based on MFTA's leave-25% cross-validation. The best results were obtained with descriptors for Gasteiger–Marsili atomic charge ( $Q$ ), the effective environment van der

Waal radius ( $R_e$ ), and group lipophilicity based on the sum of the Ghose–Crippen atomic contributions for an atom and attached hydrogens ( $L_g$ ). This QSAR model generated a correlation (**Figure 8-3**) with the following statistics:  $N = 26$ , number of PLS factors  $N_F = 2$ ,  $R = 0.88$ ,  $R^2 = 0.77$ , RMSE = 0.49, and  $Q^2 = 0.66$ . Adding additional descriptors did not substantially improve the correlation. To verify that MFTA has not simply fortuitously found a nonpredictive model, a Y-randomization test<sup>190</sup> was performed on the training set data in ten separate trials. In each trial, the activity data was randomly reordered, and a QSAR model generated. Each random data set delivered the same mean, variance, and molecular supergraph, but no real correlation of activity to structure. The resulting QSAR models generally had a good correlation ( $R_{\text{avg}} = 0.83$ ,  $R_{\text{max}} = 0.92$ ) but poor predictive ability ( $Q^2_{\text{avg}} = 0.21$ ,  $Q^2_{\text{max}} = 0.42$ ). This lends confidence that the experimental model with  $Q^2 = 0.66$  is not an artifact of the method.

Predictions for the seven compound test set with the QSAR model were made by first using MFTA to map the test set compounds with assigned descriptor values to the previously generated molecular supergraph, followed by prediction with the PLS model based on the training set (**Figure 8-3B**). Test set activities are predicted reasonably well with  $R = 0.67$  and  $R^2 = 0.45$ . For three of the compounds, the errors are somewhat substantial (about 30–40% of the training set activity span in log units), but for the other four compounds, the error is less than 20%. The mean absolute error for the complete test set is 0.74 log units, and the RMS error of prediction is 0.86 log units.

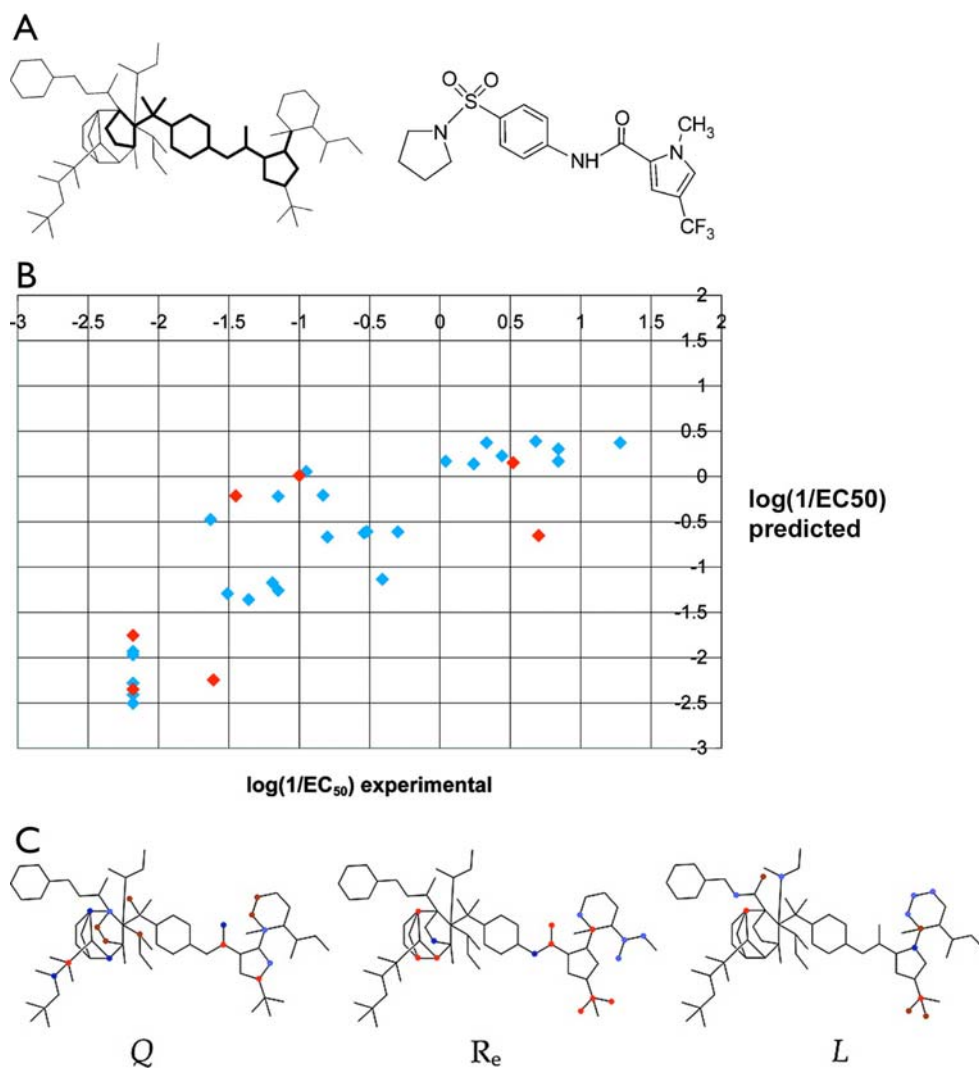


**Figure 8-3:** QSAR results for RdRp inhibitors. (A) MFTA molecular supergraph (left) formed by the 26 compounds of the training set. The superposition of compound **1** (right) is highlighted to exemplify the alignment. (B) MFTA correlation for the 26 compounds of the training set (blue) and the seven compounds of the test set (red) based on charge ( $Q$ ), effective vdW radius ( $R_e$ ), and lipophilicity ( $L_g$ ) descriptors. (C) Descriptor impact on activity shown on the molecular supergraph. The QSAR model predicts that increasing the descriptor property at the red and blue positions results in an increase and decrease in activity, respectively.

MFTA was used to visualize the descriptors' contributions to the correlation by means of a color-coded molecular supergraph (**Figure 8-3C**). Positions colored brown and red suggest that an increase in descriptor property in that part of the molecule would increase activity, red positions having more effect than brown. Conversely, light blue and blue positions suggest that an increase in descriptor property would decrease activity, blue positions having more effect than light blue. At uncolored positions, either the descriptor property is not correlated to activity or there is insufficient diversity in the training set for MFTA to develop correlation to activity. The reader should note that the attempt to display the range of substituents in 2D in sector D in (**Figure 8-3C**) leaves the impression of disorder around the sulfonyl amine group. This is inaccurate and misleading because the correlation of descriptor property to activity is limited by the property range of the substituents in the training set. The graph accurately reflects how subtle changes in the atoms' properties affect activity within the bounds of diversity in the training set.

Interpreting the descriptor impact graphs supports qualitative trends in the structure–activity data. Substituted rings and alkyl chains attached to the sulfonamide have a positive impact on activity if they increase the lipophilicity and decrease the charge on this part of the molecule. However, the QSAR model is able to parse some additional complexity in the structure–activity data by noting that increasing charge in the 3- and 4-positions of the pyrrolidine ring, as well as the *para*-position of the six-membered ring, has a favorable effect on activity. In general, substituents connected to the pyrazole ring have a favorable impact on activity if they contribute an increase in size

and lipophilicity. Increasing charge at the pyrazole ring can either positively or negatively affect activity, depending on the substituent position.

### 8.3 SAR conclusions for compound 1 analogs

Synthetic modification of the **1** lead reveals that both potency gains and structural diversity resides primarily in sector D (**Figure 8-1A**). This behavior is captured by a three-descriptor QSAR model developed using molecular field topology analysis (MFTA) and implies the sector D sulfonyl amines reside in a rather tight hydrophobic cavity. Behavior at the other end of the molecule (sector A) suggests that the pyrazole- $\text{CF}_3$  most likely sits in a pocket housing cationic Arg, His, or Lys based on comparison with  $\text{CF}_3$ -containing ligands in known protein-ligand complexes. These speculations can be further pursued in an effort to identify MV blockers that maintain potency but carry improved solubility and bioavailability properties suitable for evaluating various MeV strains and closely related viruses in animal models.

## Chapter 9: Conclusions and future directions

### 9.1 MeV fusion inhibition

Structure based drug design using a structural model of the fusion protein was a successful approach for designing antiviral compounds. However, by inadvertently targeting an intermediate in the fusion conformational cascade, the activity of the compounds was ultimately limited to the low micromolar range. A similar effect is seen in a case of HIV gp41 inhibitors which block the formation of the postfusion six helix bundle: the best of these compounds has an  $IC_{50}$  of only 5  $\mu$ M (**Figure 1-7**).<sup>37</sup> Much more potent, sub-micromolar inhibitors of fusion have been discovered which stabilize the prefusion form of fusion protein, such as those which bind HIV gp120,<sup>38</sup> Influenza HA,<sup>48</sup> and perhaps RSV F.<sup>49-62</sup> (**Figures 1-7, 1-8, and 1-9**) The RSV F inhibitors are of particular interest as these were presumed to block six helix bundle formation based on a photo-affinity labeled analogue which bonded to the HR-A domain. The nature of this domain in the prefusion form was not considered, however, and may represent the actual form of the target site capable of providing this high level of activity. The assessment of the binding site is also convoluted by the nature of mutations conferring resistance to the RSV F inhibitors, some which are located on the complementary portion of the HR-B domain in the six helix bundle, but others on the distal DI domain. This resistance profile is remarkably similar to that observed for AS-48 and MeV F, suggesting that fusion inhibition of RSV is also countered by prefusion F destabilization.

Coincidentally, one of the residues identified as important to functional MeV H-F triggering (Lys205) but distal to possible H interaction was also located in this portion of the HR-A domain. Further investigation into this target domain is therefore warranted.

Although the first attempt at discovering a ligand that can target the MeV F prefusion structure was unsuccessful, other sites, such as the aforementioned Lys205 prefusion microdomain, may prove more viable. Finally, the cell-based high throughput screening that revealed the potent RdRp inhibitor **16677** also revealed several fusion inhibitors, some of which are similar to AS-48 but others that are quite different.<sup>186</sup> The potential target sites of these ligands should be investigated.

## 9.2 H-F interaction

The proposed H-F interaction between dimeric H and trimeric F (**Figure 7-8**) has been shown to be remarkable consistent with experimental evidence, but this interaction model lacks predictive ability of both the arrangement of the H head hovering over F and physical basis for fusion triggering. The model with tetrameric H and trimeric F does provide a basis of prediction (**Figure 7-17**), but the structural implications of this model need to be investigated, such as sensitivity of the predicted H tetramer interface to mutations and the significance of residues postulated to interact between H and F but not identified in the chimera assays. Additionally, the higher order oligomeric states of multiple F and H proteins should be structurally predicted in anticipation of ongoing cryo-electron microscopy studies that should yield low-resolution structural information.

## 9.3 RdRp inhibition

A quantitative structure-activity relationship was developed for the analogues of the potent RdRp inhibitor **16677**<sup>186</sup> with a respectable predictive ability. The analysis also revealed some subtlety in the structure activity relationships such as noting that instead of increased lipophilicity always being beneficial, increasing charge in the 3- and 4-positions of the pyrrolidine ring, as well as the *para*-position of the six-membered ring,

actually has a favorable effect on activity. However, the method is of limited use toward understand how the ligands interact with the receptor. While no structural information for paramyxovirus polymerases exists, the conserved catalytic domains in other viral RNA polymerases of known structure may provide a template for building a structural model. The veracity of this model could be evaluated with its placement of known mutations that confer resistance to **16677** and its analogs.

## **Part 2: The nature of cyclostreptin's interaction with microtubules**

## 1.1 The binding of microtubule stabilizing agents

Perhaps no other disease has been on researchers' minds than cancer, yet much remains unknown. Research into microtubule stabilizing agents (MSAs) as anti-cancer drugs began in early 1980's with the isolation, structural determination, and biological evaluation of paclitaxel (PTX) (**Figure 1**), a compound isolated from the Pacific Yew tree.<sup>191, 192</sup> PTX subsequently moved into the clinic and became a blockbuster drug. In the presence of such selection pressure, however, cancers have evolved effective mechanisms of resistance through mutations in tubulin and over-expression of P-glycoprotein pumps.<sup>193</sup> PTX also exhibits significant systemic toxicity endured by cancer patients and their families.<sup>194, 195</sup> Thus, the search for novel and improved MSAs has continued and led to such diverse structures as the epothilones (**Figure 1**), dictyostatin, and discodermolide<sup>195</sup>

The continuing search for new MSAs has been aided by significant gains in understanding of microtubule structure, assembly and tubulin interaction with MSAs. In 1998, the tubulin dimer structure in paclitaxel-stabilized zinc sheets was solved by electron crystallography and finally revealed the PTX binding site.<sup>196</sup> Four years later, an 8 Å resolution microtubule structure was solved by cryoelectron microscopy.<sup>197</sup> The higher resolution tubulin dimer structure could be fitted into the microtubule, revealing that the PTX binding site was actually located on the interior of the microtubule. More recently, Buey et al. showed that the binding kinetics of PTX fluorescent analogs (**Figure 1**) were extremely fast and reduced by microtubule-associated proteins.<sup>198</sup> Both of the latter results were interpreted as inconsistent with an interior and inaccessible binding site. Such kinetic data, along with evidence that the PTX site is not present in the free

dimer but can induce polymerization, led the authors to postulate the presence of a second, low-affinity binding site in both tubulin dimers and oligomers, although its location was unknown.<sup>198</sup>

The location of this second postulated binding site might never have been determined except for the appearance of a relative newcomer to the family of MSAs, cyclostreptin (**Figure 1**). Cyclostreptin (CS), isolated from the bacterium *Streptomyces*, has an unusual ring structure with a highly-strained  $\alpha,\beta$ -unsaturated lactone susceptible to nucleophilic attack.<sup>199-201</sup> This new MSA only weakly increases microtubule polymerization, but has potent cellular activity.<sup>202</sup> It is the first MSA to irreversibly bind to  $\beta$ -tubulin in microtubules (in 1:1 stoichiometry), and the only known MSA to bind to the free tubulin dimer.<sup>203</sup> Clever mass spectrometry analysis revealed two sites of covalent attachment: Asn228, near the taxane binding site, and Thr220 located in microtubule type I pore. (For the sake of continuity, we will use the structure-based numbering for Thr220, Asn228, and His229 as in reference.<sup>196</sup> These same residues are sometimes specified according to sequence numbers Thr218, Asn226 and His227.) The binding sites are exclusive and both sites seem to effectively block other MSAs when microtubules are first treated with cyclostreptin.<sup>203</sup> No explanation is apparent for the ability of Asn228 to function as a nucleophile, but the mass spectrometry clearly indicates labeling at this position based on tandem MS peptide fragmentation. Further studies by Bia et al.<sup>204</sup> with a radioactive analog of CS showed that the binding kinetics are fast, but also characterized by a two-step reaction with differing activation energies. Bia et al. logically concluded that the Thr220 site is the location of the low-affinity

binding center and suggested that drugs such as paclitaxel which potently induce assembly might engage in more robust chemistry at this site in the protein than does CS.

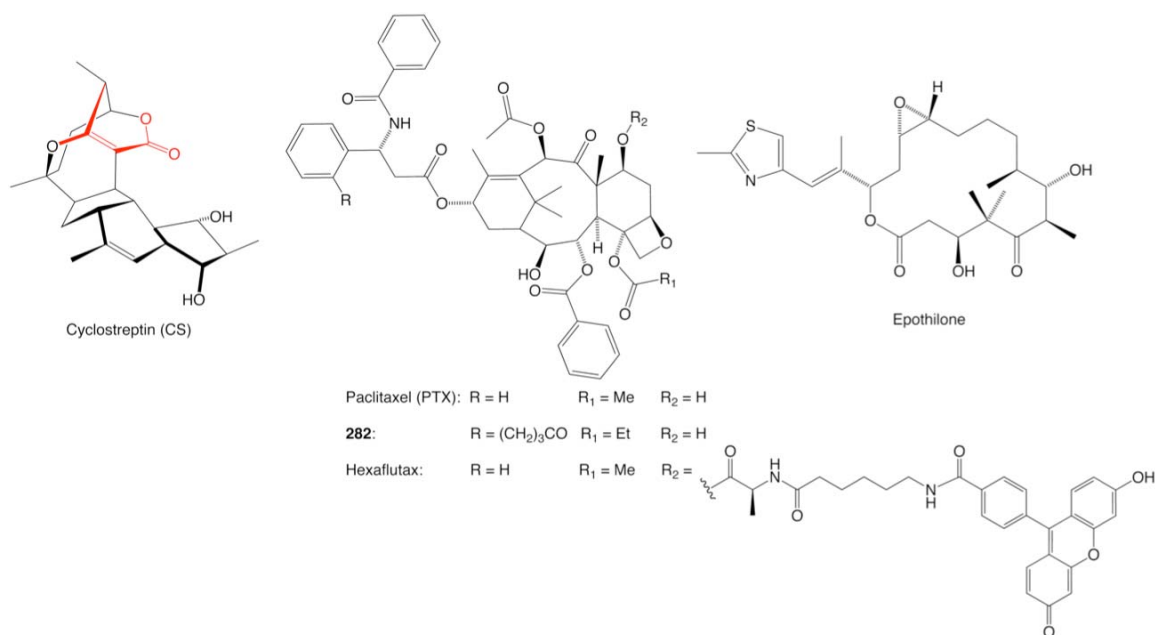


**Figure 1:** Structures of microtubule stabilizing agents. Cyclostreptin (CS, left panel), with its highly-strained  $\alpha,\beta$ -unsaturated lactone shown in red. Paclitaxel (PTX) and its analogs, **282** and the fluorescent Hexaflutax (middle panel). Epothilone (right panel).

Prior to this work, the Snyder group published models for the binding conformation of PTX<sup>205</sup> and epothilone<sup>206</sup> in tubulin based on electron microscopy and conformations derived from deconvoluted 2D NMR data using NAMFIS methodology. Such bioactive conformations led to the design and testing of new bridged analogs.<sup>207, 208</sup> The new series of the taxane analogs is characterized by a non-linear relationship between binding affinity and microtubule polymerization, exemplified by analog **282**, which has 3-fold higher affinity than PTX, but is 14-fold more effective than PTX at inducing polymerization.<sup>209</sup> This draws an interesting contrast with CS, which covalently binds, but only weakly induces microtubule polymerization.<sup>202</sup> The structural basis for the increase in polymerization with the bridged analogs is based on their effect on the M-

loop conformation, which provides most of the interaction between adjacent protofilaments.<sup>197, 210</sup> PTX has long been argued to stabilize microtubules through reshaping of the M-loop,<sup>197, 205, 210</sup> but only recently has the effect been demonstrated *in silico*.<sup>209</sup> Molecular dynamics simulations revealed that in the *apo*-tubulin dimer, the M-loop collapses into the taxane binding site, while PTX causes the loop to move outward and closer to an adjacent protofilament. The rigidity of the bridged analogs causes even more outward movement of the M-loop and further hinders the loop's mobility, eliminating conformations which lack strong lateral interactions. The ability of the bridged analogs to reshape the M-loop correlates directly with promotion of increased tubulin polymerization. Such results strongly suggest that MSAs induce filament assembly by reshaping the M-loop conformation to enhance lateral interactions between adjacent protofilaments in the microtubule.<sup>209</sup> A more recent molecular dynamics study, using a 6-subunit model of the microtubule instead of the free dimer, also concluded that PTX increases tubulin polymerization through effecting the M-loop's interaction with a neighboring protofilament, as well as influencing more distant loops that form the binding interface for the  $\alpha$ -monomer with the next dimer.<sup>211</sup>

The wealth of experimental data surrounding cyclostreptin and other fluorescent MSA interactions with tubulin is certainly sound, but structural evidence for the proposed low-affinity binding site is lacking. Two disparities are troubling: a) the absence of any defined binding site in the microtubule pore, and b) CS only weakly increases microtubule polymerization in spite of covalent attachment. In the study presented here, a combination of molecular modeling methods have been used to propose a different structural model of MSA binding consistent with the experimental findings. To this end,

molecular docking of cyclostreptin to tubulin, constrained molecular dynamics simulations of MSAs with a model of the microtubule pore, and a new evaluation of the previously reported molecular dynamics simulation of the *apo*-tubulin dimer have been used.<sup>209</sup> In light of these and previous findings, the following is proposed: a) the microtubule pore acts as funnel which slows MSA diffusion into the pore without explicit binding, b) cyclostreptin bound to Thr220 effectively blocks MSA diffusion across the pore, and c) CS only weakly increases polymerization in the free dimer because most binding occurs at Thr220 incurring little effect on the M-loop conformation.

## 1.2 Docking of cyclostreptin to the microtubule

### 1.2.1 No defined MSA binding site is present in the microtubule pore

The model of the microtubule developed previously was improved by adding residues missing in the  $\alpha$ -subunit by fitting them to lower-resolution data.<sup>212</sup> These residues do not form the core of the microtubule pore, but were added to prevent artifacts in the subsequent molecular dynamics (MD) simulations. Mapping the lipophilic surface onto the microtubule pore using Sybyl's MOLCAD module<sup>117</sup> shows that the pore is primarily hydrophilic (**Figure 2a**) unlike the known taxane binding site (**Figure 2b**) and MSA ligands like PTX, epothilone and CS (**Figure 2, c, d, and e**, respectively). The surface within the microtubule pore also lacks a defined cleft the size of an MSA like PTX, while the known taxane binding site possesses an evident concave feature roughly the size of MSA molecules (**Figure 2f**). Comparing the shape and lipophilic character of the microtubule pore to MSAs, a second binding site for MSAs in this region seems unlikely. Current MSAs, including CS, are characterized by their hydrophobicity (**Figure**

2, c-e), which complements the hydrophobic cleft forming the taxane binding site (Figure 2b).

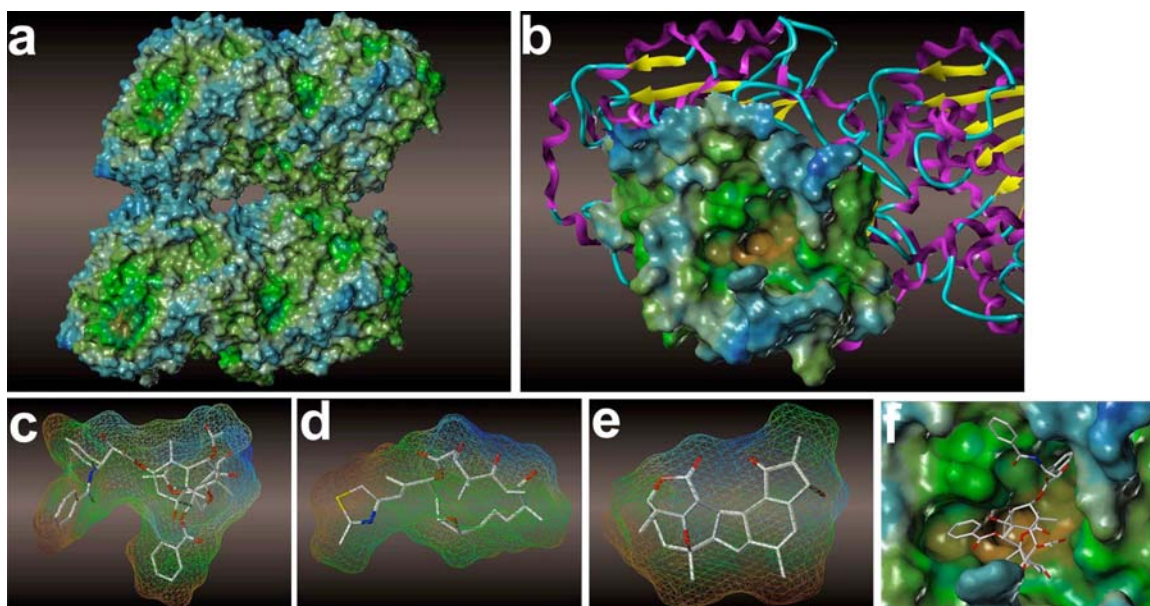


**Figure 2:** Shape and lipophilic character of tubulin and taxane site ligands viewed as solvent accessible surface colored by lipophilicity (brown, hydrophobic; green, neutral; blue, hydrophilic). (a) Microtubule pore, viewed from outside the microtubule with the protofilament axis horizontal. (b) Taxane binding site; portions of the tubulin dimer are shown as cartoon. (c-e) Ligands paclitaxel (PTX), epothilone, and cyclostreptin (CS), respectively, are shown as sticks with mesh surface. (f) Binding conformation of paclitaxel (shown as sticks) in the taxane binding site.

### 1.2.2 CS binding most favorable at the taxane binding site

To evaluate the possible binding locations for CS in the microtubule pore and dimer, blind docking using AutoDock4<sup>213</sup> was performed by Yutao Yang on the entire microtubule pore and adjacent dimers with CS as the ligand (Figure 3a). The type I microtubule pore model was used to perform this blind docking across a microtubule pore consisting of two tubulin dimers. Non-polar hydrogens were merged with their attached heavy atoms (i.e. united atoms) for both the microtubule pore and CS.

AutoGrid4 was used to calculate a grid for the entire protein aggregate consisting of two

dimers, followed by flexible ligand docking with AutoDock4. Docking calculations were carried out using the Lamarckian genetic algorithm, a population of random individuals (population size: 150), a maximum number of 2,500,000 energy evaluations and 27,000 generations, a mutation rate of 0.02 and 50 output poses.

The docking results show that CS binding is clustered at three centers: the taxane binding site (13 poses), the microtubule pore (7 poses) and the GDP binding site (5 poses). Predicted CS binding at lateral or dimer-dimer interactions of the microtubule are not shown as these sites are not truly available in the microtubule. CS docking at the taxane site is favored relative to the pore or GDP site as these 13 poses are the highest scoring in this docking experiment.

Autodock4 and Glide induced fit docking were further applied by Yutao Yang to execute focused docking of CS at these three sites with flexible residues. Two different methods of flexible protein-ligand docking were used: flexible residue docking with AutoDock4<sup>213</sup> and Prime 2.0 induced fit docking protocol within the Schrödinger 2007 Suite.<sup>214</sup> For the flexible residue AutoDock4 calculations, three independent docking runs were performed in which residues close to CS in the blind docking results were selected as flexible (12 residues in the taxane site, 12 residues in the GDP site, and 4 residues in the microtubule pore). The same algorithm and parameters employed in the blind docking were used here. For the Schrödinger induced fit docking protocol with Prime 2.0, three independent docking runs were performed at the three sites. For all three runs, Glide was used to generate 20 initial poses in the first stage of the protocol using Standard Precision docking and 50% reduced vdW radii. The second stage performed protein refinement of residues within 5 Å of the initial poses, followed by minimization of the complex. The

final stage of the induced fit procedure evaluated the poses by re-docking CS using Standard Precision Glide docking and scoring to generate the final 20 poses at each of the three sites.

The results of this focused docking (**Figure 3, b-g**) show that although all three sites could potentially bind CS, the taxane binding site presents a well-defined cluster of poses (**Figure 3, d and g**), while poses in the pore are scattered around the walls that make up the pore (**Figure 3, b and e**), reflecting the mismatch in the lipophilic surfaces of CS and the microtubule pore. This mismatch is illustrated by comparing the lipophilic surfaces of the microtubule pore and the highest-scoring pose of CS in the pore from flexible residue docking using Autodock4 (**Figure 4**). CS binding in the GDP site (**Figure 3, c and f**) seems unlikely based on the low interaction scores of even the best poses in the blind docking experiment.

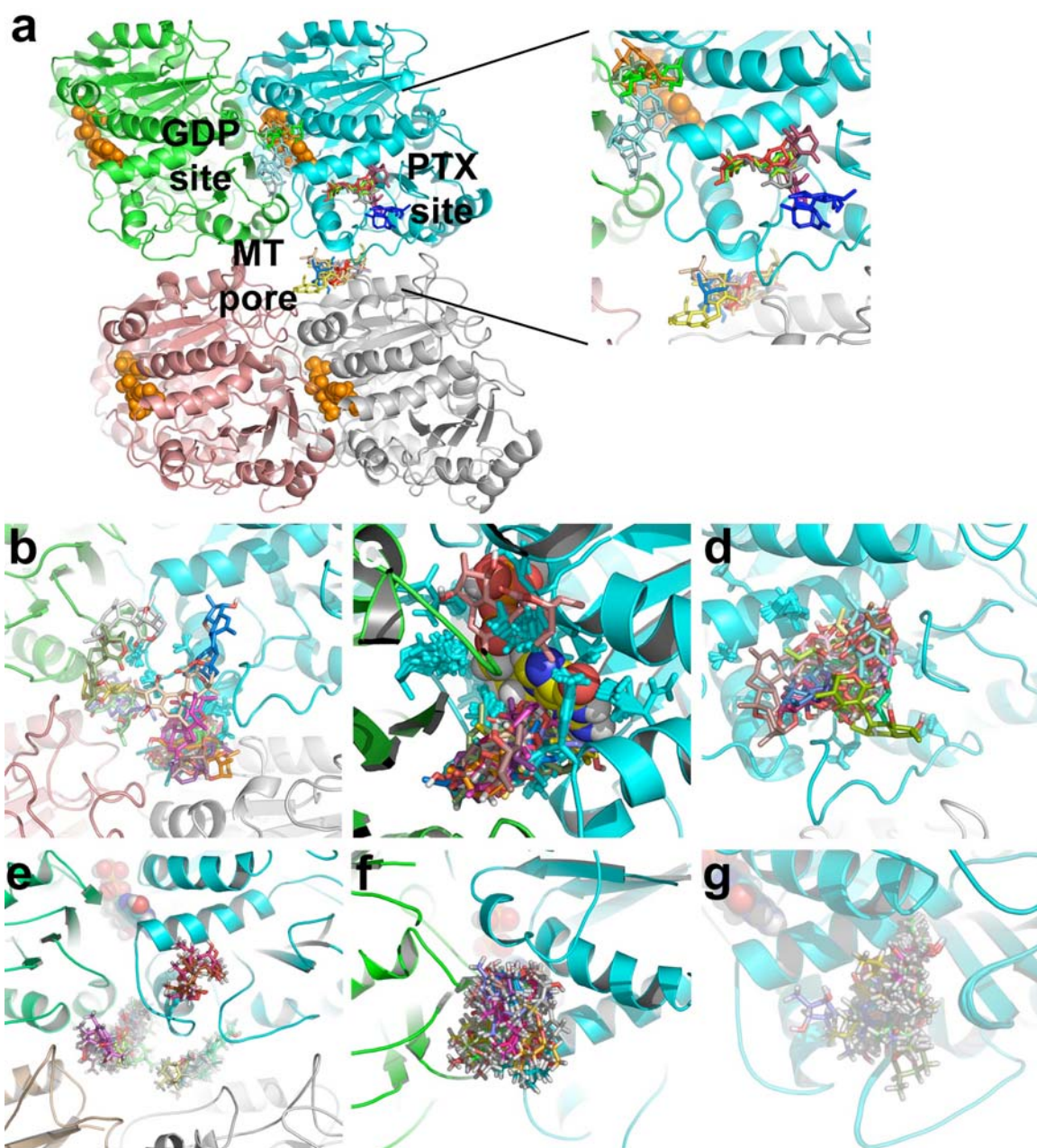


**Figure 3** (previous page): Results of docking cyclostreptin (CS) in the microtubule. The proteins are shown as cartoons colored by subunit; GDP is shown as orange space-filling spheres; CS poses are shown as sticks, colored by pose. **(a)** Top 25 poses resulting from a blind docking of CS to the entire microtubule structure. 13 poses (including the 7 highest-scoring) were placed in the taxane site, 7 poses in the microtubule (MT) pore, and 5 poses in the GDP site. An enlarged view of these three areas is shown on the right. **(b-d)** Highest-scoring 20 poses from Autodock4 flexible residue docking of CS in the microtubule pore **(b)**, GDP site **(c)**, and taxane site **(d)**. **(e-g)** Highest-scoring 20 CS poses from Glide induced fit docking protocol in the microtubule pore **(e)**, GDP site **(f)**, and taxane site **(g)**.

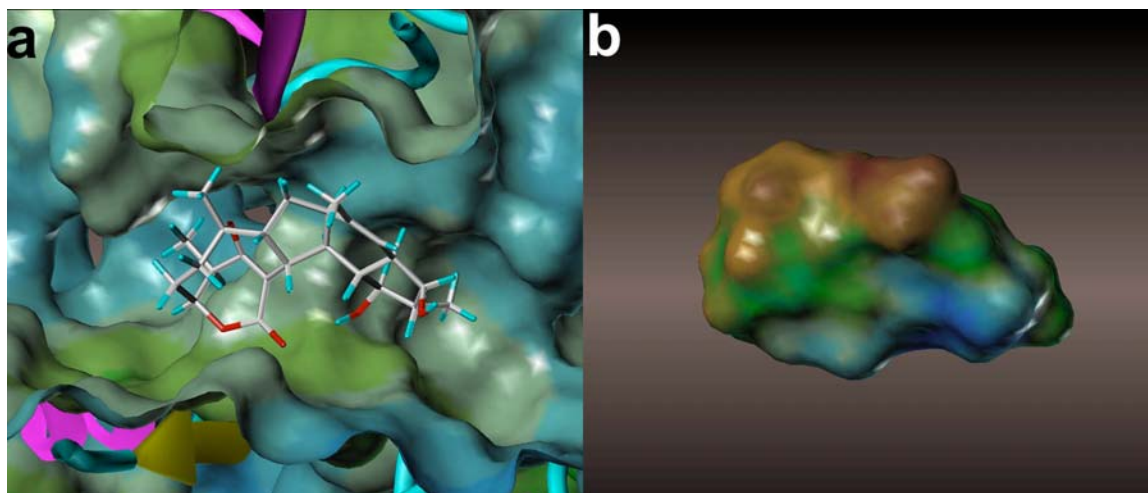


**Figure 4:** Comparison of the lipophilic character of CS and the microtubule pore based on solvent accessible surface colored by lipophilicity (brown, hydrophobic; green, neutral; blue, hydrophilic). (a) Highest-scoring pose of CS in the microtubule pore using flexible residue Autodock4 docking. CS is shown as capped sticks, the microtubule pore is viewed laterally as a lipophilic surface with portions of the protein closet to the reader clipped from view. (b) CS pose viewed from the same angle, except shown as a lipophilic surface.

### 1.3 Constrained molecular dynamics of MSAs in the microtubule pore

#### 1.3.1 MSA diffusion across the microtubule pore

To investigate the nature of interactions at the pore for cyclosporin and other MSAs, a MD protocol was devised to simulate MSA diffusion across the microtubule wall through the pore. The protocol begins with the ligand placed outside the pore and places a small distance constraint on the ligand that passes through the center of the pore. MD is run with these conditions for 4 ps. The distance constraint is then removed, and MD is run for another 4ps. In this manner the MD alternates between a constrained MD and an unconstrained MD for 200 ps. The purpose of such a protocol is to gently pull the ligand through the pore along a pathway which mimics the diffusion of MSAs across the

pore, but in a tractable timescale for MD. Details for this protocol are as follows: the type I microtubule pore model was first refined with the OPLS2005 force field<sup>100, 120, 121</sup> and GB/SA water solvation<sup>122</sup> in Macromodel 9.1.<sup>215</sup> Protein residues within 20 Å from Thr220 were allowed unrestricted movement, surrounded by a 5Å shell with harmonic distance constraints with a force constant of 200 kJ/mol-Å<sup>2</sup>. The structure was minimized in 500 steps with the PRCG method.<sup>216, 217</sup> Then a series of 1 ps molecular dynamics (MD) simulations were performed using a 0.5 fs timestep. The first was simulated at 20K, the second at 100K, the third at 200K, and the fourth at 300K. Finally, the resulting structure was refined by another 500 steps of geometry optimization. Only slight changes in the microtubule pore model resulted from this treatment. Namely, the backbone RMSD with the original structure is 0.4 Å. This microtubule structure was used as a starting point for the MD protocol which gently pulled MSA ligands through the microtubule pore. The protocol begins with the MSA ligand positioned on the exterior of the microtubule pore; while a methane molecule was positioned ~1,000 Å away from the interior of the microtubule. A very small harmonic distance constraint of 0.064kJ/mol-Å<sup>2</sup> was applied between the methane and an atom on the MSA ligand. The purpose of such a setup was to apply a small but linear constraint on the ligand even though the only available constraints in Macromodel are harmonic. The MD simulation began with 4 ps at 20K and a 0.5 fs timestep, applying the distance constraint. Then 4 ps were simulated without the distance constraint, allowing the system to relax. The simulation was continued in this manner for 200 ps, alternating every 4 ps between constraint and no constraint.

The resulting trajectories for PTX, epothilone, and hexaflutax (**Figure 5**) reveal that the pore's center is not large enough to allow MSAs to freely traverse. Side chain rearrangement and slight backbone movements for the protein are required for all of the MSAs to move through the pore. Predictably, the smaller, more flexible epothilone traverses the pore more easily than larger, more rigid molecules like PTX and hexaflutax. Epothilone escapes the pore in 40 ps, while PTX and hexaflutax require 160 and 200 ps, respectively. One feature evident from the trajectories for all the MSAs simulated is a momentary blockage of the ligand in the center of the pore while the conformations of both protein and ligand adjust. This pause in diffusion across the pore could be the basis of the fast binding kinetics seen for MSAs. Kinetic experiments in such a situation would appear to suggest rapid binding, since the environment of the ligand's fluorophore would change to a similar extent as in binding to a discrete site.

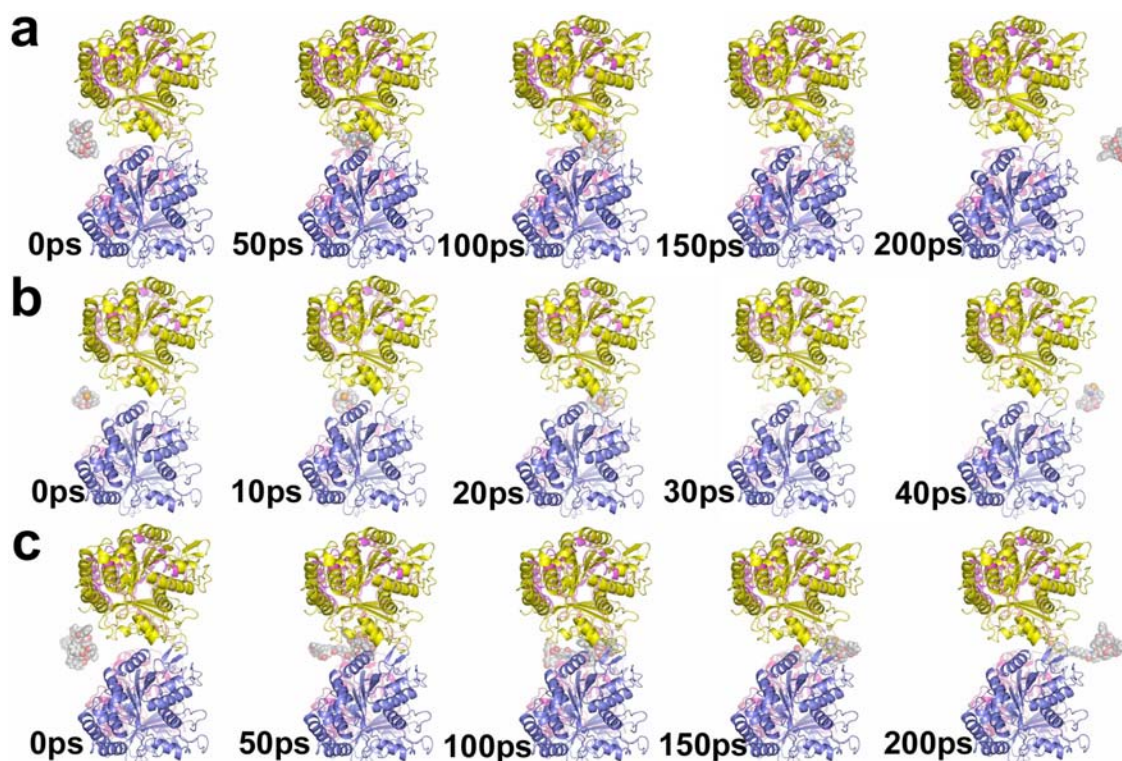


**Figure 5:** Molecular dynamics (MD) trajectories of microtubule stabilizing agents through the microtubule pore viewed laterally. The protein is shown as cartoons, colored by subunit. Microtubule axis is horizontal. (a) Paclitaxel (PTX) trajectory. PTX traverses the pore in 160 ps. (b) Epothilone trajectory. Epothilone traverses the pore in 40 ps. (c) Hexaflutax trajectory. Hexaflutax traverses the pore in 200 ps.

### 1.3.2 Blockage of MSA diffusion by cyclostreptin

The effect of CS attachment at Thr220 on MSA diffusion across the microtubule pore was investigated using the same MD protocol outlined above, but applied to a version of the microtubule pore with CS covalently attached to Thr220. The best conformation for CS in the latter pore was determined by a conformational search similar to that performed by Buey et al. using Monte Carlo searching with the AMBER\* force field and GBSA/H<sub>2</sub>O solvation model.<sup>203</sup> Thus, the resulting microtubule pore structure was relaxed and subjected to the above-described MD protocol alternating between

constrained and unconstrained MD runs. In these trajectories (**Figure 6**), the diffusion of the MSAs is blocked by CS floating in the center of the pore. This presents a much larger barrier to diffusion across the microtubule pore than the native microtubule pore. Both PTX and hexaflutax are blocked from passing through the pore in the 200 ps simulation. Epothilone is able to traverse the pore in 80 ps, twice the time required for passage through the native microtubule pore. The results are consistent with a previous competitive binding assay in which MSA binding was substantially reduced if the MSA was added subsequent to the addition of CS.<sup>203</sup>

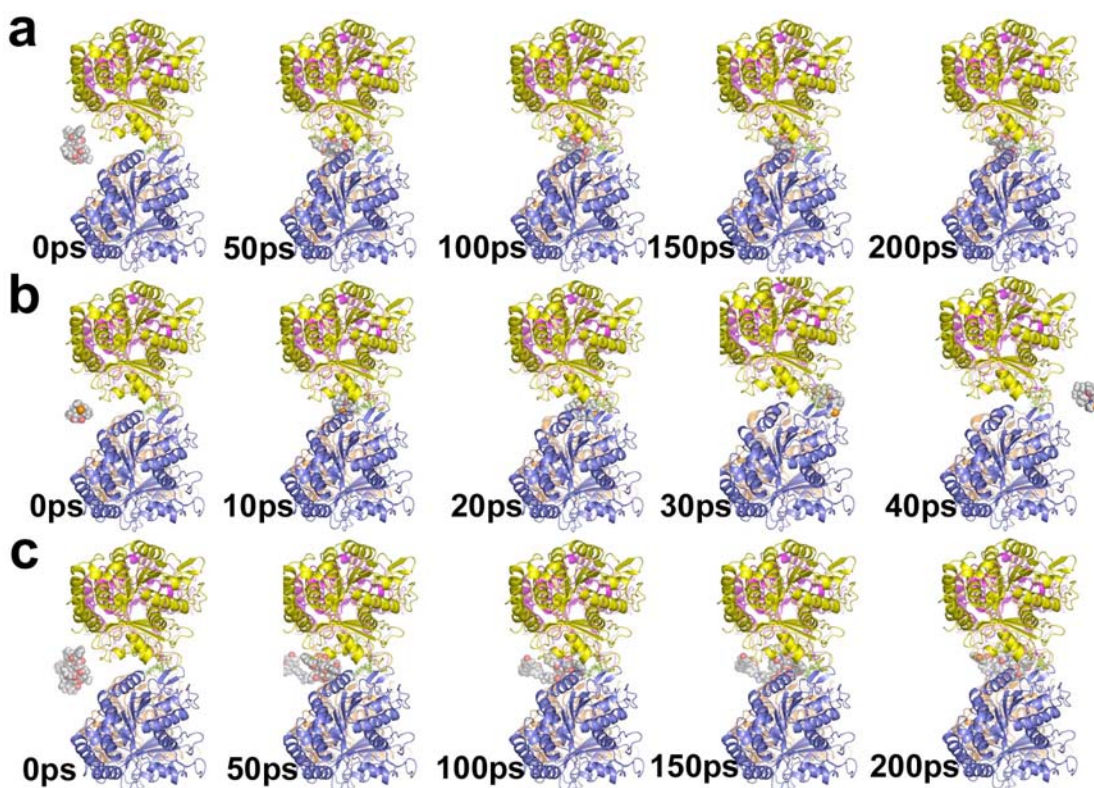


**Figure 6:** Molecular dynamics (MD) trajectories of microtubule stabilizing agents (MSAs) through the cyclostreptin-attached microtubule pore, viewed as in **Figure 5**. Cyclostreptin (CS) and Thr220 are shown as green sticks. **(a)** Paclitaxel (PTX) trajectory. PTX does not escape in 200 ps. **(b)** Epothilone trajectory. Epothilone is blocked until 80 ps. **(c)** Hexaflutax trajectory. Hexaflutax is also blocked during the simulation.

### 1.3.3 CS labels Thr220 due to its exposure in the microtubule pore

Many other potential nucleophiles are present in the microtubule, but CS selectively labels only Thr220 and Asn228. CS labeling at residues in the taxane site could in principle result from a proximity effect caused by classical noncovalent ligand binding at this site (**Figure 3, d and g**). If there is no defined docking mode in the microtubule pore, however, no such proximity effect can operate to cause reaction with Thr220. To investigate how CS might interact with the microtubule pore, the previously described MD protocol was once again applied to the native microtubule pore, this time

with CS as the ligand. Force field based MD does not allow inquiry into reaction mechanisms, but can be used to understand molecular geometry and the potential intermolecular interactions that may lead to chemical reaction. In this case, the trajectory of CS through the pore positions the drug in an interesting alignment with Thr220 after 38 ps of simulation (**Figure 7**). The Thr220 side chain is directed to the center of the pore and is located at its narrowest point. Thus, as CS travels to the microtubule lumen, it approaches Thr220 closely, exposing its electrophilic  $\alpha,\beta$ -unsaturated lactone proximal (3.8 Å) to the residue's hydroxyl group. Another feature that may facilitate reaction with Thr220 is the proximity (3.4 Å) of Lys326 with the carbonyl oxygen of CS's  $\alpha,\beta$ -unsaturated lactone. A positive charge at this position will stabilize the oxyanion intermediate resulting from nucleophilic attack by the Thr220 hydroxyl, lowering the barrier to reaction.

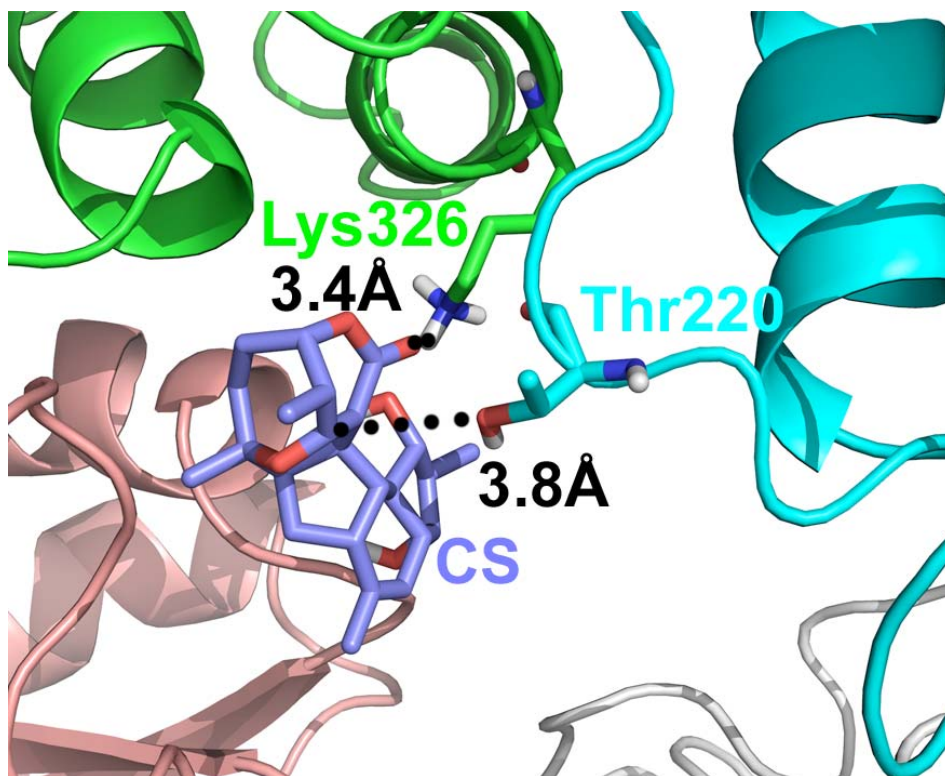


**Figure 7:** Snapshot of cyclostreptin (CS) after 38 ps of molecular dynamics (MD) through the microtubule pore. CS, Thr220, and Lys326 are shown as sticks. The hydroxyl oxygen of Thr220 is positioned 3.8 Å from the electrophilic  $\alpha,\beta$ -unsaturated lactone of CS. The positive charge of Lys326 could stabilize the resulting oxanion intermediate and is positioned 3.4 Å from the carbonyl oxygen of CS's lactone.

## 1.4 Molecular dynamics simulation of the *apo*-tubulin dimer

### 1.4.1 CS binding at the taxane site is blocked by the M-loop

As described previously,<sup>209</sup> simulations of the tubulin dimer in explicit aqueous solvent predict variation in the conformation of the M-loop as a function of the structure of the compound bound at the taxane binding site (**Figure 8**). The displacement of the M-loop from its initial position also occurs in the unliganded protein simulation (**Figure 8b**). For the latter, the M-loop shifts over the taxane binding site, covers the hydrophobic pocket (**Figure 8, c-d**) and presents a more hydrophilic surface to solvent. Since these

simulations take place in the absence of lateral interactions or constraints that might mimic those present in an assembled microtubule, this movement of the M-loop is predicted to reflect the actual conformation of a free dimer in solution. The predicted native tubulin M-loop conformation prevents access to the taxane binding site and provides a structural hypothesis for both the lack of PTX binding to the free tubulin dimer and the availability of Thr220 to binding by CS. Thr220 has 72 Å<sup>2</sup> total of solvent-exposed surface area, more than all other threonines in the *apo*-tubulin dimer. Thr335 shows the second-most with 70 Å<sup>2</sup>; all others are less than 70 Å<sup>2</sup>. This accessibility could account for the selective labeling in the free dimer state.

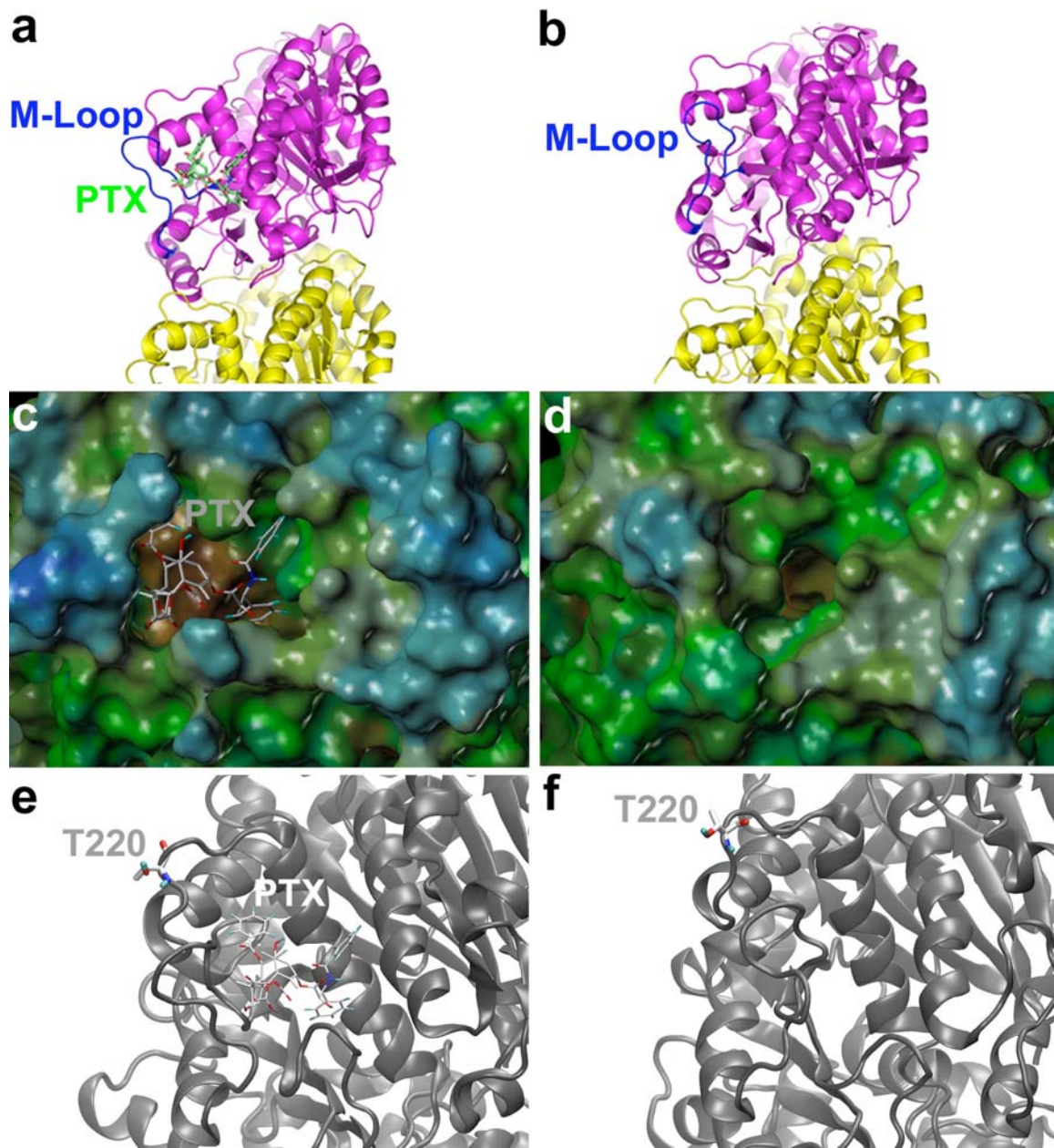


**Figure 8** (previous page): Displacement of M-loop and exposure of Thr220 in simulations of the free tubulin dimer. **(a)** With paclitaxel (PTX) bound, the M-loop is stabilized in a conformation able to form lateral interactions with a dimer in an adjacent protofilament. **(b)** In *apo*-tubulin dimer, the M-loop occludes the hydrophobic taxane binding site, preventing PTX and cyclostreptin (CS) from binding at this site. **(c)** Lipophilic character of the solvent accessible surface in the PTX bound, and **(d)** *apo*-tubulin dimer. Displacement of the M-loop covers the hydrophobic pocket and presents a more hydrophilic surface to solvent. **(e)** Position of Thr220 in PTX bound and **(f)** *apo*-tubulin dimer. In both simulations, Thr220 remains exposed and capable of reaction with CS.

### 1.4.2 Thr220 remains exposed in *apo*- and MSA-bound tubulin dimer

Comparison of the MD simulations of unliganded tubulin and the PTX-bound complex reveals that, in spite of the displacement of the M-loop in the latter, the exposure of Thr220 remains unchanged (**Figure 8, e-f**). In both simulations the residue side chain is directed away from the protein and into solvent; the two side chains found in very similar locations in both situations. The presence of an MSA within the binding site is predicted to neither modify the position nor block the solvent exposure of the residue. These observations imply that the accessibility of Thr220 to modification by CS should not be altered by conformational changes in the M-loop of the free tubulin dimer, nor changed by binding of compounds within the taxane binding pocket under free dimer conditions.

## 1.5 Conclusions on the nature of MSA binding to microtubules

### 1.5.1 Weak microtubule polymerization by CS is explained by its limited effect on the M-loop

Although CS binds covalently to both free dimer and polymerized tubulin, its effect on microtubule polymerization is weak compared to other MSAs. This phenomenon can be understood by recalling that certain bridged analogs of PTX can

enhance microtubule polymerization without increasing binding affinity, if the ligand exerts a stabilizing effect on the M-loop to provide more effective lateral interactions between protofilaments.<sup>209</sup> While CS binding at the taxane site might affect the M-loop conformation and increase microtubule formation, Thr220 labeling is not positioned to modify the M-loop. Furthermore, CS has little ability to induce polymerization at lower temperatures (< 20°C) and less affinity relative to PTX for the taxane site at 4°C versus 30°C.<sup>202</sup> This is consistent with less diffusion across the pore at lower temperature, fewer CS molecules binding to the taxane site, and less stabilization of the M-loop. Bai et al. found that a radioactive analog of CS reacts almost immediately after interacting with microtubules,<sup>204</sup> suggesting most of the labeling occurs at Thr220 with little effect on microtubule polymerization. Experiments with tubulin and the radioactive analog of CS showed that both at 0°C, in the absence of assembly, and at 20°C, prior to the onset of assembly, covalent reaction occurs only at Thr220 in tubulin dimers or small oligomers.<sup>204</sup> Consistent with these results, our simulations suggest the M-loop blocks the taxane site in tubulin dimers, although Thr220 remains exposed. These results again infer that binding at Thr220 does not effect microtubule polymerization. It seems that only under conditions where tubulin can form higher-order oligomers can CS bind the taxane site and increase polymerization.

### 1.5.2 CS labeling of Asn228 could occur through migration during MS

The binding of CS in the taxane binding site is further complicated by the fact that labeling occurs at Asn228. Primary amides such as the side chain of asparagine are poor nucleophiles. It is difficult to understand how labeling at this residue can occur. It is also evident that Asn228 is not available for interaction with CS when docked in the taxane

pocket. Asn228 is located on Helix 7, a secondary structure element forming part of the site, but its side chain points in the opposite direction, forming a bifurcated hydrogen bond with GDP (**Figure 9**). We suspect that labeling of Asn228 is an artifact arising from the tandem MS/MS peptide fragmentation conditions. An effective nucleophile, His229, is adjacent to Asn228 and resides within the taxane binding site. Docking of CS into the site revealed several poses which situate the  $\alpha,\beta$ -unsaturated lactone near the His229 side chain (**Figure 9**).

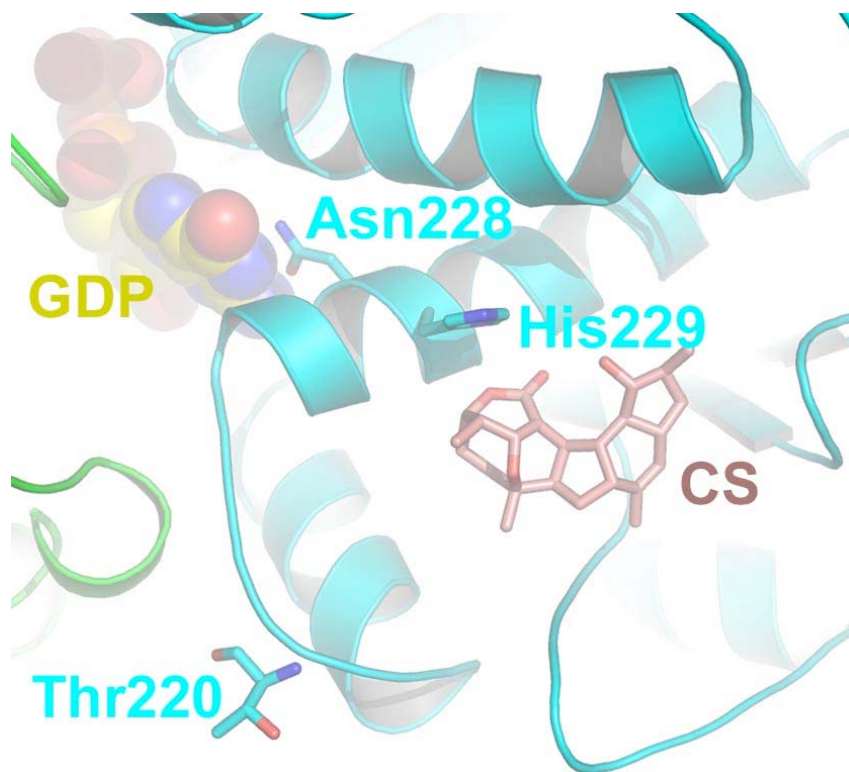
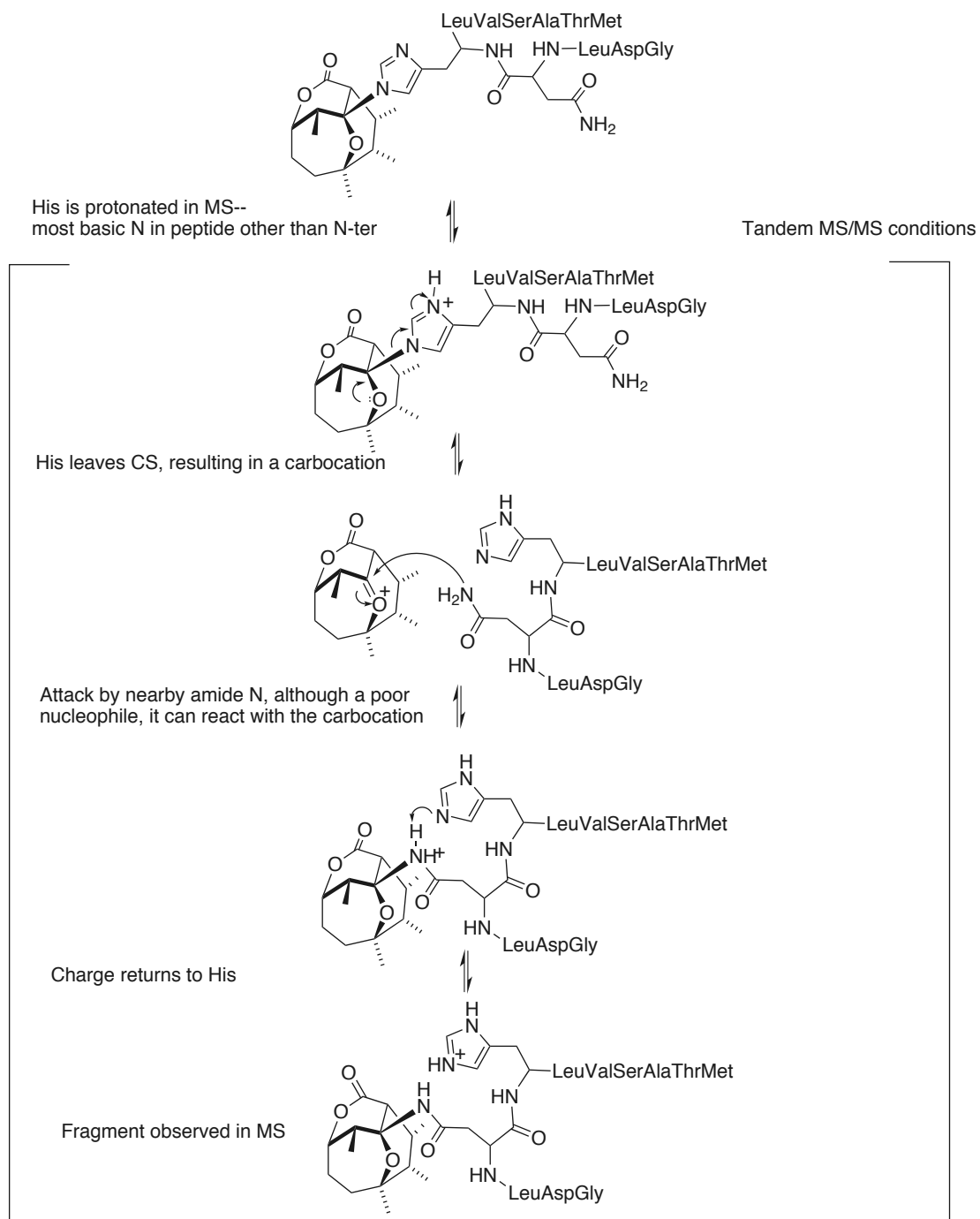


**Figure 9:** One of the docking poses which places cyclostreptin (CS) in the taxane site with its electrophilic  $\alpha,\beta$ -unsaturated lactone positioned near the nucleophilic nitrogen of His229. Thr220 is shown on the nearby H6-H7 loop. Asn228 is also shown with its bifurcated hydrogen bond to the guanosine ring of GDP.

It is therefore proposed that His229 may be the actual site of CS labeling, followed by a molecular rearrangement that transfers CS to Asn228 while the peptide fragment corresponding to peak 6 is ionized in the mass spectrometer. Peptide rearrangements occurring under fragmentation conditions are well known, such as N- and C- terminal rearrangements,<sup>218, 219</sup> loss of internal amino acids,<sup>219</sup> and scrambling of peptide sequences.<sup>220</sup> Complex rearrangements also occur in modified peptides such as cyclic pyoverdins,<sup>221</sup> as well as in carbohydrates,<sup>222</sup> and glycoconjugates.<sup>223</sup> By analyzing total ion chromatograms of six overlapping peptides resulting from chymotrypsin digestion, Buey et al. narrowed the two sites of CS attachment to two sequences: 220-

TTPTYGDLNHL-230 (peak 5) and 228-NHLVSATM-235 (peak 4).<sup>203</sup> The specifically labeled residues were determined by peptide fragmentation of peaks 2 and 5, revealing Thr220 as the first site of attachment. The second site was determined by fragmentation of peak 6, corresponding to residues 225-GDLNHLVSATM-235. This result suggested Asn228 as the site of attachment based on the b4 fragment gaining the mass of CS. Conceivably, the experimental outcome arose by migration of CS from His229 to Asn228 prior to the b4 fragmentation of the peptide (**Figure 10**). Migration may be thermodynamically driven by steric hindrance around the CS quaternary center caused by His229/imidazole attachment to CS versus the less rigid and more accessible primary amide of Asn228. Asp226 is another potential nucleophile directed into the taxane binding site, but this residue can be excluded as the peak 4 peptide in the total ion chromatogram does not contain Asp226, although it does possess the additional mass of CS. If labeling occurs at His229, the action of CS can be interpreted in the context of other taxane-site ligands: binding at a common site and influencing the conformation of the M-loop to favor productive interactions with neighboring protofilaments.

Peak 6 peptide/chymotrypsin cleavage sites, CS labeled at His.  
Sequence is GDLNHLVSATM



Asn is only primary amide in peptide--CS attachment to amide NH may be more stable than to the N of the His imidazole ring due to steric congestion at this quaternary center.

**Figure 10:** Proposed mechanism of CS migration in the peak 6 peptide from His229 to Asn228 under tandem MS/MS conditions.

### 1.5.3 Two activation energies for CS binding to tubulin are unlikely

Bai et al. reported that two reactions occur in the binding of the CS radioactive analog to microtubules with two separate activation energies, 27 kcal/mol and 8 kcal/mol, the lower of which was surprisingly observed at higher temperatures. Since this unusual phenomenon is not consistent with two competing reactions, it was explained in terms of consecutive reactions occurring at similar rates but with different activation energies; namely, binding followed by covalent reaction.<sup>204</sup> In order for such a rate reversal to be observed, however, the rate of the lower activation process would need to increase  $10^{13}$ -fold over the higher energy process, a highly unlikely event over a 20 °C change in temperature.<sup>224</sup> Typical solution-phase organic reactions at room temperature exhibit activation energies of 12-27 kcal/mol.<sup>225-230</sup> By contrast, activation energies for ligand binding fall in the considerably lower 7-15 kcal/mol window. Thus, binding of the Kazal peptide to trypsin has been measured to be 8.6 kcal/mol.<sup>231</sup> Likewise, Arrhenius plots based on published data for small molecule inhibitors of carbonic anhydrase II and the human adenosine A<sub>1</sub> receptor reveal activation energies for binding from 7-11 kcal/mol.<sup>232, 233</sup> Addition of an allosteric modulator to the human adenosine A<sub>1</sub> receptor increases the activation energy to 14.9 kcal/mol.<sup>232</sup> Finally, cyclostreptin itself is isolated and purified in methanol<sup>199</sup> and is stable in methanol and ethanol for extended periods of time at room temperature.<sup>201</sup> Consequently, the activation barrier to conjugate addition by primary alcohols, and presumably secondary alcohols like Thr, is certainly well above 20 kcal/mol. These results seem at odds with the rather high barrier for binding and low barrier for reaction observed by Bia et al.<sup>204</sup> Further kinetic experiments are needed to clarify these issues.

#### 1.5.4 Implications for the design of new MSAs

Mysteries still surround CS and its activity, such as why it reacts with selected nucleophilic residues in tubulin, but can stably be stored in ethanol,<sup>201</sup> or how the poor nucleophile Asn228 ends up being labeled by CS.<sup>203</sup> However, the suggestion of a second, low-affinity binding site for taxane ligands seems an artifact of their slow diffusion across the pore. And while the prospect of a new druggable site in tubulin is welcome, targeting the microtubule pore might well be a futile exercise.

## References

1. Harrison, S., Viral membrane fusion. *Nat. Struct. Mol. Biol.* **2008**, *15* (7), 690-698.
2. Earp, L. J.; Delos, S. E.; Park, H. E.; White, J. M., The many mechanisms of viral membrane fusion proteins. *Curr. Top. Microbiol.* **2004**, *285*, 25-66.
3. Kuzmin, P. I.; Zimmerberg, J.; Chizmadzhev, Y. A.; Cohen, F. S., A quantitative model for membrane fusion based on low-energy intermediates. *Proc. Natl. Acad. Sci. USA* **2001**, *98* (13), 7235-7240.
4. Chernomordik, L. V.; Zimmerberg, J.; Kozlov, M. M., Membranes of the world unite! *J. Cell Biol.* **2006**, *175* (2), 201-207.
5. Lamb, R. A.; Jardetzky, T. S., Structural basis of viral invasion: lessons from paramyxovirus F. *Curr. Opin. Struct. Biol.* **2007**, *17* (4), 427-436.
6. Kielian, M.; Rey, F. A., Virus membrane-fusion proteins: more than one way to make a hairpin. *Nat. Rev. Microbiol.* **2006**, *4* (1), 67-76.
7. Russell, C. J.; Kantor, K. L.; Jardetzky, T. S.; Lamb, R. A., A dual-functional paramyxovirus F protein regulatory switch segment: activation and membrane fusion. *J. Cell Biol.* **2003**, *163* (2), 363-374.
8. Weissenhorn, W.; Hinz, A.; Gaudin, Y., Virus membrane fusion. *FEBS Lett.* **2007**, *581* (11), 2150-2155.
9. Lamb, R. A.; Paterson, R. G.; Jardetzky, T. S., Paramyxovirus membrane fusion: Lessons from the F and HN atomic structures. *Virology* **2006**, *344* (1), 30-37.

10. Colman, P. M.; Lawrence, M. C., The structural biology of type I viral membrane fusion. *Nat. Rev. Mol. Cell Biol.* **2003**, *4* (4), 309-319.
11. Yin, H. S.; Paterson, R. G.; Wen, X. L.; Lamb, R. A.; Jardetzky, T. S., Structure of the uncleaved ectodomain of the paramyxovirus (hPIV3) fusion protein. *Proc. Natl. Acad. Sci. USA* **2005**, *102* (26), 9288-9293.
12. Ludwig, K.; Schade, B.; Böttcher, C.; Korte, T.; Ohlwein, N.; Baljinnyam, B.; Veit, M.; Herrmann, A., Electron cryomicroscopy reveals different F1+F2 protein states in intact parainfluenza virions. *J. Virol.* **2008**, *82* (7), 3775-3781.
13. Schowalter, R. M.; Chang, A.; Robach, J. G.; Buchholz, U. J.; Dutch, R. E., Low-pH triggering of human metapneumovirus fusion: essential residues and importance in entry. *J. Virol.* **2009**, *83* (3), 1511-1522.
14. Techaarpornkul, S.; Barretto, N.; Peeples, M. E., Functional analysis of recombinant respiratory syncytial virus deletion mutants lacking the small hydrophobic and/or attachment glycoprotein gene. *J. Virol.* **2001**, *75* (15), 6825-6834.
15. Wilson, I. A.; Skehel, J. J.; Wiley, D. C., Structure of the hemagglutinin membrane glycoprotein of influenza at 3Å resolution. *Nature* **1981**, *289* (5796), 366-373.
16. Bullough, P. A.; Hughson, F. M.; Skehel, J. J.; Wiley, D. C., Structure of influenza haemagglutinin at the pH of membrane fusion. *Nature* **1994**, *371* (6492), 37-43.
17. Chen, J.; Lee, K. H.; Steinhauer, D. A.; Stevens, D. J.; Skehel, J. J.; Wiley, D. C., Structure of the hemagglutinin precursor cleavage site, a determinant of influenza pathogenicity and the origin of the labile conformation. *Cell* **1998**, *95* (3), 409-417.
18. Chen, L.; Gorman, J. J.; McKimm-Breschkin, J.; Lawrence, L. J.; Tulloch, P. A.; Smith, B. J.; Colman, P. M.; Lawrence, M. C., The structure of the fusion glycoprotein of

Newcastle disease virus suggests a novel paradigm for the molecular mechanism of membrane fusion. *Structure* **2001**, *9* (3), 255-266.

19. Yin, H. S.; Wen, X.; Paterson, R. G.; Lamb, R. A.; Jardetzky, T. S., Structure of the parainfluenza virus 5 F protein in its metastable, prefusion conformation. *Nature* **2006**, *439* (7072), 38-44.
20. Sauter, N. K.; Hanson, J. E.; Glick, G. D.; Brown, J. H.; Crowther, R. L.; Park, S. J.; Skehel, J. J.; Wiley, D. C., Binding of Influenza-Virus Hemagglutinin to Analogs of Its Cell-Surface Receptor, Sialic-Acid - Analysis by Proton Nuclear-Magnetic-Resonance Spectroscopy and X-Ray Crystallography. *Biochemistry* **1992**, *31* (40), 9609-9621.
21. Yao, N. H.; Ledvina, P. S.; Choudhary, A.; Quioco, F. A., Modulation of a salt link does not affect binding of phosphate to its specific active transport receptor. *Biochemistry* **1996**, *35* (7), 2079-2085.
22. DeLano, W. L. *The PyMol Molecular Graphics System*, DeLano Scientific: Palo Alto, CA, 2002.
23. Gibbons, D. L.; Vaney, M. C.; Roussel, A.; Vigouroux, A.; Reilly, B.; Lepault, J.; Kielian, M.; Rey, F. A., Conformational change and protein-protein interactions of the fusion protein of Semliki Forest virus. *Nature* **2004**, *427* (6972), 320-325.
24. Lescar, J.; Roussel, A.; Wien, M. W.; Navaza, J.; Fuller, S. D.; Wengler, G.; Wengler, G.; Rey, F. A., The Fusion glycoprotein shell of Semliki Forest virus: an icosahedral assembly primed for fusogenic activation at endosomal pH. *Cell* **2001**, *105* (1), 137-148.

25. Rey, F. A.; Heinz, F. X.; Mandl, C.; Kunz, C.; Harrison, S. C., The envelope glycoprotein from tick-borne encephalitis virus at 2 Å resolution. *Nature* **1995**, *375* (6529), 291-298.
26. Bressanelli, S.; Stiasny, K.; Allison, S.; Stura, E.; Duquerroy, S.; Lescar, J.; Heinz, F.; Rey, F. A., Structure of a flavivirus envelope glycoprotein in its low-pH-induced membrane fusion conformation. *EMBO J.* **2004**, *23* (4), 728-738.
27. Roussel, A.; Lescar, J.; Vaney, M. C.; Wengler, G.; Wengler, G.; Rey, F. A., Structure and interactions at the viral surface of the envelope protein E1 of Semliki Forest virus. *Structure* **2006**, *14* (1), 75-86.
28. Roche, S.; Albertini, A.; Lepault, J.; Bressanelli, S.; Gaudin, Y., Structures of vesicular stomatitis virus glycoprotein: membrane fusion revisited. In *Cell. Mol. Life Sci.*, 2008; Vol. 65, pp 1716-1728.
29. Roche, S.; Rey, F. A.; Gaudin, Y.; Bressanelli, S., Structure of the prefusion form of the vesicular stomatitis virus glycoprotein G. *Science* **2007**, *315* (5813), 843-848.
30. Roche, S.; Bressanelli, S.; Rey, F. A.; Gaudin, Y., Crystal structure of the low-pH form of the vesicular stomatitis virus glycoprotein G. *Science* **2006**, *313* (5784), 187-191.
31. Wild, C.; Oas, T.; McDanal, C.; Bolognesi, D.; Matthews, T., A synthetic peptide inhibitor of human immunodeficiency virus replication: Correlation between solution structure and viral inhibition. *Proc. Natl. Acad. Sci. USA* **1992**, *89* (21), 10537-10541.
32. Wild, C. T.; Shugars, D. C.; Greenwell, T. K.; McDanal, C. B.; Matthews, T. J., Peptides corresponding to a predictive alpha-helical domain of human immunodeficiency virus type 1 GP41 are potent inhibitors of virus infection. *Proc. Natl. Acad. Sci. USA* **1994**, *91* (21), 9770-9774.

33. Weissenhorn, W.; Dessen, A.; Harrison, S. C.; Skehel, J. J.; Wiley, D. C., Atomic structure of the ectodomain from HIV-1 gp41. *Nature* **1997**, *387* (6631), 426-430.
34. De Clercq, E., HIV-chemotherapy and -prophylaxis: new drugs, leads and approaches. *Int. J. Biochem. Cell Biol.* **2004**, *36* (9), 1800-1822.
35. Bray, B. L., Large-scale manufacture of peptide therapeutics by chemical synthesis. *Nat. Rev. Drug Discov.* **2003**, *2* (7), 587-593.
36. De Clercq, E., Anti-HIV drugs: 25 compounds approved within 25 years after the discovery of HIV. *Int. J. Antimicrob. Ag.* **2009**, *33* (4), 307-320.
37. Frey, G.; Rits-Volloch, S.; Zhang, X.; Schooley, R. T.; Chen, B.; Harrison, S., Small molecules that bind the inner core of gp41 and inhibit HIV envelope-mediated fusion. *Proc. Natl. Acad. Sci. USA* **2006**, *103* (38), 13938-13943.
38. Lin, P. F.; Blair, W.; Wang, T.; Spicer, T.; Guo, Q.; Zhou, N. N.; Gong, Y. F.; Wang, H. G. H.; Rose, R.; Yamanaka, G.; Robinson, B.; Li, C. B.; Fridell, R.; Deminie, C.; Demers, G.; Yang, Z.; Zadjura, L.; Meanwell, N.; Colonno, R., A small molecule HIV-1 inhibitor that targets the HIV-1 envelope and inhibits CD4 receptor binding. *Proc. Natl. Acad. Sci. USA* **2003**, *100* (19), 11013-11018.
39. Chen, B.; Vogan, E. M.; Gong, H. Y.; Skehel, J. J.; Wiley, D. C.; Harrison, S. C., Structure of an unliganded simian immunodeficiency virus gp120 core. *Nature* **2005**, *433* (7028), 834-841.
40. Skehel, J. J.; Wiley, D. C., Receptor binding and membrane fusion in virus entry: The influenza hemagglutinin. *Annu. Rev. Biochem.* **2000**, *69*, 531-569.
41. Bodian, D. L.; Yamasaki, R. B.; Buswell, R. L.; Stearns, J. F.; White, J. M.; Kuntz, I. D., Inhibition of the fusion-inducing conformational change of influenza

hemagglutinin by benzoquinones and hydroquinones. *Biochemistry* **1993**, 32 (12), 2967-2978.

42. Hoffman, L. R.; Kuntz, I. D.; White, J. M., Structure-based identification of an inducer of the low-pH conformational change in the influenza virus hemagglutinin: Irreversible inhibition of infectivity. *J. Virol.* **1997**, 71 (11), 8808-8820.

43. Modis, Y., How influenza virus is locked out of the cell. *Proc. Natl. Acad. Sci. USA* **2008**, 105 (48), 18647-18648.

44. Russell, R. J.; Kerry, P. S.; Stevens, D. J.; Steinhauer, D. A.; Martin, S. R.; Gamblin, S. J.; Skehel, J. J., Structure of influenza hemagglutinin in complex with an inhibitor of membrane fusion. *Proc. Natl. Acad. Sci. USA* **2008**, 105 (46), 17736-17741.

45. Luo, G. X.; Colonna, R.; Krystal, M., Characterization of a hemagglutinin-specific inhibitor of influenza A virus. *Virology* **1996**, 226 (1), 66-76.

46. Cianci, C.; Yu, K. L.; Dischino, D. D.; Harte, W.; Deshpande, M.; Luo, G. X.; Colonna, R. J.; Meanwell, N. A.; Krystal, M., pH-dependent changes in photoaffinity labeling patterns of the H1 influenza virus hemagglutinin by using an inhibitor of viral fusion. *J. Virol.* **1999**, 73 (3), 1785-1794.

47. Luo, G. X.; Torri, A.; Harte, W. E.; Danetz, S.; Cianci, C.; Tiley, L.; Day, S.; Mullaney, D.; Yu, K. L.; Ouellet, C.; Dextraze, P.; Meanwell, N.; Colonna, R.; Krystal, M., Molecular mechanism underlying the action of a novel fusion inhibitor of influenza A virus. *J. Virol.* **1997**, 71 (5), 4062-4070.

48. Yu, K. L.; Torri, A. F.; Luo, G. X.; Cianci, C.; Grant-Young, K.; Danetz, S.; Tiley, L.; Krystal, M.; Meanwell, N. A., Structure-activity relationships for a series of

thiobenzamide influenza fusion inhibitors derived from 1,3,3-trimethyl-5-hydroxy-cyclohexylmethylamine. *Bioorg. Med. Chem. Lett.* **2002**, *12* (23), 3379-3382.

49. Cianci, C.; Genovesi, E. V.; Lamb, L.; Medina, I.; Yang, Z.; Zadjura, L.; Yang, H.; D'Arienzo, C.; Sin, N.; Yu, K. L.; Combrink, K.; Li, Z. F.; Colonno, R.; Meanwell, N.; Clark, J.; Krystal, M., Oral efficacy of a respiratory syncytial virus inhibitor in rodent models of infection. *Antimicrob. Agents Ch.* **2004**, *48* (7), 2448-2454.

50. Cianci, C.; Meanwell, N.; Krystal, M., Antiviral activity and molecular mechanism of an orally active respiratory syncytial virus fusion inhibitor. *J. Antimicro. Chemother.* **2005**, *55* (3), 289-292.

51. Cianci, C.; Yu, K. L.; Combrink, K.; Sin, N.; Pearce, B.; Wang, A.; Civiello, R.; Voss, S.; Luo, G. X.; Kadow, K.; Genovesi, E. V.; Venables, B.; Gulgeze, H.; Trehan, A.; James, J.; Lamb, L.; Medina, I.; Roach, J.; Yang, Z.; Zadjura, L.; Colonno, R.; Clark, J.; Meanwell, N.; Krystal, M., Orally active fusion inhibitor of respiratory syncytial virus. *Antimicrob. Agents Ch.* **2004**, *48* (2), 413-422.

52. Wang, X. A.; Cianci, C. W.; Yu, K. L.; Combrink, K. D.; Thuring, J. W.; Zhang, Y.; Civiello, R. L.; Kadow, K. F.; Roach, J.; Li, Z.; Langley, D. R.; Krystal, M.; Meanwell, N. A., Respiratory syncytial virus fusion inhibitors. Part 5: Optimization of benzimidazole substitution patterns towards derivatives with improved activity. *Bioorg. Med. Chem. Lett.* **2007**, *17* (16), 4592-4598.

53. Yu, K. L.; Sin, N.; Civiello, R. L.; Wang, X. A.; Combrink, K. D.; Gulgeze, H. B.; Venables, B. L.; Wright, J. J. K.; Dalterio, R. A.; Zadjura, L.; Marino, A.; Dando, S.; D'Arienzo, C.; Kadow, K. F.; Cianci, C. W.; Li, Z.; Clarke, J.; Genovesi, E. V.; Medina, I.; Lamb, L.; Colonno, R. J.; Yang, Z.; Krystal, M.; Meanwell, N. A., Respiratory

syncytial virus fusion inhibitors. Part 4: Optimization for oral bioavailability. *Bioorg. Med. Chem. Lett.* **2007**, *17* (4), 895-901.

54. Yu, K. L.; Wang, X. D. A.; Civiello, R. L.; Trehan, A. K.; Pearce, B. C.; Yin, Z. W.; Combrink, K. D.; Gulgeze, H. B.; Zhang, Y.; Kadow, K. F.; Cianci, C. W.; Clarke, J.; Genovesi, E. V.; Medina, I.; Lamb, L.; Wyde, P. R.; Krystal, M.; Meanwell, N. A., Respiratory syncytial virus fusion inhibitors. Part 3: Water-soluble benzimidazol-2-one derivatives with antiviral activity in vivo. *Bioorg. Med. Chem. Lett.* **2006**, *16* (5), 1115-1122.

55. Yu, K. L.; Zhang, Y.; Civiello, R. L.; Kadow, K. F.; Cianci, C.; Krystal, M.; Meanwell, N. A., Fundamental structure-activity relationships associated with a new structural class of respiratory syncytial virus inhibitor. *Bioorg. Med. Chem. Lett.* **2003**, *13* (13), 2141-2144.

56. Yu, K. L.; Zhang, Y.; Civiello, R. L.; Trehan, A. K.; Pearce, B. C.; Yin, Z. W.; Combrink, K. D.; Gulgeze, H. B.; Wang, X. D. A.; Kadow, K. F.; Cianci, C. W.; Krystal, M.; Meanwell, N. A., Respiratory syncytial virus inhibitors. Part 2: Benzimidazol-2-one derivatives. *Bioorg. Med. Chem. Lett.* **2004**, *14* (5), 1133-1137.

57. Andries, K.; Moeremans, M.; Gevers, T.; Willebrords, R.; Sommen, C.; Lacrampe, J.; Janssens, F.; Wyde, P. R., Substituted benzimidazoles with nanomolar activity against respiratory syncytial virus. *Antiviral Res.* **2003**, *60* (3), 209-219.

58. Bonfanti, J.; Doublet, F.; Fortin, J.; Lacrampe, J.; Guillemont, J.; Muller, P.; Queguiner, L.; Arnoult, E.; Gevers, T.; Janssens, P.; Szel, H.; Willebrords, R.; Timmerman, P.; Wuyts, K.; Janssens, F.; Sommen, C.; Wigerinck, P.; Andries, K., Selection of a respiratory syncytial virus fusion inhibitor clinical candidate, part 1:

Improving the pharmacokinetic profile using the structure-property relationship. *J. Med. Chem.* **2007**, *50* (19), 4572-4584.

59. Bonfanti, J.; Meyer, C.; Doublet, F.; Fortin, J.; Muller, P.; Queguiner, L.; Gevers, T.; Janssens, P.; Szel, H.; Willebrords, R.; Timmerman, P.; Wuyts, K.; van Remoortere, P.; Janssens, F.; Wigerinck, P.; Andries, K., Selection of a respiratory syncytial virus fusion inhibitor clinical candidate. 2. Discovery of a morpholinopropylaminobenzimidazole derivative (TMC353121). *J. Med. Chem.* **2008**, *51* (4), 875-896.

60. Douglas, J. L.; Panis, M. L.; Ho, E.; Lin, K. Y.; Krawczyk, S. H.; Grant, D. M.; Cai, R.; Swaminathan, S.; Chen, X. W.; Cihlar, T., Small molecules VP-14637 and JNJ-2408068 inhibit respiratory syncytial virus fusion by similar mechanisms. *Antimicrob. Agents Ch.* **2005**, *49* (6), 2460-2466.

61. Douglas, J. L.; Panis, M. L.; Ho, E.; Lin, K. Y.; Krawczyk, S. H.; Grant, D. M.; Cai, R.; Swaminathan, S.; Cihlar, T., Inhibition of respiratory syncytial virus fusion by the small molecule VP-14637 via specific interactions with F protein. *J. Virol.* **2003**, *77* (9), 5054-5064.

62. Morton, C. J.; Cameron, R.; Lawrence, L. J.; Lin, B.; Lowe, M.; Luttick, A.; Mason, A.; McKimm-Breschkin, J.; Parker, M. W.; Ryan, J.; Smout, M.; Sullivan, J.; Tucker, S. P.; Young, P. R., Structural characterization of respiratory syncytial virus fusion inhibitor escape mutants: homology model of the F protein and a syncytium formation assay. *Virology* **2003**, *311* (2), 275-288.

63. Cianci, C.; Langley, D. R.; Dischino, D. D.; Sun, Y.; Yu, K. L.; Stanley, A.; Roach, J.; Li, Z.; Dalterio, R.; Colonno, R.; Meanwell, N. A.; Krystal, M., Targeting a

binding pocket within the trimer-of-hairpins: small-molecule inhibition of viral fusion.

*Proc. Natl. Acad. Sci. USA* **2004**, *101* (42), 15046-15051.

64. Dabbagh, A.; Gacic-Dobo, M.; Wolfson, L.; Featherstone, D.; Strebel, P.; Okwo-Bele, J. M.; Hoekstra, E.; Salama, P.; Wassilak, S.; Uzicanin, A., Progress in global measles control and mortality reduction, 2000-2006 (Reprinted from MMWR, vol 56, pg 1237-1241, 2007). *JAMA* **2008**, *299* (4), 400-402.

65. Jansen, V. A. A.; Stollenwerk, N.; Jensen, H. J.; Ramsay, M. E.; Edmunds, W. J.; Rhodes, C. J., Measles outbreaks in a population with declining vaccine uptake. *Science* **2003**, *301* (5634), 804-804.

66. Moss, W. J.; Griffin, D. E., Global measles elimination. *Nat. Rev. Microbiol.* **2006**, *4* (12), 900-908.

67. Prevention, C. f. D. C. a., Update: Measles - United States, January-July 2008. *Morbidity and Mortality Weekly Report* **2008**, *57*, 893-896.

68. EUVAC.NET Measles surveillance first quarterly report 2008.  
[http://www.euvac.net/graphics/euvac/pdf/2008\\_first.pdf](http://www.euvac.net/graphics/euvac/pdf/2008_first.pdf).

69. EUVAC.NET Measles surveillance second quarterly report 2008.  
[http://www.euvac.net/graphics/euvac/pdf/2008\\_first.pdf](http://www.euvac.net/graphics/euvac/pdf/2008_first.pdf).

70. Kielian, M.; Jungerwirth, S., Mechanisms of enveloped virus entry into cells. *Mol. Biol. Med.* **1990**, *7* (1), 17-31.

71. Dörig, R. E.; Marcil, A.; Chopra, A.; Richardson, C. D., The human CD46 molecule is a receptor for measles virus (Edmonston strain). *Cell* **1993**, *75* (2), 295-305.

72. Manchester, M.; Eto, D. S.; Valsamakis, A.; Liton, P. B.; Fernandez-Muñoz, R.; Rota, P. A.; Bellini, W. J.; Forthal, D. N.; Oldstone, M. B., Clinical isolates of measles virus use CD46 as a cellular receptor. *J. Virol.* **2000**, *74* (9), 3967-3974.
73. Naniche, D.; Varior-Krishnan, G.; Cervoni, F.; Wild, T. F.; Rossi, B.; Rabourdin-Combe, C.; Gerlier, D., Human membrane cofactor protein (CD46) acts as a cellular receptor for measles virus. *J. Virol.* **1993**, *67* (10), 6025-6032.
74. Lamb, R. A.; Kolakofsky, D., Paramyxoviridae: The viruses and their replication. In *Fields Virology*, 4th ed.; Knipe, D. M.; Howley, P. M., Eds. Lippincott Williams & Wilkins: Philadelphia, 2001.
75. Plemper, R. K.; Lakdawala, A. S.; Gernert, K. M.; Snyder, J. P.; Compans, R. W., Structural features of paramyxovirus F protein required for fusion initiation. *Biochemistry* **2003**, *42* (22), 6645-6655.
76. Plemper, R. K.; Erlandson, K. J.; Lakdawala, A. S.; Sun, A.; Prussia, A.; Boonsombat, J.; Aki-Sener, E.; Yalcin, I.; Yildiz, I.; Temiz-Arpaci, O.; Tekiner, B.; Liotta, D. C.; Snyder, J. P.; Compans, R. W., A target site for template-based design of measles virus entry inhibitors. *Proc. Natl. Acad. Sci. U. S. A.* **2004**, *101* (15), 5628-5633.
77. Plemper, R. K.; Compans, R. W., Mutations in the putative HR-C region of the measles virus F-2 glycoprotein modulate syncytium formation. *J. Virol.* **2003**, *77* (7), 4181-4190.
78. Mathews, J. M.; Young, T. F.; Tucker, S. P.; Mackay, J. P., The core of the respiratory syncytial virus fusion protein is a trimeric coiled coil. *J. Virol.* **2000**, *74* (13), 5911-5920.

79. Baker, K. A.; Dutch, R. E.; Lamb, R. A.; Jardetzky, T. S., Structural basis for paramyxovirus-mediated membrane fusion. *Mol. Cell* **1999**, *3* (3), 309-319.
80. Plemper, R. K.; Doyle, J.; Sun, A. M.; Prussia, A.; Cheng, L. T.; Rota, P. A.; Liotta, D. C.; Snyder, J. P.; Compans, R. W., Design of a small-molecule entry inhibitor with activity against primary measles virus strains. *Antimicrob. Agents Chemother.* **2005**, *49* (9), 3755-3761.
81. Sun, A. M.; Prussia, A.; Zhan, W. Q.; Murray, E. E.; Doyle, J.; Cheng, L. T.; Yoon, J. J.; Radchenko, E. V.; Palyulin, V. A.; Compans, R. W.; Liotta, D. C.; Plemper, R. K.; Snyder, J. P., Nonpeptide inhibitors of measles virus entry. *J. Med. Chem.* **2006**, *49* (17), 5080-5092.
82. Halgren, T. A., Merck molecular force field. 2. MMFF94 van der Waals and electrostatic parameters for intermolecular interactions. *J. Comput. Chem.* **1996**, *17* (5-6), 520-552.
83. Halgren, T. A., Merck molecular force field. 3. Molecular geometries and vibrational frequencies for MMFF94. *J. Comput. Chem.* **1996**, *17* (5-6), 553-586.
84. Halgren, T. A., Merck molecular force field. 1. Basis, form, scope, parameterization, and performance of MMFF94. *J. Comput. Chem.* **1996**, *17* (5-6), 490-519.
85. Connolly, M. L., Analytical molecular surface calculation. *J. Appl. Crystallogr.* **1983**, *16* (OCT), 548-558.
86. Connolly, M. L., Solvent-accessible surfaces of proteins and nucleic acids. *Science* **1983**, *221* (4612), 709-713.

87. Powell, M. J. D., Restart procedures for the conjugate gradient method. *Math. Program.* **1977**, *12* (2), 241-254.
88. Chambers, C. C.; Hawkins, G. D.; Cramer, C. J.; Truhlar, D. G., Model for aqueous solvation based on class IV atomic charges and first solvation shell effects. *J. Phys. Chem.* **1996**, *100* (40), 16385-16398.
89. Stewart, J. J. P., Optimization of parameters for semiempirical methods. 2. Applications. *J. Comput. Chem.* **1989**, *10* (2), 221-264.
90. Derdeyn, C. A.; Decker, J. M.; Sfakianos, J. N.; Wu, X. Y.; O'Brien, W. A.; Ratner, L.; Kappes, J. C.; Shaw, G. M.; Hunter, E., Sensitivity of human immunodeficiency virus type 1 to the fusion inhibitor T-20 is modulated by coreceptor specificity defined by the V3 loop of gp120. *J. Virol.* **2000**, *74* (18), 8358-8367.
91. Heil, M. L.; Decker, J. M.; Sfakianos, J. N.; Shaw, G. M.; Hunter, E.; Derdeyn, C. A., Determinants of human immunodeficiency virus type 1 baseline susceptibility to the fusion inhibitors enfuvirtide and T-649 reside outside the peptide interaction site. *J. Virol.* **2004**, *78* (14), 7582-7589.
92. Doyle, J.; Prussia, A.; White, L. K.; Sun, A. M.; Liotta, D. C.; Snyder, J. P.; Compans, R. W.; Plemper, R. K., Two domains that control prefusion stability and transport competence of the measles virus fusion protein. *J. Virol.* **2006**, *80* (3), 1524-1536.
93. Zhao, X.; Singh, M.; Malashkevich, V. N.; Kim, P. S., Structural characterization of the human respiratory syncytial virus fusion protein core. *Proc. Natl. Acad. Sci. USA* **2000**, *97* (26), 14172-14177.

94. Chenna, R.; Sugawara, H.; Koike, T.; Lopez, R.; Gibson, T. J.; Higgins, D. G.; Thompson, J. D., Multiple sequence alignment with the Clustal series of programs. *Nucleic Acids Res.* **2003**, *31* (13), 3497-3500.
95. Schrodinger, LLC. *Prime, version 1.5*, New York, NY, 2005.
96. Vriend, G., What If - A Molecular Modeling And Drug Design Program. *Journal Of Molecular Graphics* **1990**, *8* (1), 52-&.
97. Chan, D. C.; Chutkowski, C. T.; Kim, P. S., Evidence that a prominent cavity in the coiled coil of HIV type 1 gp41 is an attractive drug target. *Proc. Natl. Acad. Sci. USA* **1998**, *95* (26), 15613-15617.
98. Berendsen, H. J. C.; Vandespoel, D.; Vandrunen, R., GROMACS: a message-passing parallel molecular-dynamics implementation. *Comput. Phys. Commun.* **1995**, *91* (1-3), 43-56.
99. Lindahl, E.; Hess, B.; van der Spoel, D., GROMACS 3.0: a package for molecular simulation and trajectory analysis. *J. Mol. Model.* **2001**, *7* (8), 306-317.
100. Jorgensen, W. L.; Tiradorives, J., The Opls Potential Functions For Proteins - Energy Minimizations For Crystals Of Cyclic-Peptides And Crambin. *J. Am. Chem. Soc.* **1988**, *110* (6), 1657-1666.
101. Jorgensen, W. L.; Chandrasekhar, J.; Madura, J. D.; Impey, R. W.; Klein, M. L., Comparison of simple potential functions for simulating liquid water. *J. Chem. Phys.* **1983**, *79* (2), 926-935.
102. Schrodinger, LLC. *QikProp, version 2.5*; New York, NY, 2005.

103. Prussia, A. J.; Plemper, R. K.; Snyder, J. P., Measles virus entry inhibitors: a structural proposal for mechanism of action and the development of resistance. *Biochemistry* **2008**, *47* (51), 13573-13583.
104. Russell, C. J.; Jardetzky, T. S.; Lamb, R. A., Membrane fusion machines of paramyxoviruses: capture of intermediates of fusion. *EMBO J.* **2001**, *20* (15), 4024-4034.
105. Calder, L. J.; González-Reyes, L.; García-Barreno, B.; Wharton, S. A.; Skehel, J. J.; Wiley, D. C.; Melero, J. A., Electron microscopy of the human respiratory syncytial virus fusion protein and complexes that it forms with monoclonal antibodies. *Virology* **2000**, *271* (1), 122-131.
106. Flores, S.; Echols, N.; Milburn, D.; Hespeneide, B.; Keating, K.; Lu, J.; Wells, S.; Yu, E. Z.; Thorpe, M.; Gerstein, M., The database of macromolecular motions: new features added at the decade mark. *Nucleic Acids Res.* **2006**, *34*, D296-D301.
107. Tripos, Inc., Tripos Bookshelf 7.3. 2006.
108. Dunitz, J. D., The Entropic Cost Of Bound Water In Crystals And Biomolecules. *Science* **1994**, *264* (5159), 670-670.
109. Chothia, C., Hydrophobic Bonding And Accessible Surface-Area In Proteins. *Nature* **1974**, *248* (5446), 338-339.
110. Chothia, C., Principles that determine the structure of proteins. *Annu Rev Biochem* **1984**, *53*, 537-72.
111. Chothia, C.; Janin, J., Principles Of Protein-Protein Recognition. *Nature* **1975**, *256* (5520), 705-708.
112. Schrodinger, LLC. *Maestro*, version 8.5, 2008.

113. Reeves, J. D.; Lee, F. H.; Miamidian, J. L.; Jabara, C. B.; Juntilla, M. M.; Doms, R. W., Enfuvirtide resistance mutations: impact on human immunodeficiency virus envelope function, entry inhibitor sensitivity, and virus neutralization. *J. Virol.* **2005**, *79* (8), 4991-4999.
114. Kilby, J. M.; Lalezari, J. P.; Eron, J. J.; Carlson, M.; Cohen, C.; Arduino, R. C.; Goodgame, J. C.; Gallant, J. E.; Volberding, P.; Murphy, R. L.; Valentine, F.; Saag, M. S.; Nelson, E. L.; Sista, P. R.; Dusek, A., The safety, plasma pharmacokinetics, and antiviral activity of subcutaneous enfuvirtide (T-20), a peptide inhibitor of gp41-mediated virus fusion, in HIV-infected adults. *AIDS Res. Hum. Retroviruses* **2002**, *18* (10), 685-693.
115. Munoz-Barroso, I.; Durell, S.; Sakaguchi, K.; Appella, E.; Blumenthal, R., Dilation of the human immunodeficiency virus-1 envelope glycoprotein fusion pore revealed by the inhibitory action of a synthetic peptide from gp41. *J. Cell Biol.* **1998**, *140* (2), 315-323.
116. Lee, J. K.; Prussia, A.; Snyder, J. P.; Plemper, R. K., Reversible inhibition of the fusion activity of measles virus F protein by an engineered intersubunit disulfide bridge. *J. Virol.* **2007**, *81* (16), 8821-8826.
117. Tripos, Inc. *Sybyl 7.2*, St. Louis, MI, 2007.
118. Lovell, S. C.; Word, J. M.; Richardson, J. S.; Richardson, D. C., The penultimate rotamer library. *Proteins* **2000**, *40* (3), 389-408.
119. Schrodinger, LLC. *Macromodel, version 9.5*, New York, NY, 2008.

120. Kaminski, G.; Duffy, E. M.; Matsui, T.; Jorgensen, W. L., Free Energies of Hydration and Pure Liquid Properties of Hydrocarbons from the OPLS All-Atom Model. *J. Phys. Chem.* **1994**, *98* (49), 13077-13082.
121. Kaminski, G. A.; Friesner, R. A.; Tirado-Rives, J.; Jorgensen, W. L., Evaluation and reparametrization of the OPLS-AA force field for proteins via comparison with accurate quantum chemical calculations on peptides. *J. Phys. Chem. B* **2001**, *105* (28), 6474-6487.
122. Still, W. C.; Tempczyk, A.; Hawley, R. C.; Hendrickson, T., Semianalytical treatment of solvation for molecular mechanics and dynamics. *J. Am. Chem. Soc.* **1990**, *112* (16), 6127-6129.
123. Godley, L.; Pfeifer, J.; Steinhauer, D.; Ely, B.; Shaw, G.; Kaufmann, R.; Suchanek, E.; Pabo, C.; Skehel, J. J.; Wiley, D. C.; et al., Introduction of intersubunit disulfide bonds in the membrane-distal region of the influenza hemagglutinin abolishes membrane fusion activity. *Cell* **1992**, *68* (4), 635-45.
124. Schrodinger, LLC. *SiteMap*, version 2.2, New York, NY, 2008.
125. Berendsen, H. J. C.; Postma, J. P. M.; Vangunsteren, W. F.; Dinola, A.; Haak, J. R., Molecular dynamics with coupling to an external bath. *J. Chem. Phys.* **1984**, *81* (8), 3684-3690.
126. Essmann, U.; Perera, L.; Berkowitz, M. L.; Darden, T.; Lee, H.; Pedersen, L. G., A smooth particle mesh Ewald method. *J. Chem. Phys.* **1995**, *103* (19), 8577-8593.
127. Maybridge Organic Chemical Catalog. 2004.
128. Schrodinger, LLC. *LigPrep*, version 2.2, New York, NY, 2008.
129. Schrodinger, LLC. *Virtual Screening Workflow*, New York, NY, 2008.

130. Schrodinger, LLC. *Prime, version 2.0*, New York, NY, 2008.
131. Delaney, J. S., Assessing the ability of chemical similarity measures to discriminate between active and inactive compounds. *Mol. Divers.* **1996**, *1* (4), 217-222.
132. ChemAxon, *Instant JChem, version 2.3*, Budapest, Hungary, 2008.
133. Warren, G.; Andrews, C. W.; Capelli, A.; Clarke, B.; LaLonde, J.; Lambert, M. H.; Lindvall, M.; Nevins, N.; Semus, S. F.; Senger, S.; Tedesco, G.; Wall, I. D.; Woolven, J. M.; Peishoff, C. E.; Head, M. S., A critical assessment of docking programs and scoring functions. *J. Med. Chem.* **2006**, *49* (20), 5912-5931.
134. Lee, J. K.; Prussi, A.; Paal, T.; White, L. K.; Snyder, J. P.; Plemper, R. K., Functional interaction between paramyxovirus fusion and attachment proteins. *J Biol Chem* **2008**, *283* (24), 16561-16572.
135. Colf, L. A.; Juo, Z. S.; Garcia, K. C., Structure of the measles virus hemagglutinin. *Nat. Struct. Mol. Biol.* **2007**, *14* (12), 1227-1228.
136. Crennell, S.; Takimoto, T.; Portner, A.; Taylor, G., Crystal structure of the multifunctional paramyxovirus hemagglutinin-neuraminidase. *Nat. Struct. Biol.* **2000**, *7* (11), 1068-1074.
137. Hashiguchi, T.; Kajikawa, M.; Maita, N.; Takeda, M.; Kuroki, K.; Sasaki, K.; Kohda, D.; Yanagi, Y.; Maenaka, K., Crystal structure of measles virus hemagglutinin provides insight into effective vaccines. *Proc. Natl. Acad. Sci. USA* **2007**.
138. Yuan, P.; Thompson, T. B.; Wurzburg, B. A.; Paterson, R. G.; Lamb, R. A.; Jardetzky, T. S., Structural studies of the parainfluenza virus 5 hemagglutinin-neuraminidase tetramer in complex with its receptor, sialyllactose. *Structure* **2005**, *13* (5), 803-815.

139. Bonaparte, M. I.; Dimitrov, A. S.; Bossart, K. N.; Crameri, G.; Mungall, B. A.; Bishop, K. A.; Choudhry, V.; Dimitrov, D. S.; Wang, L. F.; Eaton, B. T.; Broder, C. C., Ephrin-B2 ligand is a functional receptor for Hendra virus and Nipah virus. *Proc. Natl. Acad. Sci. USA* **2005**, *102* (30), 10652-10657.
140. Negrete, O. A.; Levroney, E. L.; Aguilar, H. C.; Bertolotti-Ciarlet, A.; Nazarian, R.; Tajyar, S.; Lee, B., EphrinB2 is the entry receptor for Nipah virus, an emergent deadly paramyxovirus. *Nature* **2005**, *436* (7049), 401-5.
141. Negrete, O. A.; Wolf, M. C.; Aguilar, H. C.; Enterlein, S.; Wang, W.; Muhlberger, E.; Su, S. V.; Bertolotti-Ciarlet, A.; Flick, R.; Lee, B., Two key residues in ephrinB3 are critical for its use as an alternative receptor for Nipah virus. *PLoS Pathog* **2006**, *2* (2), e7.
142. Oldstone, M. B.; Homann, D.; Lewicki, H.; Stevenson, D., One, two, or three step: measles virus receptor dance. *Virology* **2002**, *299* (2), 162-3.
143. Tatsuo, H.; Ono, N.; Tanaka, K.; Yanagi, Y., SLAM (CDw150) is a cellular receptor for measles virus. *Nature* **2000**, *406* (6798), 893-897.
144. Tatsuo, H.; Ono, N.; Yanagi, Y., Morbilliviruses use signaling lymphocyte activation molecules (CD150) as cellular receptors. *J. Virol.* **2001**, *75* (13), 5842-5850.
145. Bossart, K. N.; Broder, C. C., Paramyxovirus Entry. In *Viral Entry into Host Cells*, Pohlmann, S.; Simmons, G., Eds. Landes Bioscience: Austin, TX, 2009.
146. Hu, X. L.; Ray, R.; Compans, R. W., Functional Interactions between the Fusion Protein and Hemagglutinin-Neuraminidase of Human Parainfluenza Viruses. *J. Virol.* **1992**, *66* (3), 1528-1534.

147. McGinnes, L. W.; Morrison, T. G., Inhibition of receptor binding stabilizes newcastle disease virus HN and F protein-containing complexes. *J. Virol.* **2006**, *80* (6), 2894-2903.
148. Melanson, V. R.; Iorio, R. M., Addition of N-glycans in the stalk of the Newcastle disease virus HN protein blocks its interaction with the F protein and prevents fusion. *J. Virol.* **2006**, *80* (2), 623-633.
149. Plemper, R. K.; Hammond, A. L.; Gerlier, D.; Fielding, A. K.; Cattaneo, R., Strength of envelope protein interaction modulates cytopathicity of measles virus. *J. Virol.* **2002**, *76* (10), 5051-5061.
150. Yao, Q. Z.; Hu, X. L.; Compans, R. W., Association of the parainfluenza virus fusion and hemagglutinin-neuraminidase glycoproteins on cell surfaces. *J. Virol.* **1997**, *71* (1), 650-656.
151. Deng, R.; Wang, Z.; Mirza, A. M.; Iorio, R. M., Localization of a domain on the paramyxovirus attachment protein required for the promotion of cellular fusion by its homologous fusion protein spike. *Virology* **1995**, *209* (2), 457-469.
152. Tanabayashi, K.; Compans, R. W., Functional interaction of paramyxovirus glycoproteins: identification of a domain in Sendai virus HN which promotes cell fusion. *J. Virol.* **1996**, *70* (9), 6112-6118.
153. Tsurudome, M.; Kawano, M.; Yuasa, T.; Tabata, N.; Nishio, M.; Komada, H.; Ito, Y., Identification of Regions on the Hemagglutinin-Neuraminidase Protein of Human Parainfluenza Virus Type-2 Important for Promoting Cell-Fusion. *Virology* **1995**, *213* (1), 190-203.

154. Gravel, K. A.; Morrison, T. G., Interacting domains of the HN and F proteins of newcastle disease virus. *J. Virol.* **2003**, *77* (20), 11040-11049.
155. Tomasi, M.; Pasti, C.; Manfrinato, C.; Dallochio, F.; Bellini, T., Peptides derived from the heptad repeat region near the C-terminal of Sendai virus F protein bind the hemagglutinin-neuraminidase ectodomain. *FEBS Lett* **2003**, *536* (1-3), 56-60.
156. Nussbaum, O.; Broder, C. C.; Moss, B.; Stern, L. B.; Rozenblatt, S.; Berger, E. A., Functional and structural interactions between measles virus hemagglutinin and CD46. *J. Virol.* **1995**, *69* (6), 3341-3349.
157. Paal, T.; Brindley, M. A.; St Claire, C.; Prussia, A.; Gauss, D.; Krumm, S. A.; Snyder, J. P.; Plemper, R. K., Probing the spatial organization of Measles Virus fusion complexes. *Submitted to J. Virol.* **2009**.
158. von Messling, V.; Zimmer, G.; Herrler, G.; Haas, L.; Cattaneo, R., The hemagglutinin of canine distemper virus determines tropism and cytopathogenicity. *J Virol* **2001**, *75* (14), 6418-27.
159. Stern, L. B.; Greenberg, M.; Gershoni, J. M.; Rozenblatt, S., The hemagglutinin envelope protein of canine distemper virus (CDV) confers cell tropism as illustrated by CDV and measles virus complementation analysis. *J Virol* **1995**, *69* (3), 1661-8.
160. McGinnes, L.; Sergel, T.; Morrison, T., Mutations in the transmembrane domain of the HN protein of Newcastle disease virus affect the structure and activity of the protein. *Virology* **1993**, *196* (1), 101-110.
161. Smith, B. J.; Lawrence, M. C.; Colman, P. M., Modelling the structure of the fusion protein from human respiratory syncytial virus. *Protein Eng.* **2002**, *15* (5), 365-371.

162. Deng, R.; Mirza, A. M.; Mahon, P. J.; Iorio, R. M., Functional chimeric HN glycoproteins derived from Newcastle disease virus and human parainfluenza virus-3. *Arch. Virol. Suppl.* **1997**, *13*, 115-30.
163. Wang, Z.; Mirza, A. M.; Li, J.; Mahon, P. J.; Iorio, R. M., An oligosaccharide at the C-terminus of the F-specific domain in the stalk of the human parainfluenza virus 3 hemagglutinin-neuraminidase modulates fusion. *Virus Res* **2004**, *99* (2), 177-185.
164. Griffin, D. E., In *Fields Virology*, 5th ed.; Knipe, D. M.; Howley, P. M., Eds. Wolters Kluwer/Lippincott Williams & Wilkins: Philadelphia, PA, 2007; pp 1551-1585.
165. Lawrence, M. C.; Borg, N. A.; Streltsov, V. A.; Pilling, P. A.; Epa, V. C.; Varghese, J. N.; McKimm-Breschkin, J. L.; Colman, P. M., Structure of the haemagglutinin-neuraminidase from human parainfluenza virus type III. *J. Mol. Biol.* **2004**, *335* (5), 1343-1357.
166. Thompson, S. D.; Laver, W. G.; Murti, K. G.; Portner, A., Isolation of a Biologically-Active Soluble Form of the Hemagglutinin-Neuraminidase Protein of Sendai Virus. *J. Virol.* **1988**, *62* (12), 4653-4660.
167. Hofmann, K. S. W., TMBASE - A database of membrane spanning protein segments. *Biol. Chem. Hoppe-Seyle* **1993**, *374*, 166.
168. Cheng, J.; Randall, A. Z.; Sweredoski, M. J.; Baldi, P., SCRATCH: a protein structure and structural feature prediction server. *Nucl. Acids Res.* **2005**, *33* (suppl\_2), W72-76.
169. Jones, D. T., Protein secondary structure prediction based on position-specific scoring matrices. *J. Mol. Biol.* **1999**, *292* (2), 195-202.

170. Yuan, P.; Leser, G. P.; Demeler, B.; Lamb, R. A.; Jardetzky, T. S., Domain architecture and oligomerization properties of the paramyxovirus PIV 5 hemagglutinin-neuraminidase (HN) protein. *Virology* **2008**, *378* (2), 282-291.
171. Burkhard, P.; Kammerer, R. A.; Steinmetz, M. O.; Bourenkov, G. P.; Aebi, U., The coiled-coil trigger site of the rod domain of cortexillin I unveils a distinct network of interhelical and intrahelical salt bridges. *Struct. Fold. Des.* **2000**, *8* (3), 223-230.
172. Vongpunsawad, S.; Oezgun, N.; Braun, W.; Cattaneo, R., Selectively receptor-blind measles viruses: Identification of residues necessary for SLAM- or CD46-induced fusion and their localization on a new hemagglutinin structural model. *J. Virol.* **2004**, *78* (1), 302-313.
173. Armstrong, M. A.; Fraser, K. B.; Dermott, E.; Shirodaria, P. V., Immunoelectron microscopic studies on haemagglutinin and haemolysin of measles virus in infected HEp2 cells. *J. Gen. Virol.* **1982**, *59* (Pt 1), 187-92.
174. Dutch, R. E.; Hagglund, R. N.; Nagel, M. A.; Paterson, R. G.; Lamb, R. A., Paramyxovirus fusion (F) protein: a conformational change on cleavage activation. *Virology* **2001**, *281* (1), 138-150.
175. Gallagher, P.; Henneberry, J.; Wilson, I.; Sambrook, J.; Gething, M. J., Addition of carbohydrate side-chains at novel sites on Influenza-Virus Hemagglutinin can modulate the folding, transport, and activity of the molecule. *J. Cell Biol.* **1988**, *107* (6), 2059-2073.
176. Tsuchiya, E.; Sugawara, K.; Hongo, S.; Matsuzaki, Y.; Muraki, Y.; Li, Z. N.; Nakamura, K., Effect of addition of new oligosaccharide chains to the globular head of

influenza A/H2N2 virus haemagglutinin on the intracellular transport and biological activities of the molecule. *J Gen Virol* **2002**, *83*, 1137-1146.

177. Bowden, T. A.; Aricescu, A. R.; Gilbert, R. J. C.; Grimes, J. M.; Jones, E. Y.; Stuart, D. I., Structural basis of Nipah and Hendra virus attachment to their cell-surface receptor ephrin-B2. *Nature Structural & Molecular Biology* **2008**, *15* (6), 567-572.

178. Bowden, T. A.; Crispin, M.; Harvey, D. J.; Aricescu, A. R.; Grimes, J. M.; Jones, E. Y.; Stuart, D. I., Crystal structure and carbohydrate analysis of nipah virus attachment glycoprotein: a template for antiviral and vaccine design. *J. Virol.* **2008**, *82* (23), 11628-11636.

179. Navaratnarajah, C. K.; Vongpunsawad, S.; Oezguen, N.; Stehle, T.; Braun, W.; Hashiguchi, T.; Maenaka, K.; Yanagi, Y.; Cattaneo, R., Dynamic interaction of the measles virus hemagglutinin with its receptor signaling lymphocytic activation molecule (SLAM, CD150). *J Biol Chem* **2008**, *283* (17), 11763-11771.

180. Duhovny, D.; Nussinov, R.; Wolfson, H. J., Efficient unbound docking of rigid molecules. In *Proceedings of the 2nd workshop on algorithms in bioinformatics*, Gusfield, D. M., Ed. Springer Verlag: Rome, Italy, 2002; pp 185-200.

181. Lyskov, S.; Gray, J. J., The RosettaDock server for local protein-protein docking. *Nucleic Acids Res.* **2008**, *36*, W233-W238.

182. Daily, M. D.; Masica, D.; Sivasubramanian, A.; Somarouthu, S.; Gray, J. J., CAPRI rounds 3-5 reveal promising successes and future challenges for RosettaDock. *Proteins* **2005**, *60* (2), 181-186.

183. Gray, J. J.; Moughon, S.; Wang, C.; Schueler-Furman, O.; Kuhlman, B.; Rohl, C. A.; Baker, D., Protein-protein docking with simultaneous optimization of rigid-body displacement and side-chain conformations. *J. Mol. Biol.* **2003**, *331* (1), 281-299.
184. Wang, C.; Schueler-Furman, O.; Baker, D., Improved side-chain modeling for protein-protein docking. *Protein Sci.* **2005**, *14* (5), 1328-1339.
185. Sun, A.; Yoon, J.; Yin, Y.; Prussia, A.; Yang, Y.; Min, J.; Plemper, R. K.; Snyder, J. P., Potent non-nucleoside inhibitors of the measles virus RNA-dependent RNA polymerase complex. *J. Med. Chem.* **2008**, *51* (13), 3731-3741.
186. White, L. K.; Yoon, J. J.; Lee, J. K.; Sun, A. M.; Du, Y. H.; Fu, H.; Snyder, J. P.; Plemper, R. K., Nonnucleoside inhibitor of measles virus RNA-Dependent RNA polymerase complex activity. *Antimicrob. Agents Chemother.* **2007**, *51* (7), 2293-2303.
187. Sun, A.; Chandrakumar, N.; Yoon, J. J.; Plemper, R. K.; Snyder, J. P., Non-nucleoside inhibitors of the measles virus RNA-dependent RNA polymerase complex activity: Synthesis and in vitro evaluation. *Bioorg. Med. Chem. Lett.* **2007**, *17* (18), 5199-5203.
188. Palyulin, V. A.; Radchenko, E. V.; Zefirov, N. S., Molecular Field Topology Analysis Method in QSAR Studies of Organic Compounds. *J. Chem. Inf. Model.* **2000**, *40* (3), 659-667.
189. Mel'nikov, A. A.; Palyulin, V. A.; Zefirov, N. S., Generation of molecular graphs for QSAR studies. *Dokl. Chem.* **2005**, *402*, 81-85.
190. Wold, S.; Eriksson, L., Chemometric Methods in Molecular Design. In *Methods and Principles in Medicinal Chemistry*, van der Waterbeemd, H., Ed. VCH Publishers, Inc.: New York, 1995; Vol. 2, pp 309-317.

191. Wani, M. C.; Taylor, H. L.; Wall, M. E.; Coggon, P.; McPhail, A. T., Plant antitumor agents. VI. The isolation and structure of taxol, a novel antileukemic and antitumor agent from *Taxus brevifolia*. *J. Am. Chem. Soc.* **1971**, *93* (9), 2325-2327.
192. Schiff, P. B.; Fant, J.; Horwitz, S. B., Promotion of microtubule assembly in vitro by taxol. *Nature* **1979**, *277* (5698), 665-667.
193. Orr, G.; Verdier-Pinard, P.; Mcdaid, H.; Horwitz, S., Mechanisms of Taxol resistance related to microtubules. *Oncogene* **2003**, *22* (47), 7280-7295.
194. Nuijen, B.; Bouma, M.; Schellens, J. H.; Beijnen, J. H., Progress in the development of alternative pharmaceutical formulations of taxanes. *Invest. New Drugs* **2001**, *19* (2), 143-153.
195. Jordan, M. A.; Wilson, L., Microtubules as a target for anticancer drugs. *Nat. Rev. Cancer* **2004**, *4* (4), 253-265.
196. Nogales, E.; Wolf, S. G.; Downing, K. H., Structure of the alpha beta tubulin dimer by electron crystallography. *Nature* **1998**, *391* (6663), 199-203.
197. Li, H.; DeRosier, D. J.; Nicholson, W. V.; Nogales, E.; Downing, K. H., Microtubule structure at 8 Å resolution. *Structure* **2002**, *10* (10), 1317-1328.
198. Díaz, J. F.; Barasoain, I.; Souto, A. A.; Amat-Guerri, F.; Andreu, J. M., Macromolecular accessibility of fluorescent taxoids bound at a paclitaxel binding site in the microtubule surface. *J. Biol. Chem.* **2005**, *280* (5), 3928-3937.
199. Sato, B.; Muramatsu, H.; Miyauchi, M.; Hori, Y.; Takase, S.; Hino, M.; Hashimoto, S.; Terano, H., A new antimitotic substance, FR182877. I. Taxonomy, fermentation, isolation, physico-chemical properties and biological activities. *J. Antibiot.* **2000**, *53* (2), 123-130.

200. Sato, B.; Nakajima, H.; Hori, Y.; Hino, M.; Hashimoto, S.; Terano, H., A new antimetabolic substance, FR182877. II. The mechanism of action. *J. Antibiot.* **2000**, *53* (2), 204-206.
201. Vosburg, D. A.; Vanderwal, C. D.; Sorensen, E. J., A synthesis of (+)-FR182877, featuring tandem transannular Diels-Alder reactions inspired by a postulated biogenesis. *J. Am. Chem. Soc.* **2002**, *124* (17), 4552-4553.
202. Edler, M. C.; Buey, R. M.; Gussio, R.; Marcus, A. I.; Vanderwal, C. D.; Sorensen, E. J.; Diaz, J. F.; Giannakakou, P.; Ernest, H., Cyclostreptin (FR182877), an antitumor tubulin-polymerizing agent deficient in enhancing tubulin assembly despite its high affinity for the taxoid site. *Biochemistry* **2005**, *44* (34), 11525-11538.
203. Buey, R. M.; Calvo, E.; Barasoain, I.; Pineda, O.; Edler, M. C.; Matesanz, R.; Cerezo, G.; Vanderwal, C. D.; Day, B. W.; Sorensen, E. J.; López, J. A.; Andreu, J. M.; Hamel, E.; Díaz, J. F., Cyclostreptin binds covalently to microtubule pores and luminal taxoid binding sites. *Nat. Chem. Biol.* **2007**, *3* (2), 117-125.
204. Bai, R.; Vanderwal, C. D.; Díaz, J. F.; Hamel, E., Interaction of a cyclostreptin analogue with the microtubule taxoid site: the covalent reaction rapidly follows binding. *J. Nat. Prod.* **2008**, *71* (3), 370-374.
205. Snyder, J. P.; Nettles, J. H.; Cornett, B.; Downing, K. H.; Nogales, E., The binding conformation of Taxol in beta-tubulin: A model based on electron crystallographic density. *Proc. Natl. Acad. Sci. USA* **2001**, *98* (9), 5312-5316.
206. Nettles, J. H.; Li, H. L.; Cornett, B.; Krahn, J. M.; Snyder, J. P.; Downing, K. H., The binding mode of epothilone A on alpha,beta-tubulin by electron crystallography. *Science* **2004**, *305* (5685), 866-869.

207. Ganesh, T.; Guza, R. C.; Bane, S.; Ravindra, R.; Shanker, N.; Lakdawala, A. S.; Snyder, J. P.; Kingston, D. G. I., The bioactive Taxol conformation on beta-tubulin: Experimental evidence from highly active constrained analogs. *Proc. Natl. Acad. Sci. USA* **2004**, *101* (27), 10006-10011.
208. Ganesh, T.; Yang, C.; Norris, A.; Glass, T.; Bane, S.; Ravindra, R.; Banerjee, A.; Metaferia, B.; Thomas, S. L.; Giannakakou, P.; Alcaraz, A. A.; Lakdawala, A. S.; Snyder, J. P.; Kingston, D. G. I., Evaluation of the tubulin-bound paclitaxel conformation: Synthesis, biology, and SAR studies of C-4 to C-3 ' bridged paclitaxel analogues. *J. Med. Chem.* **2007**, *50* (4), 713-725.
209. Shanker, N.; Kingston, D. G. I.; Ganesh, T.; Yang, C.; Alcaraz, A. A.; Geballe, M. T.; Banerjee, A.; McGee, D.; Snyder, J. P.; Bane, S., Enhanced microtubule binding and tubulin assembly properties of conformationally constrained paclitaxel derivatives. *Biochemistry* **2007**, *46* (41), 11514-11527.
210. Nogales, E.; Whittaker, M.; Milligan, R. A.; Downing, K. H., High-resolution model of the microtubule. *Cell* **1999**, *96* (1), 79-88.
211. Mitra, A.; Sept, D., Taxol allosterically alters the dynamics of the tubulin dimer and increases the flexibility of microtubules. *Biophys. J.* **2008**, *95* (7), 3252-3258.
212. Nettles, J. H. The molecular pharmacology of compounds that affect tubulin dynamics. Emory University, Atlanta, 2005.
213. Morris, G. M.; Goodsell, D. S.; Halliday, R. S.; Huey, R.; Hart, W. E.; Belew, R. K.; Olson, A. J., Automated docking using a Lamarckian genetic algorithm and an empirical binding free energy function. *J. Comput. Chem.* **1998**, *19* (14), 1639-1662.

214. Sherman, W.; Day, T.; Jacobson, M. P.; Friesner, R. A.; Farid, R., Novel procedure for modeling ligand/receptor induced fit effects. *J. Med. Chem.* **2006**, *49* (2), 534-553.
215. Schrodinger, L. *MACROMODEL, version 9.1*, New York, NY, 2007.
216. Polak, E.; Ribiere, G., Note on convergence of conjugate direction methods. *Rev. Fr. Inform. Rech. O.* **1969**, *3* (16), 35.
217. Klessig, R.; Polak, E., Efficient implementations of polak-ribiere conjugate gradient algorithm. *Siam J. Control* **1972**, *10* (3), 524.
218. Gonzalez, J.; Besada, V.; Garay, H.; Reyes, O.; Padron, G.; Tambara, Y.; Takao, T.; Shimonishi, Y., Effect of the position of a basic amino acid on C-terminal rearrangement of protonated peptides upon collision-induced dissociation. *J. Mass Spectrom.* **1996**, *31* (2), 150-158.
219. Vachet, R. W.; Bishop, B. M.; Erickson, B. W.; Glish, G. L., Novel peptide dissociation: Gas-phase intramolecular rearrangement of internal amino acid residues. *J. Am. Chem. Soc.* **1997**, *119* (24), 5481-5488.
220. Harrison, A. G.; Young, A. B.; Bleiholder, C.; Suhai, S.; Paizs, B., Scrambling of sequence information in collision-induced dissociation of peptides. *J. Am. Chem. Soc.* **2006**, *128* (32), 10364-10365.
221. Schaefer, M.; Fuchs, R.; Budzikiewicz, H.; Springer, A.; Meyer, J.; Linscheid, M., Structure elucidation of cyclic pyoverdins and examination of rearrangement reactions in MS/MS experiments by determination of exact product ion masses. *J. Mass Spectrom.* **2006**, *41* (9), 1162-1170.

222. Harvey, D. J.; Mattu, T. S.; Wormald, M. R.; Royle, L.; Dwek, R. A.; Rudd, P. M., "Internal residue loss": Rearrangements occurring during the fragmentation of carbohydrates derivatized at the reducing terminus. *Anal. Chem.* **2002**, *74* (4), 734-740.
223. Dal Piaz, F.; De Leo, M.; Braca, A.; De Simone, F.; De Tommasi, N., Intramolecular interchain reactions in bidesmosidic glycosides, a new insight into carbohydrate rearrangements induced by electrospray ionisation. *Rapid Commun. Mass Spectrom.* **2007**, *21* (3), 286-296.
224. Carey, F. A.; Sundberg, R. J., *Advanced Organic Chemistry*. Kluwer Academic/Plenum Publishers: New York, 2000; Vol. Part A, p 192-204.
225. Maskill, H., *Structure and Reactivity in Organic Chemistry*. Oxford University Press: Oxford, 1999; p 20-23.
226. Arno, M.; Zaragoza, R. J.; Domingo, L. R., A DFT study of the asymmetric (S)-5-(pyrrolidin-2-yl)-1H-tetrazole catalyzed Michael addition of carbonyl compounds to nitroalkenes. *Tetrahedron: Asymmetry* **2007**, *18* (2), 157-164.
227. Borowka, J.; van Wullen, C., Computational studies on the copper(II) catalyzed Michael reaction. *J. Organomet. Chem.* **2006**, *691* (21), 4474-4479.
228. Csuros, Z.; Sallay, P.; Deak, G., Synthesis of 2,4,6-triarylpyrylium fluorobarates from aromatic aldehydes and aryl methyl ketones. 4. Reaction kinetics of michael addition of chalcone and acetophenone, catalyzed by boron trifluoride. *Acta Chimica Academiae Scientiarum Hungaricae* **1973**, *79* (3), 341-348.
229. Ivanova, S.; Aleksiev, D. I., Kinetic studies on the reaction of sulfinic acids with conjugated alkenes, V: Kinetics of the addition of arenesulfinic acids to 1-aryl-1-

arylsulfonyl-2-nitroethenes. *Phosphorus Sulfur Silicon Relat. Elem.* **2006**, *181* (7), 1593-1600.

230. Yasuda, M.; Chiba, K.; Ohigashi, N.; Katoh, Y.; Baba, A., Michael addition of stannyl ketone enolate to alpha,beta-unsaturated esters catalyzed by tetrabutylammonium bromide and an ab initio theoretical study of the reaction course. *J. Am. Chem. Soc.* **2003**, *125* (24), 7291-7300.

231. Schweitz, H.; Vincent, J. P.; Lazdunski, M., Trypsin-pancreatic secretory inhibitor (Kazal inhibitor) interaction. Kinetic and thermodynamic properties. *Biochemistry* **1973**, *12* (15), 2841-2846.

232. Dalpiaz, A.; Pavan, B.; Ngos, F. N.; Franchetti, P.; IJzerman, A. P., Temperature dependence of the affinity enhancement of selective adenosine A(1) receptor agonism: a thermodynamic analysis. *Eur. J. Pharmacol.* **2002**, *448* (2-3), 123-131.

233. Navratilova, I.; Papalia, G. A.; Rich, R. L.; Bedinger, D.; Brophy, S.; Condon, B.; Deng, T.; Emerick, A. W.; Guan, H.; Hayden, T.; Heutmekers, T.; Hoorelbeke, B.; McCroskey, M. C.; Murphy, M. M.; Nakagawa, T.; Parmeggiani, F.; Qin, X.; Rebe, S.; Tomasevic, N.; Tsang, T.; Waddell, M. B.; Zhang, F. F.; Leavitt, S.; Myszka, D. G., Thermodynamic benchmark study using Biacore technology. *Anal. Biochem.* **2007**, *364* (1), 67-77.